KAUNAS UNIVERSITY OF TECHNOLOGY

MATAS GUŽAUSKAS

TUNING OF INTRAMOLECULAR AND INTERMOLECULAR CHARGE TRANSFER EMISSIONS OF NEW ORGANIC MATERIALS FOR SENSING AND ELECTROLUMINESCENT DEVICES

Doctoral dissertation
Technological Sciences, Materials Engineering (T 008)

2025, Kaunas

The dissertation has been prepared at the Department of Polymer Chemistry and Technology of the Faculty of Chemical Technology of Kaunas University of Technology in 2020–2024. The research has been sponsored by the Research Council of Lithuania.

Research supervisor:
Chief Researcher Dr. Hab. Dmytro VOLYNIUK (Kaunas University of Technology, Technological Sciences, Materials Engineering, T 008).

Research consultant:
Dr. Rita BUTKUTĖ (Kaunas University of Technology, Technological Sciences, Chemical Engineering, T 005).

Edited by: English language editor Birutė Jurkšaitė (Publishing House *Technologija*), Lithuanian language editor Rita Malikenienė (Publishing House *Technologija*).

The dissertation defence will be held on 7 February 2025, at 1 p.m. in a public meeting of the Dissertation Defence Board of the Materials Engineering science field at the Rectorate hall of Kaunas University of Technology.

Address: K. Donelaičio 73-402, LT-44249 Kaunas, Lithuania.
Phone: (+370) 608 28 527; e-mail doktorantura@ktu.lt

The dissertation was sent out on 7 January 2025.
The dissertation is available on http://ktu.edu and at the Library of Kaunas University of Technology (Gedimino 50, LT-44239 Kaunas, Lithuania).

KAUNO TECHNOLOGIJOS UNIVERSITETAS

MATAS GUŽAUSKAS

NAUJŲ ORGANINIŲ MEDŽIAGŲ, SKIRTŲ JUTIKLIAMS IR ELEKTROLUMINESCENCINIAMS PRIETAISAMS, INTRAMOLEKULINĖS IR TARPMOLEKULINĖS KRŪVIO PERNAŠOS EMISIJOS REGULIAVIMAS

Daktaro disertacija
Technologijos Mokslai, medžiagų inžinerija (T 008)

2025, Kaunas

Disertacija rengta 2020–2024 metais Kauno technologijos universiteto Cheminės Technologijos fakultete Polimerų Chemijos ir Technologijos katedroje. Mokslinius tyrimus rėmė Lietuvos mokslo taryba.

Mokslinis vadovas:
vyriausiasis mokslo darbuotojas habil. dr. Dmytro VOLYNIUK (Kauno technologijos universitetas, technologijos mokslai, medžiagų inžinerija, T 008).

Mokslinis konsultantas:
dr. Rita Butkutė (Kauno technologijos universitetas, technologijos mokslai, chemijos inžinerija, T 005).

Redagavo: anglų kalbos redaktorė Birutė Jurkšaitė (leidykla „Technologija“), lietuvių kalbos redaktorė Rita Malikenienė (leidykla „Technologija“).

Medžiagų inžinerijos mokslo krypties disertacijos gynimo taryba:
prof. habil. dr. Sigitas TAMULEVIČIUS (Kauno technologijos universitetas, technologijos mokslai, medžiagų inžinerija, T 008) – **pirmininkas**;
vyr. m. d. dr. Šarūnas Meškinis (Kauno technologijos universitetas, technologijos mokslai, medžiagų inžinerija, T 008);
prof. dr. Jolita Ostrauskaitė (Kauno technologijos universitetas, technologijos mokslai, medžiagų inžinerija, T 008);prof. dr. Törmä Päivi (Alto universitetas, Suomija, gamtos mokslai, fizika, N 002);prof. dr. Gediminas Račiukaitis (Valstybinis mokslinių tyrimų institutas Fizinių ir technologijos mokslų centras, gamtos mokslai, fizika, N 002).

Disertacija bus ginama viešame Medžiagų inžinerijos mokslo krypties disertacijos gynimo tarybos posėdyje 2025 m. vasario 7 d. 13 val. Kauno technologijos universiteto Rektorato salėje.

Adresas: K. Donelaičio g. 73-402, LT-44249 Kaunas, Lietuva.
Tel: (+370) 608 28 527; el. paštas doktorantura@ktu.lt

Disertacija išsiųsta 2025 m. sausio 7 d.
Su disertacija galima susipažinti interneto svetainėje http://ktu.edu ir Kauno technologijos universiteto bibliotekoje (Gedimino g. 50, LT-44239 Kaunas, Lietuva).

CONTENTS

LIST OF TABLES

LIST OF FIGURES

LIST OF ABBREVIATIONS

1 – bis(4-(5,5-dioxido-10*H*-phenothiazin-10-yl)phenyl)methanone
2 – 10,10'-(sulfonylbis(4,1-phenylene))bis(10*H*-phenothiazine 5,5-dioxide)
3 – 2-(3,6-di-tert-butyl-9*H*-carbazol-9-yl)-10-hexylacridin-9(10*H*)-one
4 – 2,7-bis(3,6-di-tert-butyl-9*H*-carbazol-9-yl)-10-hexylacridin-9(10*H*)-one
5 – 10-hexyl-2-(10*H*-phenoxazin-10-yl)acridin-9(10*H*)-one
6 – 10-hexyl-2,7-di(10*H*-phenoxazin-10-yl)acridin-9(10*H*)-one
7 – 2,7-bis(3-(10*H*-phenoxazin-10-yl)phenyl)-10-hexylacridin-9(10*H*)-one
8 – 2,10-bis(3,6-di-tert-butyl-9*H*-carbazol-9-yl)-5,12-dioctylquinolino[2,3-b]acridine 7,14(5*H*,12*H*)-dione
9 – 3,6-di-tert-butyl-9-(2',4',6'-trifluoro-[1,1'-biphenyl]-3-yl)-9*H*-carbazole
10 – 9,9'-(2',4',6'-trifluoro-[1,1'-biphenyl]-3,5-diyl)bis(3,6-di-tert-butyl-9*H*-carbazole)
A – acceptor
ACQ – aggregation caused quenching
Acr – acridone
AFM – atomic force microscopy
AIE – aggregation-induced emission
AIEE – aggregation-induced enhanced emission
Al – aluminium
CE – current efficiency
CIE – Commission Internationale de l'Éclairage
CT – charge transfer
CV – cyclic voltammetry
D – donor
DF – delayed fluorescence
DMAC-TRZ – 10-(4-(4,6-diphenyl-1,3,5-triazin-2-yl)phenyl)-9,9-dimethyl-9,10-dihydroacridine
DMF – dimethylformamide
DSC – differential scanning calorimetry
EA – electron affinity
EBL – electron blocking layer
E_C – Coulombic energy
E_g – band gab
EL – electroluminescence
EML – emissive layer
E_{OX} – oxidation energy
EQE – external quantum efficiency
E_{red} – reduction energy
E_S – singlet level energy
E_T – triplet level energy
ETL – electron transporting layer
Fc – ferrocene

FET – field effect transistor
FWHM – full width at half maximum
GMP – Gibson-Monkman-Penfold mechanism
HAT-CN – 1,4,5,8,9,11-hexaazatriphenylenehexacarbonitrile
HBL – hole blocking layer
HIL – hole injection layer
HLCT – hybrid local charge transfer
HOMO – highest occupied molecular orbital
HTL – hole transporting layer
I – intensity
ICT – intermolecular charge transfer
IP – ionization potential
IQE – internal quantum efficiency
ISC – intersystem crossing
ITO – indium tin oxide
k_{DF} – delayed fluorescence rate constant
k_{ISC} – intersystem crossing rate constant
k_{PF} – prompt fluorescence rate constant
k_{RISC} – reverse intersystem crossing rate constant
K_{SV} – Stern-Volmer rate constant
L – brightness
LE – local excitation
LiF – lithium fluoride
LUMO – lowest unoccupied molecular orbital
mCBP – 3,3′-di(9*H*-carbazol-9-yl)-1,1′-biphenyl
mCP – 1,3-bis(*N*-carbazolyl)benzene
MO – molecular orbital
MoO_3 – molybdenum oxide
NPB – *N*,*N*′-di(1-naphthyl)-*N*,*N*′-diphenyl-(1,1′-biphenyl)-4,4′-diamine
NTO – natural transition orbitals
OFET – organic field effect transistor
OLED – organic light emitting diode
OSC – organic solar cell
PE – photoelectron spectroscopy
PF – prompt fluorescence
PhNZ – phenothiazine
PL – photoluminescence
PLQY – photoluminescence quantum yield
PO-T2T – 2,4,6-tri[3-(diphenylphosphinyl)phenyl]-1,3,5-triazine
P_{Sol} – solvent polarizability
QAcr – quinacridone
RISC – reverse intersystem crossing
R_q – root mean square roughness
S – singlet

SM66 – 3,6-di-tert-butyl-9-(2-(1-phenyl-1*H*-benzo[d]imidazol-2-yl)phenyl)−9*H*-carbazole
T – triplet
TA – transient absorption
TADF – thermally activated delayed fluorescence
TAPC – 1,1-bis[(di-4-tolylamino)phenyl]cyclohexane
T_{cr} – crystallisation temperature
TCTA – tris(4-carbazoyl-9-ylphenyl)amine
tCz – tertbutyl carbazole
TDDFT – time-dependent density functional theory
TEMPO – (2,2,6,6-tetramethylpiperidin-1-yl)oxyl
T_g – glass transition temperature
TGA – thermogravimetric analysis
THF – tetrahydrofuran
TICT – twisted intramolecular charge transfer
T_D – mass loss temperature
T_m – melting temperature
TOF – time of flight
TPBi – 2,2',2"-(1,3,5-benzinetriyl)-tris(1-phenyl-1-*H*-benzimidazole)
TSPO1 – diphenyl[4-(triphenylsilyl)phenyl]phosphine
UV – ultraviolet
UV-Vis – ultraviolet–visible spectroscopy
V_{on} – turn-on voltage
XRD – X-ray diffraction
ZEONEX – cyclo olefin polymer
β – field dependence parameter
ΔE_{ST} – singlet-triplet energy gap
η_{out} – outcoupling coefficient
λ – wavelength
μ_0 – mobilities at absent electric field
μ_e – electron mobility
μ_h – hole mobility
τ – time
Φ – quantum yield

1. INTRODUCTION

At this point, it would be a cliché to state that Tang and Van Slyke made the first organic light-emitting diode (OLED)[1]. Although they were pioneers in this field, the device they produced was quite simplistic. Over the past 30 years, researchers around the world have developed optoelectronic devices with more complex structures[2–5], more intricate emission mechanisms than simple fluorescence[6–12], and even devices with simple structures that show excellent properties[13–16]. Although Tang and Van Slyke's device pales in comparison to those of today, they demonstrated that organic materials can serve as a viable alternative for optoelectronic applications.

They were not wrong. In 2022, the organic semiconductor market was valued at 116.9 billion USD, and by 2030, it is predicted to reach 566 billion USD[17,18]. The rising potential of organic semiconductors is due to their applicability in numerous fields, such as OLEDs, organic solar cells (OSCs)[19], organic field-effect transistors (OFETs)[20], and organic sensors (e.g., gas, UV, visible light, radiation)[21–24]. Another factor contributing to the growth of organic electronics is their suitability for flexible electronics (e.g., rollable screens, e-papers, smart sensors)[25–28]. Finally, organic semiconductors, compared to their inorganic counterparts, are more sustainable and eco-friendly due to their recyclability [29] and low production[30,31] costs. These and other factors are driving the rapid expansion of this field.

However, it is the flexibility and intrinsic qualities of organic semiconductors that hold their true promise. Conventional inorganic semiconductors are based on rigid crystalline structures[32], whereas organic semiconductors are composed of dynamic molecules. The molecular structure, rotation, vibration, and movement that define their characteristics also influence the material's optical and electrical behaviour. Due to their natural flexibility, their properties can change in response to external stimuli. For example, Zhu et al. demonstrated that exposure to UV light enhances the fluorescence of perylene Schiff-base derivatives[33]. This effect, believed by the researchers to be caused by the UV-induced trans-to-cis isomerization of the molecules, modifies the chemical structure and increases fluorescence intensity. The potential to create very sensitive and selective sensors for a range of applications, from UV radiation detection to optical communications wavelength monitoring, is made possible by this sensitivity to electromagnetic radiation. Similarly, Wang et al. improved the performance of solution-processed OLEDs by using annealing treatments to adjust the molecular transition dipole moment[34] of the emission layers. By simply altering the annealing temperature, scientists were able to fine-tune the molecular arrangement, resulting in improved carrier mobility and more efficient light emission. This demonstrates the extent to which external influences may affect the behaviour of organic semiconductors and suggests promising possibilities for constructing cutting-edge optoelectronic devices by carefully manipulating these molecules.

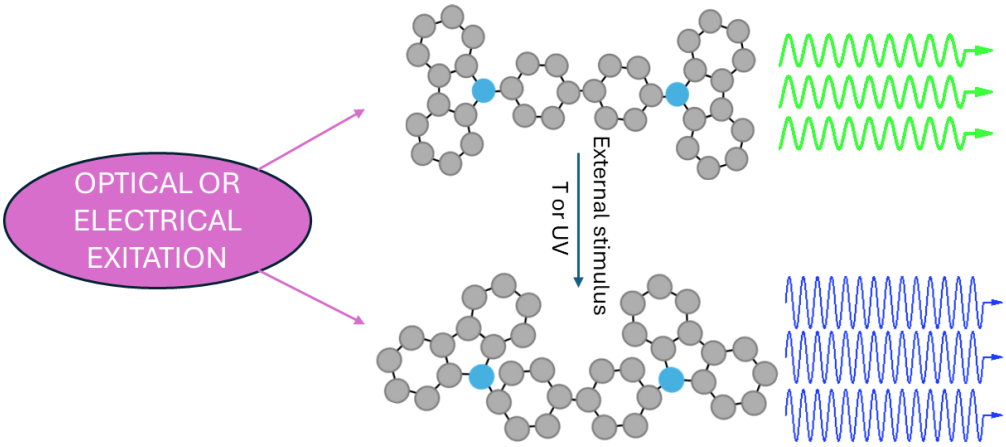

Fig. 1. Simplified schematic showing how external stimulus affects molecule and its properties

Motivated by these potential outcomes, this work explores how external stimuli affects the optical properties of three distinct series of organic semiconductors.

In this dissertation, three series of organic semiconductors are presented. Each series of compounds exhibits changes in their emissive properties due to external stimuli, such as UV light or temperature. The discussed properties demonstrate that conformation and/or morphology changes induced by external stimuli influence thermally activated delayed fluorescence (TADF) properties (Fig. 1). Furthermore, TADF enhancement due to external stimuli exploitation and application is presented as sensors or OLED devices.

This research contributes to the expanding knowledge in the field by examining the fundamental principles that regulate the behaviour of organic semiconductors and investigating the effects of external stimuli on their properties. The discoveries establish a foundation for the development of state-of-the-art optoelectronic devices with enhanced performance, efficiency, and sustainability.

The goal of this study is to examine how the molecular conformation, packing, and morphology of organic semiconductor compounds influence their photophysical, electrophysical, and optoelectronic properties when exposed to various external stimuli.

To accomplish this goal, the following tasks were established:

- Conduct a photophysical study of the selected compounds to determine their emission mechanisms;
- Explore the potential of benzophenone and phenothiazine-5,5-dioxide derivatives for UV sensing by investigating the dependence of their TADF intensity on UV excitation;
- Design, fabricate, and characterise the electroluminescent properties of OLEDs containing acridone and quinacridone derivatives;
- Investigate the impact of structural properties of acridone and phenoxazine derivatives on their photophysical properties for OLED applications;

- Study the exciplex-forming properties of trifluorobiphenyl and carbazole derivatives for electroluminescent devices.

The novelty of this work

- The phenomenon of photostimulated fluorescence in an organic emitter, where both emission colour and intensity vary under UV stimulus, is reported for the first time in benzophenone and diphenyl sulfone derivatives with phenothiazine-5,5-dioxide moieties. This work reveals a new mechanism for photostimulated fluorescence, which involves conformational isomerisation between two stable conformers of the dye molecule under UV irradiation.
- A series of innovative compounds derived from acridone and quinacridone with various donor segments was investigated. The emitted light from these compounds spans a broad spectrum of colours, ranging from blue to orange, influenced by their molecular structure and the presence of doping in a host material compound demonstrated distinctive characteristics, such as thermally activated delayed fluorescence and aggregation-induced emission enhancement, resulting in highly efficient light emission in OLEDs.
- Thermally controlled mechanochromic luminescence, where emission colours can be reversibly changed by external stimuli, such as grinding, fuming, heating, or annealing, is demonstrated for the first time using phenoxazine-substituted acridones. This work presents a novel approach to understanding how annealing-induced crystallisation affects the TADF characteristics of these compounds, significantly increasing the external quantum efficiency (EQE) of OLEDs.
- New carbazole-based emitters are characterised in this work, demonstrating their potential for application in high-efficiency OLEDs with EQEs of up to 7.8%. This study uniquely explores the formation of blue- and green-emitting exciplexes in OLED devices using a fluorinated acceptor, highlighting the importance of understanding interfacial exciplex formation for device optimisation.

Interrelation of the articles

This dissertation is structured around the scientific findings of four papers, each published in a first-quartile, top-tier journal. Copies of these publications and a complete list can be found in Sections 7 and 9, respectively. The key interrelation among the scientific results described in these articles is their contribution to tuning the charge-transfer emissions of novel organic light-emitting semiconductors, thereby enhancing their potential for practical applications. For instance, the first article demonstrates that the green charge-transfer emission of compounds containing benzophenone, diphenyl sulfone, or phenothiazine-5,5-dioxide moieties can be tuned to blue charge-transfer emission under UV excitation. These findings show the potential for applications in UV sensors. The second and third articles reveal that the charge-transfer emissions of the investigated compounds can be extensively tuned, and, in some cases, even reversed. Such tuning significantly enhances their thermally activated delayed fluorescence properties, resulting in improved electroluminescent performance in OLEDs. The fourth article presents findings on tuning ultraviolet intramolecular charge-transfer emissions to sky-blue intermolecular charge-

transfer emissions using an exciplex-based approach. Notably, thermally activated delayed fluorescence properties were activated for sky-blue intermolecular charge-transfer emissions, in contrast to ultraviolet intramolecular charge-transfer emissions, highlighting their potential for OLED applications.

These scientific findings on tuning charge-transfer emissions in organic light-emitting semiconductors have significant implications for the fields of materials science and contribute to the dissertation's overall objective of understanding how molecular conformations, packing, and morphology affect the photophysical, electrophysical, and optoelectronic characteristics of organic semiconductor compounds in response to external stimuli. They investigate the effects of heat treatment and UV irradiation on these characteristics, emphasising the importance of molecular packing and morphology in influencing the performance of organic electronic devices, such as OLEDs. By addressing these factors, the papers provide a comprehensive understanding of how external stimuli can induce changes at the molecular level, affecting the functionality of these substances in electronic devices.

Contribution of the author

The research presented in this dissertation was conducted by the author in collaboration with researchers from Kaunas University of Technology, KTH Royal Institute of Technology, Warsaw University of Technology, Vilnius University, the University of Glasgow, and CY Cergy Paris University. The author characterised the photophysical, photoelectrical, charge-transporting, and electroluminescent properties, as well as analysed all results from measurements conducted with collaborators across three compound series. Edgaras Narbutaitis synthesised benzophenone and diphenyl sulfone derivatives with phenothiazine-5,5-dioxide moieties, and crystallographic measurements were performed with his assistance. Theoretical calculations were conducted in collaboration with Dr. G. V. Baryshnikov, Dr. B. F. Minaev, and Dr. H. Ågren from KTH Royal Institute of Technology. The second series of acridone and quinacridone derivatives was synthesised by Dr. I. Kleszewicz-Bajer and Dr. M. Makowska-Janusik from Warsaw University of Technology. Together with their assistance, circular voltammetry measurements and theoretical calculations were conducted. The thermal properties were determined by Dr. M. Mahmoudi. X-ray diffraction (XRD) and atomic force microscopy measurements were performed with the help of Dr. A. Lazauskas from the Institute of Materials Science, Kaunas University of Technology. The transient absorption measurements were conducted by Dr. V. Jasinskas and Dr. V. Gulbinas from Vilnius University. The third series of trifluorophenyl and carbazole moieties was synthesised by Dr. R. Keruckiene and L. Liepenyte. The thermal properties were measured by Dr. J. Simokaitiene. Theoretical calculations were performed by Dr. J. Cameron from the University of Glasgow and Dr. G. Sini from CY Cergy Paris University. All charge mobility measurements and manuscript preparations were carried out with the help of Dr. Habil. D. Volyniuk. Dr. Habil. J. V. Grazulevicius assisted with article editing, review, and connecting with collaborators.

The articles incorporated in this dissertation are reproduced with the full legal consent of both the authors and publishers.

2. LITERATURE REVIEW

To predict the semiconducting and light-emitting properties of organic materials, understanding their electrical configurations is crucial. The electrical configurations of organic semiconductors originate from the atomic orbitals (AOs) of carbon, which contain six electrons. Carbon atoms can form chemical bonds with other atoms through various hybridised orbitals, including the sp, sp^2, and sp^3. For example, each carbon atom in the ethylene molecule has three sp^2 hybrid orbitals for bonding with other atoms[35]. The 1s orbital of a hydrogen atom combines with one of the sp^2 hybrid orbitals creating a molecular orbital (MO) known as an σ-orbital. Bonding is an important process in organic chemistry in which carbon atoms form bonds through sp^2 hybrid orbitals, resulting in the formation of a double bond. The π-electron cloud spreads across carbon atoms, creating a separate molecular π-orbital. This structure results in the formation of bonding and anti-bonding orbitals, with the anti-bonding orbital having a higher energy level than the bonding orbital. The π-orbitals are represented as π- and π*-MOs, respectively[36]. The best example of this is benzene, which consists of six carbon atoms connected by hybrid sp^2 orbitals, resulting in the formation of six π-bonding MOs[37]. The π-electron cloud exhibits delocalisation across the carbon atoms, facilitating electron mobility between them. The highest occupied molecular orbital (HOMO) refers to the highest energy level that contains electrons, while the lowest unoccupied molecular orbital (LUMO) refers to the energy level at which no electrons are present. The energy difference between the HOMO and the LUMO represents the amount of energy needed to stimulate an electron within the molecule. Photon absorption and emission processes are energetically favourable on π-orbitals, whereas σ-electrons are less likely to be stimulated due to the greater energy required for electronic transitions between σ-orbitals. The HOMO-LUMO energy gap diminishes as the π-conjugation system expands, resulting in enhanced π-electron delocalisation[38]. The HOMO and LUMO orbitals play critical roles in electronic transitions, including light absorption and emission. When light is absorbed, electrons transition to an empty π* state, resulting in the formation of a hole. An exciton refers to a Coulomb-bound hole-electron pair generated in an organic material[39].

Excitons are generated either through light absorption or by injected charges. They may return to their lowest energy state through various processes, such as light emission, non-radiative energy relaxation, or separation. Luminescence is one of the primary characteristics of organic semiconductors, and exciton properties are closely linked to the emitted light. There are three main types of excitons: Wannier-Mott[40], charge-transfer (CT)[41], and Frenkel excitons[42]. Frenkel excitons exhibit localisation on individual molecule fragments and are often referred to as locally excited (LE) excitons. LE excitons have a higher degree of localisation and are less affected by the surrounding environment, whereas CT excitons can be impacted by the polarity of their surroundings due to their solvatochromic properties[43]. Additionally, excitons possess multiplicity, which refers to the overall spin of a two-particle system.

Electrons and holes are fermions with spin values of 1/2 or -1/2. In a two-particle model, the total spin of an exciton can only be 1 or 0. The spin projection along the z-axis can take values of -1, 0, 1, or 0, respectively. A triplet exciton brings together particles in their ground and excited states, while a singlet exciton involves particles with spins opposite to each other[44]. Excitons in organic semiconductors have the ability to alter their multiplicity due to spin-orbit coupling. The LE or CT nature of the singlet and triplet states is controlled by their exciton radius[45].

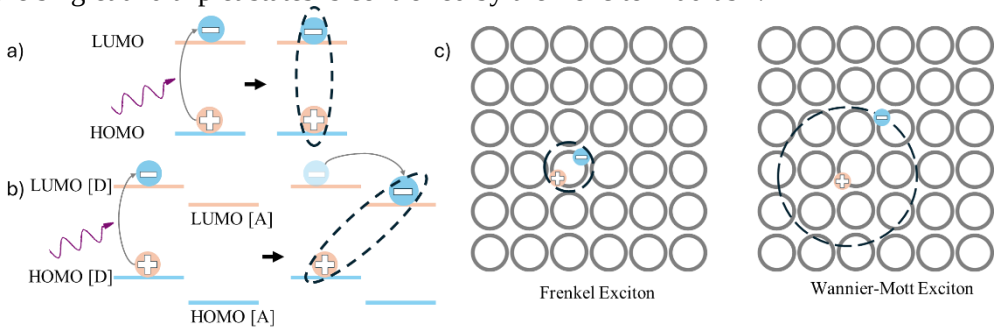

Fig. 2. Formation of Frenkel excitons (a) and charge-transfer excitons (b); radius of Frenkel and Wannier-Mott excitons (c)

It is essential to note that the conformation of a molecule affects its absorption and emission properties. The surrounding medium often influences the molecular conformation, thereby affecting the overlap of MOs. For example, molecules dissolved in low-polarity solvents may exhibit LE exciton emission, whereas in higher-polarity media, they may show both LE and CT exciton emission or only CT emission. Additionaly, the molecular conformation in solution can be affected by external stimuli, such as temperature[46] or UV[47].

Similarly, the emissive properties of solid-state samples depend on their molecular conformations. Emissive qualities can be significantly influenced by molecular packing[48], aggregate[49] formation, morphology[50], and whether the sample is crystalline[51] or amorphous[52]. For some molecules, aggregation can reduce emission intensity, which is known as aggregation-caused quenching (ACQ)[53]. Typical luminophores exhibit strong emissive properties in their isolated molecular form but may experience varying degrees of ACQ when grouped together or clustered. The aromatic rings of neighbouring luminophores, especially those with disc- or rod-like structures, undergo strong intermolecular π–π stacking interactions, causing the excited states to return to the ground state, which suppresses emission[54]. The opposite effect is observed when the emissive properties are improved by aggregation. This effect is called aggregation-induced emission (AIE). Depending on the structure of a molecule, isolated molecules may lose significant energy after excitation due to rotation and vibrational dissipation[53,55]. However, in aggregated forms, these factors are avoided because of the restrictions of intramolecular rotation[56,57], vibration[58,59], and movement[60,61]. These aggregate restrictions help reduce the losses caused by vibrational dissipation.

Furthermore, the morphology of the layer is crucial, especially in the field of OLEDs. The morphology of emissive layers, whether crystalline or amorphous, can significantly influence their properties. The optimal molecular alignment of organic crystals reduces traps, improves thermal stability, enhances charge carrier mobility, and increases light extraction efficiency in OLEDs, making them valuable for optoelectronic devices[62]. In particular, organic field-effect transistors exhibit superior performance compared to amorphous organic materials. However, the disadvantage of crystalline semiconductors is the difficulty in obtaining them in a thin and homogeneous form[63]. On the other hand, amorphous layers are easier to obtain. Amorphous organic films are frequently used in most OLEDs due to their flat surfaces, which ensure excellent uniformity and stability, even in the presence of high electric fields[64]. Amorphous films for OLEDs can be classified into two categories: vacuum-processed films and solution-processed films. The fabrication of high-purity, ideal multilayer structures enables the commercialisation of vacuum-processed films. Recently, Reineke et al. [65] presented work showing how forming an ultra-stable glass emitting layer can significantly increase the efficiency and lifetime of OLEDs[65]. As they established, due to material evaporation at a temperature close to the glass transition (0.85 T_g), they achieved better horizontal orientation of linear-shaped molecules, resulting in improved $\pi - \pi$ MO overlap and increased charge mobility. In conclusion, layer morphology is an important topic in organic optoelectronics, and understanding it is crucial, as both crystalline and amorphous materials have their advantages and disadvantages.'

As mentioned above, many factors affect the properties of organic semiconductors, including MOs, molecular conformation, interaction between molecules, and morphology. These various factors influencing organic semiconductor properties are especially critical in optoelectronic applications, where they govern the materials' ability to emit light. When the first OLED was produced in 1987, its emission was characterised as simple fluorescence. The phenomenon of fluorescence has been known since the Middle Ages[66] and is described as the energy relaxation of excited molecules back to the ground state, emitting a photon without changing the electron spin. As it cannot harvest triplet excitons, the emission results in an internal quantum efficiency[67] of 25 %. Later researchers developed phosphorescent OLEDs using organometallic emitters. These types of emitters allow for triplet exciton participation in the emission mechanism due to the strong spin-orbit coupling caused by the metal atom implemented into the organic structures. The advantage of OLEDs with phosphorescent emitters is their ability to achieve 100% internal quantum efficiency (IQE) and high electroluminescent stability[68]. However, a disadvantage is the incorporation of rare earth metals, such as Ir, Eu, Tb, Gd, Pt, and others[69], into the emitter structure. In 2012, Adachi et al.[70] demonstrated a process that achieved 100% IQE while avoiding the use of rare earth metals[70]. This process is known as thermally activated delayed fluorescence (TADF). The TADF effect arises from the presence of CT excitons in a molecule, which are created when the molecule has both a donor (D) moiety and an acceptor (A) moiety. The D component provides electrons, while the A component accepts them. This process involves the transmission of both holes and

electrons in opposite directions. When a molecule containing D-A or D-A-D moieties is subjected to optical excitation, the D component absorbs energy, causing an electron to migrate from the ground state (S_0) to the singlet state of the donor (S_1). This leads to the formation of a lower energy charge transfer singlet state (^{1}CT), where electrons are converted from the upper levels[71]. Typically, an intersystem crossing (ISC) mechanism occurs, enabling the movement of electrons from the ^{1}CT state to the triplet charge transfer state (^{3}CT). When the energy difference between ^{1}CT and ^{3}CT is minimal and the thermal energy of the surroundings is abundant, reverse intersystem crossing (RISC) may occur, converting electrons from a triplet state to a singlet state, resulting in delayed fluorescence. TADF emitters exhibit higher efficiency than fluorescence emitters due to their ability to capture both singlet and triplet excitons[72]. Additionally, TADF emitters can be easier to design and synthesise than phosphorescence emitters[73].

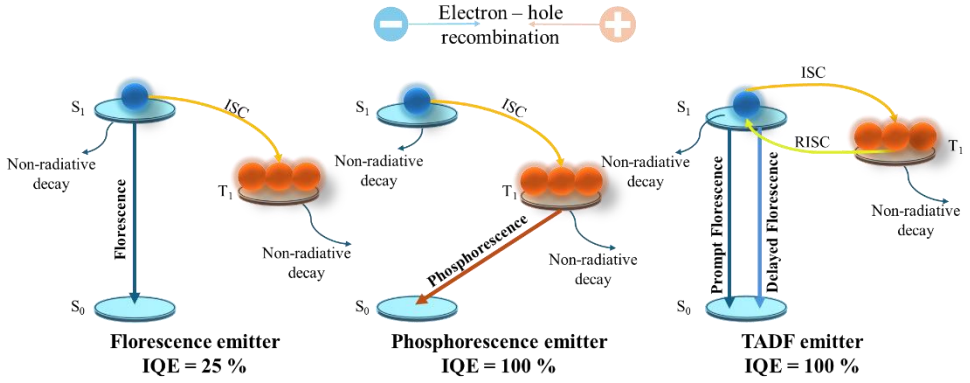

Fig. 3. Fluorescence, phosphorescence, and TADF emission mechanisms

The categorisation of electron donors and acceptors is based on a relative scale, although the interaction of inductive and resonant effects can complicate this. Charge transfer between strong and weak donor or acceptor moieties is possible in such cases[74,75]. Tsuchiya et al. presented the first example of TADF materials using strong and weak electron donors, which acted as an acceptor, in the D-D' type molecular architecture[76]. More recently, Adachi et al. demonstrated a donor-only D-π-D type compound that showed TADF properties[74].

Additionally, TADF can occur not only in single D-A or D-A-D type molecules but also between different D and A type molecules. The working principle is similar to that of typical TADF molecules; however, CT occurs between electron-donating and electron-accepting molecules[77]. In this case, a short-lived excited-state complex known as an exciplex is formed between the donor and acceptor molecules. The exciplex emission process involves the transfer of electrons from the LUMO of the donor to the LUMO of the acceptor. The energy difference between the singlet and triplet levels of the exciplex is minimal due to the spatial separation of the HOMO and LUMO between the donor and acceptor molecules[78]. Therefore, the exciplex tends to exhibit TADF features because of the small gap between singlet and triplet states, allowing triplet excitons to be transformed into singlet excitons by RISC during

thermal stimulation. This process leads to efficient singlet exciton emission through radiative transition[79]. A few years ago, Guzauskas et al. identified two exciplex species with high energy and two exciplex species with low energy in solid-state combinations that generate exciplexes[80]. The researchers claimed that these two bands could be separated by thermal annealing, which caused changes in the molecular conformations and packing as the morphology of the samples changed. These findings confirm the two-fold properties of exciplexes and present opportunities for the development of new exciplex-forming systems with high photoluminescence quantum yields (PLQY) and effective exciplex-based electronics.

3. REVIEW OF ARTICLES

This chapter contains information derived from the author's articles, which are listed in Chapter 9.

3.1. Polymorph acceptor-based triads with photoinduced TADF for UV sensing (Scientific publication No. 1, Q1)

This chapter is based on an article published in *Chemical Engineering Journal* (2021), Volume 425, Article 131549[81]. This work employs the acceptor–acceptor–acceptor design approach of TADF compounds by including the phenothiazine-5,5-dioxide, benzophenone, and diphenyl sulfone moieties, which exhibit varying electron-accepting characteristics. The chemical structures bis(4-(5,5-dioxido-10*H*-phenothiazin-10-yl)phenyl)methanone (**1**) and 10,10'-(sulfonylbis(4,1-phenylene))bis(10*H*-phenothiazine 5,5-dioxide) (**2**) are presented in Fig. 4.

Compounds containing benzophenone 10,10'-(sulfonylbis(4,1-phenylene))bis(10H-phenothiazine 5,5-dioxide) or diphenyl sulfone with phenothiazine-5,5-dioxide fragments were synthesised using nucleophilic substitution and oxidation processes. The structures were confirmed by ^{1}H and ^{13}C nuclear magnetic resonance (NMR), mass spectroscopy (MS), and single-crystal X-ray diffraction. The information retrieved from X-ray diffraction showed that these structures are promising as TADF materials due to the almost perpendicular dihedral angle between benzophenone or diphenyl sulfone and phenothiazine-5,5-dioxide. For compound **1**, two polymorphs were identified, showing different twist angles between the benzophenone and phenothiazine-5,5-dioxide fragments, with modest bending.

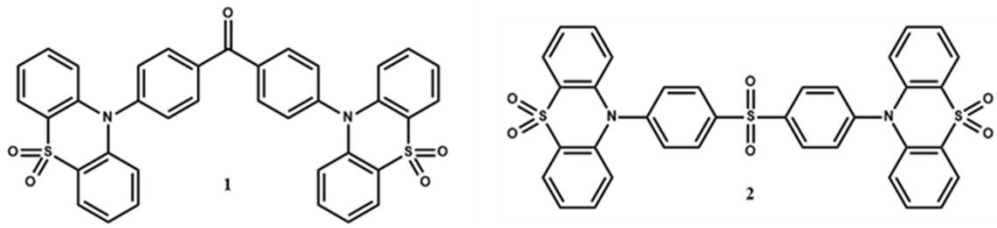

Fig. 4. Molecular structures of compounds **1** and **2**

Electronic structure and emission properties investigation was performed in numerous media. Compounds **1** and **2** showed UV absorption spectra (Fig. 5a), with absorption peaks at 300, 320, and 328 nm, which can be attributed to $\pi \rightarrow \pi^*$ transitions of the phenothiazine-5,5-dioxide moieties. The varying polarity of selected media did not affect the low-energy absorption bands of compound **2**. For compound **1**, an absorption tail in the 340 -370 nm range was observed, which can be assigned to intramolecular charge transfer (ICT) between benzophenone and phenothiazine-5,5-dioxide moieties. This conjecture aligns with the results of time-dependent density functional theory (TD DFT) calculations, where the excitation energy was calculated as 3.08 eV and 3.27 eV for compounds **1** and **2**, respectively.

Although no observable CT absorption band was detected for compound **2**, the emission spectra of compounds **1** and **2** can be characterised as ICT (Fig. 5b)[82,83]. As

confirmed by X-ray analysis, the molecular structures of compounds **1** and **2** have the capacity to twist, which can result in the overlap of LE and CT states, creating a hybridised local and charge transfer (HLCT) state. Nonetheless, Lippert–Mataga plots for compounds **1** and **2** showed a single slope (Fig. 5c), whereas HLCT emitters exhibit two slopes[84,85].

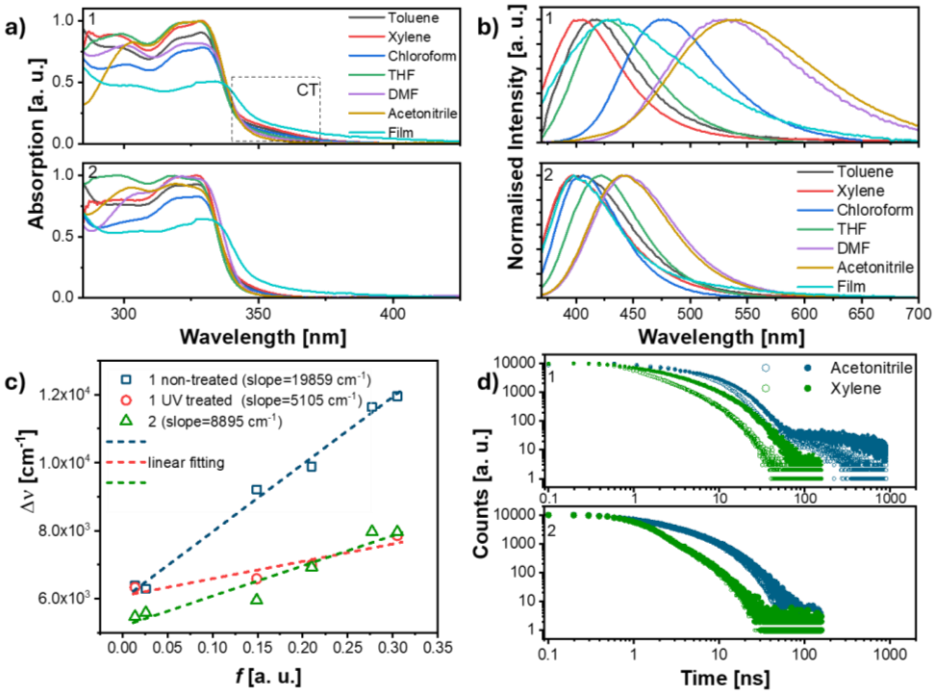

Fig. 5. Absorption (a), PL spectra (b), Lippert–Mataga plots (c), and PL decays (d) measured for both oxygenated (dotted lines) and deoxygenated (solid lines) solutions and solid films of compounds **1** and **2**

The HOMO expansion is significantly impacted by the torsion angle between the benzophenone phenyl ring and the plane of phenothiazine-5,5-dioxide. The junction of C=O or SO_2 group also influences the spectral properties of the excited state, CT characteristics, and transition intensity, though the torsion angle remains the main factor. Despite the large singlet–triplet energy gap solution of compound **1** in tetrahydrofuran (THF) (0.49 eV), the emission lifetime curves of air-equilibrated and deoxygenated solutions of nonpolar xylene and highly polar acetonitrile show components of both prompt and delayed fluorescence. The long-lived delayed fluorescence component of the solution of compound **1** in acetonitrile is due to vibronically induced TADF (Fig. 5d)[86,87]. This idea was confirmed by the emission intensity increase after deoxygenation of the toluene solution of compound **1** (Fig. 6a). Additionally, a further increase in emission was observed following UV treatment, likely due to the more thorough deoxygenation induced by UV[88,89]. On the other hand, compound **1** dissolved in a more polar solvent exhibited a noticeable blue-

shift in the spectrum for UV-treated samples (Fig. 6d). This represents the first observation of photostimulated fluorescence in an organic semiconductor. However, a different type of emission lifetime curve was observed for compound **2** (Fig. 5d), and no photostimulated fluorescence was detected for compound **2** in any medium.

As previously mentioned, a colour-switchable emission (Fig. 6a), with a spectral maximum ranging from 414 to 440 nm, was observed for compound **1** in more polar solutions. The alterations in emission colour and intensity are attributed to various mechanisms, for example, polymorphism, conformer formation, protonation, and limitation of hydrogen bonding[90–92].

The absorption spectra of thin films of compounds **1** and **2** exhibit a small red shift compared to the spectra of solutions, while maintaining the same shape of low-energy bands (Fig. 5a). Under UV excitation, the thin films of compounds **1** and **2** display a single-band blue emission, with peak wavelengths at 432 nm and 400 nm, respectively (Fig. 5b). Unlike the photoluminescence (PL) decays observed at various emission wavelengths for the film of compound **2**, the film of compound **1** exhibited a distinct, long-lasting fluorescence component at higher emission wavelengths (Fig. 5d). In conclusion, compounds **1** and **2** demonstrate the TADF properties.

Further investigation of the photostimulated emission phenomena of compound **1** reveals the existence of two unique emission effects. First, the emission spectra shift from a lower energy region to a higher energy region; this is particularly distinct in dimethylformamide (DMF) solution, where the emission shifts from green to blue (Fig. 6d). Second, there is an increase in blue emission intensity following exposure to UV irradiation. Investigating these mechanisms is essential for understanding the potential of compound **1**.

The first emission effect, described by the blue shifting of the emission spectra from the high wavelength region to the lower wavelength region, is produced by changes in the molecular conformation of compound **1**. Under UV irradiation, compound **1** changes from one stable conformer to another. A comparison of ^{1}H NMR spectra of non-treated and UV-treated solutions of compound **1** revealed that no photodegradation occurred.

The photostimulated fluorescence phenomenon is likely caused by conformational changes in the molecular structure of compound **1** in untreated and UV-treated solutions. Distinct blue and green emissions were observed in the polymorph samples A and B of compound **1**, which were produced from crystals formed in acetone and DMF, respectively (Fig. 7a). The first emission effect is associated with changes in the molecular conformation of compound **1**, resulting in a shift of the emission spectrum colour from the low-energy band to the high-energy band. This change occurs when the polymorphs transition from one stable conformer to a second stable conformer after exposure to additional UV treatment. The observed impact is not caused by the limitation of hydrogen bonding, as the PL spectrum of sonicated DMF solutions exhibited a red shift even when compared to freshly prepared DMF solutions (Fig. 6b). The transition of the emission spectra from the low to the high-energy range in the solution of compound **1** after exposure to UV light is not caused by changes in particular conformers (quasi axial–quasi axial, quasi

equatorial–quasi equatorial, and quasi axial–quasi equatorial) of the phenothiazine 5,5-dioxide moiety[93].

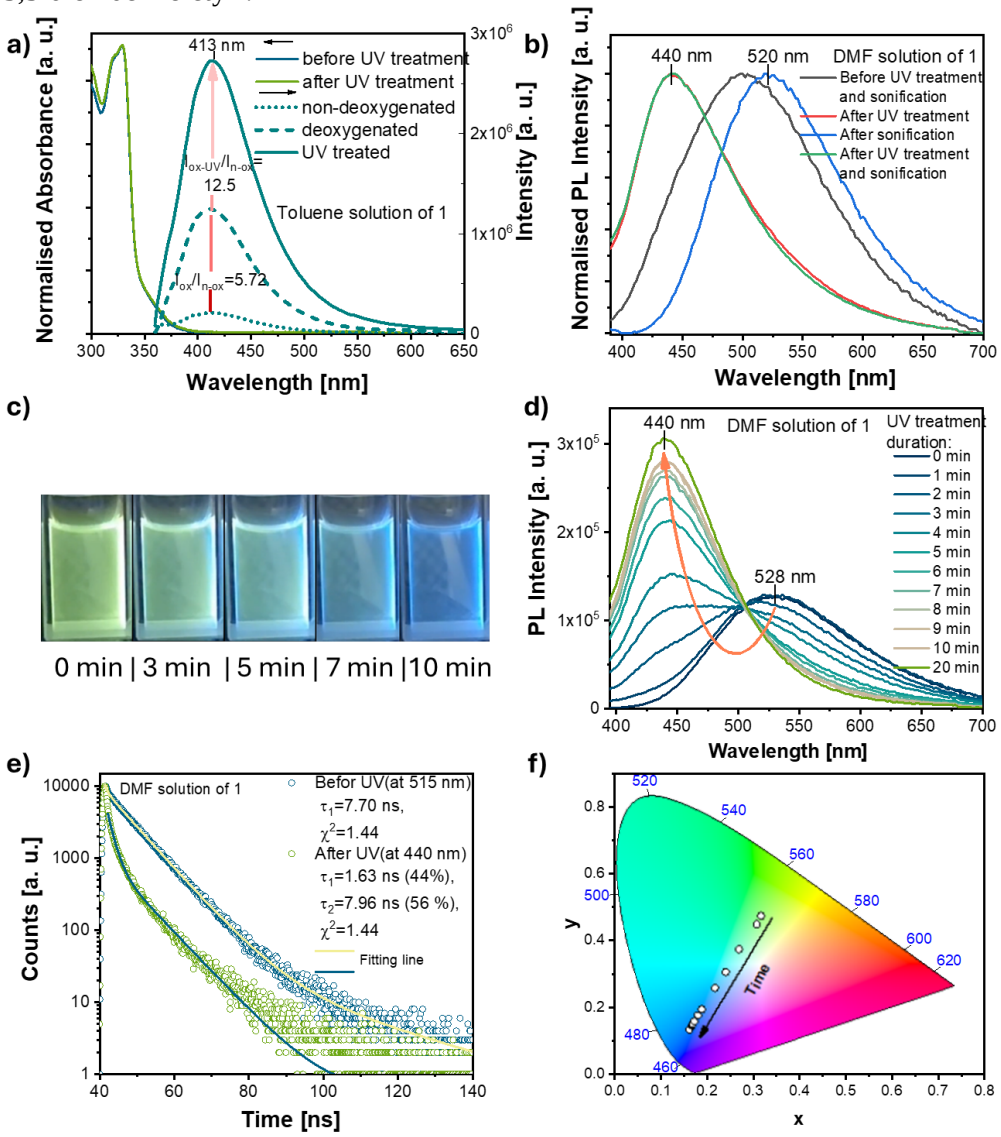

Fig. 6. Absorption and PL spectra solution of compound **1** in toluene solution before and after deoxygenation or UV treatment (a); PL spectra of compound **1** in DMF before and after sonification or UV treatment (b); image showing how the emission from the DMF solution of compound **1** changed over time during UV treatment (c); PL spectra of compound **1** in DMF after various durations of UV treatment (d); PL decay of compound **1** in DMF solution before and after UV treatment (e); plot of the coordinate changes during UV treatment from CIE 1931 (f)

The second emission effect, specifically the progressive increase of blue emission (peak at 440 nm) and the decrease of green emission (peak at 528 nm) in the DMF solution of compound **1** under continuous UV exposure, is caused by the concentration redistribution of polymorph types A and B (Fig. 6b, c, d, f). According to TD DFT calculations, blue-emitting conformer A oscillator strength for S_0–S_1 is higher than that of the green-emitting conformer B (0.017 vs. 0.003, respectively). The theoretical calculations further confirmed that the photostimulated phenomena arise from photo-induced isomerisation.

Although there is a small change in the PL spectra of compound **1** in different polarity solutions that were UV treated, there is still an observable solvatochromic effect. In comparison, the UV-treated toluene solution of compound **1** has an emission peak at 413 nm, while the UV-treated DMF solution exhibits a PL maximum at 440 nm (Fig. 6 a, d). The Lippert–Mataga plot of the UV-treated compound **1** exhibits a very low slope (5105 cm-1), which is indicative of ICT states, but it is significantly higher for LE states (Fig. 5c). This observation indicates that the emission of the UV-treated solutions of compound **1** is not associated with a purely ICT or LE process.

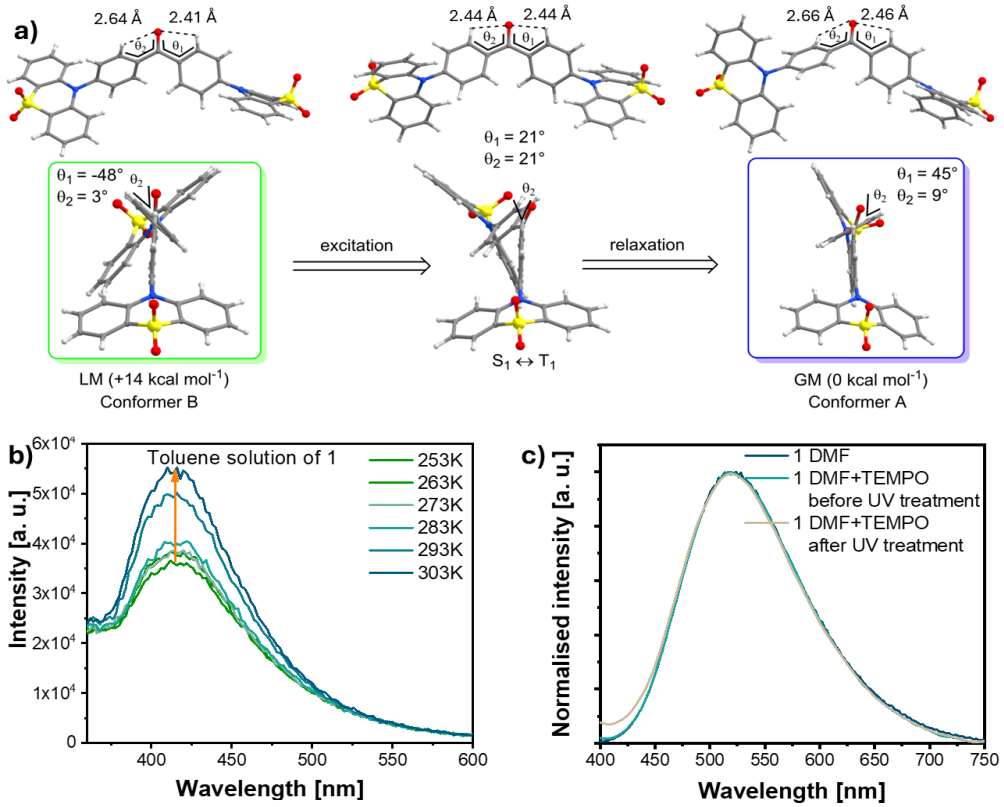

Fig. 7. (a) The conformational isomerisation between the global minimum blue-emissive conformer A and the local minimum green-emissive (LM) conformer B via the excited S_1 or T_1 state of compound **1**; (b) PL spectra of the toluene solutions of compound **1** treated with UV light and recorded at various temperatures; (c) PL

spectra of the DMF solution of compound **1** before and after UV treatment, with the addition of the TEMPO additive

While not always necessary, the TADF phenomenon can be enhanced when the energy-separated mixed ICT and LE S_1 and T_1 excited states are connected through an intermediate triplet state (such as T_2) with LE character. This connection can occur through vibronic coupling, which is a key factor in the Gibson-Monkman-Penfold mechanism of reverse intersystem crossing (RISC) in some TADF emitters [71,86].

The increase in PL intensity of the toluene solution of compound **1** after UV treatment can be explained by a higher population of the T_1 state and the subsequent delayed fluorescence mediated by RISC. The emission in toluene is influenced by the presence of oxygen and temperature, with the PL intensity increasing as the temperature rises (Fig. 7b). This effect is comparable to the observation of photostimulated fluorescence in phosphorescent derivatives of phenothiazine 5,5-dioxide, which is believed to be caused by increased π–π interactions[87].

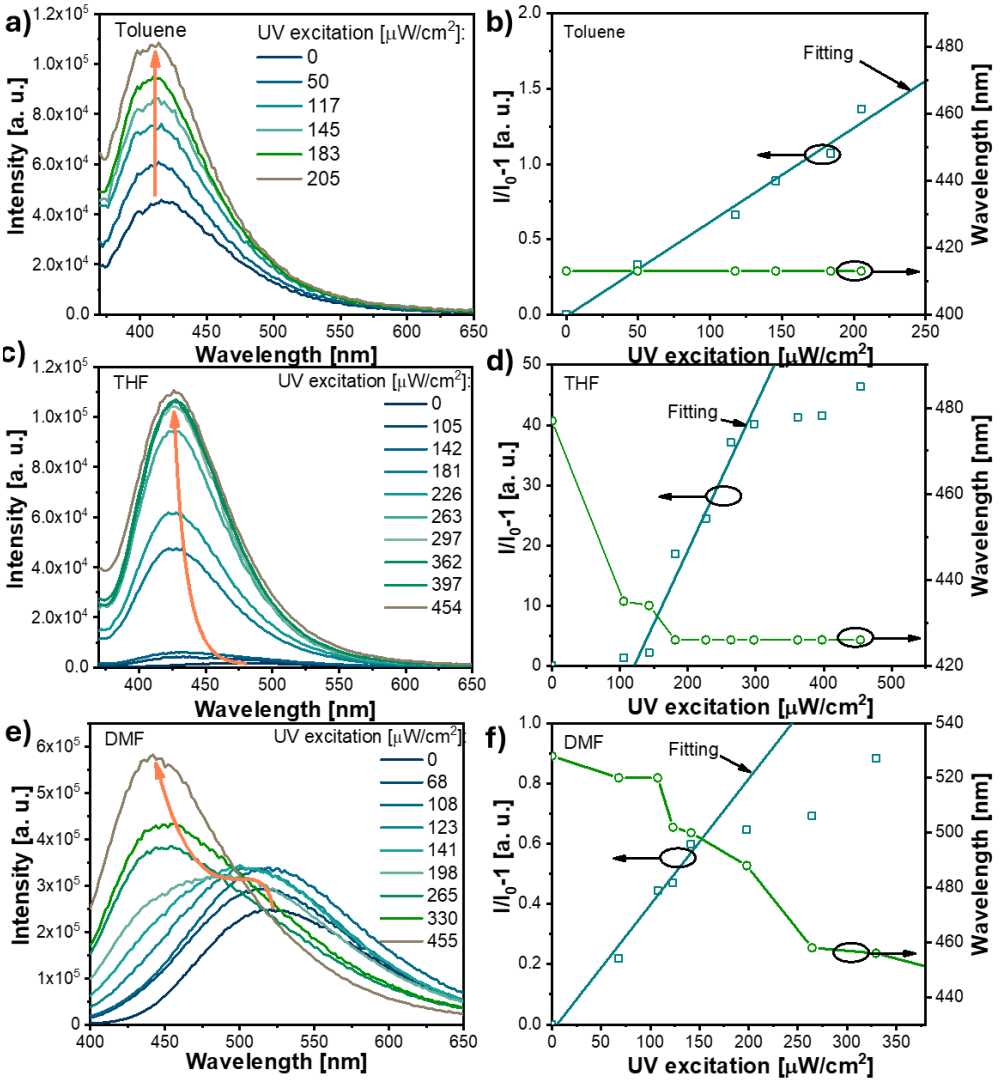

Fig. 8. PL spectra (a, c, e), Stern-Volmer plots, and the dependence of emission wavelength on UV excitation intensity (b, d, f) for compound **1** in various solvents are presented

Furthermore, the theory that photostimulated fluorescence is caused by conformational changes in compound **1** was supported by analysing the steady-state emission of compound **1** solutions with the addition of 2,6,6-tetramethyl-1-piperidinyloxy free radical (TEMPO). TEMPO has the property of preventing the transition of compound **1** to the triplet state upon UV irradiation[94]. The PL spectra of toluene and DMF solutions containing TEMPO did not change after UV exposure, indicating that the fluorescence mechanism of compound **1** may involve radical

formation (Fig. 7c). Nonetheless, there can be limitations on molecular torsion under UV exposure due to the presence of TEMPO[95].

A comprehensive study was conducted to investigate the impact of UV irradiation intensity on the emission of compound **1**, which is a UV-sensitive material used in optical sensors. The PL spectra of compound **1** were measured using different excitation strengths after being sequentially irradiated for 10 minutes. The PL intensity of the toluene solution containing compound **1** consistently increased with the intensity of UV irradiation. Consequently, the detection limit was very low, measuring less than 10 $\mu W/cm^2$. The solution of compound **1** in toluene exhibited no changes in colour or wavelength.

Both the PL intensity and the emission wavelength showed a gradual increase in THF and DMF solutions (Fig. 8b, c). The Stern-Volmer plots for the THF and DMF solutions of compound **1** exhibit discernible linear zones (Fig. 8e, f)[96]. For example, while analysing the THF Stern-Volmer plot across the range of UV irradiation energy from 150 to 250 $\mu W/cm^2$, the THF solution showed a Stern-Volmer constant (K_{SV}) value of 0.242 $[\mu W/cm^2]^{-1}$, which was significantly higher than the K_{SV} value obtained from the toluene solution, which was $6.26 \cdot 10^{-3}$ $[\mu W/cm^2]^{-1}$. The fit of the THF solution to the plot had an R^2 value greater than 0.957. The DMF solution of compound **1** exhibited the lowest K_{SV} value of $4.2 \cdot 10^{-3}$ $[\mu W/cm^2]^{-1}$ when the Stern-Volmer plot was analysed within the range of up to 150 $\mu W/cm^2$ of UV irradiation energy.

3.2. Acridone and quinacridone derivatives with carbazole or phenoxazine substituents: synthesis, electrochemistry, photophysics, and application as TADF electroluminophores (Scientific publication No. 2, Q1)

This chapter is based on an article published in *Journal of Materials Chemistry C* (2022), Volume 10, pp. 12377–12391[97]. Six acridone and quinacridone derivatives, which include either carbazole or phenoxazine substituents, were intentionally created and synthesised to investigate the impact of the D and A connecting pattern (D–A, D–A–D, or D–*π*–A–*π*–D) on their photophysical, electrochemical characteristics, as well as their application in OLEDs. The chemical structures of the following compounds are presented in Fig. 9: 2-(3,6-di-tert-butyl-9*H*-carbazol-9-yl)-10-hexylacridin-9(10*H*)-one (**3**), 2,7-bis(3,6-di-tert-butyl-9*H*-carbazol-9-yl)-10-hexylacridin-9(10*H*)-one (**4**), 10-hexyl-2-(10*H*-phenoxazin-10-yl)acridin-9(10*H*)-one (**5**), 10-hexyl-2,7-di(10*H*-phenoxazin-10-yl)acridin-9(10*H*)-one (**6**), 2,7-bis(3-(10*H*-phenoxazin-10-yl)phenyl)-10-hexylacridin-9(10*H*)-one (**7**), and 2,10-bis(3,6-di-tert-butyl-9*H*-carbazol-9-yl)-5,12-dioctylquinolino[2,3-b]acridine-7,14(5*H*,12*H*)-dione (**8**).

The redox properties of electroactive compounds are crucial for determining electron affinity (EA) and ionisation potential (IP), which are predictive parameters for electronic and optoelectronic applications. In this study, a representative cyclic voltammetry (CV) analysis of acridone monosubstituted with carbazole (**3**) is presented in Fig. 10.

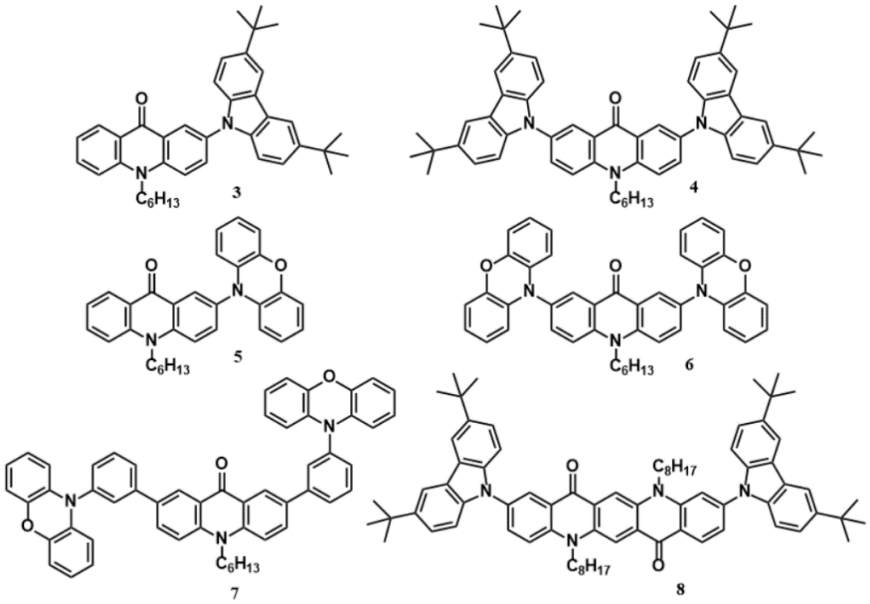

Fig. 9. Molecular structure of compounds **3–8**

Carbazole moieties undergo reversible oxidation to a radical cation, followed by consecutive irreversible oxidation processes, which may involve oligomerisation or polymerisation if appropriate coupling positions in the carbazole aromatic rings are available[98]. The CV of compound **3** reveals two oxidation processes of reversible and quasi-reversible nature, at E^0_{ox1} = 0.653 V and E^0_{ox2} = 1.132 V, respectively, essentially excluding dimerisation or oligomerisation (Fig. 10a). Unsubstituted acridone undergoes quasi-reversible oxidation at 1.020 V. The reduction of compound **3** is largely irreversible and occurs at relatively low potentials, with the maximum cathodic peak at -2.399 V vs. Fc/Fc+. Compound **4**, which contains two carbazole substituents symmetrically connected to the central acridone unit, can be considered a D–A–D molecule. Consecutive oxidations of the two carbazole groups occur at potentials E^0_{ox1} = 0.639 V and E^0_{ox2} = 0.804 V. The first oxidation potential is very similar to that registered for the oxidation of compound **3**; an increase in the oxidation potential of the second carbazole unit may indicate some delocalisation of the radical cation charge across the whole molecule, making the abstraction of the second electron more difficult[99]. Further oxidation of this cation requires polarisation to relatively high potentials, resulting in the irreversible oxidation of the central acridone unit. The first two reversible oxidation processes at E_{0ox1} = 0.600 V and E_{0ox2} = 0.729 V can be explained by the continuous oxidation of carbazole moieties in compound **8**, which differs from compound **4** by the central acceptor unit (quinacridone and acridone) (Fig. 10a). The oxidation of carbazole units in compound **8** occurs at lower potentials and within a narrower potential range compared to compound **4**, reflecting the effect of the central acceptor unit. In compound **8**, the central unit is more

extended, resulting in better delocalisation of the radical cation charge formed in the first oxidation step[100].

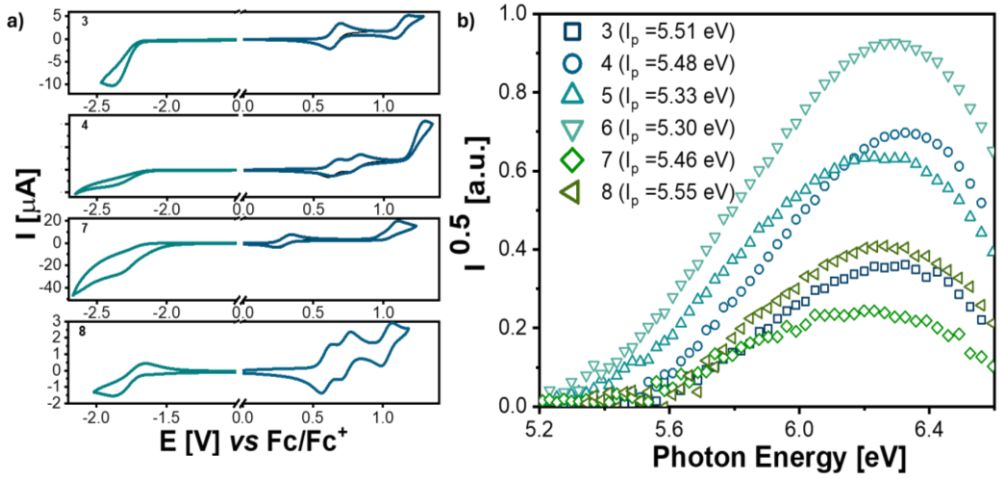

Fig. 10. Cyclic voltammograms recorded for samples **3**, **4**, **7**, and **8** (a), with 0.1 M Bu_4NBF_4 in CH_2Cl_2 as the electrolyte and a scan rate of 50 mV/s. Photoelectron emission spectra of thin layers of compounds **3–8** placed in a vacuum (b)

For the calculations of IP and EA of **3**–**8** from the electrochemical data, compounds **3**–**7** exhibit similar, low reduction potentials and, consequently, low EAs in the range of 2.50–2.65 eV. The only exception is compound **8**, which contains a significantly more extended quinacridone core. Its reduction potential is approximately 400–500 mV higher compared to compounds **3**–**7**, resulting in an EA exceeding 3.0 eV. Phenoxazine-functionalised acridones (**5**–**7**) exhibit $E_{ox1onset}$ values that are 300–320 mV lower than those of carbazole-substituted compounds (**3**, **4**, and **8**). Consequently, their IPs are also lower, barely exceeding 5.0 eV.

Table 1. Redox potentials, electron affinities (EA_{EL}), and ionisation potentials (IP_{CV}) obtained by electrochemical methods, with ionisation potentials (IP_{PE}) determined by photoelectron emission spectroscopy (PE)

Characteristic	**3**	**4**	**5**	**6**	**7**	**8**
$E_{red.onset}$[(a)], V	-2.27	-2.22	-2.23	-2.16	-2.23	-1.77
$E_{ox\ onset}$[(a)], V	0.651	0.637	0.317	0.332	0.294	0.6
EA_{CV}[(b)], eV	2.53	2.58	2.57	2.64	2.57	3.03
IP_{CV}[(c)], eV	5.45	5.44	5.12	5.13	5.09	5.4
IP_{PE}[(d)], eV	5.51	5.48	5.33	5.3	5.46	5.55

(a) Potential vs. Fc/Fc+
(b) Calculated using the equation: EA = e (Ered.onset + 4.8) [eV]
(c) Calculated using the equation: IP = –e (Eox.onset + 4.8) [eV]
(d) Measured by photoelectron spectroscopy in air (see Fig. 6b)

It is instructive to verify whether a correlation exists between IP values derived from electrochemical data (IP_{CV}) and those obtained via photoelectron emission

spectroscopy (IP_{PE}). The photoelectron emission spectra for compounds **3**–**8** are shown in Fig. 10b, while IP_{PE} values calculated from these spectra are presented in Table 1.

It should be noted that different physical quantities are measured in both cases. IP_{CV}, determined for compounds dissolved in a non-aqueous solvent, corresponds to the ionisation energy, which is modified by electrostatic interactions between the ionised molecule and its polarisable environment. In the case of IP_{PE}, the measurements are obtained from surface molecules of a thin solid film. Although IP_{PE} values are higher than IP_{CV} values, the observed values for phenoxazine derivatives are consistently lower than those for carbazole derivatives.

The absorption spectra of compounds **3**–**8** are characterised by bands attributed to their D and A segments, such as acridone (Acr) and tert-butylcarbazole (tCz) for compounds **3** and **4**, acridone (Acr) and phenoxazine (PhNZ) for compounds **5**–**7**, and quinacridone (QAcr) and tCz for compound **8** (Fig. 11a, b). These bands are marked by thin vertical lines at 389 nm for Acr, 290 nm ($\pi\rightarrow\pi^*$) and 307–335 nm ($n\rightarrow\pi^*$) for tCz, 313 nm for PhNZ, and at 290 and 504 nm for QAcr. Slight red shifts and broadening of these bands are observed in the spectra of all studied compounds (**3**–**8**), particularly in the low-energy regions. This observation can be attributed to the formation of ICT states due to interactions between the electron-donating and electron-accepting moieties.

The absorption spectra of solid thin films of **3**–**8** are similar to those of the corresponding toluene solutions but are characterised by even greater broadening. Two possible origins for these effects can be proposed: aggregation or stronger ICT. The latter seems more plausible, considering the ICT-induced shapes (non-structured) of the corresponding PL spectra for all studied compounds (Fig. 11c, d). In contrast, the specific features of the PL spectra for toluene solutions of compounds **3**, **4**, and **7**, **8** originate from the recombination of the LE states formed mainly by the electron-accepting moieties (acridone or quinacridone) (Fig. 11c). Compounds **5** and **6** demonstrate ICT-shaped PL spectra both in toluene solutions and in the solid-state, which is likely due to strong D-A interactions (Fig. 11c, d).

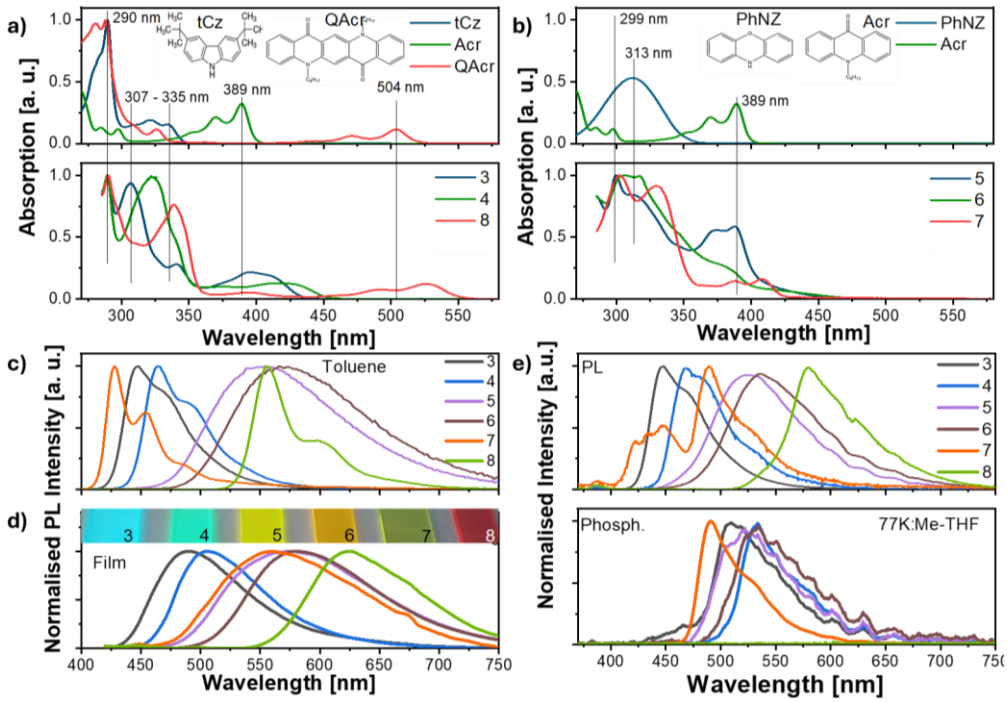

Fig. 11. Absorption spectra (a, b) of toluene solutions containing compounds **3–8** and comparison spectra of tCz, QAcr, PhNZ, and Acr; PL spectra of compounds **3–8** in toluene (c) and their vacuum-deposited films (d); PL and phosphorescence spectra (e) of compounds **3–8** in methyl tetrahydrofuran (Me-THF) at 77 K with a 1 ms delay for phosphorescence spectra following 330 nm excitation; inset of (d) displays photographs of vacuum-deposited films under UV light

The PL spectrum of a 10% molecular dispersion of compound **7** in 1,3-bis(*N*-carbazolyl)benzene (mCP) exhibits two distinct bands at 452 and 525 nm (Fig. 12a). These bands arise from the recombination of LE and ICT states. In contrast, only one band is observed in the spectra of the remaining compounds (**3**–**6** and **8**). The PL spectra of molecular dispersions in hosts with low polarity (dielectric constant of mCP = 2.84)[101] experience a hypsochromic shift compared to neat films, confirming the dominance of ICT character in the excited states of solid films **3**–**8**.

Time-resolved spectroscopic studies show long-lived emission of molecular dispersions of compounds **5**–**7** in mCP under vacuum conditions (Fig. 12b). The measured PL decays of the samples demonstrated long-lived emission, which can be attributed to delayed fluorescence, supported by the absence of visible changes in the shape of the PL spectra and an increase in intensity after the removal of air. The evacuation-induced increase in the intensity of the PL spectra of solutions and molecular dispersions of compounds **5**–**7** strongly indicates the triplet origin of this delayed fluorescence. As demonstrated, the long-lived fluorescence of compounds **5** and **6** is TADF in nature. Compounds **3**, **4**, and **8** dispersed in the mCP host exhibit a single-component PL decay curve, which can be attributed to fluorescence.

Table 2. Photophysical parameters, including singlet and triplet energies, of compounds **3–8**

Characteristic	**Media**	**3**	**4**	**5**	**6**	**7**	**8**
λ_{MAX}^{tol}[(a)], nm	Tol.	448, 469	464, 490*	551	571	429, 454, 488*	555, 600
λ_{MAX}^{solid}[(a)], nm	Neat film	490	506	565	581	558	625
λ_{MAX}^{solid}[(a)], nm	mCP	462	479	525	541	452, 525	594
PLQY[(b)], %	Tol./ mCP	69/66	61/68	1.5/35	2/31	8.6/15.4	92/35
E_{S1}[(c)], eV	Me-THF	2.92	2.79	2.68	2.59	3.02	2.31
E_{T1}[(c)], eV		2.58	2.46	2.59	2.53	2.64	–
ΔE_{ST}[(d)], eV		0.34	0.33	0.09	0.06	0.38	–

(a) Wavelength at the peak of the emission spectrum
(b) PLQYs of compounds 3–8 measured in oxygen-free conditions
(c) First singlet (E_{S1}) and triplet (E_{T1}) energies were taken at the onset of the high-energy edges of the PL (fluorescence) and phosphorescence spectra, respectively, registered for Me-THF solutions of compounds 3–8 at the temperature of liquid nitrogen (77 K)
(d) Energy difference between E_{S1} and E_{T1}

PL emission and PL lifetime measurements were performed for the films of compound **5**: mCP in air and vacuum conditions at different temperatures (Fig. 13a–d). The PL decay curves of TADF compounds are characterised by a component exhibiting prompt fluorescence in the nanosecond range and another in the microsecond range. The delayed fluorescence intensity increased with rising temperature, proving that the thermally activated process was responsible for this delayed fluorescence. The study employed PL decay techniques on films of compound 5 at various temperatures to gain understanding of the properties of delayed fluorescence. The temperature and delayed fluorescence intensity showed a positive correlation in the PL decay curves, indicating the possibility of a thermally activated process (Fig. 13d). The small singlet-triplet splitting of 0.06 eV and low activation energy of 12 meV for RICS were consistent with the compound's TADF characteristics (Fig. 13e, f). The Arrhenius equation[102],

$$k_{RISC} = Ae^{\left(\frac{-E_a}{k_bT}\right)}; \quad (1)$$

where E_a is the activation energy, k_B is the Boltzmann constant, and A is the frequency factor involving the spin–orbit coupling constant, was used to fit the temperature dependence of the rates of RICS for compound **5** to calculate the activation energy (E_a).

Compounds **5**–**7** are characterised by rather low PLQY values in solution, with significantly increased PLQY values in their solid-matrix dispersions, attributed to aggregation-induced emission enhancement (AIEE) (Fig. 14a, b; Table 2)[103].

PL measurements of their dispersions in THF and water mixtures were conducted to further investigate the photophysical properties of compounds **3**–**8** in the solid state (Fig. 14a–c). The emission intensities (integrated area of PL spectra) of dispersions of compounds **3**–**8** in the THF-water mixtures with water fractions ranging from 0% to 90% are shown in Fig. 14a–c. The emission intensities of compounds **3**, **4**, and **8 decreases** with increasing water fractions in the solution mixture, which is typical for compounds exhibiting aggregation-caused quenching (ACQ)[104].

Quantum chemical calculations were performed using DFT/B3LYP-GD3BJ/6-311++G(d, p) method to support the experimental results. These calculations determined the geometries of all studied compounds, elucidated the spatial distribution of frontier orbitals, and calculated their energies. Theoretical calculations of IPs and EAs were also conducted to provide theoretical support for the electrochemical and PE data.

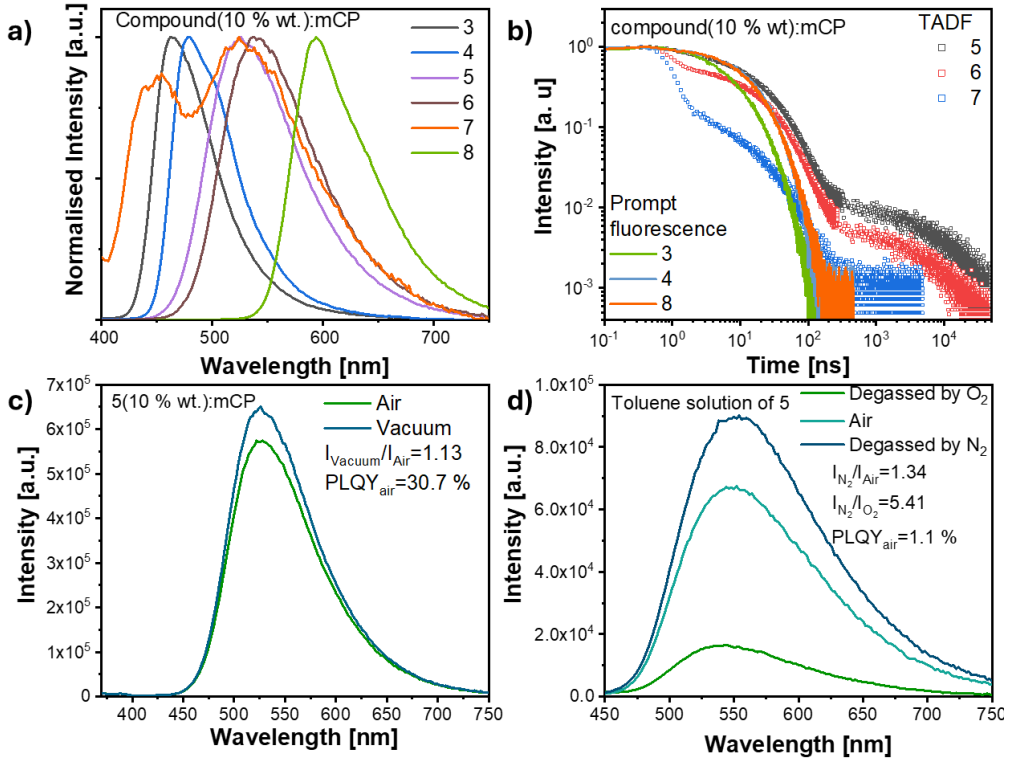

Fig. 12. PL spectra of molecular dispersions (10 wt.% in mCP) of compounds **3**–**8**, shown in (a), with their PL decays in (b); normalised PL spectra for the dispersion of compound **5** (10 wt.% in mCP) in air and under vacuum are shown in (c); PL spectra of toluene solutions of compound **5**, including the as-prepared state (in air), after deoxygenation, and after reoxygenation, are shown in (d)

Compounds were characterised by either one donor (tCz or PhNZ) and one acridone-type acceptor (compounds **3** and **5**) or two donors (tCz or PhNZ) and one

acceptor (Acr or QAcr, compounds **4, 6**, and **8**). Compound **7** differs in that its acceptor part (Acr) is connected to two donor parts (phenoxazine) via 1,3-phenylene linkers. The twist angles in carbazole-containing compounds are approximately 25° smaller than those in compounds with phenoxazine substituents. It was found that the HOMO levels of acridones substituted with carbazole (compounds **3** and **4**) are lower lying than the corresponding levels of acridones functionalised with phenoxazine (compounds **5**, **6**, and **7**). The solvation effect increased the band gap for all investigated compounds, except **8**, due to a more pronounced decrease in the HOMO level and only a slight decrease in the LUMO level. Interactions with solvent compounds increase the electric dipole moment of compounds **3**–**7** but decrease the polarity of **8**, which remains relatively small compared to the values calculated for compounds **3**–**8** overall.

Distributions of frontier orbitals within different parts of the studied compounds, along with their energies, determine the spectroscopic and redox properties of the electroactive compounds. These distributions are closely related to the molecular geometry. In compounds **5**, **6,** and **7**, the donor and acceptor parts are nearly perpendicular, while in the case of compound **7**, the phenoxazine unit is also almost perpendicular to the 1,3-phenylene linker. Therefore, the HOMO and LUMO of **5**, **6,** and **7** are located on different parts of the compounds, with the HOMO being essentially limited to the phenoxazine unit and HOMO-1, LUMO, and LUMO+1 to the acridone unit.

The spatial separation of HOMO and LUMO orbitals in **5**, **6**, and **7** is manifested in the calculated transitions, inhibiting transitions of dominant HOMO→LUMO configurations, such as the $S_0 \rightarrow S_1$ transitions. The lowest energy transition with non-negligible oscillator strength is HOMO-1→LUMO for **5**, whereas for **6** and **7**, it corresponds to the HOMO-2→LUMO transition. A smaller dihedral angle in carbazole derivatives of acridone and quinacridone significantly changes the distribution of frontier orbitals.

The experimental results show that the PLQY of phenoxazine derivatives solutions (compounds **5**, **6**, and **7**) is significantly lower than that of carbazole derivatives (compounds **3**, **4**, and **8**), as the low oscillator strength of the $S_0 \rightarrow S_1$ transition limits fluorescence.

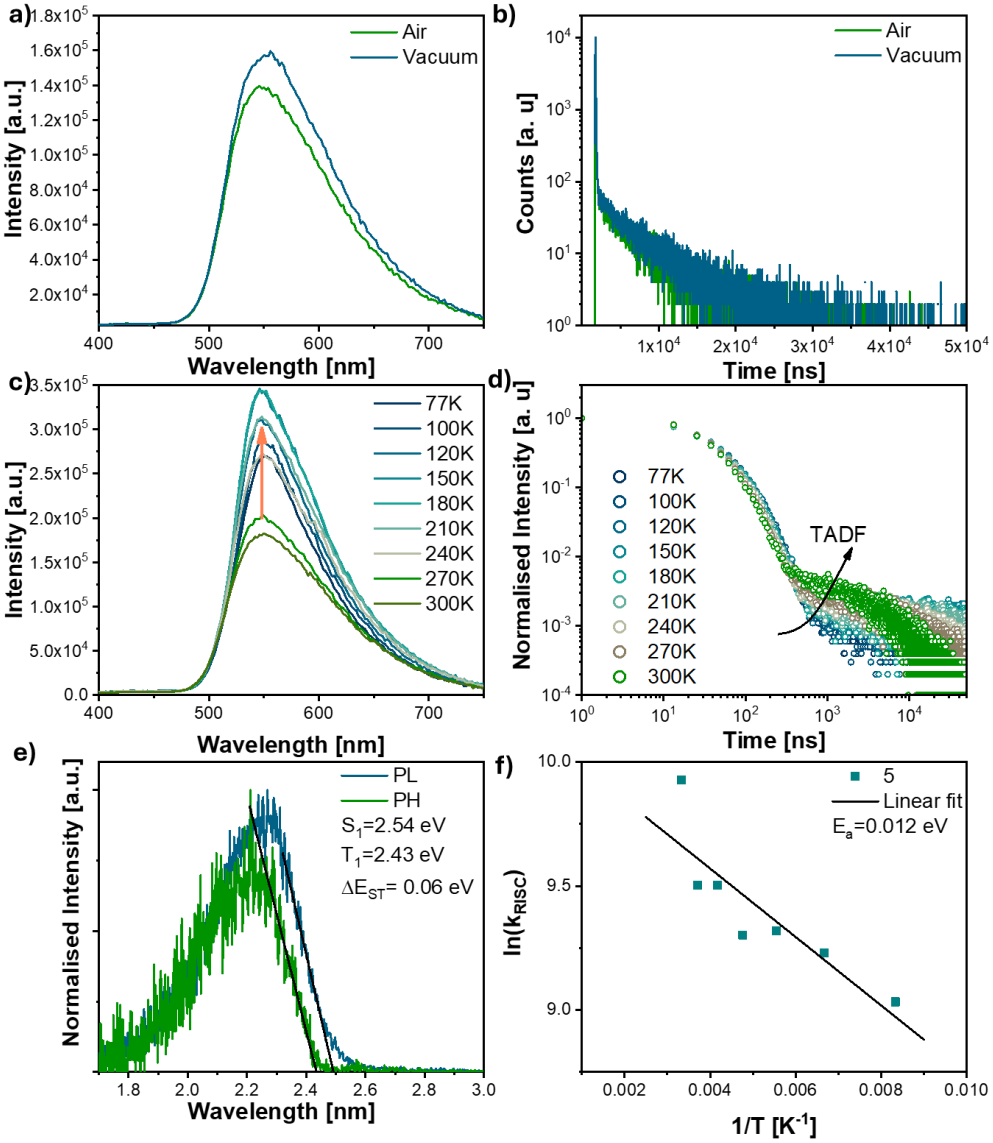

Fig. 13. PL spectra and decay curves of compound **5** (10 wt.% in mCP): PL spectra (a) and PL decay curves (b) at ambient temperature in vacuum and air; PL spectra (c) and PL decay curves (d) across temperatures in an inert environment; PL and phosphorescence spectra (e) at 77K; temperature-dependent (f) RISC rate for calculating TADF activation energy (E_A)

The strict spatial separation of the HOMO and LUMO, with the HOMO located on the phenoxazine moiety, results in one-step oxidation of both substituents in compounds **6** and **7**, which are oxidized independently at the same potential. The extension of HOMO orbitals across the whole molecule in carbazole derivatives results in a two-step oxidation of carbazole moieties in compounds **4** and **8**, as the

charge formed during the oxidation of one carbazole unit is transmitted to the second substituent via delocalisation, making consecutive oxidation more difficult.

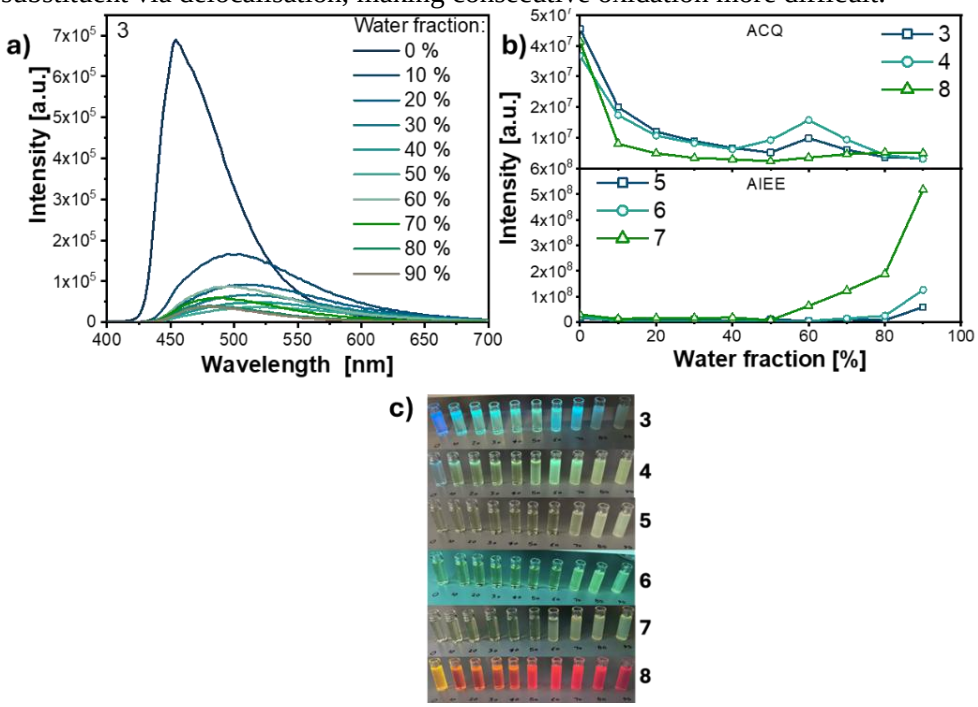

Fig. 14. PL spectra of compound **3** dipersed in THF-water mixtures with varying water persentages (a); integrated PL spectra areas plotted against water volume percentages in the THF-water dispersions of compounds **3**–**8** (b); images of compounds **3**–**8** dispersions under UV light exposure (c)

Table 3. Hole and electron mobility parameters at room temperature for vacuum-deposited layers of compounds **3**–**8**

Characteristic	3	4	5	6	7	8
μ_h, cm^2 V^{-1} s^{-1}[a]	1.3×10^{-5}	1.6×10^{-5}	4.6×10^{-5}	8.5×10^{-5}	2.4×10^{-5}	2.5×10^{-3}
μ_0, cm^2 V^{-1} s^{-1}[b]	1.9×10^{-7}	1.9×10^{-8}	1.8×10^{-7}	2.2×10^{-7}	6.8×10^{-7}	4.5×10^{-5}
β, (cm V^{-1})$^{1/2}$[c]	7.8×10^{-3}	1.1×10^{-2}	5.5×10^{-3}	1.0×10^{-1}	6.1×10^{-3}	6.8×10^{-3}
μ_e, cm^2 V^{-1} s^{-1}	–	1.8×10^{-5}	1.3×10^{-5}	–	–	–
μ_0, cm^2 V^{-1} s^{-1}	–	1.8×10^{-8}	6.6×10^{-8}	–	–	–
β, (cm V^{-1})$^{1/2}$	–	1.1×10^{-2}	8.6×10^{-3}	–	–	–

(a) Hole (μ_h) and electron (μ_e) mobilities measured from time-of-flight (TOF) measurements at electric field (E) of 3.6 × 105 V/cm

(b) Mobilities measured in the absence of an electric field (μ_0)

(c) Field dependence parameter (β) for Poole-Frenkel type mobility, expressed as $\mu = \mu_0 \cdot e^{\beta \frac{E1}{2}}$

Charge mobilities in the emissive layers of OLEDs are crucial for proper device operation. Considering the applications of compounds **3–8** as electroluminophores in OLEDs, their charge transport properties were examined using the TOF technique. The experiments were conducted with diode-type samples consisting of indium tin oxide (ITO), a thick organic layer, and aluminium (Al). Dispersive TOF current transients, with observed transit times (τ_{tr}) recorded in log-log scales, were obtained either under applied positive voltages (for holes) or negative voltages (for electrons) at the optically transparent ITO electrode. Compounds **3**, **6–8** exhibited unipolar behaviour, showing measurable mobility for holes only. In contrast, compounds **4** and **5** were bipolar, exhibiting both p-type (hole) and n-type (electron) transport. The highest value of hole mobility ($\mu_h = 2.5\times10^{-3}$ cm^2 V^{-1} s^{-1}) at an electric field of 3.6×10^5 V/cm was found for the quinacridone derivative (compound **8**) (Table 3). This finding was not unexpected, as high hole mobilities measured in either field-effect transistor (FET)[105,106] or diode configurations[107] have been reported for various quinacridone core-containing compounds. The hole mobilities of the remaining compounds were lower by over one to two orders of magnitude. The observed hole mobility values are characteristic of donor-acceptor compounds that exhibit TADF, where the molecular segments are strongly twisted[108,109]. The results of fitting the Poole-Frenkel electric field dependences[110] of the experimental charge carrier mobilities led to relatively high field dependence parameters. The β values varied within the range from 5.5×10^{-3} (cm V^{-1})$^{1/2}$ for compound **5** to 1.1×10^{-2} (cm V^{-1})$^{1/2}$ for compound **4**, as determined at room temperature for all investigated compounds (**3–8**). These values can be attributed to the relatively strong dispersive transport. Compounds **4** and **5** were found to be bipolar, exhibiting similar electron mobilities of 1.8×10^{-5} and 1.3×10^{-5} cm^2 V^{-1}s^{-1}, respectively, at the same electric field. Moreover, the μ_e values of compounds **4** and **5** were comparable to their μ_h values, indicating well-balanced hole and electron transport, which is crucial for the use of these compounds in electroluminescent devices such as OLEDs.

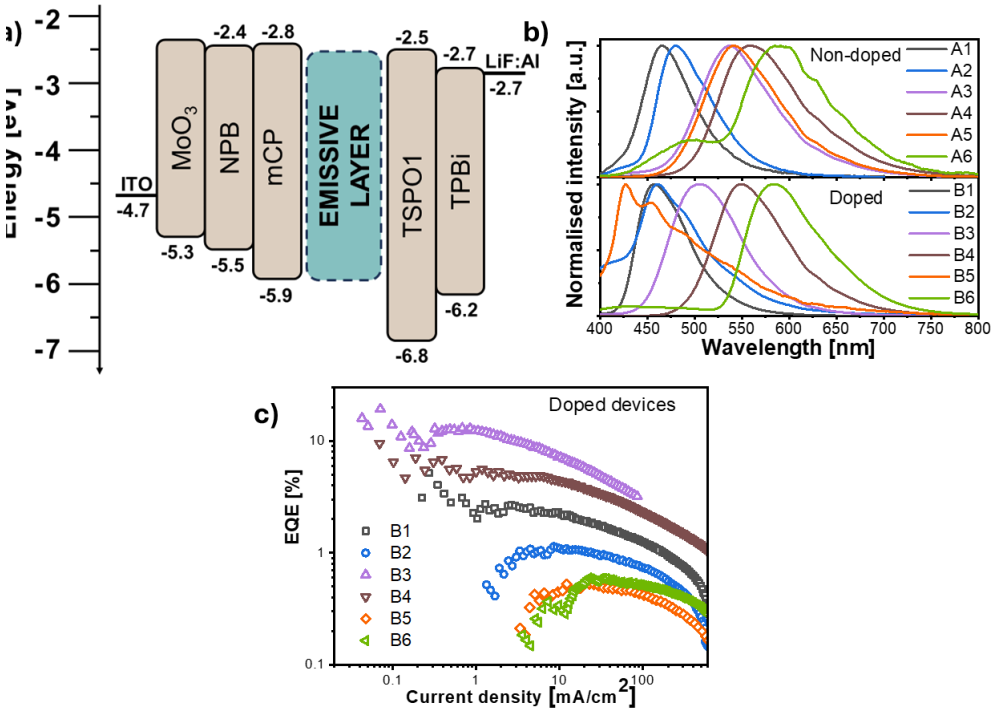

Fig. 15. Equilibrium energy diagram (a); EL spectra of non-doped (A1–A6) and doped (B1–B6) devices (b); EQE dependence on current density for devices B1–B6 (c)

The compounds **3–8** were utilised as emitters in OLEDs. The layers of the fabricated devices were as follows: molybdenum trioxide (MoO_3) (0.35 nm), *N*,*N*′-di(1-naphthyl)-*N*,*N*′-diphenyl-(1,1′-biphenyl)-4,4′-diamine (NPB) (44 nm), mCP (4 nm), emissive layer (24 nm), diphenyl[4-(triphenylsilyl)phenyl]phosphine oxide (TSPO1) (4 nm), 2,2',2''-(1,3,5-Benzinetriyl)-tris(1-phenyl-1-*H*-benzimidazole) (TPBi) (40 nm), lithium fluoride (LiF) (0.35 nm), and aluminium. The functionalisation of acridone or quinacridone with only two types of donors, tCz and PhNZ, results in a series of electroluminophores whose emission spectra cover a significant portion of the visible spectrum from blue to orange. All electro-optical and electrophysical properties of the fabricated OLEDs are presented in Table 4. Non-doped and doped emissive layers (EMLs) of tCz-substituted acridone emit blue electroluminescence (EL). Devices with non-doped EMLs consisting of PhNZ-substituted acridone emit green (CIE 1931 coordinates of (0.336; 0.567)) and yellow (CIE 1931 coordinates of (0.439; 0.541)) light, respectively (Fig. 15b; Table 4). The observed bathochromic shift of the spectra of A3 and A4, compared to those recorded for A1 and A2, is attributed to stronger donor-acceptor interactions in acridone-phenazine derivatives. However, dispersions of compounds **5** and **6** in mCP (devices B3 and B4) yield EL spectra that are hypsochromically shifted with respect to the

spectra measured for A3 and A4 devices, displaying CIE 1931 colour coordinates characteristic of the blue region. This colour change can be attributed to the interactions of the luminophore with the mCP host, a phenomenon somewhat similar to solvatochromism. Interestingly, yellow EL was observed for the EML in device A5, whereas blue EL was obtained for device B5, indicating layers exhibiting different EL mechanisms. This difference cannot be attributed to solvatochromism but rather to a distinct combination of ICT and LE emissions, as previously reported for indolocarbazole-type emitters[111,112]. Thus, weakening of donor-acceptor interactions in compound **5** dispersed in mCP, compared to the neat luminophore film (undoped EML), results in a switch from ICT to LE emission, which is more intensive under electrical excitation than under optical excitation.

Undoped and doped EMLs of the only quinacridone derivative studied in this research yield orange, close to red, EL. Unexpectedly, a high energy-band peaking at approximately 490 nm is observed in the EL spectrum of device A6. This band could be attributed to the electroplex emission of compound **8**, as it appears only under electrical excitation. Its presence could be advantageous for the development of white OLEDs, as previously proposed[113].

Table 4. Output electroluminescent parameters of OLEDs with non-doped (A1–A6) and doped (B1–B6) EMLs

Device name	EML	λ_{EL}[(a)], nm	V_{ON}[(b)], V	L_{max}[(c)], cd/m^2	CE_{max}[(d)], cd/m^2	PE_{max}[(e)], lm/W	EQE_{max}[(f)], %
A1	**3**	464	5.7	7475	2.56	0.9	1.6
A2	**4**	481	7.9	5135	1.53	0.4	0.7
A3	**5**	540	5.1	21200	8.02	3.6	2.3
A4	**6**	563	6.1	13200	3.8	1.26	1.3
A5	**7**	542	6.3	8460	2.77	0.91	0.76
A6	**8**	484,585	11.4	443	0.4	0.06	0.12
B1	**3**:mCP	458	5	4270	6.7	3.8	4
B2	**4**:mCP	459	6.4	2150	1.7	0.7	1.2
B3	**5**:mCP	505	4.7	7950	37.1	19.8	13
B4	**6**:mCP	548	3.5	22520	23.5	20.5	7.2
B5	**7**:mCP	426,455	5.4	1820	0.8	0.4	0.5
B6	**8**:mCP	587	6	4010	1.4	0.5	0.6

(a) EL maximum (λ_{EL})
(b) Turn-on voltage (V_{ON})
(c) Maximum brightness (L_{MAX})
(d) Maximum current (CE_{MAX})
(e) Power efficiency (PE_{MAX})
(f) External quantum efficiency (EQE_{MAX})
Device structure: MoO_3(0.35nm)/ NPB(44nm)/mCP (4 nm) EML (24nm)/ TSPO1(4nm)/ TPBi(40nm)/LiF(0.35nm)/Al

In conclusion, by utilising only two donor and two acceptor building blocks in the synthesis of D-A, D-A-D or D-π-A-π-D compounds, it is possible to fabricate emitters that cover large portions of the visible spectrum. The lowest turn-on voltage

(3.5 V) was measured for device B4, which is consistent with the lowest ionisation potential of compound **6** (IP_{PE} = 5.3 eV), as determined by PE spectroscopy, and its second highest hole mobility. The significant differences in maximum brightness values among the fabricated devices can be attributed to variations in emitter efficiencies and a different sensitivity of the human eye to various emission colours. The outstanding TADF/AIEE emissive and bipolar charge-transporting properties of compound **5** should be emphasised. Devices A3 and B3 demonstrated the highest maximum EQEs of 2.3% and 13%, respectively. The transient electroluminescence (TREL) signal, which reaches milliseconds, provides evidence for the significant participation of triplet excitons in the EL of device B3, based on TADF emitter **5**. With further optimisation, OLEDs utilising compound **5** could potentially exhibit improved output parameters compared to those reported in this study.

Compounds **6** and **5** have comparable emission characteristics; however, devices A4 and B4 exhibit reduced maximum EQE efficiencies due to the imbalanced transit of holes and electrons within the EML. While compound **6** functions solely as a hole conductor, compound **5** conducts both holes and electrons. Compound **3** achieves impressive maximum EQEs of 1.6% and 4%, suggesting its potential as a promising candidate for conventional fluorescent OLEDs (Fig 15b). These high efficiencies are largely attributed to compound **3**'s high solid-state PLQY value. Although the doped films of compounds **3** (66% PLQY) and **4** (68% PLQY) exhibit high values, the EQE of OLEDs using these compounds remains comparatively low. The absence of TADF characterisation in these compounds limits their potential for triplet harvesting in OLEDs. Hence, the theoretical upper limit of their EQE values should not exceed 5% based on the following formula[114]:

$$\eta_{ext} = \gamma \cdot \Phi_{PL} \cdot \chi \cdot \eta_{out}; \quad (2)$$

where γ is the charge balance factor, Φ_{PL} is the PLQY value, χ is the exciton recombination efficiency, and η_{out} is the outcoupling coefficient.

The highest EQE of device B1 is 4%, approaching the theoretical maximum of 4.65%, based on assumed values of 1 for γ, 0.25 for χ, and 0.3 for η_{out}. OLEDs using compounds **5** and **6**, which demonstrate TADF, achieve notably higher EQE values due to their enhanced exciton recombination efficiency. These results demonstrate the impact of the connection between donor and acceptor moieties on the electroluminescent properties of the compounds. The observed effect is attributed not to solvatochromism but rather to a unique combination of ICT and LE emissions, a phenomenon previously documented in indolocarbazole-type emitters.

3.3. Thermally controllable tuning of emission properties in phenoxazine-substituted acridones: a step towards efficient organic light-emitting diodes using crystalline emitters (Scientific publication No. 3, Q1)

This chapter is based on an article published in *Advanced Optical Materials* (2023), Volume 11, Article 2301059[115]. It continues the investigation from the previous chapter, focusing on phenoxazine-substituted acridones (compounds **5**, **6**, and **7**). This research aims is to examine the impact of morphological transitions in these materials on their photophysical and EL properties. The chemical structures of the compounds studied are shown in Fig. 16.

This study examines the thermal characteristics of compounds **5**, **6**, and **7** as thermally tunable crystalline electroluminophores in OLEDs. The results of these investigations allow for the determination of the optimal annealing temperature for the deposited films. Compound **5** demonstrates excellent thermal stability, withstanding temperatures above 300 ºC without significant changes. Additionally, it begins to show a 5% mass loss at 343 ºC. Upon cooling, it forms a molecular glass, with no apparent crystallisation peak. Compounds **6** and **7** exhibit similar properties but with notably higher values for T_m, T_g, and T_{cr} (Table 5).

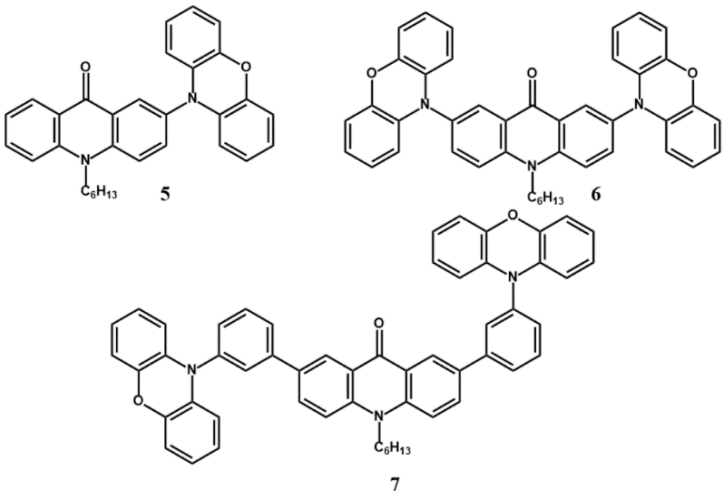

Fig. 16. Molecular structure of compounds **5**–**7**

To investigate the potential solvatochromic characteristics of compounds **5**, **6**, and **7**, two solvents with dissimilar dielectric constants were chosen. The absorption spectra of the compounds, when dissolved in hexane and THF, are nearly indistinguishable, resembling spectra previously documented for toluene solutions (Fig. 17a–c)[116]. An absorption band with low intensity is observed at wavelengths greater than 400 nm, indicating that it is likely due to the CT electronic transition. The PL spectra of THF solutions of compounds **5** and **6** show a red shift and a broader full width at half maximum (FWHM) compared to those of hexane solutions. This result can be attributed to the higher solvent polarity. The confirmation of CT luminescence

is further supported by this observation, as well as the presence of the CT absorption band[117].

Table 5. Thermal characteristics of compounds **5**, **6**, and **7**

Characteristic	5	6	7
$T_{d\text{-}5\%}$[(a)], ºC	343	408	441
T_g[(b)], ºC	57	117	128
T_{cr}[(c)], ºC	122	210, 258	225, 269
T_m[(d)], ºC	204	255, 262	217, 266, 283

(a) 5% mass loss temperature ($T_{d\text{-}5\%}$)
(b) Glass-transition temperature (T_g)
(c) Crystallisation temperature (T_{cr})
(d) Melting temperature (T_m)

The solvent dependence of ^{1}CT in compound **5** was observed, with a lower energy level in more polar THF solutions than in less polar hexane solutions. This state exhibited lower energy than the ^{1}LE states of phenoxazine and N-hexylacridone, which mimic the electron-donating and electron-accepting components of compound **5**. The results for compound **6** mirrored those observed for compound **5**. In contrast, the PL spectrum of compound **7** dissolved in THF showed two clearly distinguishable bands. However, when dissolved in hexane, the spectrum closely resembled that of N-hexylacridone (Fig. 17d). These bands may be regarded as a characteristic manifestation of twisted internal charge transfer (TICT) states (Fig. 17c)[118].

The PL spectrum of the melted compound **5** displays a distinct peak at 557 nm (Fig. 18a), which falls within the yellow region of the electromagnetic spectrum. This suggests a shift towards longer wavelengths compared to the PL spectrum of the original crystalline sample. The PL decay curve of the sample shows two distinct components (Fig. 18d). The first component, with a lifetime (τ_1) of 42.3 ns, is typical of PF. The second component, with a lifetime (τ_2) of 3108 ns, is a sign of DF. The annealed film sample of compound **5** exhibits distinct luminescent characteristics. The emission spectra of the sample shifted to shorter wavelengths, specifically peaking at 465 nm, compared to the emission spectrum of the original sample (Fig. 18a). The PL spectrum of compound **5** dissolved in hexane roughly resembles it to that of the original crystalline sample. Furthermore, it exhibits a bathochromic shift relative to the long-wavelength emission bands of N-hexylacridone and phenoxazine solutions (Fig. 17d, e). The observed hypsochromic shift in the ^{1}CT emission of the annealed crystalline sample is attributed to conformational restrictions and solvation irregularities typical of the solid state. The annealed compound **5** exhibits a blue-shifted ^{1}CT emission, characterised by a short decay time (τ_1) of 2.8 ns, commonly associated with rapid fluorescence. No persistent fluorescence is detected. The lifetime of this phenomenon is slightly longer than the predicted lifetimes of ^{1}LE emissions in the solutions of N-hexylacridone (1.14 ns) and phenoxazine (2.67 ns) (Fig. 17f).

The emission colours of the powders exhibit a strong dependence on their crystallinity, which can be modulated by external stimuli. The crystallinity of the

compound **5** powder samples, as determined by X-ray diffraction, was 46.3%, 88.6%, 86.2%, 49.8%, and 61.1% for the pristine, ground, annealed, melted, and re-annealed samples, respectively, demonstrating the impact of different treatments on the material's structure. Through thermal annealing at a crystallisation temperature (T_{cr}), the crystallinity of the material is enhanced, resulting in a shift towards the blue end of the emission spectra. Interestingly, the emission changes observed in this case can be reversed. When the yellow-emitting melted sample **5** is annealed, it turns blue, and when the blue-emitting annealed compound **5** is melted, it reverts to yellow.

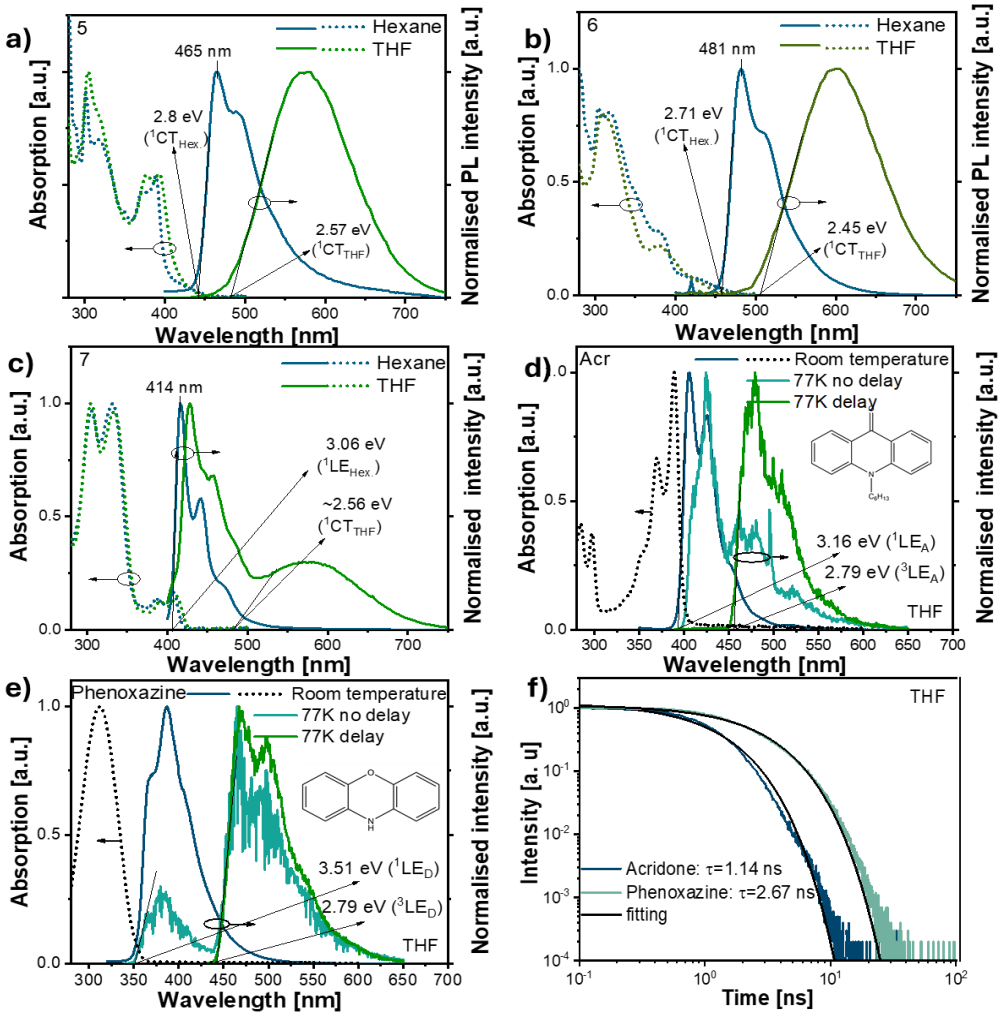

Fig. 17. Absorption and PL spectra of solutions of compounds **5** (a), **6** (b), and **7** (c) are compared with those of solutions of the electron-accepting N-hexyl acridone (Acr) (d) and the electron-donating phenoxazine (e); the phosphorescence spectra obtained 1 ms after stimulating the acridone or phenoxazine solutions in Me-THF at 77 K and the degradation curves (f) of Acr and phenoxazine in THF solutions are shown

By manipulating the crystallisation process, one can alter the molecular structure of compound **5**, leading to different PL spectra depending on the specific form. When **5** is melted, it shows a yellow emission with a broad PL spectrum (FWHM 114 nm) and a relatively long lifetime (τ_1 = 42.3 ns). Conversely, annealed **5** produces a blue emission with a distinct PL spectrum (FWHM 57 nm) and a much shorter lifetime (τ_1 = 2.8 ns), similar to the emission of **5** when dissolved in hexane. This suggests that crystallisation renders the emission of annealed **5** independent of environmental polarity.

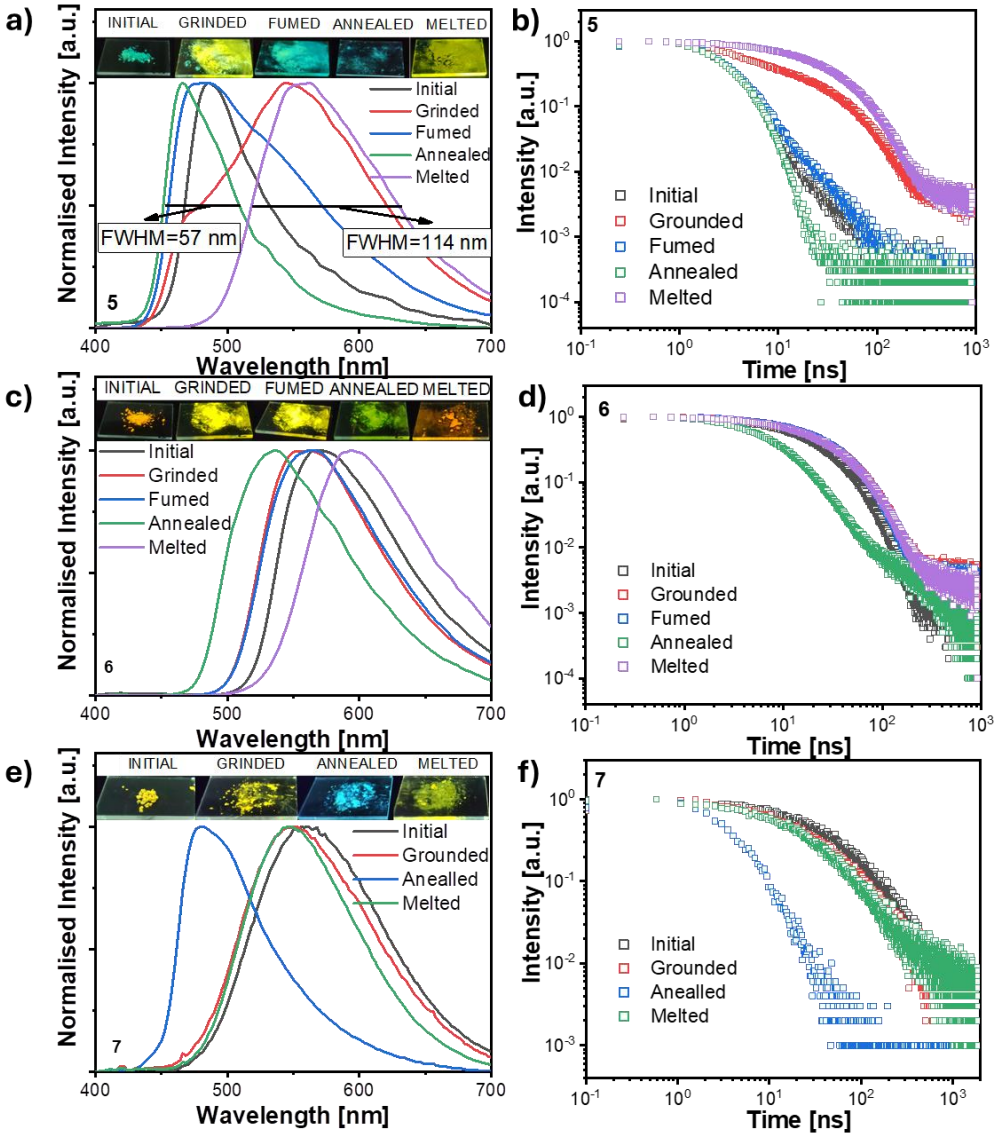

Fig. 18. Mechanoluminescent characteristics of compounds **5**, **6**, and **7**; PL spectra (a, c, e) and PL decay curves (b, d, f) of the original samples and samples subjected

to external stimuli (grinding, fuming, annealing, and melting) were analysed; insets show photographs of the samples under UV excitation

The emission properties of vacuum-deposited films of phenoxazine-substituted acridones **5**, **6**, and **7** can be tuned by thermal annealing, which influences their crystallinity. The vacuum-deposited films exhibit complete amorphousness, and their photoluminescence spectra closely resemble those observed for the melted powder form.

The spectral characteristics of compounds **6** and **7** are likely due to ^{1}CT emissions. The PL spectra of compound **6** powders show an FWHM of approximately 103 nm under various conditions. The properties of these compounds are influenced by the differences in dihedral angles between the phenoxazine and acridone moieties. Although ^{1}LE emission is evident in solution for compound **7**, it is not detected in solid form. The PL spectrum with the narrowest FWHM of 57 nm is observed for compound **5**, indicating its potential for OLED applications, followed by compound **6** with an FWHM of 103 nm and compound **7** with an FWHM of 73 nm. The FWHM values for compounds **5** and **6** in the ZEONEX matrix are similar, measuring 73 nm and 87 nm, respectively. However, compound **7** in ZEONEX displays a broader spectrum of 156 nm, which is attributed to the overlapping ^{1}LE and ^{1}CT emissions, as observed in THF solutions.

The PL spectra closely resemble those observed for the melted powder form of compound **5**. Crystallisation induced by thermal annealing of the amorphous film at a critical temperature of 122 ºC causes a hypsochromic shift in its spectrum, changing the wavelength from 565 to 467 nm. X-ray diffraction analysis reveals a crystallinity index of 68% for the vacuum-deposited annealed film of compound **5** (Fig. 19b).

The amorphous and crystalline films of compound **5** exhibit notable differences in their PL decay curves, which highlight their turn-on/turn-off TADF capabilities (Fig. 19d). The crystalline films of compound **5** do not show TADF due to a substantial energy difference (ΔE_{ST} = 0.28 eV) between their singlet and triplet states, which hinders efficient RISC. By altering the degree of crystallinity by varying the annealing duration, the emission colour of films deposited under vacuum can be tuned.

The as-prepared films of compound **5** exhibit TADF characteristics that closely resemble those of 9,9-dimethyl-9,10-dihydroacridin-4,6-triphenyl-1,3 (DMAC-TRZ)[117]. The steady-state and time-resolved PL spectra of DMAC-TRZ dispersions in matrices with low and high polarity exhibit variations due to distinct conformational and static dielectric disorders. Consistent with theoretical expectations, the annealed films of compound **5** exhibit emission spectra shifted toward the blue end of the spectrum (Fig. 19a). The blue shift of the PL spectrum caused by annealing can be interpreted as a spectroscopic demonstration of these events.

To assess the suitability of the surface morphology of thermally annealed films for the production of “crystalline” OLEDs, atomic force microscopy (AFM) (Fig. 19f) measurements were conducted on both the as-prepared and annealed films of compound **5** vacuum-deposited on a glass substrate. The film that has not undergone

annealing has a relatively uniform surface, with some morphological features exhibiting an average height of 4.44 nm and a root mean square roughness (R_q) of 2.50 nm. The surface of the annealed film is somewhat more uneven, as indicated by randomly positioned ridges with an average height of 18.83 nm and an R_q value of 6.35 nm. Both the non-annealed and annealed films exhibit sufficiently low roughness values, which meet the acceptable OLED[119] criteria.

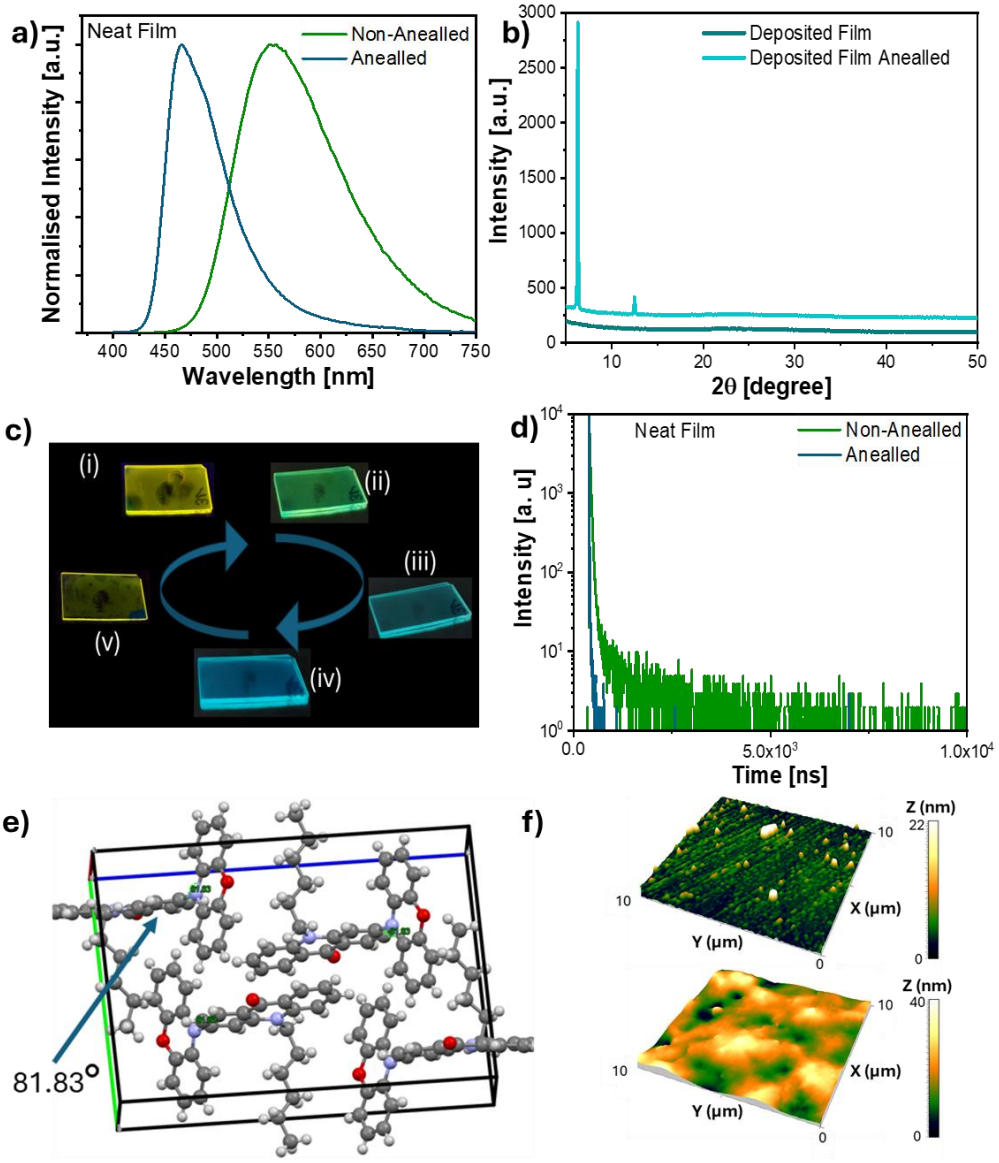

Fig. 19. PL spectra of film **5** before and after annealing (a); XRD-GI diffractograms of film **5** before and after annealing (b); photographs of film **5** at different annealing

stages under UV excitation (c); molecular arrangement and dihedral angle of **5** (d); AFM topography of film **5**: as-prepared and annealed (e)

The work examines the emission characteristics of guest-host compound mixture films and their use as emissive layers in OLEDs. The annealed films of compound **5**, deposited via vacuum, did not exhibit the TADF effect. Furthermore, when used as emissive layers, these films did not result in OLEDs with high EQE (.

Table 7).

To accomplish triplet harvesting, the effects of hosting were examined throughout compound **5**. The PL spectrum of a molecular dispersion of compound **5** (1 wt %) in an inert polymer matrix (ZEONEX) indicates that its emission band, which reaches its highest intensity at 513 nm, undergoes a hypsochromic shift to 476 nm after thermal annealing at T_{cr} (Fig. 20a).

The distinct morphologies of the PL spectra of the non-annealed and annealed samples indicate that annealing reduces the level of conformational and/or solvation disorder. compounds that have reached conformational equilibrium exhibit improved characteristics in terms of TADF[117]. The process of annealing-induced crystallisation significantly enhances the luminous properties of the examined **5**: ZEONEX films. The crystallinity indices, obtained from the XRD-GI diffractograms, are 37.5% and 78.6% for the annealed samples of 10% and 20% molecular dispersions of compound **5** in ZEONEX, respectively. The PL decay curves of both the non-annealed and annealed samples of compound **5** dispersed in ZEONEX display forms that are distinctive of TADF emitters (Fig. 20e)[70]. Annealing significantly enhances the TADF efficacy. For non-annealed mixtures of compound **5**, the emission intensities measured in a vacuum I_{vac} were 2.3 times greater than those measured in air I_{air}. For the annealed dispersions, the measured I_{vac} value was six times greater than the I_{air} value (Fig. 20b). This observation can be attributed to the susceptibility of triplet states to oxygen.

The annealed dispersions of compounds **5** and **6** in ZEONEX exhibit nearly 100% total PLQY (Table 6). The high PLQY values were attributed the combination of AIEE and TADF. The PF and DF durations derived from the bi-exponential fitting of the PL decay curves are listed in Table 6. By calculating the integrals of the PL decay curves measured in a vacuum for the dispersions of **5** and **6** in ZEONEX, we were able to determine the proportions of PF and DF contributions, as well as the quantum yields of PF and DF.

The measured k_{RISC} values (1.92×10^6 s^{-1} for **5**, 1.46×10^6 s^{-1} for 6, and 3.3×10^5 s^{-1} for **7**) are among the highest ever recorded values for TADF emitters[120–123]. The ratios greater than 1 for k_{RISC}/k_{ISC} suggest that RISC is faster than ISC, thereby preventing non-emissive energy losses via triplet states. According to El Sayed's rule, the RISC process is forbidden between electronic states that are comparable in nature, such as π-π* CT[124]. This results in quicker RISC in compounds with TADF through the intermediate ^{3}LE excited state. In contrast to the efficient ISC process observed in donor-acceptor compounds, this mechanism involves the presence of an intermediate ^{3}LE excited state between the singlet ^{1}CT and triplet ^{3}CT excited states[125]. The energies of the ^{1}LE states of phenoxazine and N-hexylacridone in compounds **5**, **6**,

and **7** are greater than those of the corresponding ^{1}CT and ^{3}CT states. Consequently, both ISC and RISC processes may not exhibit the expected efficiency level upon initial examination. Additional factors to consider include variations in relaxation rates between singlets and triplets, as well as the intermingling of energy levels[8]. RISC processes are more efficient than ISC for the annealed dispersions of **5**, **6**, and **7** in ZEONEX.

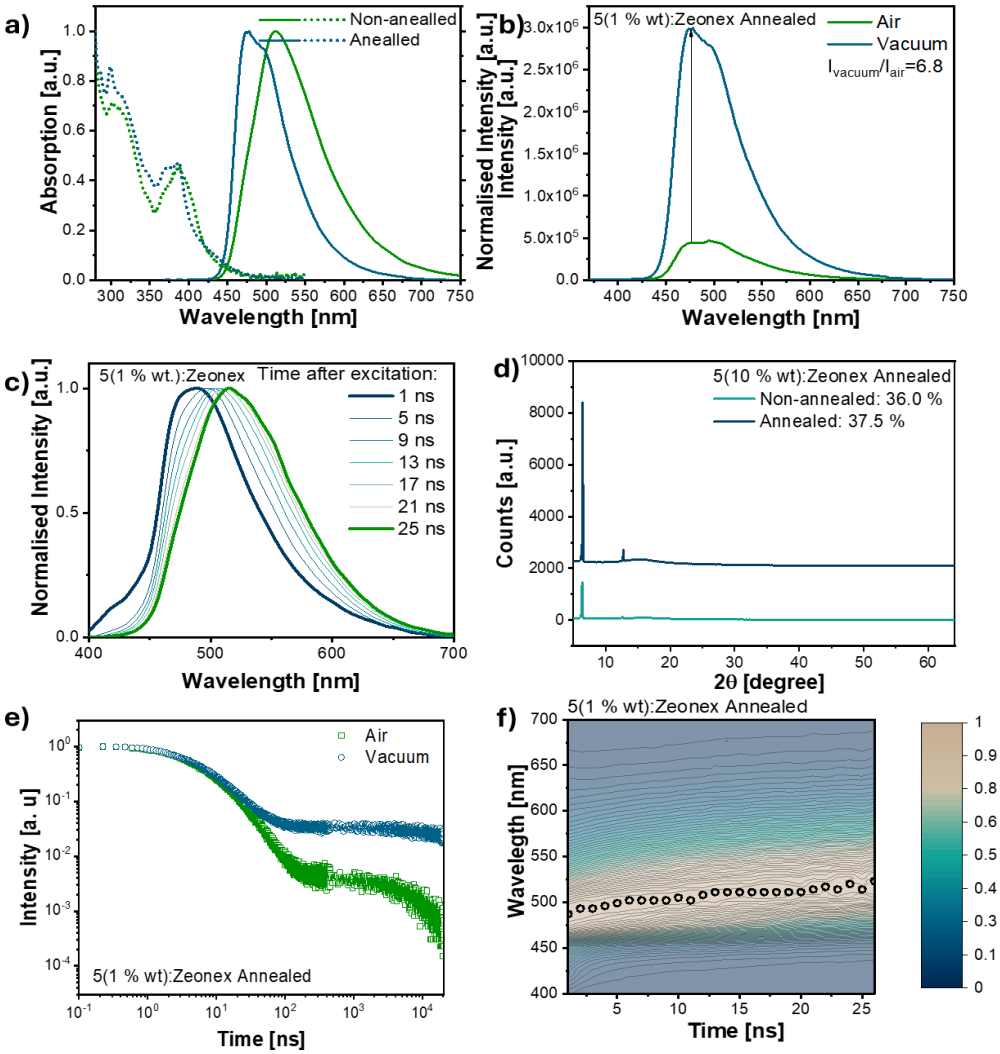

Fig. 20. Absorption and PL spectra of molecular dispersions of 5 (1 wt %) in ZEONEX (a); PL spectra in air and vacuum (b); time-resolved PL spectra of annealed films of molecular dispersion of **5** (1 wt %) (c, f); XRD-GI diffractograms of molecular dispersion of **5** (10 wt %) in ZEONEX before and after annealing (d); PL decay curves of molecular dispersions of **5** (1 wt %) in ZEONEX in air and vacuum (e)

The cause of the significant amplification of TADF observed in the annealed samples of **5** dispersed in ZEONEX was investigated using ultrafast time-resolved spectroscopy. Both the untreated and annealed samples exhibited no noticeable alterations in their form over time. However, there was a gradual shift in the PL spectrum over a longer period (Fig. 20c, f). The time-resolved changes in the PL spectra of compounds that display TADF are attributed to conformational disorder, which is a characteristic shared by most standard TADF compounds[126–129].

The pristine sample exhibited a picosecond decay component, which is not present in the PL decay curve of the annealed sample. The TA spectra exhibited two prominent induced absorption bands, without any negative band resulting from the stimulated emission within the fluorescence band area. This observation suggests that the CT origin of the PL bands is the main factor influencing the TA spectra.

Unlike the PL decay, the transient absorption dynamics exhibited no significant differences between the unaltered and heat-treated materials. The distinct behaviours of PL and TA suggest that the rapid decay of PL in the unaltered samples is unlikely due to the relaxation of excited compounds back to their ground state. However, only a small fraction of the compounds in the original sample undergo rapid relaxation to a non-radiative excited state. This condition may occur when the N-hexylacridone and phenoxazine parts twist in a completely perpendicular manner, disrupting the overlap of π orbitals.

The enhanced temporal resolution of the TA measurements revealed additional phenomena not apparent in the PL decay curves. The extended wavelength-induced absorption band showed rapid partial decay in less than 1 picosecond, which is tentatively attributed to the anticipated relaxation of the localised excited state to the CT state. The ultrafast PL and TA dynamics exhibited a high degree of quantitative similarity in the film with a 10 wt.% concentration of compound **5** in ZEONEX.

Table 6. Photophysical parameters of annealed films of molecular annealed dispersions of **5**, **6**, and **7** in ZEONEX obtained under inert atmosphere

Characteristic	**5**:ZEONEX	**6**:ZEONEX	**7**:ZEONEX
FWHM[(a)], nm	73	87	156
PLQY, %	100	100	36.5
τ_{PF}[(b)], ns	22.77	22.8	26.59
τ_{DF}[(c)], ns	50965	44157	44908
PF[(d)], %	0.65	1.29	1.9
DF[(e)], %	99.35	98.71	98.1
Φ_{PF}[(f)], %	0.65	1.29	0.69
Φ_{DF}[(g)], %	99.35	98.7	35.81
k_{PF}[(h)], s^{-1}	2.89×10^5	5.64×10^5	2.6×10^5
k_{DF}[(i)], s^{-1}	1.95×10^4	2.24×10^4	7.97×10^3
k_{ISC}[(j)], s^{-1}	2.87×10^5	5.57×10^5	2.55×10^5
k_{RISC}[(k)], s^{-1}	2.97×10^6	1.74×10^6	4.2×10^5

(a) Full width at half maximum (FWHM)
(b) Prompt fluorescence lifetime (τ_{PF})
(c) Delayed fluorescence lifetime (τ_{DF})

(d, e) Fractional intensities of prompt (A_1) and delayed (A_2) fluorescence, obtained through fitting of the PL decay curve using the formula $I_{PL} = A_1 e^{\left(-\frac{t}{\tau_{PF}}\right)} + A_2 e^{\left(-\frac{t}{\tau_{DF}}\right)}$ [45]
(f, g) Quantum yields of prompt (Φ_{PF}) and delayed fluorescence (Φ_{DF})
(h) Prompt fluorescence rate constant (k_{PF})
(i) Delayed fluorescence rate constant (k_{DF})
(j) Intersystem crossing rate constant (k_{ISC})
(k) Reverse intersystem crossing rate constant (k_{RISC})

This work examines how the alignment of singlet and triplet excited states of compound **5**, generated by annealing, affects the EL capabilities of organic luminophores in OLEDs. The fabricated OLEDs consisted of the following layers: MoO_3 (0.35 nm), NPB (44 nm), a light-emitting layer (24 nm), TSPO1 (4 nm), TPBi (40 nm), LiF (0.35 nm), and an aluminium electrode. The emission layers were composed of a 10 wt. % dispersion of compound **5** in various host materials, including NPB, 3,3′-di(9*H*-carbazol-9-yl)-1,1′-biphenyl (mCBP), 3,6-di-tert-butyl-9-(2-(1-phenyl-1*H*-benzo[d]imidaz (SM-66)[130], and tris(4-carbazoyl-9-ylphenyl)amine (TCTA). The EL characteristics values are provided in .

Table 7.

Table 7. Output electroluminescent parameters of OLEDs untreated by thermal annealing (C1–C5) and thermally annealed (C1A–C5A) EMLs

Device	**EML**	**λ_{EL}, nm**	**V_{ON}, V**	**L_{max}, cd/m^2**	**CE_{max}, cd/m^2**	**PE_{max}, lm/W**	**EQE_{max}, %**
C1	NPB:**5**	523	5.9	5710	3.6	1.5	1.1
C1A	NPB:**5**	524	6.1	10210	3.4	1.3	1
C2	mCBP:**5**	527	4.7	21080	15.3	8.1	4.2
C2A	mCBP:**5**	527	5.3	16910	21.9	9.5	5.9
C3	SM-66:**5**	500	5.7	4410	15.1	6.9	5.8
C3A	SM-66:**5**	495	5.2	3280	21.3	12.2	10.11
C4	TCTA:**5**	526	4.3	15990	30.1	17.5	8.6
C4A	TCTA:**5**	526	3.8	14800	62.4	49.1	20.7
C5	**5**	545	5.6	17250	6.2	2.4	1.9
C5A	**5**	520	5.7	9700	3.5	1.6	1.1

Device structure: MoO_3 (0.35 nm)/NPB (44 nm)/EML (24 nm)/TSPO1 (4 nm)/TPBi (40 nm)/LiF (0.35 nm)/Al

Device C5 achieved a maximum EQE of 1.9%, which is somewhat lower than the previously reported maximum EQE of 2.3% for reference devices. Thermal annealing of the emissive layer, composed solely of emitter **5**, deteriorated its electroluminescent characteristics instead of enhancing them. The calculated EQE values for OLED C5A were barely above 1%, which was expected, as the annealed layers of pure **5** did not exhibit any TADF. OLEDs constructed using a non-annealed layer of **5** (10%) dispersed in mCP, as described in a previous publication, exhibited a higher EQE (13%) compared to the devices (C1–C4) studied in this work. Devices C1–C4, which were not annealed, exhibited an EQE of up to 8.6% when TCTA was used as the host material. However, device C4A, which included the annealed

emissive layer of **5** dispersed in TCTA, achieved significant enhancement in its highest EQE values, reaching up to 20.7%. This enhancement may be partially attributed to emitter crystallisation, as shown by the presence of crystalline phases in the diffractogram of the guest-host emissive layer. Upon annealing the emissive layer, devices C2A and C3A exhibited significant enhancement in their maximum EQE.

The findings clearly demonstrate that the thermal annealing of emissive layers with guest-host properties, including **5** as a luminophore, is a key factor in enhancing device performance. It is assumed that heat application allows the singlet and triplet excited states in **5** to reach equilibrium, thereby promoting efficient TADF. The superior EQE values of device C4A, reaching 20.7%, may be due to the high stiffness of the host material, TCTA, which has the highest T_g of 151 °C[131] compared to other hosts (95 °C of NPB[132], 90 °C or mCBP[133], and 100 °C of SM66[130]). Therefore, it is anticipated that the annealing process, which leads to molecular structure rearrangement and contributes to crystallisation, could significantly enhance the electroluminescent capabilities of organic luminophores that are currently considered inefficient.

3.4. An experimental and theoretical study of exciplex-forming compounds containing trifluorobiphenyl and 3,6-di-tert-butylcarbazole units and their performance in OLEDs (Scientific publication No. 4, Q1)

This chapter is based on an article published in *Journal of Materials Chemistry C* (2020), Volume 8, pp. 14186–14195[134]. This study investigates two compounds containing trifluorophenyl and carbazole moieties. The influence of the number of donor groups on the characteristics of the materials is examined based on experimental findings. The compounds demonstrated the ability to form exciplexes with suitable electron-accepting compounds. The chemical structures of the investigated compounds 3,6-di-tert-butyl-9-(2',4',6'-trifluoro-[1,1'-biphenyl]-3-yl)-9*H*-carbazole (**9**) and 9,9'-(2',4',6'-trifluoro-[1,1'-biphenyl]-3,5-diyl)bis(3,6-di-tert-butyl-9*H*-carbazole) (**10**) are shown in Fig. 21.

The study investigates the morphological transitions and thermal stability of derivatives **9** and **10** using differential scanning calorimetry (DSC) and thermogravimetric analysis (TGA) measurements. Both compounds were isolated after synthesis and purification as crystalline materials, with endothermic melting signals observed in the first heating scans of the DSC measurements. Compound **10** showed higher melting (292 °C) and crystallisation temperatures (134 °C) due to its more symmetrical structure and overall higher molar mass (Table 8). No additional morphological transitions were detected during the cooling and heating scans of the DSC measurements, indicating a tendency to transform to an amorphous solid state.

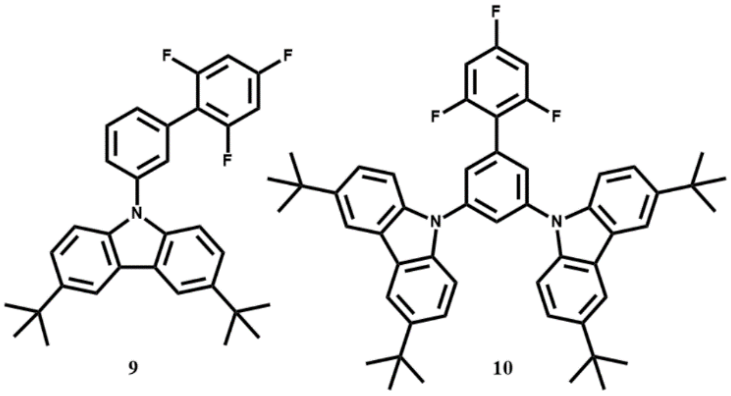

Fig. 21. Molecular structure of compounds **9** and **10**

CV was applied to study the electrochemical properties of derivatives 9 and 10. Both compounds exhibited reversible oxidation, and ionisation energy values were estimated from the oxidation onset potentials relative to ferrocene. Ionisation potential values obtained from PE measurements were found to be comparable for both compounds and higher than those estimated by CV (

Table 9). Minor differences in ionisation energy values obtained through different methods can be attributed to environmental variations between the solution and solid states.

Table 8. Thermal characteristics of compounds **9** and **10**

Compound	T_M, °C	T_{Cr}, °C	$T_{D-5\%}$, °C
9	134	-	277
10	292	134	369

The optical absorption properties of compounds **9** and **10** were investigated by analysing their UV-Vis absorption spectra in both solution and film forms (Fig. 22a). The energy gap values determined from the edges of the UV spectra of solutions of derivatives **9** and **10** in toluene (Table 9) were found to be similar due to the same electron-donating moiety present in both compounds. This observation suggests that the absorption properties of solutions and solid films of **9** and **10** are primarily due to contributions from donor-local excited states.

Table 9. Photophysical, electrochemical, and photoelectrical characteristics of compounds **9** and **10**

Characteristic	Media	9	10
λ_{Abs}[(a)], nm	Toluene solution/thin film	297, 346/ 298, 347	297, 346/ 230, 345
λ_{FL}, nm		354, 370/ 355, 366, 460	352, 367/ 352, 374, 439
E_g^{opt}[(b)], eV		3.49	3.41
Stokes shift[(c)], cm^{-1}		653/649	493/577
PLQY, %		3.67/3.03	3.63/3.05
S_1/T_1[(d)], eV	THF solution	0.64	0.58
ΔE_{ST}[(e)], eV		13/1	28/1
IP_{PE}, eV	Thin film	5.98	6.17
EA_{PE}, eV		2.49	2.76

(a) λ_{Abs} represents the wavelengths of absorption maxima
(b) E_g^{opt} is the optical gap, estimated as $1240/\lambda_{Abs\ onset}$, where $\lambda_{Abs\ onset}$ is the onset wavelength of absorption
(c) Stokes shift is calculated as $\lambda_{Fl}–\lambda_{Abs}$
(d) S_1 is the singlet energy, estimated as $1240/\lambda_{Flu\ onset}$; T_1 is the triplet energy, estimated as $1240/\lambda_{PH\ onset}$
(e) ΔE_{ST} is calculated as $T_1–S_1$

The photophysical characteristics of compounds **9** and **10** are influenced by their geometric structures and change upon excitation (Fig. 22a;

Table 9). The emission bands of compounds **9** and **10**, which exhibit vibronic structures, appear in the deep blue region when dissolved in toluene at room temperature. The PLQY values for toluene solutions of compounds **9** and **10** were measured to be 13% and 28%, respectively. The triplet energy values obtained from the initiation points of the phosphorescence (PH) spectra were located in the blue area. The measured ΔE_{ST} values were relatively high, which is typical of fluorescence emission. Additionaly, the photophysical characteristics of compounds **9** and **10** were also examined in their solid-state form. The PL spectra of thin films displayed vibronic structures similar to those of their toluene solutions (Fig. 22a). The solid samples exhibited low PLQY values (around 1%) due to quenching from aggregation (

Table 9)[135]. The PL spectra of compound **9** were sensitive to oxygen, with a ratio of PL intensities (I_{vac}/I_{Air}) of 1.9. The solid sample of compound **10** exhibited PL decay curves with two distinct components: LE states at higher energies and a CT component at lower energies. The variations in the emission spectra and oxygen sensitivity observed in the solid samples of compounds **9** and **10**, as well as the discrepancies in their oxygen sensitivity, can be attributed to the distinct substitution patterns of the trifluorobiphenyl moiety. The photophysical characteristics of these compounds were also evaluated in doped systems, considering the emission quenching due to aggregation.

The study aimed to investigate the photophysical properties of compounds **9** and **10** in doped systems, considering the aggregation-induced quenching of emission. Compounds **9** and **10** formed sky-blue exciplexes with the electron acceptor 2,4,6-tris[3-(diphenylphosphinyl)phenyl]-1,3,5-triazine (PO-T2T), one of the most widely studied exciplex-forming acceptors[80,136]. The spectra of solid films of molecular mixtures of **9** and **10** with PO-T2T showed significant red shifts compared to the PL spectra of non-doped films of these compounds (Fig. 22c). The PL spectra of both exciplex-forming systems were broad and characteristic of CT.

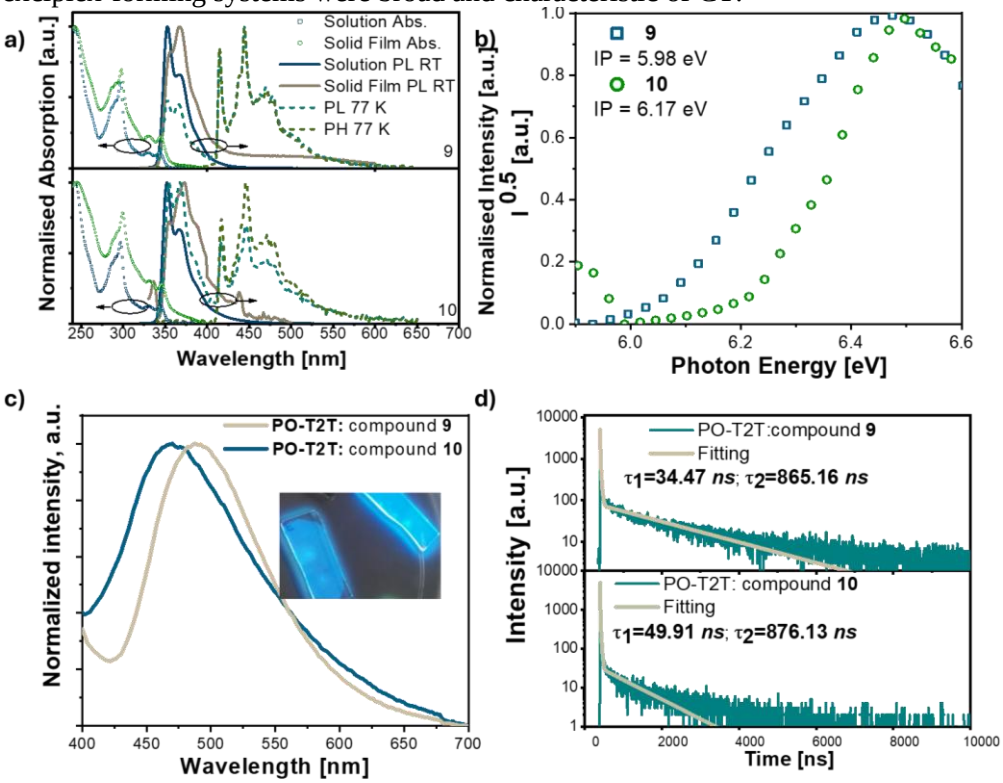

Fig. 22. UV–Vis absorption, PL emission spectra of dilute toluene solutions and thin films at room temperature, and PL and phosphorescence of diluted THF solutions at 77 K of compounds **9** and **10** (a); photoelectron emission spectra of solid samples

recorded in air (b); PL spectra (c) and PL decay curves (d) of formed exciplex systems **9**:PO-T2T and **10**:PO-T2T

The exciplex-forming mixtures **9**:PO-T2T and **10**:PO-T2T exhibited low PLQY values of 4% and 2% under air conditions. The PL spectra of exciplexes **9**:PO-T2T and **10**:PO-T2T peaked at the wavelengths of 489 nm and 470 nm (2.48 eV and 2.67 eV), respectively. This observation can be explained by the relatively high IP^D values of compounds **9** and **10** (Fig. 22,

Table 9), according to Eq. 3[137]:

$$h\nu_{ex}^{max} \simeq IP^{D} - EA^{A} - E_{C}; \quad (3)$$

where IP^{D} is the ionization potential of the donor, EA^{A} is the electron affinity of the acceptor, and E_C is the electron–hole Coulombic attraction energy (2.49 eV for **9**:PO-T2T and 2.67 eV for **10**:PO-T2T). The trifluorobiphenyl moiety was primarily used to increase the ionisation potential of compounds **9** and **10**, resulting in the blue-shifted emission of exciplexes formed between compound **9** (or **10**) and PO-T2T.

PL decays in the μs range were characterised by exciplex emission rather than monomer emission. The nanosecond-lived components of the decay curves correspond to prompt fluorescence, while the longer-lived components can be attributed to TADF. The intensity of the long-lived component is higher at 295 K than at 77 K, confirming the TADF nature of the exciplex emissions (Fig. 22d). The TADF origin of the delayed fluorescence in the exciplex-forming systems **9**: PO-T2T and **10**: PO-T2T was further verified by measuring the relationship between the PL intensity and laser pump pulse, where the slope values of the straight lines were close to 1[138].

The research is centred on advancing OLEDs by using exciplex-forming combinations of the acceptor PO-T2T and donors **9** and **10** to create the EML. Additional layers were incorporated to enhance device performance, including 1,4,5,8,9,11-hexaazatriphenylenehexacarbonitrile (HAT-CN) as the hole injection layer (HIL), 4,4'-cyclohexylidenebis[*N*,*N*-bis(4-methylphenyl)benzenamine] (TAPC) as the hole transporting layer (HTL), mCP as the electron blocking layer (EBL), TSPO1 as the hole blocking layer (HBL), and TPBi as the electron transporting layer (ETL) (Fig. 23a). D2 exhibited superior OLED properties compared to other samples due to the use of the exciplex system **10**:PO-T2T as the emissive layer. Sample D2 exhibited a greater luminosity of 4100 cd/m^2, as well as higher maximum current, power, and EQE of 24.8 cd/A, 12.2 lm/W, and 7.8%, respectively (Fig. 23c, Table 10). The efficiency decline in D2 was slower than that in D1, likely due to the greater thermal stability of compound **10** compared to compound **9**. When the brightness increased from 100 cd/m^2 to 1000 cd/m^2, the current, power, and EQE also rose, possibly because of an improved balance of charge carriers within the light-emitting layer at higher voltages. Monkman et al. observed a similar effect, where exciplex-forming mixes with low film PLQYs were used to generate OLEDs with high EQE[139]. Based on our current understanding, these are the most notable features achieved from exciplex systems incorporating a fluorinated donor[140–142].

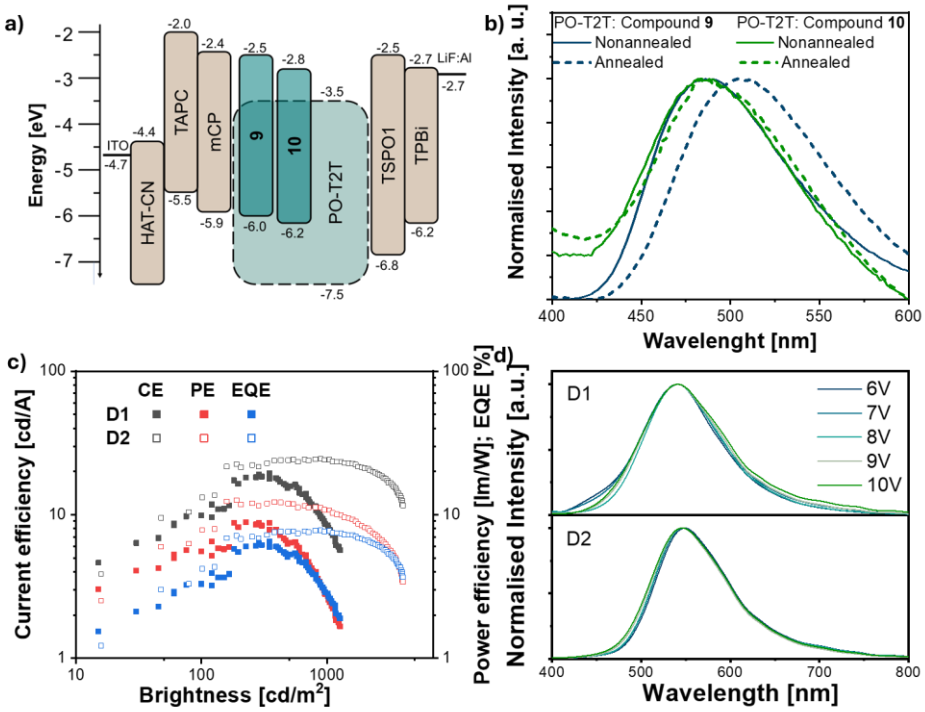

Fig. 23. Equilibrium energy diagram and OLED structures (a); PL spectra of non-annealed and annealed exciplex mixtures (b); EQEs, current efficiency (CE), and power efficiency (PE) versus brightness plots (c); EL spectra recorded at various driving voltages of devices D1 and D2 (d)

The EL spectra of devices D1 and D2 do not show a correlation with the PL spectra of 9:PO-T2T and 10:PO-T2T, as both are detected in the blue area of the electromagnetic spectrum (Fig. 22c, Fig. 23d). Notably, since the device construction lacks any functional material that might be identified by the presence of a comparable green emission, this phenomenon may be attributed to the formation of exciplexes with lower energy levels (Fig. 23b)[80]. Only the exciplex system with compound 9 demonstrated the ability to form such lower-energy states, and the PL spectra of annealed exciplex systems did not align with the EL spectra of the OLEDs. It should be also noted that the EL spectra of devices D1 and D2 may be influenced by exciplex emissions from other exciplex-forming systems. These systems can form at interfaces or even through spacers[138,143], such as mCP:PO-T2T[144–146] (emitting at a wavelength of 472 nm), TAPC:PO-T2T[147] (emitting at a wavelength of 550 nm), and TAPC:TPBi[147] (emitting at a wavelength of 442 nm). The TAPC compound demonstrates excimer (450 nm) and electromer (580 nm) emissions[148], although none emits in the green region.

It is likely that the EL spectra of devices D1 and D2 result from the combined emissions of exciplexes formed by **9**:PO-T2T (**10**:PO-T2T) and TAPC-based exciplex

TAPC:PO-T2T (or electromer of TAPC). Devices D1 and D2 produced green EL. The EL spectra of both the TAPC-free and TAPC-containing devices were accurately recreated for different configurations, supporting the hypothesis that two or more EL species overlap.

Table 10. EL characteristics of exciplex-based OLEDs with compounds 9 and 10

Device	**λ_{max}, nm**	**V_{on}, V**	**L_{max}, cd/m^2**	**CE / PE / EQE, cd/A / lm/W / %**		
				Max[(a)]	**@ 100 cd/m^2**[(b)]	**@ 1000 cd/m^2**[(c)]
D1	541	4.8	1250	19.7/8.4/6.5	9.9/5.5/3.3	8.5/2.7/2.8
D2	546	4.8	4100	24.8/12.2/7.8	13.2/7.8/4.2	24.3/10.7/7.7

CE, PE, and EQE (a) maximum values (b) at 100 cd/m^2 and 1000 cd/m^2 brightness (c); device structure: HAT-CN (10nm)/TAPC (40nm)/mCP (4 nm)/EML (24nm)/TSPO1 (4nm)/TPBi (40nm)/LiF (0.35nm)Al

The synthesised compounds demonstrated strong exciplex-forming abilities when combined with the electron acceptor 2,4,6-tris[3-(diphenylphosphinyl)phenyl]-1,3,5-triazine. Highly efficient exciplex-based OLEDs were developed, achieving high maximum CE, PE, and EQE achieved for devices based on exciplex EL.

4. CONCLUSIONS

1. The comprehensive photophysical study elucidated the distinct emission mechanisms of the three-compound series. Intramolecular charge transfer was attributed to benzophenone and diphenyl sulfone derivatives, and benzophenone derivatives exhibited thermally activated delayed fluorescence. Acridone derivatives with phenoxazine moieties exhibited thermally activated delayed fluorescence, while prompt fluorescence was observed for carbazole-containing acridones and quinacridones. For the third series of compounds, prompt fluorescence was observed, consisting of trifluorobiphenyl and carbazole derivatives. These insights provide a foundation for tailoring these compounds for specific optoelectronic applications.
2. The photophysical study of benzophenone derivatives revealed that UV irradiation induces structural alterations, resulting in both enhanced thermally activated delayed fluorescence intensity and shifts in emission colour. This dual response, combined with high sensitivity and a tunable detection range depending on the solvent, positions benzophenone derivatives as promising candidates for efficient and versatile UV sensors.
3. The characterisation of acridone and quinacridone derivatives demonstrated the ability to tune the emission colour across the visible spectrum, from blue to orange, by varying the substituents. Phenoxazine-substituted acridones exhibit thermally activated delayed fluorescence and aggregation-induced enhanced emission, leading to high electroluminescence quantum yields of up to 13%.
4. Investigating the structure-property relationships of acridone and phenoxazine derivatives revealed that thermal annealing induces crystallisation, leading to a significant enhancement in thermally activated delayed fluorescence kinetics. This thermally induced crystallisation was instrumental in achieving remarkable improvements in the external quantum efficiency of OLEDs incorporating these compounds, increasing from 8.6% to 20.7% after annealing. This highlighs the critical role of morphology control in optimising device performance.
5. The study of trifluorobiphenyl and carbazole derivatives revealed their ability to form exciplexes with electron-accepting materials, resulting in sky-blue emission with thermally activated delayed fluorescence properties. These exciplex systems, when employed as emissive layers in OLEDs, demonstrated a high external quantum efficiency of 7.7% and colour tunability, highlighting their potential for the development of high-performance, versatile electroluminescent devices.

5. SANTRAUKA

5.1. Įžanga

Organiniai puslaidininkiai optoelektronikos srityje tapo perspektyvia alternatyva neorganiniams puslaidininkiams. Nuo 1987 m., kai buvo sukurtas pirmasis organinis šviesos diodas (OLED)[1], ši sritis smarkiai išaugo. Prognozuojama, kad iki 2030 m. rinka pasieks 566 mlrd USD[17,18]. Tokį susidomėjimo didėjimą galima paaiškinti keliais veiksniais, įskaitant organinių puslaidininkių universalumą, jų pritaikomumą įvairiuose srityse (OLED, organiniai saulės elementai[19], tranzistoriai[20], jutikliai[21,22]), jų potencialą lanksčiojoje elektronikoje ir jų tvarumą dėl perdirbamumo ir pigios gamybos[25,29].

Vis dėlto organiniai puslaidininkiai iš tiesų yra perspektyvūs dėl savo lankščių ir jiems būdingų savybių. Įprastinių neorganinių puslaidininkių kristalinės struktūros yra nelankščiomis[32], o organinius puslaidininkius sudaro dinamiškos molekulės. Jų savybes lemianti molekulinė struktūra, sukimasis, vibracija ir judėjimas turi įtakos optiniam ir elektriniam medžiagos elgesiui. Dėl natūralaus lankstumo jų savybės gali būti keičiamos reaguojant į išorinius dirgiklius. Pavyzdžiui, Zhu ir kt. parodė, kad UV spindulių poveikis padidino perileno Schiffo bazės darinių fluorescenciją[33]. Tyrėjai teigė, kad šį įvykį lėmė UV spinduliuotės sukelta molekulių trans-cis izomerizacija, dėl kurios pakinta cheminė forma ir padidėja fluorescencijos intensyvumas. Dėl šio jautrumo elektromagnetinei spinduliuotei atsiranda galimybė sukurti labai jautrius ir selektyvius jutiklius, skirtus įvairioms reikmėms – nuo UV spinduliuotės aptikimo iki optinio ryšio bangų ilgio stebėjimo. Panašiai Wang ir kt. pagerino tirpalu apdorotų OLED veikimą, atlikdami atkaitinimo procedūras, kurios pakeitė emisijos sluoksnių molekulinio pereinamojo dipolinio momento kryptį[34]. Keisdami tik atkaitinimo temperatūrą, mokslininkai galėjo tiksliai sureguliuoti šių molekulių išsidėstymą, todėl pagerėjo nešiklių judrumas ir efektyviau skleidžiama šviesa. Tai parodo, kokią didelę įtaką organinių puslaidininkių elgsenai gali turėti išoriniai veiksniai, ir rodo, kad kruopščiai manipuliuojant šiomis molekulėmis galima sukurti pažangius optoelektroninius prietaisus.

Šioje disertacijoje gilinamasi į sudėtingą organinių puslaidininkių pasaulį tiriant tris skirtingas junginių serijas: benzofenono ir difenilsulfono darinius su fentiazin-5,5-dioksido dalimis, akridono ir chinakridono darinius su karbazolo arba fenoksazino pakaitalais ir junginius, kuriuose yra trifluorfenilo ir karbazolo fragmentų. Šios šeimos pasižymi neįprastais emisinių savybių pokyčiais reaguojant į išorinius dirgiklius, pavyzdžiui, UV šviesą ar temperatūrą. Šie pokyčiai susiję su molekulinės konformacijos ir morfologijos pokyčiais, todėl išryškėja galimybės kurti jutiklius ir OLED, kurie naudoja TADF reiškinį.

Nagrinėjant pagrindinius organinių puslaidininkių elgsenos principus ir tiriant išorinių dirgiklių poveikį jų savybėms, šis tyrimas prisideda prie didėjančio šios srities žinių bagažo. Išvados atveria kelią kurti inovatyvius optoelektroninius prietaisus, pasižyminčius didesniu našumu, efektyvumu ir tvarumu.

Šio tyrimo tikslas – ištirti, kaip organinių puslaidininkinių junginių molekulinės konformacijos, struktūros ir morfologija veikia jų fotofizikines,

elektrofizikines ir optoelektronines savybes veikiant skirtingiems išoriniams veiksniams.

Šiam tikslui pasiekti buvo suformuluotos tokios užduotys:

- atlikti pasirinktų junginių fotofizikinius tyrimus, nustatant jų emisijos mechanizmus;
- ištirti benzofenono ir fenotiazin-5,5-dioksido junginio potencialą UV jutikliams, tiriant jų TADF intensyvumo priklausomybę nuo UV sužadinimo;
- suprojektuoti, pagaminti ir charakterizuoti OLED, kurių sudėtyje yra akridono ir chinakridono junginių, elektroliuminescencines savybes;
- ištirti akridono ir fenoksazino darinių struktūros savybių įtaką fotofizikinėms jų savybėms ir pritaikyti OLED gamyboje;
- įvertinti naujų trifluorbifenilo ir karbazolo darinių pagrindu sudarytų eksipleksų emisijos mechanizmą ir jų pritaikomumą OLED.

Darbo naujumas:

- Tiriant benzofenono ir difenilsulfono dariniais su fentiazin-5,5-dioksido dalimis, pirmą kartą nustatytas organinių spinduolių fotostimuliuojamos fluorescencijos reiškinys, kai, veikiant UV spinduliams, kinta ir emisijos spalva, ir intensyvumas. Darbe atskleistas naujas fotostimuliuojamos fluorescencijos mechanizmas, kuris, veikiant UV spinduliams, apima konformacinę izomerizaciją tarp dviejų stabilių dažiklio molekulės konformerų.

- Akridono ir chinakridono darinių su skirtingais donoriniais fragmentais, iš kurių gaunamos įvairių spalvų – nuo mėlynos iki oranžinės – elektroliuminescencinės medžiagos, apibūdinimas. Darbe parodyta dispergavimo ir molekulinės struktūros įtaka šių junginių emisijos charakteristikoms ir jų potencialus naudojimas aukšto efektyvumo TADF/AIEE OLED ir kituose optoelektroniniuose prietaisuose.

- Termiškai kontroliuojama mechanochrominė liuminescencija, kai emisijos spalva gali būti grįžtamai keičiama išoriniais dirgikliais, tokiais kaip grūdimas, veikimas tirpiklio garais, išlydimas ar atkaitinimas, pirmą kartą pademonstruota naudojant akridonus su fenoksazino fragmentais. Darbe parodoma, kaip atkaitinimo sukelta kristalizacija daro įtaką šių junginių TADF charakteristikoms, o tai labai padidina išorinį OLED kvantinį efektyvumą.

- Šiame darbe charakterizuojami nauji karbazolo pagrindo emiteriai, kurie taip pat rodo, kad juos galima naudoti aukšto efektyvumo OLED, kurių išorinis kvantinis efektyvumas siekia 7,8 %. Darbe, naudojant akceptorių su fluoro atomus, nagrinėjamas mėlynai ir žaliai spinduliuojančių eksipleksų susidarymas OLED įrenginiuose, pabrėžiant būtinybę suprasti eksipleksų susidarymą ant paviršiaus optimizuojant įrenginius.

5.2. Rezultatų Aptarimas

5.2.1. Polimorfinių akceptorių pagrindu sukurtos tridalės medžiagos su fotoindukuotu TADF, skirtos UV spindulių jutimui

Šis skyrius parengtas straipsnio, 2021 m. paskelbto mokslo žurnale „Chemical Engineering Journal“ (Volume 425, 13154974), pagrindu[81]. Šiame darbe naudojamas

TADF junginių donorų–akceptorių–donorų projektavimo metodas, įtraukiant fentiazin-5,5-dioksido, benzofenono ir difenilsulfono dalis, pasižyminčias skirtingomis elektronus priimančiomis savybėmis. Šių junginių cheminės struktūros pateikta 24a pav.

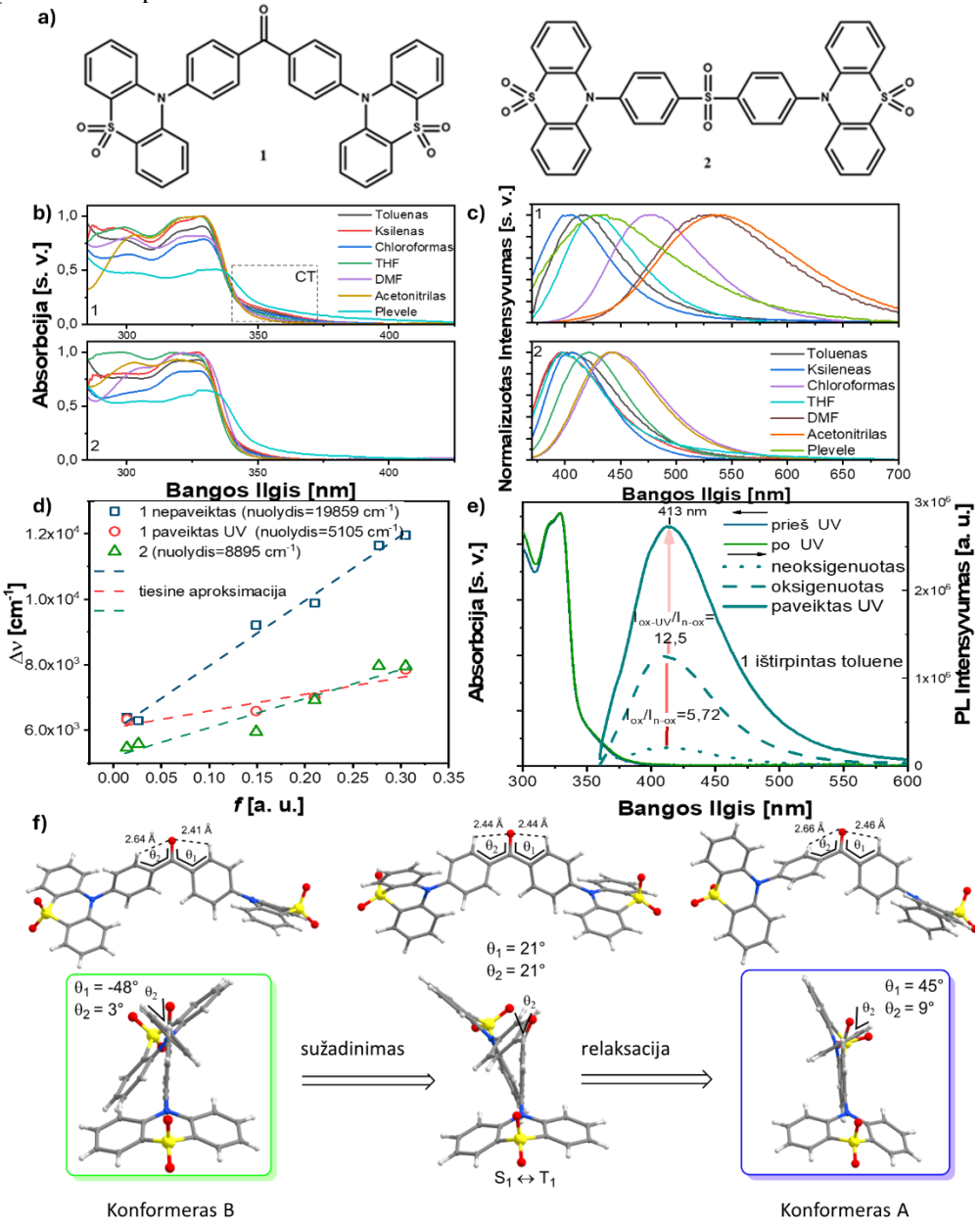

24 pav. 1 ir **2** junginio cheminė struktūra (a), **1** ir **2** junginių absorbcijos (b), fotoliuminescencijos (PL) spektrai (c). Lipperto–Matagos diagramos (d) **1** junginio tolueno tirpalo PL spektrai prieš, po deoksigenacijos ir apdorojimo UV spinduliais

(e), konformacinė izomerizacija tarp mėlynai emituojančio konformerio A ir žaliai emituojančio konformerio B (f)

1 ir **2** junginių UV sugerties spektrai buvo panašūs, o maksimumai buvo ties 300, 320 ir 328 nm, daugiausia dėl fentiazinų 5,5-dioksido dalies $\pi \rightarrow \pi^*$ perėjimų (24b pav.). Šios mažos energijos absorbcijos juostos nebuvo jautrios skirtingam tirpalų poliškumui. Tačiau **1** junginys turėjo papildomą sugerties juostą 340–370 nm diapazone, kuri, tikėtina, atsirado dėl intramolekulinio krūvio pernašos (ICT) tarp fentiazin-5,5,5-dioksido ir benzofenono vienetų. Abiejų junginių emisijai būdingas ICT, kaip rodo jų PL spektrų batochrominiai poslinkiai labai poliškuose tirpikliuose (24c pav.). Didesnis **1** junginio Lipperto–Matagos grafiko nuolydis rodo, kad jo ICT pobūdis yra stipresnis nei **2** junginio, o **1** junginiui apskaičiuotas 19 859 cm^{-1} nuolydžio parametro vertė yra viena didžiausių, palyginti su efektyviais donorinio-akceptorinio tipo TADF emiteriais (24 f pav.).

1 ir **2** junginių cheminė struktūra yra jautri molekuliniam sukimuisi, dėl kurio sužadinimo metu gali susidaryti hibridizuotos vietinio krūvio pernašos (HLCT) būsenos. Tačiau šios emisijos **1** ir **2** negalima apibūdinti HLCT dėl to, kad Lipperto–Matagos diagramos fiksuotos tik su vienu nuolydžiu (24 f pav.). THF tirpalo **1** greitąją ir uždelstąją fluorescenciją galima atpažinti atliekant nuo laiko priklausančius matavimus ore ir deoksigenuotuose ksileno ir acetonitrilo tirpaluose (24 d pav.). Labai poliškame acetonitrilo tirpiklyje ilgai trunkanti fluorescencijos gyvavimo komponentė greičiausiai yra susijusi su TADF. Tai pirmasis organinių dažiklių emisijos reiškinio, vadinamo fotostimuliuota fluorescencija, stebėjimas.

Abiejų junginių fotoliuminescencijos (PL) charakteristikos, kai jie ištirpinti tirpale, labai skiriasi. **1** junginys, išsiskiriantis aiškiomis ICT savybėmis ir ištirpęs poliniuose tirpikliuose, pasižymi raudonu PL spektro poslinkiu. Šis poslinkis atsiranda dėl efektyvaus krūvininkų atskyrimo, kai medžiagą veikia šviesa, todėl keičiasi ir spinduliuojamos šviesos spalva, ir intensyvumas. Be to, **1** junginys pasižymi savitomis reakcijomis, kai yra veikiamas UV spinduliais, jo molekulinėje struktūroje įvyksta grįžtamieji pokyčiai, dėl kurių keičiasi spalva ir emisijos intensyvumas. Šis reiškinys vadinamas fotostimuliuota fluorescencija. **2** junginys identiškomis aplinkybėmis pasižymi ne tokiais reikšmingais PL charakteristikų pokyčiais, o tai rodo silpnesnes ICT savybes ir skirtingą elgesį esant sužadintos būsenos, palyginti su **1** junginiu.

Tyrime nagrinėjami **1** junginio fotostimuliuojamos fluorescencijos reiškiniai naudojant UV spindulių sužadinimą. Veikiant UV spinduliuotei, **1** ir **2** plėvelės skleidė mėlyną šviesą (24 c pav.). Išspinduliuojamos šviesos PL spektrai buvo vientisi, o **1** ir **2** plėvelių maksimalus intensyvumas buvo ties 432 nm ir 400 nm atitinkamai.

Fotostimuliuotos fluorescencijos reiškinys rodo du skirtingus emisijos reiškinius: 1) emisijos spektrų (spalvų) poslinkį iš ilgesnių į trumpesnius bangų ilgius, veikiant UV spinduliams (iš žalios į mėlyną); 2) mėlynos emisijos intensyvumo padidėjimą veikiant UV spinduliams. Norint išsamiai suprasti pagrindinius procesus įvairiose terpėse, būtina nuodugniai ištirti šių efektų kilmę.

Tyrimai rodo, kad **1** tirpalo spalvos ir fluorescencijos intensyvumo pokyčiai, veikiant UV spinduliais, nėra susiję su **1** tirpalo molekulinės struktūros cheminiais pokyčiais, pavyzdžiui, skilimu ar protonizacija. Skirtingi **1** junginio polimorfai pasižymėjo mėlyna ir žalia emisija, kuri skyrėsi priklausomai nuo dvisienių kampų tarp fentiazino 5,5-dioksido ir benzofenono vienetų ir tarp benzofenono molekulių fenilinių žiedų (24 f pav.)[93]. Pirmasis emisijos efektas, susijęs su emisijos spektro perėjimu iš mažos energijos juostos į didelės energijos juostą, yra susijęs su **1** molekulių molekulinės konformacijos pokyčiais.

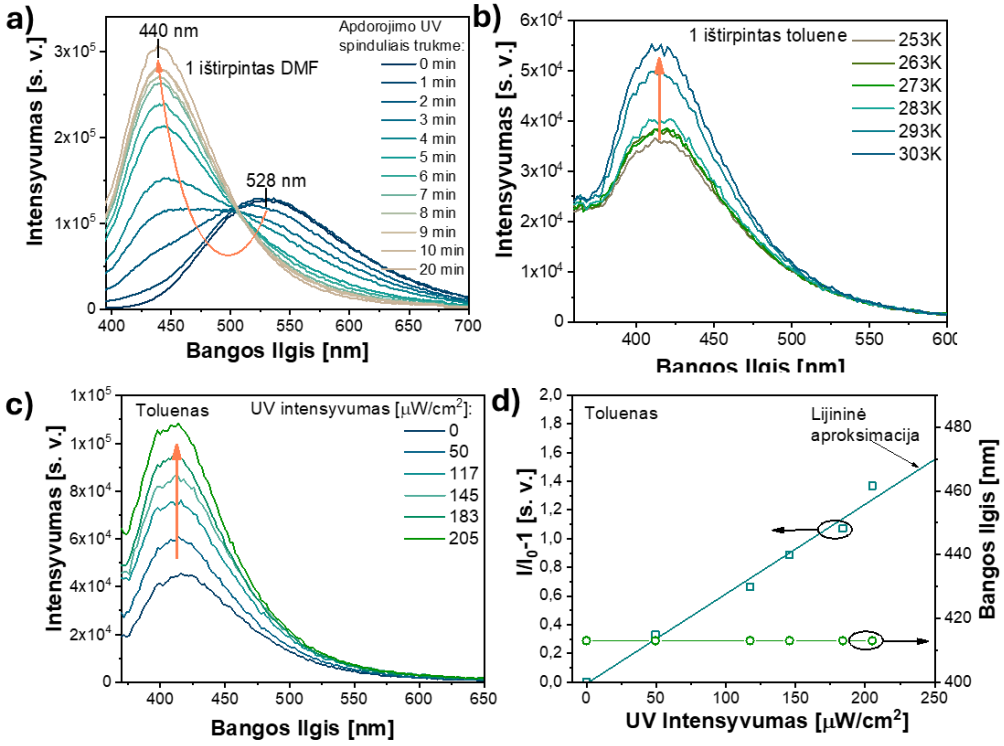

25 pav. 1 DMF tirpalo PL spektrai po įvairios trukmės UV apdorojimo (a); **1** tolueno tirpalo, apdoroto UV spinduliais ir užfiksuoto įvairiose temperatūrose, PL spektrai (c); pateikiami **1** junginio THF tirpalo fotoliuminescencijos spektrai (c); Sterno–Volmerio diagramos ir emisijos bangos ilgio priklausomybė nuo UV spinduliuotės intensyvumo (d).

Buvo tiriama S_1 energija įvairiose kristalinėse struktūrose. Prognozuota, kad A polimorfo monokristalo S_1 būsenos energija yra 3,09 eV, o B polimorfo monokristalo – mažesnė (2,84 eV). Šį skirtumą lemia konformaciniai skirtumai ir efektyvi π-delokalizacija virš benzofenono grupės B polimorfo, todėl ryšio ilgio kaita yra mažesnė. Mažesnę LUMO orbitalės energiją lemia delokalizacija virš benzofenono fragmentų. Ryšio ilgio kaita yra ryškesnė fentiazino 5,5-dioksido molekulės **1** polimorfo B dalyje, o tai lemia HOMO orbitalės lokalizaciją. Galutinis skirtumas tarp HOMO-LUMO tarpų sutampa su energijos skirtumu tarp S_1 būsenų

(0,25 eV), todėl išryškėja ribinių MO energijos vaidmuo nustatant S_1 būsenų vertikaliąsias energijas.

TADF reiškinys demonstruojamas parodant, kad energiškai atskirtos mišrios ICT+LE S_1 ir T_1 sužadintosios būsenos yra vibroniškai susietos per tarpinę LE pobūdžio T_2 būseną. T_1 eksitonų populiacijos padidėjimas ir vėlesnė RISC sukelta uždelstoji fluorescencija lemia stebimą **1** tolueno tirpalo emisijos intensyvumo padidėjimą po nuolatinio UV stimuliavimo (24 e pav.). Fotostimuliuojamą intensyvumo padidėjimą skatina tripletinių eksitonų skaičiaus padidėjimas ir tolesnis jų perėjimas į singletus. Kaip fotostimuliuojamos fluorescencijos priežastis taip pat siūloma konformacinė izomerizacija tarp žalia ir mėlyna emisija pasižyminčių junginio **1** molekulių formų. DMF tirpalų, kuriuose yra TEMPO priedų, bet PL spektrai, veikiami UV spindulių, nepasikeitė, o tai rodo, kad fotostimuliuojamos fluorescencijos mechanizmas gali vykti per radikalų tarpinį produktą (25 b pav.)[95].

Siekiant įrodyti, kad **1** junginys gali būti panaudotas kaip UV spinduliams jautri medžiaga optiniams jutikliams, PL spektrai buvo užregistruoti esant skirtingiems UV apšvietos galingumams, švitinant 10 minučių (25 c pav.). **1** tolueno tirpalo PL intensyvumas palaipsniui didėjo didėjant UV spinduliuotės intensyvumui ir pasižymėjo maža jutimo riba, mažesne nei 10 μW/cm^2. **1** tolueno tirpalo PL tiesiškai atitiko Sterno–Volmerio priklausomybę $I_0/I_{-1} = K_{SV}$[UV], esant skirtingam UV spinduliuotės intensyvumui. Buvo gauta $6{,}26\cdot10^{-3}$ [μW/cm^2]$^{-1}$ K_{SV} vertė **1** tirpalui toluene (25 f pav.). Skirtingas tiesines sritis galima nustatyti Sterno–Volmerio grafikuose, sudarytuose **1** THF ir DMF tirpalams. Pavyzdžiui, **1** THF tirpalo K_{SV} vertė buvo didžiausia (0,242 [μW/cm^2]$^{-1}$) 150–250 μW/cm^2 UV spinduliuotės galingumo intervale.

Mažiausia K_{SV} buvo gauta **1** DMF tirpalui ($4{,}2\cdot10^{-3}$ [μW/cm^2]$^{-1}$), kai UV spinduliuotės energijos diapazonas buvo iki 150 μW/cm^2. DMF tirpalas pasižymėjo žalios į mėlyną spalvą pereinančia kaita skirtingoms UV spinduliuotės dozėms.

5.2.2. Akridono ir chinakridono dariniai su karbazolo arba fenoksazino pakaitais: elektrochemija, fotofizika ir taikymas kaip TADF elektroliuminoforai

Šis skyrius parengtas straipsnio, 2022 m. paskelbto mokslo žurnale „Journal of Materials Chemistry C“ (Volume 10, 12377–1239190), pagrindu[97]. Šeši akridono ir chinakridono dariniai, kuriuose yra karbazolo arba fenoksazino pakaitų, buvo tikslingai sukurti ir susintetinti siekiant ištirti donorinio (D) ir akceptorinio (A) jungimo modelio (D-A, D-A-D arba D-π-A-π-D) įtaką jų fotofizikinėms savybėms ir taikymui OLED. **3**–**8** junginių cheminė struktūra pateikta 26 a pav.

3–**8** junginių absorbcijos spektrams būdingos D ir A fragmentų juostos, pavyzdžiui, **3** ir **4** junginių atveju – akridono (Acr) ir tert-butilkarbazolo (tCz), **5**–**7** junginių atveju – akridono (Acr) ir fenoksazino (PhNZ), o **8** junginio atveju – chinakridono (QAcr) ir tCz (3 b, c pav). Juostos pažymėtos siauromis vertikaliomis linijomis: Acr – 389 nm, tCz – 290 nm ($\pi\rightarrow\pi^*$) ir 307–335 nm ($n\rightarrow\pi^*$), PhNZ – 313 nm, QAcr – 290 nm ir 504 nm. Nedideli šių juostų poslinkiai ir išsiplėtimas matomi visų tirtų junginių (**3**–**8**) spektruose, ypač mažos energijos srityse. Šį reiškinį

galima paaiškinti ICT būsenų, atsirandančių dėl elektronus atiduodančių ir elektronus priimančių molekulių sąveikos, atsiradimu.

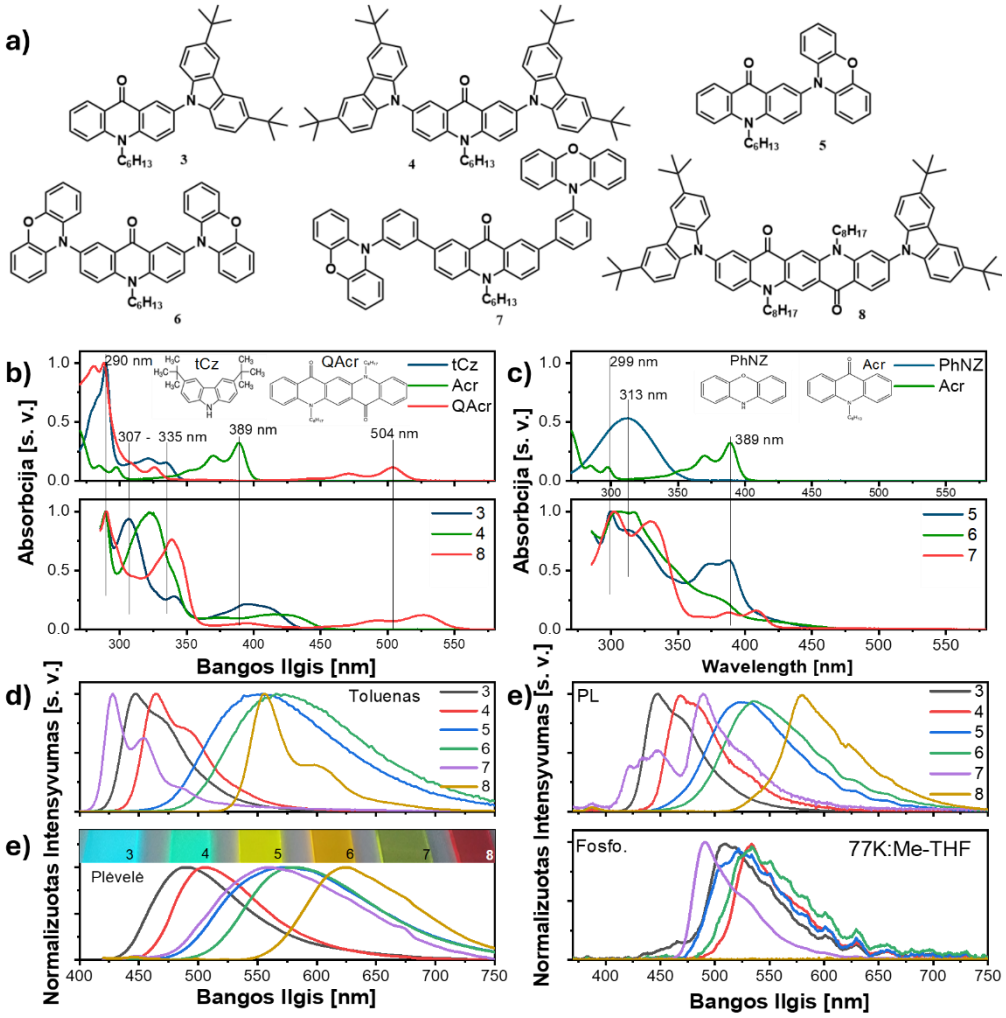

26 pav. 3–8 junginių molekulinė struktūra (a). Pateikiami tolueno tirpalų, turinčių **3–8** junginių, sugerties spektrai (b, c) ir palyginimui tCz, QAcr, PhNZ ir Acr sugerties spektrai. Be to, pateikti toluene ištirpintų **3–8** junginių (d) ir jų vakuume nusodintų plėvelių (e) PL spektrai. Pateikiami **3–8** junginių, ištirpintų Me-THF, PL ir fosforescencijos spektrai (f), užregistruoti 77 K temperatūroje. Fosforescencijos spektrams fiksuoti po sužadinimo naudotas 1 milisekundės delsos laikas. Sužadinti naudotas 330 nm bangos ilgis. (e) intarpe pateiktos vakuume nusodintų plėvelių nuotraukos, kai jos buvo veikiamos UV spindulių

Kietųjų sluoksnių **3–8** sugerties spektrai yra tokie patys kaip ir analogiškų tolueno tirpalų, tik jie yra daug platesni. Šį poveikį galima paaiškinti vienu iš dviejų veiksnių: agregacija arba didesniu ICT. Jis labiau tikėtinas, atsižvelgiant į visų tirtų

medžiagų atitinkamų PL spektrų formas, kurias sukelia ICT. Priešingai, tam tikri tolueno **3**, **4** ir **7**, **8** tirpalų PL spektrų aspektai atsiranda dėl LE būsenų rekombinacijos, kurią daugiausia sukuria elektronus priimančios molekulės. **5** ir **6** turi ICT formos PL spektrus tiek tolueno tirpaluose, tiek esant kietos būsenos, kurie susidaro dėl stiprių D-A sąveikų (26 d, e pav.).

11 lentelė. 3–**8** junginių fotofizikiniai parametrai, įskaitant singletų ir tripletų energijas

Parametrai	**Terpė**	**3**	**4**	**5**	**6**	**7**	**8**
$\lambda_{MAX}^{tol(a)}$**, nm**	Tol.	448, 469	464, 490*	551	571	429, 454, 488	555, 600
$\lambda_{MAX}^{plėvelės(a)}$**, nm**	Sluoksnis	490	506	565	581	558	625
$\lambda_{MAX}^{plėvelės(a)}$**, nm**	mCP	462	479	525	541	452, 525	594
PLQY[(b)]**, %**	Tol./ mCP	69/66	61/68	1,5/35	2/31	8,6/15,4	92/35
E_{S1}[(c)]**, eV**	Me-THF	2,92	2,79	2,68	2,59	3,02	2,31
E_{T1}[(c)]**, eV**		2,58	2,46	2,59	2,53	2,64	–
ΔE_{ST}[(d)]**, eV**		0,34	0,33	0,09	0,06	0,38	–

(a) bangos ilgis emisijos spektro smailėje; (b) PLQY, išmatuotos inertinėje aplinkoje; (c) singletinio (E_{S1}) ir tripletinio (E_{T1}) lygmens energijos paimtos iš atitinkamai PL (fluorescencijos) ir fosforescencijos spektrų, užregistruotų Me-THF tirpalų skysto azoto temperatūroje (77 K); (d) energijos skirtumas tarp E_{S1} ir E_{T1}.

Liuminescencijos ir laikinės spektroskopijos eksperimentai atskleidė ilgai trunkančią **5**–**7** junginių disperguotų mCP emisiją vakuumo sąlygomis (27 a, b pav.). PL spektrų forma prieš ir po vakuumavimo nepasikeitė. Tai patvirtina hipotezę, kad šią ilgai išliekančią emisiją sukėlė uždelstoji fluorescencija. Dėl deguonies pašalinimo padidėjęs tirpalų ir **5**–**7** junginių molekulinių dispersijų PL spektrų intensyvumas aiškiai rodo, kad uždelstą fluorescenciją sukelia tripletai (27c pav).

PL ir PL gyvavimo trukmės buvo matuotos su **5** junginio plėvelėmis oro ir vakuumo aplinkoje įvairiose temperatūrose (27 d–g pav.). TADF junginių PL gyvavimo trukmės kreivė apibūdinta fluorescencijos komponente nanosekundžių ir uždelstosios fluorescencijos komponente mikrosekundžių intervale. Uždelstosios fluorescencijos intensyvumas didėjo kylant temperatūrai, o tai rodo, kad uždelstąją fluorescenciją sukėlė temperatūros sužadintas mechanizmas. **5**–**7** junginių PLQY reikšmės tirpaluose yra palyginti mažos, tačiau daug didesnės PLQY reikšmės kietoje mCP matricoje, skirtingai nei **3**, **4** ir **8** junginio vertės šiose terpėse, o tai galima priskirti agregacijos sukeltam emisijos sustiprėjimui (AIEE) (11 lentelė)[103].

Taip pat pateikti **3**–**8** junginių dispersijų THF ir vandens mišiniuose PL matavimų rezultatai (27 h, i pav.). **3** junginio emisijos intensyvumas mažėjo didėjant vandens procentinei daliai tirpalo mišinyje, kaip būdinga junginiams, pasižymintiems ACQ[104]. ACQ taip pat nustatyta **4** ir **8** junginiuose. **5**–**7** junginiai buvo disperguoti

THF ir vandens mišiniuose, o emisijos intensyvumas nuolat didėjo didėjant vandens procentinei daliai, o tai rodo, kad **5**–**7** junginiai pasižymi AIEE.

Elektros pernešimas OLED emisiniuose sluoksniuose yra labai svarbus prietaiso veikimui, ypač elektroliuminoforų, esančių vienkomponenčiuose sluoksniuose, arba OLED legiruotuosiuose sluoksniuose. Šiame darbe, taikant lėkio trukmės (TOF) metodą, buvo ištirtos **3**–**8** elektroliuminoforų, krūvio pernašos savybes. Nustatyta, kad **3**, **6**–**8** junginiai yra vienpoliai, kuriuose pastebimas tik skylių judrumas, tačiau **4** ir **5** junginiai yra ambipoliniai, kuriuose vyksta ir p tipo (skylių), ir n tipo (elektronų) pernaša. Chinakridono darinys pasižymėjo didžiausia skylių judrumo verte.

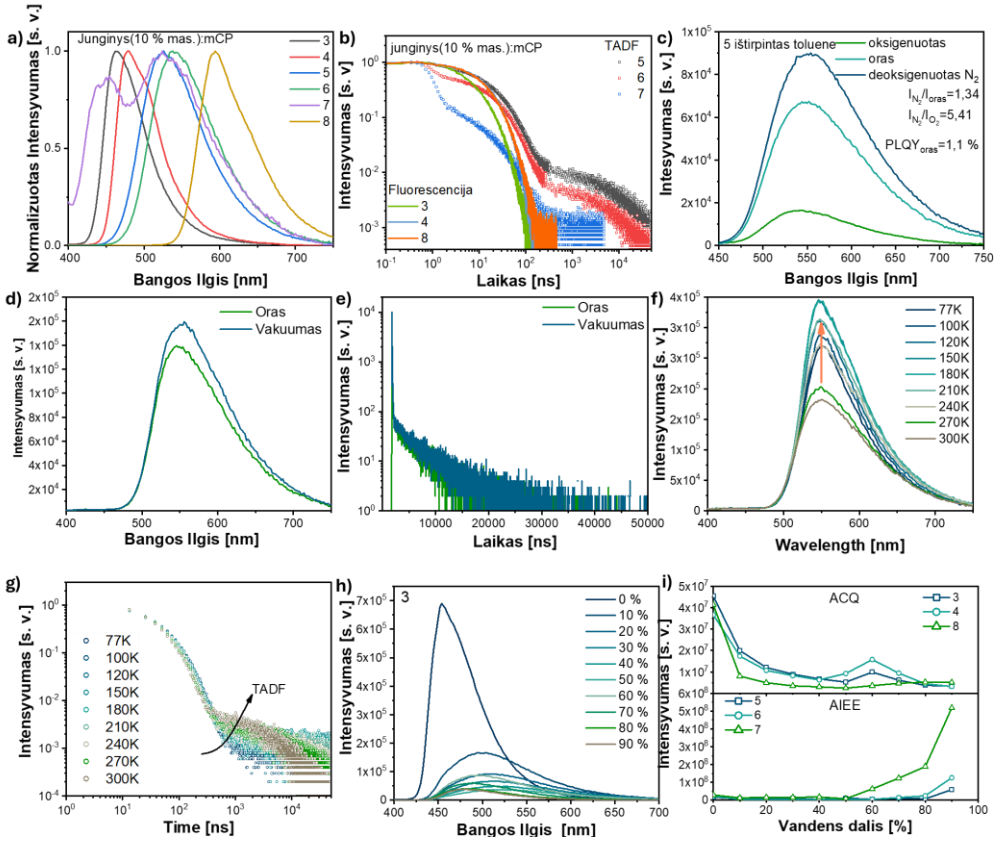

27 pav. 3–**8** junginių molekulinių dispersijų (10 % masės mCP matricoje) PL spektrai (a). Šių dispersijų PL gesimo kreivės (b). **5** junginio tolueno tirpalų PL spektrai ore, po deoksigenavimo ir po pakartotinio oksigenavimo (c). **5**(10 % masės): mCP PL spektrai (d) ir PL gyvavimo trukmių kreivės (e) kambario temperatūroje vakuume ir ore. PL spektrai (f) ir PL gyvavimo trukmių kreivės (g) išmatuotos esant įvairiai temperatūrai inertinėje aplinkoje. **3** junginio dispersijų THF ir vandens mišiniuose su skirtingomis procentinėmis vandens dalimis fotoliuminescencijos spektrai (h). Integruoti fotoliuminescencijos spektrų plotai

buvo pavaizduoti priklausomai nuo vandens kiekio procentinės dalies junginių dispersijose THF ir vandens mišiniuose (j)

12 lentelė. OLED su nelegiruotaisiais (A1-A6) ir legiruotaisiais (B1-B6) EML elektroliuminescenciniai parametrai

Prietaisas	EML	λ_{EL}[(a)], nm	V_{ON}[(b)], V	L_{max}[(c)], cd/m^2	CE_{max}[(d)], cd/m^2	PE_{max}[(e)], lm/W	EQE_{max}[(f)], %
A1	**3**	464	5,7	7475	2,56	0,9	1,6
A2	**4**	481	7,9	5135	1,53	0,4	0,7
A3	**5**	540	5,1	21200	8,02	3,6	2,3
A4	**6**	563	6,1	13200	3,8	1,26	1,3
A5	**7**	542	6,3	8460	2,77	0,91	0,76
A6	**8**	484,585	11,4	443	0,4	0,06	0,12
B1	**3:mCP**	458	5	4270	6,7	3,8	4
B2	**4:mCP**	459	6,4	2150	1,7	0,7	1,2
B3	**5:mCP**	505	4,7	7950	37,1	19,8	13
B4	**6:mCP**	548	3,5	22520	23,5	20,5	7,2
B5	**7:mCP**	426,455	5,4	1820	0,8	0,4	0,5
B6	**8:mCP**	587	6	4010	1,4	0,5	0,6

(a) didžiausiasis EL (λ_{EL}); (b) įjungimo įtampa (V_{ON}); (c) didžiausiasis ryškumas (L_{MAX}); (d) didžiausioji srovės (CE_{MAX}); (e) galios (PE_{MAX}) ir (f) išoriniai kvantiniai ($EQEM_{AX}$) efektyvumai. Prietaiso struktūra: MoO_3(0,35nm)/ NPB(44nm)/mCP (4 nm)/ EML (24nm)/ TSPO1(4nm)/ TPBi(40nm)/LiF(0,35nm)/Al

Susintetinti akridono ir chinakridono dariniai turi potencialą būti pritaikyti įvairiose srityse, įskaitant elektrochromines medžiagas, aktyviais sluoksniais bipoliniuose arba p kanalo lauko efekto tranzistoriuose ir elektroliuminoforus šviesą skleidžiančiuose dioduose. Pastebėta elektroliuminescencija yra susijusi tik su EML emisija, o gautų EL spektrų padėtys ir formos tiksliai atitinka PL spektrus, gautus iš grynų (nelegiruotųjų) ir disperguotų mCP (legiruotųjų) **3**–**8** sluoksnių (28 b pav., 12 lentelė).

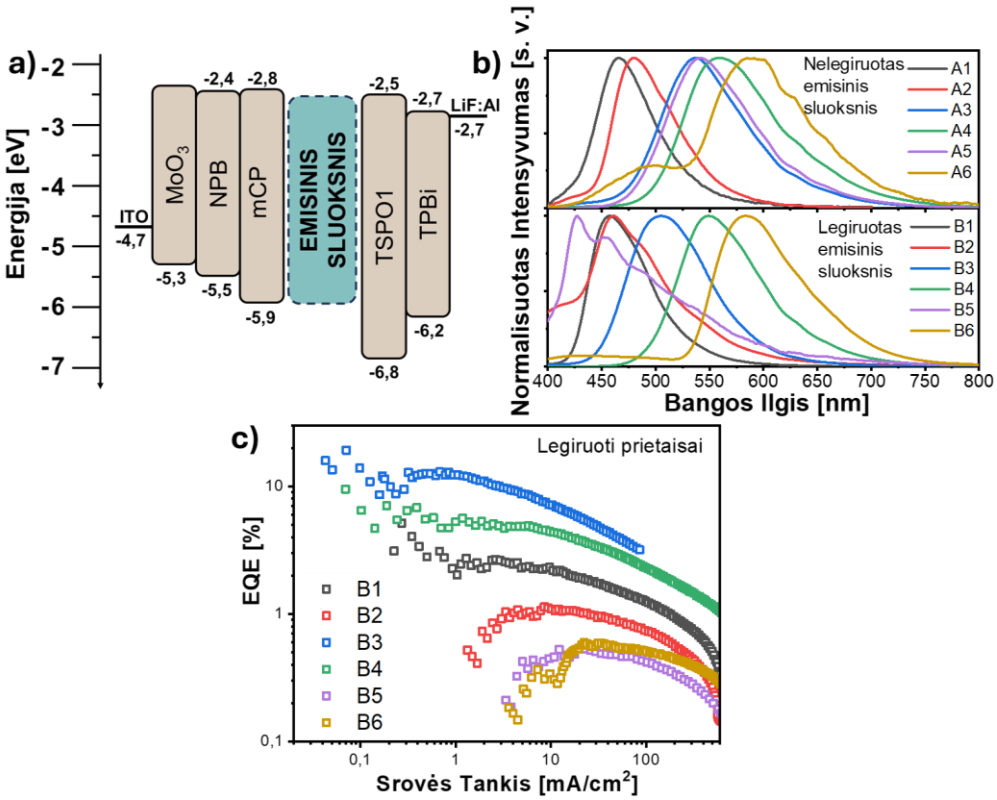

28 pav. OLED struktūros energijos diagrama (a), pagamintų prietaisų A1-A6 ir B1-B6 EL spektrai (b), prietaisų B1-B6 išorinio EQE priklausomybė nuo srovės tankio

Akridoną arba chinakridoną funkcionalizavus tik dviem donorais – tCz ir PhNZ – gaunami įvairūs elektroliuminoforai, kurių emisijos spektrai svyruoja nuo mėlynos iki oranžinės spalvos. Akridono su tCz pakaitalu nelegiruoti emisiniu sluoksniu šviestukai pasižymi mėlynos spalvos elektroliuminescencija. **5** ir **6** dispersijos mCP (prietaisai B3 ir B4) pasižymi EL spektrais, kurie, palyginti su A3 ir A4 prietaisų spektrais, yra hipsochromiškai pasislinkę, o jų spalvos koordinatės CIE1931 būdingos mėlynai sričiai. Įdomu tai, kad A5 ir B5 prietaisai parodė geltonos ir mėlynos spalvos elektroliuminescenciją, o tai rodo, kad sluoksniai pasižymi skirtingais elektroliuminescencijos procesais. Tirto vienintelio chinakridono darinio nelegiruotasis ir legiruotasis EML sukuria elektroliuminescenciją, artimą raudonai spalvai. Prietaiso A6 EL spektruose aptikta didelės energijos juosta, kurios viršūnė yra apie 490 nm, kurią galima panaudoti kuriant baltos spalvos OLED. Nelegiruotųjų EML, sudarytų iš **3**–**8** junginių (prietaisai A1-A6), CIEx vertės svyravo nuo 0,15 iki 0,439.

Pastebėtos išskirtinės **5** junginio TADF/AIEE emisijos ir bipolinio krūvininkų pernešimo galimybės, o A3 ir B3 pasižymėjo didžiausiomis EQE vertėmis – atitinkamai 2,3 % ir 13 %. Įdomu, kad **3** junginio, kurio prietaisai A1 ir B1 pasižymėjo

maksimaliu EQE – atitinkamai 1,6 ir 4 %, o tai gali būti laikoma labai perspektyviu pavyzdžiu gaminant fluorescencinius OLED.

5.2.3. Termiškai kontroliuojamas akridonų su fenoksazino pakaitais emisijos savybių derinimas - vienas iš žingsnių į priekį kuriant efektyvius organinius šviesos diodus, pagrįstus kristaliniais emiteriais

Šis skyrius parengtas straipsnio, 2023 m. paskelbto žurnale „Advanced Optical Materials“ (Volume 11, 2301059108), pagrindu[115]. Šis darbas yra ankstesnio skyriaus tęsinys, kuriame daugiausia dėmesio skiriama fenoksazinu pakeistiems **5, 6** ir **7** akridonams. Šio tyrimo tikslas – ištirti šių medžiagų morfologinio perėjimo įtaką fotofizikinėms ir elektroliuminescencinėms savybėms. Tirtų molekulių **5**, **6** ir **7** cheminė struktūra pateikta 26 a pav.

5, **6** ir **7**, kaip kristalinių elektroliuminoforų OLED, šiluminės savybės buvo tiriamos termogravimetrijos (TGA) ir diferencinės skenuojančiosios kalorimetrijos (DSC) metodais. Gauti rezultatai leido nustatyti vakuuminio garinimo metodu paruoštų plėvelių tinkamą atkaitinimo temperatūrą. **5** yra termiškai stabilus aukštesnėje nei 300 ºC temperatūroje, o endoterminė lydymosi smailė pastebėta 204 ºC temperatūroje kaitinant pirmąkart. Atvėsus **5** susidaro molekulinis stiklas ir nėra pastebimos kristalizacijos smailės. Be to, **6** ir **7** šiluminės savybės panašios, tačiau jų T_m, T_g ir T_{cr} yra daug aukštesnės (13 lentelė).

13 lentelė. 5, 6 ir 7 medžiagos terminės charakteristikos

Parametrai	5	6	7
$T_{d-5\,\%}$[(a)], ºC	343	408	441
T_g[(b)], ºC	57	117	128
T_{cr}[(c)], ºC	122	210, 258	225, 269
T_m[(d)], ºC	204	255, 262	217, 266, 283

(a) 5 % masės nuostolių temperatūra ($T_{d-5\,\%}$), b) stiklėjimo temperatūra (T_g), c) kristalizacijos temperatūra (T_{cr}), d) lydymosi temperatūra (T_m).

Siekiant ištirti galimas solvatochromines savybes, buvo pasirinkti du skirtingos dielektrinės konstantos tirpikliai: heksanas ir THF. Heksano ir THF tirpalų absorbcijos spektrai buvo beveik identiški anksčiau aprašytiems atitinkamų tolueno tirpalų absorbcijos spektrams[116]. **5** ir **6** THF tirpalų, palyginti su heksano tirpalais, PL spektrai buvo pasislinkę žemesnės energijos bangų regione ir pasižymėjo didesniu visu pločiu ties puse maksimumo (FWHM), o tai patvirtina CT liuminescenciją (29 a–c pav.).

Sintezės metu susiformavusių kristalinių **5**, **6** ir **7** mėginių PL spektrų maksimumai buvo atitinkamai ties 486, 571 ir 558 nm. Šie spektrai aiškiai rodo, kad tirti dariniai pasižymi mechanochrominio tipo (MC) liuminescencija. Trynimas, veikiant tirpiklio garais, kaitinimas iki lydymosi temperatūros ir kaitinimas (terminis atkaitinimas) iki kristalizacijos temperatūros gali turėti didelę įtaką jų emisijos savybėms (29 d–f pav.). Išlydytas **5** pasižymi geltona emisija TADF savybėmis, tačiau atkaitintas **5** emituoja mėlynai ir nėra TADF (29 g pav.).

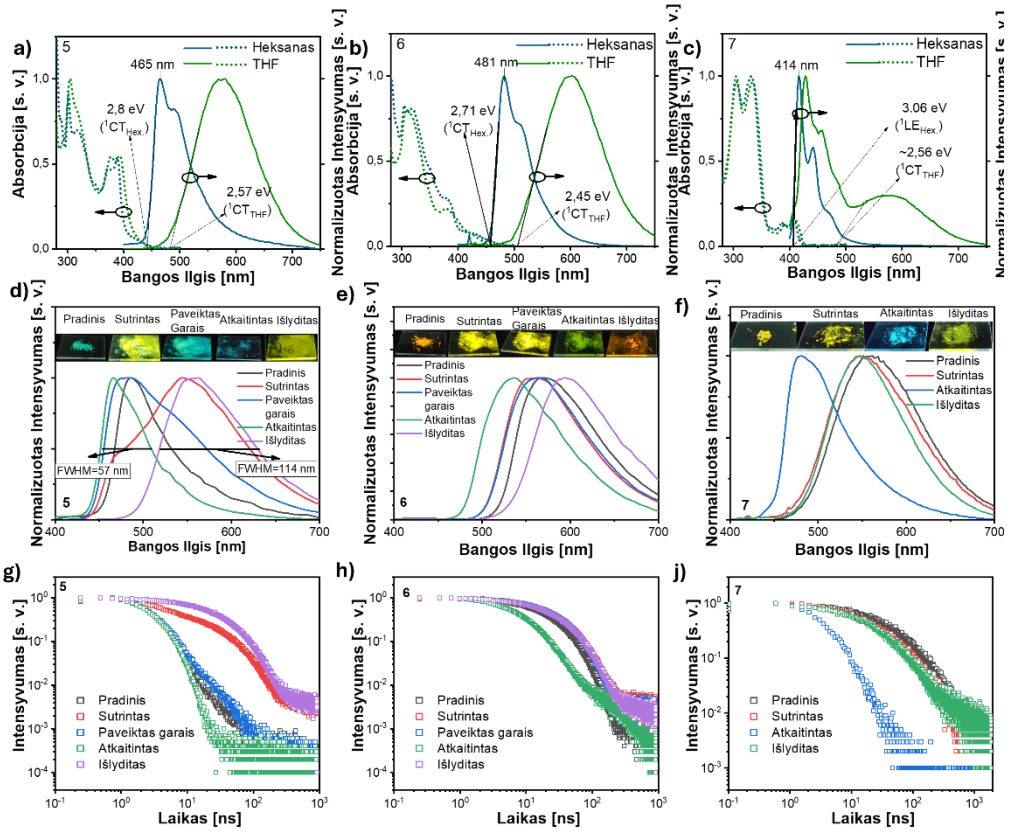

29 pav. Tirpalų, kuriuose yra **5** (a), **6** (b) ir **7** (c) junginių, absorbcijos ir PL spektrai. Ištirtos **5**, **6** ir **7** mechanoliuminescencinės savybės. Buvo išmatuotos bandinių veikiamų išoriniais dirgikliais (malimu, veikimu tirpiklio garais, atkaitinimu, lydymu), PL spektrai (g-j) ir PL gyvavimo trukmių kreivės (g-j)

Šis darbas rodo, kad tokių junginių kaip **5** emisijos spalvos gali būti priklausomos nuo skirtingų kristališkumo laipsnio, kuris padidėja terminio atkaitinimo metu. Tai sukelia hipsochrominius jų emisijos spektrų pokyčius, kuriuos galima kontroliuoti kaitinant ir lydant (29 e pav.). **5** molekulinis išsidėstymas esant kietai būsenai gali būti sureguliuotas kristalizacijos metu, todėl susidaro įvairių formų PL spektrai. Išlydytas **5** skleidžia geltoną šviesą, kurios spektras neturi struktūros, FWHM yra 114 nm, o gyvavimo trukmė τ_1 – 42,3 ns (29 g pav.). Atkaitintame **5** emisijos spektre matoma ryški vibroninė struktūra, kurios FWHM yra 57 nm, o gyvavimo trukmė trumpa – 2,8 ns. **5** yra perspektyviausias emiteris taikyti OLED dėl prietaiso spalvos grynumo. ZEONEX matricose disperguotų **5** ir **6** PL spektrų FWHM vertės panašios (atitinkamai 73 ir 87 nm). ZEONEX matricoje disperguoto **7** PL spektras yra plačiausias, jo FWHM yra 156 nm dėl ^{1}LE ir ^{1}CT emisijų dalinio sutapimo (14 lentelė).

Akridonų su fenoksazino pakaitais (**5**, **6** ir **7**) vakuume nusodintų plėvelių emisijos charakteristikos gali būti reguliuojamos termiškai kontroliuojant

kristalizaciją. Vakuume nusodintos **5** plėvelės yra visiškai amorfinės, o jų PL spektrai yra tokie patys kaip išlydytų miltelių pavidalo **5**. Dėl terminio atkaitinimo 122 ºC temperatūroje sukeliamos kristalizacijos vyksta hipsochrominis plėvelės spektro poslinkis nuo 565 nm iki 467 nm. XRDGI metodu gautas kristališkumo indeksas yra 68 % (30 b pav.).

Amorfinės ir kristalinės **5** plėvelės pasižymi labai skirtingomis PL gyvavimo trukmių kreivėmis, o tai rodo jų TADF savybių įjungimo ir išjungimo galimybes. Kristalinės **5** plėvelės nepasižymi TADF dėl aukšto tripleto-singleto energijos tarpo (ΔE_{ST}) – 0,28 eV. Vakuume nusodintų plėvelių spinduliuotės spalvą galima reguliuoti keičiant kristališkumo laipsnį, naudojant atkaitinimo laiką. Spalvos pokyčiai yra grįžtamieji.

5 monokristalų rentgeno spindulių analizė parodė, kad fenoksazino ir akridono dalys sudaro 81,83° dvisienį kampą. Tai patvirtina hipotezę, kad kristalizacija atkaitintose **5** plėvelėse sumažina konformacinius ir statinius dielektrinius netolygumus. Užfiksuotas atkaitinimo sukeltas PL spektro poslinkis link didesnės energijos bangų regiono gali būti interpretuojamas kaip šių įvykių spektroskopinė išraiška. Priešingai, švariose amorfinėse **5** plėvelėse galima tikėtis didelių konformacinių ir statinių dielektrinių pakitimų, dėl kurių PL spektras pasislenka link mažesnės energijos bangos ilgio regiono.

Vakuuminiu būdu atkaitintoms **5** plėvelėms TADF efekto nebuvo, todėl jas naudojant kaip emisinius sluoksnius nebuvo galima sukurti OLED su dideliu išoriniu kvantiniu efektyvumu. **5** plėvelės emisijos spektras, kurio maksimumas yra 513 nm, po terminio atkaitinimo T_{cr} temperatūroje hipsochrominiu principu pasislenka iki 476 nm (30 a pav.).

Skirtinga nekaitintų ir atkaitintų bandinių PL spektrų morfologija rodo, kad atkaitinimas sumažina konformacinę netvarką. Konformaciniu požiūriu subalansuotos molekulės pasižymi geresnėmis TADF charakteristikomis. XRDGI difraktogramos rodo, kad atkaitintų mėginių, kuriuose yra atitinkamai 10 % **5** molekulinių dispersijų ZEONEX, kristališkumo indeksai yra 37,5 % ir 78,6 % (30 e pav.).

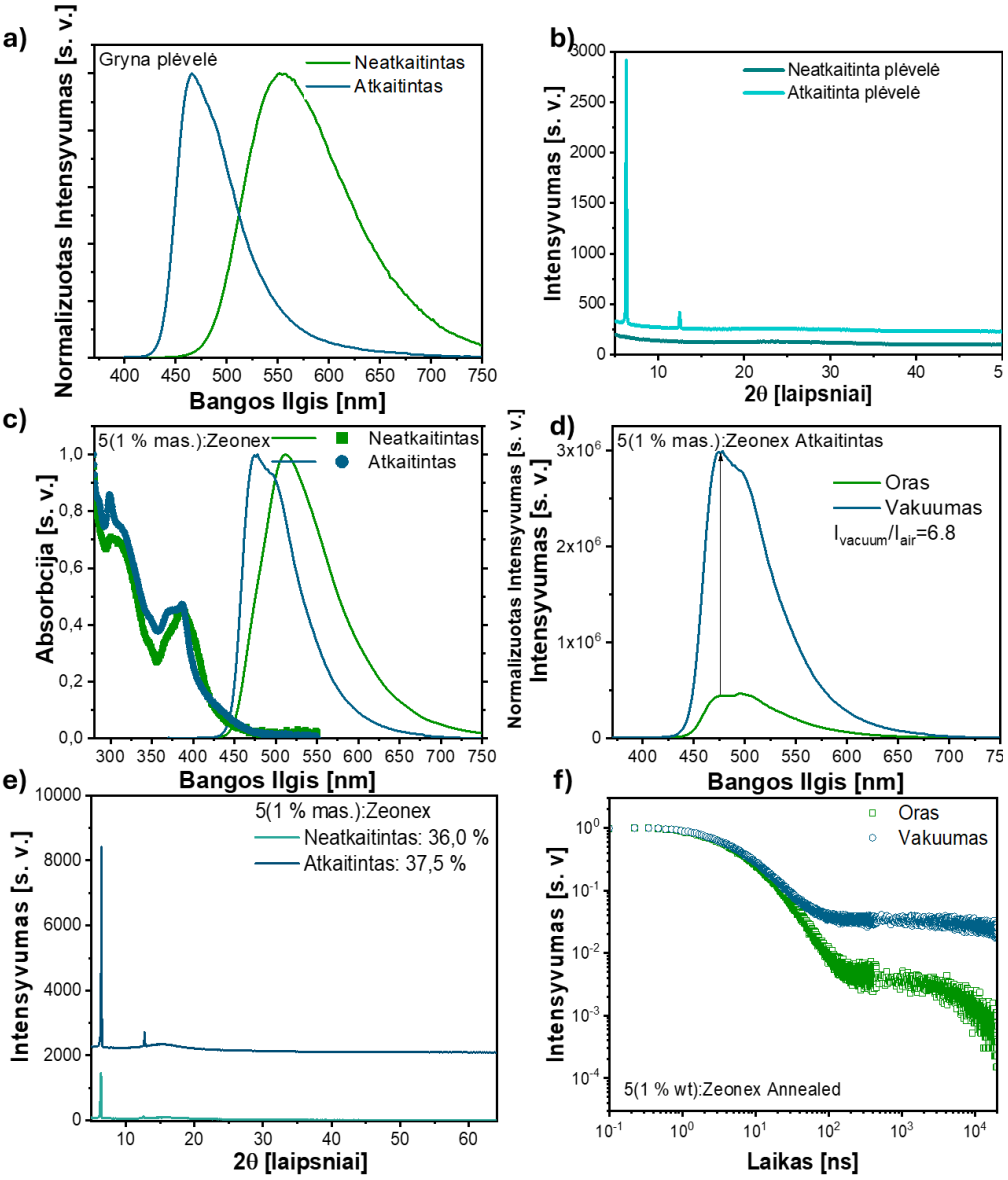

30 pav. Vakuume nusodintos 5 plėvelės PL spektrai (a) buvo išmatuoti prieš atkaitinimą ir po jo. 5 junginio vakuume nusodintos plėvelės (b) ir molekulinės dispersijos (10 % masės) ZEONEX (e) prieš terminį atkaitinimą ir po XRDGI difraktogramos. Molekulinės dispersijos **5** (1 masės %) ZEONEX (c) sugerties ir PL spektrai. Atkaitintos **5** (1 masės %) molekulinės dispersijos ZEONEX plėvelės PL spektrai (d), PL gyvavimo trukmių kreivės (f) ore ir vakuume

ZEONEX legiruotojo nekaitinto ir atkaitinto **5** PL gesimo kreivės rodo TADF emiterio tipą. Atkaitinimas gerokai padidina TADF efektyvumą, nes neatkaitinto bandinio emisijos intensyvumas, išmatuotas vakuume (I_{vac}), yra 2,3 karto didesnis nei

užfiksuotas ore (I_{air}), kai atkaitintos dispersijos atveju užfiksuotas I_{vac} buvo šešis kartus didesnis už I_{air} (30 d pav.). Šis pranašumas paaiškinamas didesniu tripletų būsenų jautrumu deguoniui, kuris padidina tripletų naudojimą atvirkštinės interkombinacinės konversijos metu.

Atkaitintos **5** ir **6** junginių dispersijos ZEONEX matricoje dėl AIEE ir TADF derinio, PLQY vertės yra artimos 100 % (14 lentelė). Integruodami plotus po PL skilimo kreivėmis, užfiksuotomis vakuume **5** ir **6** kietoje ZEONEX terpėje, nustatytos PF ir DF indėlio procentines dalys, taip pat Φ_{PF} ir Φ_{DF} kvantines išeigos. Šie duomenys buvo panaudoti fluorescencijos (k_{PF}) ir uždelstosios fluorescencijos (k_{DF}) gesimo greičio konstantoms, taip pat interkombinacinės konversijos (k_{ISC}) ir atvirkštinės interkombinacinės konversijos greičio konstantoms apskaičiuoti.

14 lentelė. Atkaitintų **5**, **6** ir **7** jungimių dispersijų ZEONEX matricoje sluoksnių, gautų inertinėje aplinkoje, fotofizikiniai parametrai

Parametrai	**5**:ZEONEX	**6**:ZEONEX	**7**:ZEONEX
FWHM[a], nm	73	87	156
PLQY, %	100	100	36,5
τ_{PF}[b], ns	22,77	22,8	26,59
τ_{DF}[c], ns	50965	44157	44908
PF[d], %	0,65	1,29	1,9
DF[e], %	99,35	98,71	98,1
Φ_{PF}[f], %	0,65	1,29	0,69
Φ_{DF}[g], %	99,35	98,7	35,81
k_{PF}[h], s^{-1}	$2,89\times10^5$	$5,64\times10^5$	$2,6\times10^5$
k_{DF}[i], s^{-1}	$1,95\times10^4$	$2,24\times10^4$	$7,97\times10^3$
k_{ISC}[j], s^{-1}	$2,87\times10^5$	$5,57\times10^5$	$2,55\times10^5$
k_{RISC}[k], s^{-1}	$2,97\times10^6$	$1,74\times10^6$	$4,2\times10^5$

(a) visas plotis ties puse maksimumo (FWHM); (b) greitosios fluorescencijos trukmė (τPF); (c) uždelstosios fluorescencijos trukmė (τ_{DF}); (d, e) greitosios (PF) ir uždelstosios (DF) fluorescencijos daliniai intensyvumai, apskaičiuoti taikant formulę $I_{PL} = A_1 e^{\left(-\frac{t}{\tau_{PF}}\right)} + A_2 e^{\left(-\frac{t}{\tau_{DF}}\right)}$. [; (f, g) greitosios ($\Phi_{PF}$) ir uždelstosios fluorescencijos (Φ_{DF}) kvantinis našumas; (h) greitosios fluorescencijos greičio konstanta (k_{PF}); (i) uždelstosios fluorescencijos greičio konstanta (k_{DF}); (j) ISC greičio konstanta (k_{ISC}); (k) RISC greičio konstanta (k_{RISC}).

Tyrime nagrinėjama atkaitinimo sukelto **5**, cheminės medžiagos, naudojamos organiniuose šviesos dioduose (OLED), singletinių ir tripletinių sužadintųjų būsenų suderinimo įtaka (15 lentelė). OLED buvo pagaminti ir išbandyti naudojant įvairias medžiagas, įskaitant MoO3 (0,35 nm), NPB (44 nm), šviesą spinduliuojantį sluoksnį (24 nm), TSPO1 (4 nm), TPBi (40 nm) ir LiF (0,35 nm)/Al. Spinduliuojančius sluoksnius sudarė 10 mas. % **5** dispersija įvairiose matricose, pavyzdžiui, N,N′-di(1-naftil)-N,N′-difenil-(1, 1′-bifenil)-4, 4′-diaminas (NPB), 3,3′-di(9H-karbazol-9-il)-1,1′-bifenilas (mCBP), 3,6-di-terc-butil-9-(2-(1-fenil-1H-benzo[d]imidazolas) (SM66), tris(4-karbazil-9-ilfenil)aminas (TCTA). Didžiausias C5 įrenginio EQE buvo 1,9 %, t. y. šiek tiek mažesnis nei ankstesnis didžiausias 2,3 %. Grynojo **5** emisinio sluoksnio terminis atkaitinimas ne pagerino, o pablogino jo elektroliuminescencines

savybes. Naudojant TCTA kaip pagrindinę matricą, neatkaitinto C4 prietaiso EQE siekė iki 8,6 %. Tačiau C4A prietaiso su atkaitintu **5** emisiniu sluoksniu, legiruotu TCTA, didžiausios EQE vertės gerokai padidėjo – iki 21,7 %. Šį pagerėjimą iš dalies lėmė kristalizacija, kaip rodo kristalinių fazių buvimas spinduolio-matricos emisijos sluoksnio difraktogramoje. Rezultatai rodo, kad terminis spinduolio-matricos emisinių sluoksnių, kuriuose yra **5** liuminoforo, atkaitinimas yra svarbus komponentas, gerinantis prietaiso veikimą.

15 lentelė. OLED, termiškai atkaitintų (C1–C5), ir termiškai atkaitintų (C1A–C5A) EML elektroliuminescenciniai parametrai

Prietaisas	**EML**	λ_{EL}, **nm**	V_{ON}, **V**	L_{max}, **cd/m²**	CE_{max}, **cd/m²**	PE_{max}, **lm/W**	EQE_{max}, **%**
C1	NPB:**5**	523	5,9	5710	3,6	1,5	1,1
C1A	NPB:**5**	524	6,1	10210	3,4	1,3	1
C2	mCBP:**5**	527	4,7	21080	15,3	8,1	4,2
C2A	mCBP:**5**	527	5,3	16910	21,9	9,5	5,9
C3	SM-66:**5**	500	5,7	4410	15,1	6,9	5,8
C3A	SM-66:**5**	495	5,2	3280	21,3	12,2	10,11
C4	TCTA:**5**	526	4,3	15990	30,1	17,5	8,6
C4A	TCTA:**5**	526	3,8	14800	62,4	49,1	20,7
C5	**5**	545	5,6	17250	6,2	2,4	1,9
C5A	**5**	520	5,7	9700	3,5	1,6	1,1

Prietaiso struktūra: MoO3(0,35 nm) / NPB(44 nm) / EML (24 nm) / TSPO1(4 nm) / TPBi(40 nm) / LiF(0,35 nm)/ Al

5.2.4. Eksperimentinis eksipleksus sudarančių junginių, kuriuose yra trifluorbifenilo ir 3,6-di-tert-butilkarbazolo vienetų tyrimas ir jų veikimas OLED

Šis skyrius parengtas straipsnio, 2020 m. paskelbto žurnale „Journal of Materials Chemistry C“ (Volume 8, 14186–14195125), pagrindu. Šiame tyrime nagrinėjami du junginiai, kuriuose yra trifluorfenilo ir karbazolo dalių. Donorinių grupių kiekio įtaka medžiagų savybėms nagrinėjama remiantis duomenimis, surinktais taikant eksperimentinius metodus. Nustatyta, kad šie junginiai gali sudaryti eksipleksus su tinkamomis elektronus priimančiomis molekulėmis. Ištirtų molekulių cheminė struktūra pateikta 31 a pav.

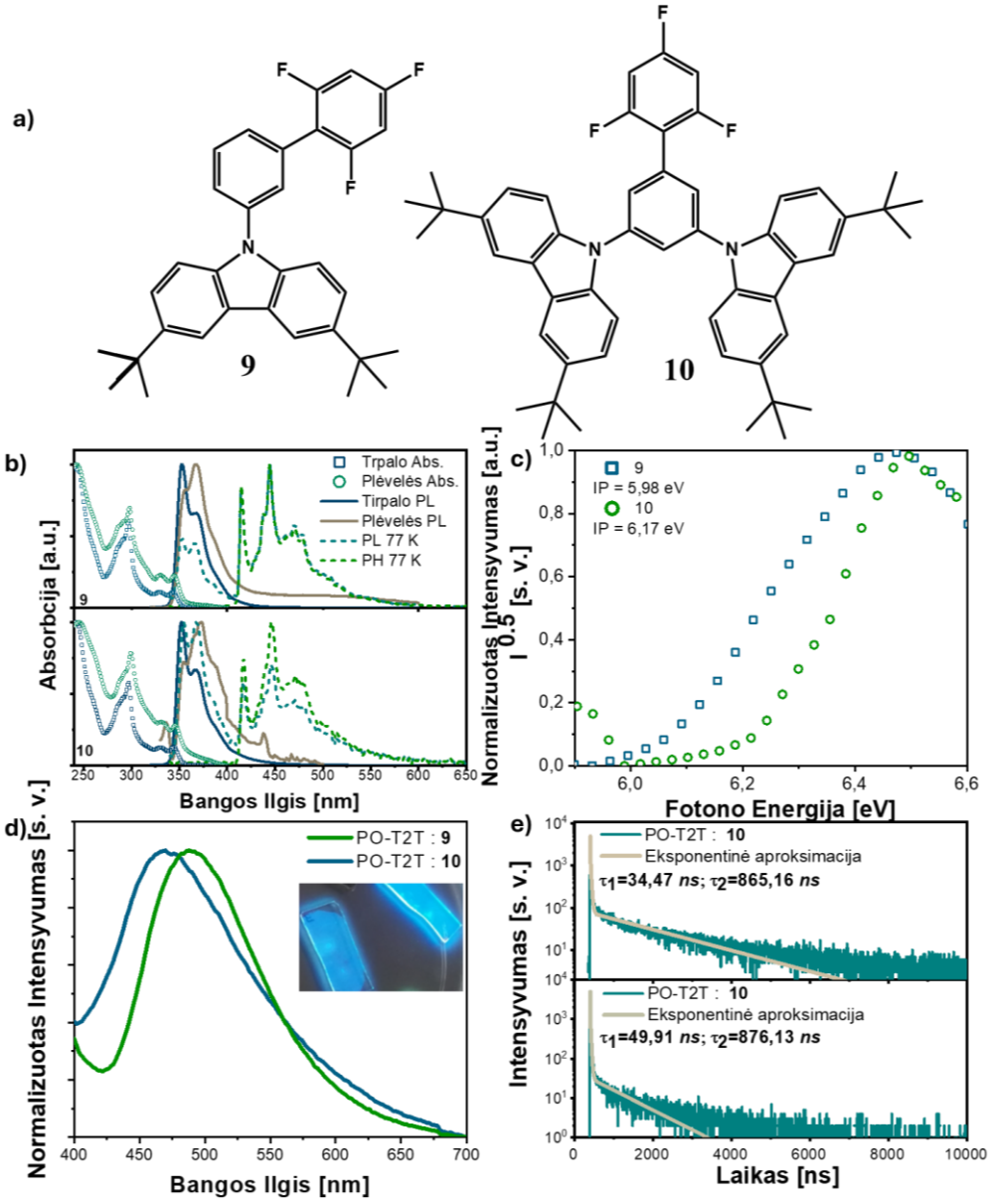

31 pav. 9 ir **10** junginio molekulinės struktūros (a). **9** ir **10** junginių tolueno tirpalų ir kietų sluoksnių UV-Vis sugerties, PL emisijos spektrai kambario temperatūroje ir THF tirpalų fotoliuminescencijos ir fosforescencijos spektrai 77 K temperatūroje (b). Kietųjų bandinių fotoelektronų emisijos spektrai, užregistruoti ore (c). Susiformavusių eksipleksų sistemų **9**:PO-T2T ir **10**:PO-T2T PL spektrai (d) ir PL gyvavimo trukmių kreivės (e)

Buvo ištirtos **9** ir **10** junginių medžiagų savybės. DSC eksperimentai parodė, kad, kaitinant **9** junginį iki amorfinės būsenos, kristalizacijos ir lydymosi požymių

nenustatyta. Tačiau **10** junginys pasižymėjo kristalizacija (T_{Cr} = 134 °C). Atlikus **9** junginio TGA tyrimą, nustatyta, kad visas junginys prarado masę, todėl nenustatyta terminio skilimo temperatūros.

Ciklinė voltamperometrija ir fotoelektronų emisijos spektrometrija parodė abiejų junginių grįžtamąją oksidaciją su panašiomis jonizacijos energijos ir draustinės juostos vertėmis. Tai rodo, kad abiejuose junginiuose yra panašios π elektronų konjuguotos sistemos. Fotoelektronų emisijos spektrometrija parodė panašias abiejų medžiagų jonizacijos potencialo vertes (31 c pav., 16 lentelė). Abiejų junginių ultravioletinių spindulių spektruose tolueno tirpale draustinės juostos vertės buvo panašios dėl tos pačios elektronus atiduodančios dalies (31 b pav.). Jų spektrų panašumas į karbazolo toluene spektrus rodo, kad lokalios donorinės sužadintosios būsenos reguliuoja absorbcijos savybes tirpaluose ir kietosiose plėvelėse (31 b pav.).

Atlikus **9** ir **10** junginių PL tyrimus tolueno tirpale kambario temperatūroje, buvo nustatytos vibroninės struktūros emisijos juostos gilios mėlynos spalvos srityje, o PLQY vertė buvo 13 % ir 28 % (16 lentelė). Mažos Stokso poslinkio vertės praskiestuose tolueno tirpaluose rodo ribotą geometriją ir tirpiklio reorganizaciją po sužadinimo. Tiriant fosforescencijos spektrus nustatyta, kad abiejų medžiagų tripletų energijos vertės yra mėlynojoje srityje, o eksperimentinės ΔE_{ST} vertės atitinka teorinius skaičiavimus. Abiejų junginių kietosios būsenos plėvelės pasižymėjo panašiais vibroninės struktūros PL spektrais, tačiau dėl agregacijos sukelto gesinimo jų PLQY vertės buvo mažesnės (~1 %)[135]. **9** junginio PL spektras buvo jautrus deguoniui, o PL intensyvumo santykis (I_{vac}/I_{air}) buvo 1,9, o tai rodo tripletines būsenas galimai dėl RISC. **9** junginio kietojo bandinio PL gesimo kreivės parodė dvi komponentes: nanosekundžių trukmės komponentę, atsirandančią dėl LE būsenos, esant aukštesnėms energijoms, ir ilgiau trunkančią CT komponentę.

16 lentelė. 9 ir **10** fotofizikinės, elektrocheminės ir fotoelektrinės savybės

Parametras	**Terpė**	**9**	**10**
λ_{Abs}[(a)], nm	Tolueno tirpalas/plonas sluoksnis	297, 346 / 298, 347	297, 346 / 230, 345
λ_{FL}[(b)], nm		354, 370 / 355, 366, 460	352, 367 / 352, 374, 439
E_g^{opt}[(c)], eV		3,49	3,41
Stokso poslinkis[(d)], cm^{-1}		653 / 649	493 / 577
PLQY[(g)], %		13/1	28 / 1
S_1/T_1[(e)], eV	THF tirpalas	3,67 / 3,03	3,63 / 3,05
ΔE_{ST}[(f)], eV		0,64	0,58
IP_{PE}[(i)], eV	Plonas sluoksnis	5,98	6,17
EA_{PE}[(j)], eV		2,49	2,76

(a) λ_{Abs} – sugerties maksimumų bangos ilgiai; (b) E_g^{opt} – optinė draustinė juosta, (c) Stokso poslinkis = λ_{Fl}–λ_{Abs}; (d) S_1 – singleto energija, T_1 – tripleto energija, (e) IP_{PE} – jonizacijos potencialas, įvertintas fotoelektronų emisijos spektrometrijos metodu ore; (f) IP_{CV} – jonizacijos potencialas, įvertintas CV metodu.

Atsižvelgiant į agregacijos sukeltą gesinimą grynose plėvelėse, **9** ir **10** junginių fotofizikinės savybės buvo ištirtos legiruotosiose sistemose. Du junginiai su PO-

T2T[128], elektronus priimančiu junginiu, sukūrė žydros spalvos eksipleksus. Šių junginių kietosios plėvelės pasižymėjo į CT panašiais PL spektrais, palyginti su grynomis plėvelėmis (31 d pav.). Oro sąlygomis eksipleksus sudarančių mišinių **9**:PO-T2T ir **10**:PO-T2T PLQY vertės buvo atitinkamai 4 % ir 2 %. Eksipleksus sudarančių mišinių **9** ir **10**: PO-T2T PL gyvavimo trukmių charakteristikos skyrėsi nuo monomerų emisijos gyvavimo trukmių (31 e pav.). Šių mišinių PL gyvavimo trukmių kreivėse išsiskyrė nanosekundžių trukmės fluorescencijos ir TADF komponentė. PL gyvavimo trukmių eksperimentai kambario temperatūroje ir 77 K temperatūroje patvirtino eksipleksų emisijos TADF pobūdį, nes sustiprėjo uždelstosios fluorescencijos komponentės intensyvumas 295 K. Inertinėje atmosferoje padidėjo uždelstos emisijos komponento intensyvumas, palyginti su matavimu ore, o tai rodo tripletų indėlį į emisijos mechanizmą. TADF kilmė eksipleksus sudarančiose sistemose **9**: PO-T2T ir **10**: PO-T2T buvo patvirtinta matuojant PL intensyvumo priklausomybę nuo lazerio impulso stiprumo, kurio nuolydžio vertė yra apie 1[138].

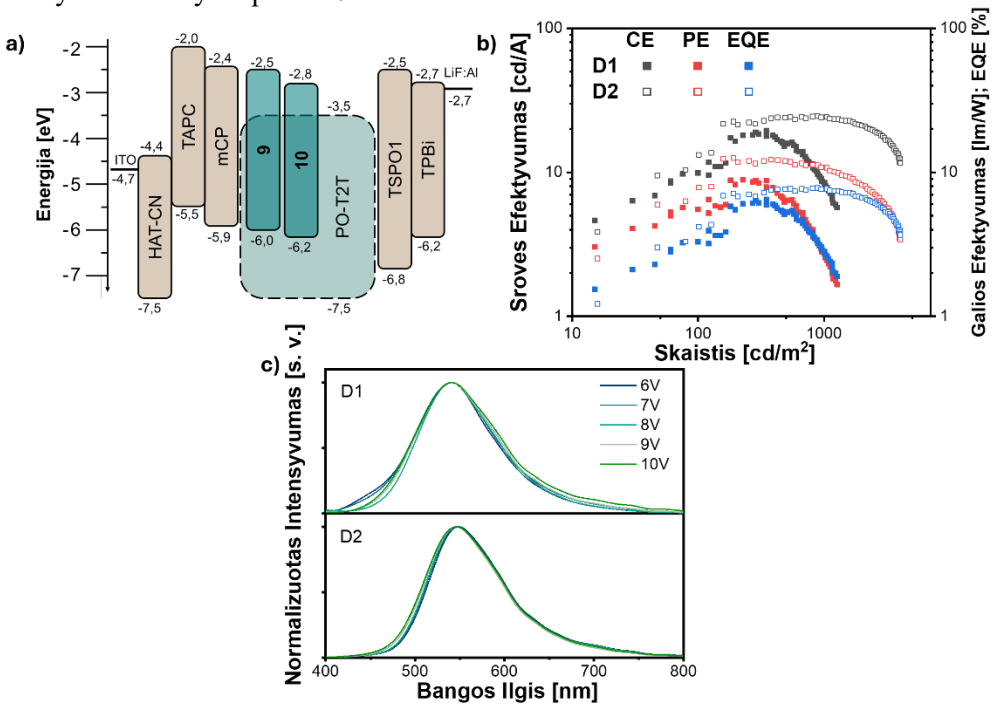

32 pav. OLED energijos diagrama ir struktūra (a); srovės, galios ir išorinio kvantinio efektyvumo priklausomybės nuo ryškumo grafikai (b); EL spektrai, užfiksuoti esant skirtingoms įtampoms (c)

OLED su akceptoriaus PO-T2T ir donorų **9** ir **10** mišiniai kaip EML buvo efektyvūs. OLED D2, veikiantis su **10**:PO-T2T eksiplekso sistema, buvo pranašesnis už D1 – jo ryškumas siekė 4100 cd/m², palyginti su 1250 cd/m². D1 CE buvo 19,7 cd/A, PE – 12,2 lm/W, o EQE – 6,5 %, o D2 CE – 24,8 cd/A, PE – 12,2 lm/W, o EQE – 7,8 % (32 c pav., 17 lentelė). Didesnis **10** junginio terminis stabilumas lėmė

mažesnį efektyvumo kritimą, kai ryškumas buvo padidintas nuo 100 iki 1000 cd/m². Tai lėmė geresnį srovės, galios ir išorinį kvantinį efektyvumą dėl geresnio krūvininkų balanso EML, esant aukštesnei įtampai.

17 lentelė. 9 ir **10** junginių eksipleksų pagrindu pagamintų OLED EL charakteristikos

Prietaisas	**λ_{max}, nm**	**V_{on}, V**	**L_{max}, cd/m²**	**CE / PE / EQE, cd/A / lm/W / %**		
				Max	**@ 100 cd/m²**	**@ 1000 cd/m²**
D1	541	4.8	1250	19,7/8,4/6,5	9,9/5,5/3,3	8,5/2,7/2,8
D2	546	4.8	4100	24,8/12,2/7,8	13,2/7,8/4,2	24,3/10,7/7,7

Prietaiso struktūra: HAT-CN(10 nm) / TAPC(40 nm) / mCP(4 nm) / EML(24 nm) / TSPO1(4 nm) / TPBi(4 0nm)/ LiF(0,35 nm) / Al

OLED prietaisų EL spektrai nesutapo su **9**:PO-T2T ir **10**:PO-T2T PL spektrais (32 c pav.). PL spektrai skleidė mėlyną, o EL spektrai – žalią šviesą, o tai rodo, kad įrenginyje yra mažesnės energijos eksipleksų. Prietaiso struktūroje esančių eksitonų sąveikų subtilumą patvirtino terminis PL plėvelių atkaitinimas, kurio metu **9**:PO-T2T spektrai buvo pasislinkę link žemesnės energijos bangų regiono, tačiau **10**:PO-T2T spektrai buvo panašūs. Žalia elektroliuminescencija, priešingai nei mėlyna PL, atsirado dėl iš dalies sutampančių emisijų iš įvairių eksipleksų darinių OLED struktūroje.

5.3. Išvados

1. Atlikus išsamų fotofizikinį tyrimą paaiškėjo skirtingi trijų junginių šeimų emisijos mechanizmai: benzofenono ir difenilsulfono dariniams buvo priskirta intramolekulinė krūvio pernaša, o benzofenono dariniai pasižymėjo termiškai aktyvuota uždelstąja fluorescencija. Akridono dariniai su fenoksazino dalimis taip pat pasižymėjo termiškai aktyvuota uždelstąja fluorescencija, o karbazolo turinčių akridonų ir chinakridonų – greita fluorescencija. Fluorescencijos emisijos mechanizmu pasižymėjo trečia junginių grupė, kurią sudaro trifluorbifenilo ir karbazolo dariniai. Šios įžvalgos sudaro pagrindą pritaikyti šiuos junginius konkrečioms optoelektroninėms reikmėms.
2. Atlikus benzofenono darinių fotofizikinius tyrimus, paaiškėjo, kad UV spinduliuotė sukelia struktūrinius pokyčius, dėl kurių padidėja tiek termiškai aktyvuotos uždelstosios fluorescencijos intensyvumas, tiek emisijos spalvos pokyčiai. Ši dviguba reakcija kartu su dideliu jautrumu ir reguliuojamu aptikimo diapazonu, priklausomai nuo tirpiklio, leidžia benzofenono darinius laikyti perspektyviais efektyviais ir universaliais UV jutikliais.
3. Akridono ir chinakridono darinių charakterizavimas parodė, kad, keičiant pakaitalus, galima reguliuoti emisijos spalvą regimajame spektre nuo mėlynos iki oranžinės, o fenoksazinu pakeisti akridonai pasižymi termiškai aktyvuota uždelsta fluorescencija / agregacijos sukelta sustiprinta emisija, todėl elektroliuminescencijos kvantinė išeiga pasiekia 13 %.

4. Tiriant akridono ir fenoksazino darinių struktūros ir savybių ryšius paaiškėjo, kad terminis atkaitinimas sukelia kristalizaciją, dėl kurios labai pagerėja termiškai aktyvuotos uždelstos fluorescencijos kinetika. Ši termiškai sukelta kristalizacija padėjo pasiekti didelį OLED su šiais junginiais išorinio kvantinio efektyvumo pagerėjimą, kuris po atkaitinimo padidėjo nuo 8,6 % iki 20,7 %. Tuo pabrėžiamas svarbus morfologijos kontrolės vaidmuo optimizuojant prietaiso veikimą.
5. Tiriant trifluorbifenilo ir karbazolo darinius, paaiškėjo jų gebėjimas sudaryti ekscipleksus su elektronus priimančiomis medžiagomis, dėl kurių atsiranda dangaus mėlynumo spinduliuotė, pasižyminti termiškai aktyvuotos uždelstos fluorescencijos savybėmis. Šios ekscipleksų sistemos, panaudotos kaip OLED emisiniai sluoksniai, pasižymėjo dideliu išoriniu kvantiniu efektyvumu (7,7 %) ir spalvų derinimo galimybėmis, todėl išryškėjo jų potencialas kuriant didelio našumo ir universalius elektroliuminescencinius prietaisus.

6. LITERATURE

1. TANG, C.W.; VANSLYKE, S.A.; Organic electroluminescent diodes. *Applied Physics Letters* [interactive]. 1987. Vol. **51**, no. 12, p. 913–915. [viewed on 2020-04-05]. Access via: http://aip.scitation.org/doi/10.1063/1.98799.

2. FUNG, Man-Keung; LI, Yan-Qing; LIAO, Liang-Sheng; Tandem Organic Light-Emitting Diodes. *Advanced Materials* [interactive]. 2016. Vol. **28**, no. 47, p. 10381–10408. Access via: http://doi.wiley.com/10.1002/adma.201601737.

3. HUNG, Wen Yi; FANG, Guan Cheng; LIN, Shih Wei;et al. The first tandem, all-exciplex-based woled. *Scientific Reports* . 2014. Vol. **4**. [viewed on 2020-05-18]. .

4. LIAO, Chia-Wei; HSU, Yu-Chien; CHU, Che-Chia;et al. Aggregation-induced emission tetraphenylethene type derivatives for blue tandem organic light-emitting diodes. *Organic Electronics* [interactive]. 2019. Vol. **67**, p. 279–286. [viewed on 2019-03-07]. Access via: https://www.sciencedirect.com/science/article/pii/S1566119918306670.

5. LEE, Jae Hyun; LEE, Jonghee; KIM, Yong Hyun;et al. Effect of trap states on the electrical doping of organic semiconductors. *Organic Electronics* . 2014. Vol. **15**, no. 1, p. 16–21. [viewed on 2023-07-01]. .

6. LEE, Dong Ryun; HAN, Si Hyun; LEE, Jun Yeob; Metal-free and purely organic phosphorescent light-emitting diodes using phosphorescence harvesting hosts and organic phosphorescent emitters. *Journal of Materials Chemistry C* [interactive]. 2019. Vol. **7**, no. 37, p. 11500–11506. [viewed on 2022-09-15]. Access via: https://pubs.rsc.org/en/content/articlehtml/2019/tc/c9tc03203g.

7. YERSIN, H. (Hartmut); WILEY INTERSCIENCE (ONLINE SERVICE) *Highly efficient OLEDs with phosphorescent materials* [interactive]. . [s.l.]: Wiley-VCH, 2007. 438 p. ISBN 9783527405947.

8. ANDRULEVICIENE, Viktorija; LEITONAS, Karolis; VOLYNIUK, Dmytro;et al. TADF versus TTA emission mechanisms in acridan and carbazole-substituted dibenzo[a,c]phenazines: Towards triplet harvesting emitters and hosts. *Chemical Engineering Journal* . 2021. Vol. **417**, p. 127902. [viewed on 2023-07-01].

9. YU, Ling; WU, Zhongbin; XIE, Guohua;et al. Molecular design to regulate the photophysical properties of multifunctional TADF emitters towards high-performance TADF-based OLEDs with EQEs up to 22.4% and small efficiency roll-offs. *Chemical Science* [interactive]. 2018. Vol. **9**, no. 5, p. 1385–1391. [viewed on 2018-12-10]. Access via: http://xlink.rsc.org/?DOI=C7SC04669C.

10. AYDEMIR, Murat; XU, Shidang; CHEN, Chengjian;et al. Photophysics of an Asymmetric Donor–Acceptor–Donor′ TADF Molecule and Reinterpretation of Aggregation-Induced TADF Emission in These Materials. *The Journal of Physical Chemistry C* [interactive]. 2017. Vol. **121**, no. 33, p. 17764–17772. [viewed on 2020-01-04]. Access via: https://pubs.acs.org/doi/10.1021/acs.jpcc.7b06299.

11. SARMA, Monima; WONG, Ken Tsung; Exciplex: An Intermolecular Charge-Transfer Approach for TADF. *ACS Applied Materials and Interfaces* . 2018. Vol. **10**, no. 23, p. 19279–19304. [viewed on 2020-05-18]. .

12. PAN, Yuyu; HUANG, Jing; LI, Weijun;et al. Theoretical investigation of high-efficiency organic electroluminescent material: HLCT state and hot exciton process. *RSC Advances* [interactive]. 2017. Vol. **7**, no. 32, p. 19576–19583. [viewed on 2024-04-29]. Access via: https://pubs.rsc.org/en/content/articlehtml/2017/ra/c7ra01270e.

13. IKEDA, Naoya; ODA, Susumu; MATSUMOTO, Ryuji;et al. Solution-Processable Pure Green Thermally Activated Delayed Fluorescence Emitter Based on the Multiple Resonance Effect. *Advanced Materials* . 2020. Vol. **32**, no. 40, p. 1–6. .

14. PENG, Jinghong; XU, Xinjun; FENG, Xin Jiang;et al. Fabrication of solution-processed pure blue fluorescent OLED using exciplex host. *Journal of Luminescence* [interactive]. 2018. Vol. **198**, p. 19–23. [viewed on 2019-01-30]. Access via: https://www.sciencedirect.com/science/article/pii/S0022231317318355.

15. KWON, Jang-Hyuk; PODE, Ramchandra; High Efficiency Red Phosphorescent Organic Light-Emitting Diodes with Simple Structure. *Organic Light Emitting Diode - Material, Process and Devices* [interactive]. 2011. no. June. Access via: http://www.intechopen.com/books/organic-light-emitting-diode-material-process-and-devices/high-efficiency-red-phosphorescent-organic-light-emitting-diodes-with-simple-structure.

16. SHAOQING ZHUANG XIAO YANG, LEI WANG, Wenzhi ZHANG; [interactive]. . Access via: http://journal.hep.com.cn/foe.

17. Organic Semiconductor Market Size, Share, Industry Forecast by 2032. [interactive]. [viewed on 2024-04-29] Access via: https://www.emergenresearch.com/industry-report/organic-semiconductor-market.

18. OLED Info | The OLED Experts. [interactive]. [viewed on 2019-05-26] Access via: https://www.oled-info.com/.

19. GREEN, Martin A.; The path to 25% silicon solar cell efficiency: History of silicon cell evolution. *Progress in Photovoltaics: Research and Applications* [interactive]. 2009. Vol. **17**, no. 3, p. 183–189. [viewed on 2022-12-03]. Access via: https://onlinelibrary.wiley.com/doi/full/10.1002/pip.892.

20. WANG, Cong; ZHANG, Xiaotao; DONG, Huanli;et al. Challenges and Emerging Opportunities in High-Mobility and Low-Energy-Consumption Organic Field-Effect Transistors. *Advanced Energy Materials* [interactive]. 2020. Vol. **10**, no. 29, p. 2000955. [viewed on 2022-12-15]. Access via: https://onlinelibrary.wiley.com/doi/full/10.1002/aenm.202000955.

21. POTJKE-KAMLOTH, Karin; Chemical Gas Sensors Based on Organic Semiconductor Polypyrrole. *Critical Reviews in Analytical Chemistry* [interactive]. 2002. Vol. **32**, no. 2, p. 121–140. [viewed on 2024-04-29]. Access via: https://www.tandfonline.com/doi/abs/10.1080/10408340290765489.

22. ZHANG, Jing Lin; NAN, Ya Xiong; LI, Hai Guo;et al. A new wide bandgap organic semiconductor and its application in organic UV sensors with tunable response wavelength. *Sensors and Actuators B: Chemical* . 2012. Vol. **162**, no. 1, p. 321–326. [viewed on 2024-04-29]. .

23. MANOUSIADIS, Pavlos P.; YOSHIDA, Kou; TURNBULL, Graham A.;et al. Organic semiconductors for visible light communications. *Philosophical*

Transactions of the Royal Society A [interactive]. 2020. Vol. **378**, no. 2169. [viewed on 2024-04-29]. Access via: https://royalsocietypublishing.org/doi/10.1098/rsta.2019.0186.

24. RAVAL, Harshil N.; TIWARI, Shree Prakash; NAVAN, Ramesh R.;et al. Determining ionizing radiation using sensors based on organic semiconducting material. *Applied Physics Letters* [interactive]. 2009. Vol. **94**, no. 12, p. 123304. [viewed on 2024-04-29]. Access via: /aip/apl/article/94/12/123304/151860/Determining-ionizing-radiation-using-sensors-based.

25. LIAO, Caizhi; ZHANG, Meng; YAO, Mei Yu;et al. [s.l.]: Wiley-VCH Verlag, 2015. [viewed on 2020-04-25].

26. GUEDES, Andre F.S.; TARTARI, Simone; CUNHA, Idaulo J.; Flexible Optoelectronic Technology Applied in Organic Light Emitting Diode (OLED). . [viewed on 2021-11-18]. .

27. RIM, You Seung; BAE, Sang Hoon; CHEN, Huajun;et al. [s.l.]: Wiley-VCH Verlag, 2016. [viewed on 2020-04-25].

28. KONWAR, Gargi; RAGHUWANSHI, Vivek; SAXENA, Pulkit;et al. Solution Processed Organic Transistors on Paper Substrate for Sustainable Electronics. *IEEE Transactions on Electron Devices* . 2024. Vol. **71**, no. 1, p. 762–768. [viewed on 2024-04-29]. .

29. LEE, Junwoo; PARK, Sang Ah; RYU, Seung Un;et al. Green-solvent-processable organic semiconductors and future directions for advanced organic electronics. *Journal of Materials Chemistry A* [interactive]. 2020. Vol. **8**, no. 41, p. 21455–21473. [viewed on 2024-04-29]. Access via: https://pubs.rsc.org/en/content/articlehtml/2020/ta/d0ta07373c.

30. MCGEHEE, Michael D.; GOH, Chiatzun; Organic Semiconductors for Low—Cost Solar Cells. *AIP Conference Proceedings* [interactive]. 2008. Vol. **1044**, no. 1, p. 322–330. [viewed on 2024-04-29]. Access via: /aip/acp/article/1044/1/322/861090/Organic-Semiconductors-for-Low-Cost-Solar-Cells.

31. YANG, Dezhi; MA, Dongge; Development of Organic Semiconductor Photodetectors: From Mechanism to Applications. *Advanced Optical Materials* [interactive]. 2019. Vol. **7**, no. 1, p. 1800522. [viewed on 2024-04-29]. Access via: https://onlinelibrary.wiley.com/doi/full/10.1002/adom.201800522.

32. OHTA, Jitsuo; UENO, Kohei; KOBAYASHI, Atsushi;et al. Feasibility of fabricating large-area inorganic crystalline semiconductor devices. *Intelligent Nanosystems for Energy, Information and Biological Technologies* [interactive]. 2016. p. 249–275. [viewed on 2024-10-09]. Access via: https://link.springer.com/chapter/10.1007/978-4-431-56429-4_13.

33. ZHU, Mingguang; GUO, Hongyu; CAI, Kaicong;et al. Novel fluorescence-enhancing effect based on light-induced E/Z isomerization of perylene diimides with Schiff-base groups on bay-positions. *Dyes and Pigments* . 2017. Vol. **140**, p. 179–186. [viewed on 2024-10-09]. .

34. WANG, Shuai; ZHU, Zhongchang; SHI, Chaojun;et al. Enhanced performance of solution-processed OLEDs by altering the molecular transition dipole moment orientation of emission layers. *Spectrochimica Acta Part A: Molecular and Biomolecular Spectroscopy* . 2022. Vol. **271**, p. 120933. [viewed on 2024-10-09]. .

35. WEINELT, M.; HUBER, W.; ZEBISCH, P.;et al. The electronic structure of ethylene on Ni(110): an experimental and theoretical study. *Surface Science* . 1992. Vol. **271**, no. 3, p. 539–554. [viewed on 2024-04-29]. .

36. KNUPFER, M.; PEISERT, H.; Electronic Properties of Interfaces between Model Organic Semiconductors and Metals. *Physics of Organic Semiconductors* [interactive]. 2006. p. 41–67. [viewed on 2024-04-29]. Access via: https://onlinelibrary.wiley.com/doi/full/10.1002/3527606637.ch2.

37. LIU, Yu; KILBY, Phil; FRANKCOMBE, Terry J.;et al. The electronic structure of benzene from a tiling of the correlated 126-dimensional wavefunction. *Nature Communications 2020 11:1* [interactive]. 2020. Vol. **11**, no. 1, p. 1–5. [viewed on 2024-04-29]. Access via: https://www.nature.com/articles/s41467-020-15039-9.

38. CHEN, Fang Chung; Organic Semiconductors. *Encyclopedia of Modern Optics* . 2018. Vol. **1–5**, p. 220–231. [viewed on 2024-04-29]. .

39. BALDO, M.A.; O'BRIEN, D.F.; THOMPSON, M.E.;et al. Excitonic singlet-triplet ratio in a semiconducting organic thin film. . [viewed on 2024-04-29]. .

40. LA ROCCA, G.C.; Wannier–Mott Excitons in Semiconductors. . 2003. Vol. **31**, p. 97–128. [viewed on 2024-04-30]. .

41. ZHU, X.Y.; YANG, Q.; MUNTWILER, M.; Charge-transfer excitons at organic semiconductor surfaces and interfaces. *Accounts of Chemical Research* [interactive]. 2009. Vol. **42**, no. 11, p. 1779–1787. [viewed on 2024-04-30]. Access via: https://pubs.acs.org/doi/full/10.1021/ar800269u.

42. SHIAU, Shiue Yuan; COMBESCOT, Monique; A fresh view on Frenkel excitons: Electron–hole pair exchange and many-body formalism. *Annals of Physics* . 2023. Vol. **458**, p. 169431. [viewed on 2024-04-30]. .

43. PAVLOVICH, Vladimir S.; Solvatochromism and Nonradiative Decay of Intramolecular Charge-Transfer Excited States: Bands-of-Energy Model, Thermodynamics, and Self-Organization. *ChemPhysChem* [interactive]. 2012. Vol. **13**, no. 18, p. 4081–4093. [viewed on 2024-04-30]. Access via: https://onlinelibrary.wiley.com/doi/full/10.1002/cphc.201200426.

44. KÖHLER, A.; BÄSSLER, H.; Triplet states in organic semiconductors. *Materials Science and Engineering: R: Reports* . 2009. Vol. **66**, no. 4–6, p. 71–109. [viewed on 2024-04-30]. .

45. LUNT, Richard R.; BENZIGER, Jay B.; FORREST, Stephen R.; Relationship between Crystalline Order and Exciton Diffusion Length in Molecular Organic Semiconductors. *Advanced Materials* [interactive]. 2010. Vol. **22**, no. 11, p. 1233–1236. [viewed on 2024-04-30]. Access via: https://onlinelibrary.wiley.com/doi/full/10.1002/adma.200902827.

46. ZHOU, Ding; LIN, Min; LIU, Xun;et al. Conducting the temperature-dependent conformational change of macrocyclic compounds to the lattice dilation of

quantum dots for achieving an ultrasensitive nanothermometer. *ACS Nano* [interactive]. 2013. Vol. **7**, no. 3, p. 2273–2283. [viewed on 2024-04-30]. Access via: https://pubs.acs.org/doi/full/10.1021/nn305423p.

47. DONON, Jeremy; HABKA, Sana; MONS, Michel;et al. Conformational analysis by UV spectroscopy: the decisive contribution of environment-induced electronic Stark effects. *Chemical Science* [interactive]. 2021. Vol. **12**, no. 8, p. 2803–2815. [viewed on 2024-04-30]. Access via: https://pubs.rsc.org/en/content/articlehtml/2021/sc/d0sc06074g.

48. YANG, Jie; ZHEN, Xu; WANG, Bin;et al. The influence of the molecular packing on the room temperature phosphorescence of purely organic luminogens. *Nature Communications* [interactive]. 2018. Vol. **9**, no. 1, p. 1–10. [viewed on 2021-01-28]. Access via: www.nature.com/naturecommunications.

49. JIA, Junhui; ZHANG, Huijuan; Mechanofluorochromic properties of tert-butylcarbazole-based AIE-active D-π-A fluorescent dye. *Journal of Photochemistry and Photobiology A: Chemistry* . 2018. Vol. **353**, p. 521–526. [viewed on 2022-06-13]. .

50. ITO, Suguru; Mechanochromic luminescence of soft crystals: Recent systematic studies in controlling the molecular packing and mechanoresponsive properties. *Journal of Photochemistry and Photobiology C: Photochemistry Reviews* . 2022. Vol. **51**, p. 100481. [viewed on 2022-12-15]. .

51. YANG, Xinxiao; FENG, Xiao; XIN, Jianhui;et al. High-performance crystalline organic light-emitting diodes based on multi-layer high-quality crystals. *Organic Electronics* . 2019. Vol. **64**, p. 236–240. [viewed on 2022-12-15]. .

52. CHAN, Cyrus Y.H.; TSUNG, K.K.; CHOI, W.H.;et al. Achieving time-of-flight mobilities for amorphous organic semiconductors in a thin film transistor configuration. *Organic Electronics* . 2013. Vol. **14**, no. 5, p. 1351–1358. [viewed on 2023-07-01]. .

53. HONG, Yuning; LAM, Jacky W.Y.; TANG, Ben Zhong; Aggregation-induced emission. *Chemical Society Reviews* [interactive]. 2011. Vol. **40**, no. 11, p. 5361–5388. [viewed on 2024-05-03]. Access via: https://pubs.rsc.org/en/content/articlehtml/2011/cs/c1cs15113d.

54. ZHELEV, Zhivko; OHBA, Hideki; BAKALOVA, Rumiana; Single quantum dot-micelles coated with silica shell as potentially non-cytotoxic fluorescent cell tracers. *Journal of the American Chemical Society* [interactive]. 2006. Vol. **128**, no. 19, p. 6324–6325. [viewed on 2024-05-03]. Access via: https://pubs.acs.org/doi/full/10.1021/ja061137d.

55. MEI, Ju; LEUNG, Nelson L.C.; KWOK, Ryan T.K.;et al. Aggregation-Induced Emission: Together We Shine, United We Soar! *Chemical Reviews* [interactive]. 2015. Vol. **115**, no. 21, p. 11718–11940. [viewed on 2024-05-03]. Access via: https://pubs.acs.org/doi/full/10.1021/acs.chemrev.5b00263.

56. ZHAO, Engui; LAM, Jacky W.Y.; HONG, Yuning;et al. How do substituents affect silole emission? *Journal of Materials Chemistry C* [interactive]. 2013. Vol. **1**, no. 36, p. 5661–5668. [viewed on 2024-05-03]. Access via: https://pubs.rsc.org/en/content/articlehtml/2013/tc/c3tc30880d.

57. CHEN, Bin; NIE, Han; LU, Ping;et al. Conjugation versus rotation: good conjugation weakens the aggregation-induced emission effect of siloles. *Chemical Communications* [interactive]. 2014. Vol. **50**, no. 34, p. 4500–4503. [viewed on 2024-05-03]. Access via: https://pubs.rsc.org/en/content/articlehtml/2014/cc/c4cc00653d.

58. YUAN, Chunxue; SAITO, Shohei; CAMACHO, Cristopher;et al. Hybridization of a flexible cyclooctatetraene core and rigid aceneimide wings for multiluminescent flapping π systems. *Chemistry - A European Journal* . 2014. Vol. **20**, no. 8, p. 2193–2200. [viewed on 2024-05-03]. .

59. NISHIUCHI, Tomohiko; TANAKA, Keita; KUWATANI, Yoshiyuki;et al. Solvent-induced crystalline-state emission and multichromism of a bent π-surface system composed of dibenzocyclooctatetraene units. *Chemistry - A European Journal* . 2013. Vol. **19**, no. 13, p. 4110–4116. [viewed on 2024-05-03]. .

60. BANAL, James L.; WHITE, Jonathan M.; GHIGGINO, Kenneth P.;et al. Concentrating Aggregation-Induced Fluorescence in Planar Waveguides: A Proof-of-Principle. *Scientific Reports 2014 4:1* [interactive]. 2014. Vol. **4**, no. 1, p. 1–5. [viewed on 2024-05-03]. Access via: https://www.nature.com/articles/srep04635.

61. LIU, Jie; MENG, Qing; ZHANG, Xiaotao;et al. Aggregation-induced emission enhancement based on 11,11,12,12,-tetracyano-9,10-anthraquinodimethane. *Chemical Communications* [interactive]. 2013. Vol. **49**, no. 12, p. 1199–1201. [viewed on 2024-05-03]. Access via: https://pubs.rsc.org/en/content/articlehtml/2013/cc/c2cc38817k.

62. LIU, Dan; ZHU, Feng; YAN, Donghang; Crystalline organic thin films for crystalline OLEDs (I): orientation of phenanthroimidazole derivatives. *Journal of Materials Chemistry C* [interactive]. 2022. Vol. **10**, no. 7, p. 2663–2670. [viewed on 2024-05-03]. Access via: https://pubs.rsc.org/en/content/articlehtml/2022/tc/d1tc04286f.

63. YANG, Xinxiao; FENG, Xiao; XIN, Jianhui;et al. Highly efficient crystalline organic light-emitting diodes. *Journal of Materials Chemistry C* [interactive]. 2018. Vol. **6**, no. 33, p. 8879–8884. [viewed on 2024-05-03]. Access via: https://pubs.rsc.org/en/content/articlehtml/2018/tc/c8tc03069c.

64. BRULATTI, Pierpaolo; FATTORI, Valeria; MUZZIOLI, Sara;et al. Tuning the colour and efficiency in OLEDs by using amorphous or polycrystalline emitting layers. *Journal of Materials Chemistry C* [interactive]. 2013. Vol. **1**, no. 9, p. 1823–1831. [viewed on 2024-05-03]. Access via: https://pubs.rsc.org/en/content/articlehtml/2013/tc/c2tc00448h.

65. RÀFOLS-RIBÉ, Joan; WILL, Paul Anton; HÄNISCH, Christian;et al. High-performance organic light-emitting diodes comprising ultrastable glass layers. *Science Advances* [interactive]. 2018. Vol. **4**, no. 5. [viewed on 2024-05-03]. Access via: https://www.science.org/doi/10.1126/sciadv.aar8332.

66. VALEUR, Bernard; ARIO, M.; BERBERAN-SANTOS, N.; A Brief History of Fluorescence and Phosphorescence before the Emergence of Quantum Theory. *J. Chem. Educ* . 2011. Vol. **88**, p. 731–738. [viewed on 2024-06-27]. .

67. WOLF, David E.; Fundamentals of Fluorescence and Fluorescence Microscopy. *Methods in Cell Biology* . 2007. Vol. **81**, p. 63–91. [viewed on 2024-05-03]. .

68. MINAEV, Boris; BARYSHNIKOV, Gleb; AGREN, Hans; Principles of phosphorescent organic light emitting devices. *Physical Chemistry Chemical Physics* [interactive]. 2014. Vol. **16**, no. 5, p. 1719–1758. [viewed on 2024-05-03]. Access via: https://pubs.rsc.org/en/content/articlehtml/2014/cp/c3cp53806k.

69. KAPPAUN, Stefan; SLUGOVC, Christian; LIST, Emil J.W.; Phosphorescent Organic Light-Emitting Devices: Working Principle and Iridium Based Emitter Materials. *International Journal of Molecular Sciences 2008, Vol. 9, Pages 1527-1547* [interactive]. 2008. Vol. **9**, no. 8, p. 1527–1547. [viewed on 2024-05-03]. Access via: https://www.mdpi.com/1422-0067/9/8/1527/htm.

70. UOYAMA, Hiroki; GOUSHI, Kenichi; SHIZU, Katsuyuki;et al. Highly efficient organic light-emitting diodes from delayed fluorescence. *Nature 2012 492:7428* [interactive]. 2012. Vol. **492**, no. 7428, p. 234–238. [viewed on 2022-12-15]. Access via: https://www.nature.com/articles/nature11687.

71. GIBSON, Jamie; MONKMAN, Andrew P.; PENFOLD, Thomas J.; The Importance of Vibronic Coupling for Efficient Reverse Intersystem Crossing in Thermally Activated Delayed Fluorescence Molecules. *ChemPhysChem* [interactive]. 2016. Vol. **17**, no. 19, p. 2956–2961. [viewed on 2021-01-28]. Access via: http://doi.wiley.com/10.1002/cphc.201600662.

72. PHAN HUU, D.K. Andrea; SASEENDRAN, Sangeeth; DHALI, Rama;et al. Thermally Activated Delayed Fluorescence: Polarity, Rigidity, and Disorder in Condensed Phases. *Journal of the American Chemical Society* [interactive]. 2022. Vol. **144**, no. 33, p. 15211–15222. [viewed on 2022-12-15]. Access via: https://pubs.acs.org/doi/full/10.1021/jacs.2c05537.

73. MÉHES, Gábor; GOUSHI, Kenichi; POTSCAVAGE, William J.;et al. Influence of host matrix on thermally-activated delayed fluorescence: Effects on emission lifetime, photoluminescence quantum yield, and device performance. *Organic Electronics* [interactive]. 2014. Vol. **15**, no. 9, p. 2027–2037. [viewed on 2018-12-10]. Access via: https://linkinghub.elsevier.com/retrieve/pii/S1566119914002067.

74. MAMADA, Masashi; YADA, Sawako; HAYAKAWA, Masahiro;et al. Donor-only substituted benzene achieves thermally activated delayed fluorescence. *Communications Chemistry 2024 7:1* [interactive]. 2024. Vol. **7**, no. 1, p. 1–6. [viewed on 2024-10-09]. Access via: https://www.nature.com/articles/s42004-024-01301-4.

75. FARGES, Jean Pierre; GUTMANN, Felix; Charge-Transfer Complexes in Electrochemistry. *Mod Aspects Electrochem* [interactive]. 1977. no. 12, p. 267–314. [viewed on 2024-10-14]. Access via: https://link.springer.com/chapter/10.1007/978-1-4615-7452-1_5.

76. TSUCHIYA, Youichi; TSUJI, Keita; INADA, Ko;et al. Molecular Design Based on Donor-Weak Donor Scaffold for Blue Thermally-Activated Delayed Fluorescence Designed by Combinatorial DFT Calculations. *Frontiers in Chemistry*

[interactive]. 2020. Vol. **8**, p. 530689. [viewed on 2024-10-09]. Access via: www.frontiersin.org.

77. GU, Jiannan; TANG, Zhenyu; GUO, Haoqing;et al. Intermolecular TADF: bulk and interface exciplexes. *Journal of Materials Chemistry C* [interactive]. 2022. Vol. **10**, no. 12, p. 4521–4532. [viewed on 2024-05-06]. Access via: https://pubs.rsc.org/en/content/articlehtml/2022/tc/d1tc04950j.

78. HE, Shou Jie; WANG, Deng Ke; JIANG, Nan;et al. Tunable Excitonic Processes at Organic Heterojunctions. *Advanced Materials* . 2016. Vol. **28**, no. 4, p. 649–654. [viewed on 2024-05-06]. .

79. SHAO, Jianhua; CHEN, Cong; ZHAO, Wencheng;et al. Recent Advances of Interface Exciplex in Organic Light-Emitting Diodes. *Micromachines 2022, Vol. 13, Page 298* [interactive]. 2022. Vol. **13**, no. 2, p. 298. [viewed on 2024-05-06]. Access via: https://www.mdpi.com/2072-666X/13/2/298/htm.

80. GUZAUSKAS, Matas; VOLYNIUK, Dmytro; TOMKEVICIENE, Ausra;et al. Dual nature of exciplexes: exciplex-forming properties of carbazole and fluorene hybrid trimers. *Journal of Materials Chemistry C* . 2019. Vol. **7**, no. 1, p. 25–32. [viewed on 2020-05-18]. .

81. GUŽAUSKAS, Matas; NARBUTAITIS, Edgaras; VOLYNIUK, Dmytro;et al. Polymorph acceptor-based triads with photoinduced TADF for UV sensing. *Chemical Engineering Journal* . 2021. Vol. **425**, p. 131549. [viewed on 2022-12-15]. .

82. LI, Weijun; PAN, Yuyu; YAO, Liang;et al. A Hybridized Local and Charge-Transfer Excited State for Highly Efficient Fluorescent OLEDs: Molecular Design, Spectral Character, and Full Exciton Utilization. *Advanced Optical Materials* [interactive]. 2014. Vol. **2**, no. 9, p. 892–901. [viewed on 2021-01-28]. Access via: http://doi.wiley.com/10.1002/adom.201400154.

83. GRABOWSKI, Zbigniew R.; ROTKIEWICZ, Krystyna; RETTIG, Wolfgang; [interactive]. .[s.l.]: Chem Rev, 2003. [viewed on 2021-01-28] Access via: https://pubmed.ncbi.nlm.nih.gov/14531716/.

84. KUMAR KONIDENA, Rajendra; JUSTIN THOMAS, K.R.; KUMAR DUBEY, Deepak;et al. A new molecular design based on hybridized local and charge transfer fluorescence for highly efficient (>6%) deep-blue organic light emitting diodes. *Chemical Communications* [interactive]. 2017. Vol. **53**, no. 86, p. 11802–11805. [viewed on 2021-01-28]. Access via: https://pubs.rsc.org/en/content/articlehtml/2017/cc/c7cc07139f.

85. ZHANG, Shitong; YAO, Liang; PENG, Qiming;et al. Achieving a Significantly Increased Efficiency in Nondoped Pure Blue Fluorescent OLED: A Quasi-Equivalent Hybridized Excited State. *Advanced Functional Materials* [interactive]. 2015. Vol. **25**, no. 11, p. 1755–1762. [viewed on 2021-01-28]. Access via: http://doi.wiley.com/10.1002/adfm.201404260.

86. ETHERINGTON, Marc K.; GIBSON, Jamie; HIGGINBOTHAM, Heather F.;et al. Revealing the spin–vibronic coupling mechanism of thermally activated delayed fluorescence. *Nature Communications* [interactive]. 2016. Vol. **7**, no. 1,

p. 13680. [viewed on 2018-12-10]. Access via: http://www.ncbi.nlm.nih.gov/pubmed/27901046.

87. YANG, Jie; ZHEN, Xu; WANG, Bin;et al. The influence of the molecular packing on the room temperature phosphorescence of purely organic luminogens. *Nature Communications* [interactive]. 2018. Vol. **9**, no. 1, p. 1–10. [viewed on 2021-01-28]. Access via: www.nature.com/naturecommunications.

88. WAN, Shigang; LU, Wei; Reversible Photoactivated Phosphorescence of Gold(I) Arylethynyl Complexes in Aerated DMSO Solutions and Gels. *Angewandte Chemie International Edition* [interactive]. 2017. Vol. **56**, no. 7, p. 1784–1788. [viewed on 2021-01-28]. Access via: http://doi.wiley.com/10.1002/anie.201610762.

89. GMELCH, Max; THOMAS, Heidi; FRIES, Felix;et al. Programmable transparent organic luminescent tags. *Science Advances* [interactive]. 2019. Vol. **5**, no. 2, p. eaau7310. [viewed on 2021-01-28]. Access via: http://advances.sciencemag.org/.

90. LIU, Dong; ZHANG, Zhenyu; ZHANG, Hongyu;et al. A novel approach towards white photoluminescence and electroluminescence by controlled protonation of a blue fluorophore. *Chemical Communications* [interactive]. 2013. Vol. **49**, no. 85, p. 10001–10003. [viewed on 2021-01-28]. Access via: www.rsc.org/chemcomm.

91. DATA, Przemyslaw; OKAZAKI, Masato; MINAKATA, Satoshi;et al. Thermally Activated Delayed Fluorescence vs Room Temperature Phosphorescence by Conformation Control of Organic Single Molecules. *Journal of Materials Chemistry C* . 2019. .

92. HLADKA, Iryna; VOLYNIUK, Dmytro; BEZVIKONNYI, Oleksandr;et al. Polymorphism of derivatives of tert -butyl substituted acridan and perfluorobiphenyl as sky-blue OLED emitters exhibiting aggregation induced thermally activated delayed fluorescence. *Journal of Materials Chemistry C* [interactive]. 2018. Vol. **6**, no. 48, p. 13179–13189. [viewed on 2021-01-28]. Access via: https://pubs.rsc.org/en/content/articlehtml/2018/tc/c8tc04867c.

93. OKAZAKI, Masato; TAKEDA, Youhei; DATA, Przemyslaw;et al. Thermally activated delayed fluorescent phenothiazine-dibenzo[a,j]phenazine-phenothiazine triads exhibiting tricolor-changing mechanochromic luminescence. *Chemical Science* [interactive]. 2017. Vol. **8**, no. 4, p. 2677–2686. [viewed on 2021-01-28]. Access via: www.rsc.org/chemicalscience.

94. LIN, Yan; CHEN, Jingrong; XIE, Puhui;et al. Study on emission quenching by 2,2,6,6-tetramethyl-1-piperidinyloxy free radical. *Research on Chemical Intermediates* . 2000. Vol. **26**, no. 7–8, p. 793–803. [viewed on 2024-04-19]. .

95. ZHOU, Xiao; SHI, Chao; LONG, Saran;et al. Highly Efficient Photosensitizers with Molecular Vibrational Torsion for Cancer Photodynamic Therapy. *ACS Central Science* [interactive]. 2023. Vol. **9**, no. 8, p. 1679–1691. [viewed on 2024-04-23]. Access via: https://pubs.acs.org/doi/full/10.1021/acscentsci.3c00611.

96. CARRAWAY, E.R.; DEMAS, J.N.; DEGRAFF, B.A.;et al. Photophysics and Photochemistry of Oxygen Sensors Based on Luminescent Transition-Metal

Complexes. *Analytical Chemistry* [interactive]. 1991. Vol. **63**, no. 4, p. 337–342. [viewed on 2021-01-28]. Access via: https://pubs.acs.org/sharingguidelines.

97. KULSZEWICZ-BAJER, Irena; GUZAUSKAS, Matas; MAKOWSKA-JANUSIK, Małgorzata;et al. Acridone and quinacridone derivatives with carbazole or phenoxazine substituents: synthesis, electrochemistry, photophysics and application as TADF electroluminophores. *Journal of Materials Chemistry C* [interactive]. 2022. Vol. **10**, no. 34, p. 12377–12391. [viewed on 2023-03-20]. Access via: https://pubs.rsc.org/en/content/articlehtml/2022/tc/d2tc02270b.

98. KARON, Krzysztof; LAPKOWSKI, Mieczyslaw; Carbazole electrochemistry: a short review. *Journal of Solid State Electrochemistry* [interactive]. 2015. Vol. **19**, no. 9, p. 2601–2610. [viewed on 2021-11-09]. Access via: https://link.springer.com/article/10.1007/s10008-015-2973-x.

99. PANDER, Piotr; MOTYKA, Radoslaw; ZASSOWSKI, Pawel;et al. Electrochromic Properties of Novel Selenophene and Tellurophene Derivatives Based on Carbazole and Triphenylamine Core. *Journal of Physical Chemistry C* [interactive]. 2017. Vol. **121**, no. 21, p. 11027–11036. [viewed on 2024-04-19]. Access via: https://pubs.acs.org/doi/full/10.1021/acs.jpcc.7b00216.

100. KURZEP, Piotr; SKÓRKA, Łukasz; ZAGORSKA, Malgorzata;et al. New quinacridone derivatives with π-extended conjugation in central core. *RSC Advances* [interactive]. 2017. Vol. **7**, no. 14, p. 8627–8632. [viewed on 2021-11-09]. Access via: https://pubs.rsc.org/en/content/articlehtml/2017/ra/c6ra28567h.

101. SKUODIS, Eigirdas; BEZVIKONNYI, Oleksandr; TOMKEVICIENE, Ausra;et al. Aggregation, thermal annealing, and hosting effects on performances of an acridan-based TADF emitter. *Organic Electronics* . 2018. Vol. **63**, p. 29–40. [viewed on 2021-11-09]. .

102. NIKOLAENKO, Andrey E.; CASS, Michael; BOURCET, Florence;et al. Thermally Activated Delayed Fluorescence in Polymers: A New Route toward Highly Efficient Solution Processable OLEDs. *Advanced Materials* [interactive]. 2015. Vol. **27**, no. 44, p. 7236–7240. [viewed on 2024-04-23]. Access via: https://onlinelibrary.wiley.com/doi/full/10.1002/adma.201501090.

103. ZHAO, Zheng; ZHANG, Haoke; LAM, Jacky W.Y.;et al. Aggregation-Induced Emission: New Vistas at the Aggregate Level. *Angewandte Chemie International Edition* [interactive]. 2020. Vol. **59**, no. 25, p. 9888–9907. [viewed on 2021-11-09]. Access via: https://onlinelibrary.wiley.com/doi/full/10.1002/anie.201916729.

104. ZUO, Yunfei; WANG, Xing; WU, Decheng; Uniting aggregation-induced emission and stimuli-responsive aggregation-caused quenching, single molecule achieved multicolour luminescence. *Journal of Materials Chemistry C* [interactive]. 2019. Vol. **7**, no. 46, p. 14555–14562. [viewed on 2024-04-19]. Access via: https://pubs.rsc.org/en/content/articlehtml/2019/tc/c9tc05258e.

105. MARSZALEK, Tomasz; KRYGIER, Izabela; PRON, Adam;et al. Self-assembly and charge carrier transport of sublimated dialkyl substituted quinacridones. *Organic Electronics* . 2019. Vol. **65**, p. 127–134. [viewed on 2021-11-09]. .

106. WANG, Chenguang; CHEN, Dong; CHEN, Weiping;et al. Polymorph, assembly, luminescence and semiconductor properties of a quinacridone derivative with extended π-conjugated framework. *Journal of Materials Chemistry C* [interactive]. 2013. Vol. **1**, no. 35, p. 5548–5556. [viewed on 2021-11-09]. Access via: https://pubs.rsc.org/en/content/articlehtml/2013/tc/c3tc30803k.

107. PHAM, Hong Duc; JAIN, Sagar M.; LI, Meng;et al. Dopant-free novel hole-transporting materials based on quinacridone dye for high-performance and humidity-stable mesoporous perovskite solar cells. *Journal of Materials Chemistry A* [interactive]. 2019. Vol. **7**, no. 10, p. 5315–5323. [viewed on 2021-11-09]. Access via: https://pubs.rsc.org/en/content/articlehtml/2019/ta/c8ta11361k.

108. GUDEIKA, Dalius; LEE, Jiun Haw; LEE, Pei Hsi;et al. Flexible diphenylsulfone versus rigid dibenzothiophene-dioxide as acceptor moieties in donor-acceptor-donor TADF emitters for highly efficient OLEDs. *Organic Electronics* . 2020. Vol. **83**, p. 105733. [viewed on 2021-11-09]. .

109. HEUN, S.; BORSENBERGER, P.M.; A comparative study of hole transport in vapor-deposited molecular glasses of N,N′,N″,N‴-tetrakis(4-methylphenyl)-(1,1′-biphenyl)-4,4′-diamine and N,N′-diphenyl-N,N′-bis(3-methylphenyl)-(1,1′-biphenyl)-4,4′-diamine. *Chemical Physics* . 1995. Vol. **200**, no. 1–2, p. 245–255. [viewed on 2021-11-09]. .

110. GANICHEV, S.; ZIEMANN, E.; PRETTL, W.;et al. Distinction between the Poole-Frenkel and tunneling models of electric-field-stimulated carrier emission from deep levels in semiconductors. *Physical Review B* [interactive]. 2000. Vol. **61**, no. 15, p. 10361. [viewed on 2024-04-19]. Access via: https://journals.aps.org/prb/abstract/10.1103/PhysRevB.61.10361.

111. LUO, Dongxiang; LI, Xiang Long; ZHAO, Yu;et al. High-Performance Blue Molecular Emitter-Free and Doping-Free Hybrid White Organic Light-Emitting Diodes: An Alternative Concept to Manipulate Charges and Excitons Based on Exciplex and Electroplex Emission. *ACS Photonics* [interactive]. 2017. Vol. **4**, no. 6, p. 1566–1575. [viewed on 2021-11-09]. Access via: https://pubs.acs.org/doi/full/10.1021/acsphotonics.7b00364.

112. JATAUTIENE, Egle; SIMOKAITIENE, Jurate; SYCH, Galyna;et al. Adjustment of electronic and emissive properties of indolocarbazoles for non-doped OLEDs and cholesteric liquid crystal lasers. *Applied Materials Today* . 2021. Vol. **24**, p. 101121. [viewed on 2021-11-09]. .

113. VIPIN, C.K.; SHUKLA, Atul; RAJEEV, Kavya;et al. White Organic Light-Emitting Diodes from Single Emissive Layers: Combining Exciplex Emission with Electromer Emission. *Journal of Physical Chemistry C* [interactive]. 2021. Vol. **125**, no. 41, p. 22809–22816. [viewed on 2024-04-23]. Access via: https://pubs.acs.org/doi/full/10.1021/acs.jpcc.1c06323.

114. TSUTSUI, Tetsuo; Progress in electroluminescent devices using molecular thin films. *MRS Bulletin* [interactive]. 1997. Vol. **22**, no. 6, p. 39–45. [viewed on 2021-01-19]. Access via: https://link.springer.com/article/10.1557/S0883769400033613.

115. GUZAUSKAS, Matas; VOLYNIUK, Dmytro; KULSZEWICZ-BAJER, Irena;et al. Thermally Controllable Tuning of Emission Properties of Phenoxazine-Substituted Acridones as One Step Forward to Efficient Organic Light-Emitting Diodes Based on Crystalline Emitters. *Advanced Optical Materials* [interactive]. 2023. Vol. **11**, no. 24, p. 2301059. [viewed on 2024-04-22]. Access via: https://onlinelibrary.wiley.com/doi/full/10.1002/adom.202301059.

116. KULSZEWICZ-BAJER, Irena; ZAGORSKA, Malgorzata; BANASIEWICZ, Marzena;et al. Effect of the substituent position on the electrochemical, optical and structural properties of donor–acceptor type acridone derivatives. *Physical Chemistry Chemical Physics* [interactive]. 2020. Vol. **22**, no. 16, p. 8522–8534. [viewed on 2022-12-15]. Access via: https://pubs.rsc.org/en/content/articlehtml/2020/cp/d0cp00521e.

117. PHAN HUU, D.K. Andrea; SASEENDRAN, Sangeeth; DHALI, Rama;et al. Thermally Activated Delayed Fluorescence: Polarity, Rigidity, and Disorder in Condensed Phases. *Journal of the American Chemical Society* [interactive]. 2022. Vol. **144**, no. 33, p. 15211–15222. [viewed on 2023-04-11]. Access via: https://pubs.acs.org/doi/full/10.1021/jacs.2c05537.

118. SASAKI, Shunsuke; DRUMMEN, Gregor P.C.; KONISHI, Gen Ichi; Recent advances in twisted intramolecular charge transfer (TICT) fluorescence and related phenomena in materials chemistry. *Journal of Materials Chemistry C* [interactive]. 2016. Vol. **4**, no. 14, p. 2731–2743. [viewed on 2023-01-18]. Access via: https://pubs.rsc.org/en/content/articlehtml/2016/tc/c5tc03933a.

119. KIM, Ki-Beom; TAK, Yoon-Heung; HAN, Yoon-Soo;et al. Relationship between Surface Roughness of Indium Tin Oxide and Leakage Current of Organic Light-Emitting Diode. *Japanese Journal of Applied Physics* [interactive]. 2003. Vol. **42**, no. Part 2, No. 4B, p. L438–L440. [viewed on 2024-06-28]. Access via: https://iopscience.iop.org/article/10.1143/JJAP.42.L438.

120. ZHENG, Xujun; HUANG, Rongjuan; ZHONG, Cheng;et al. Achieving 21% External Quantum Efficiency for Nondoped Solution-Processed Sky-Blue Thermally Activated Delayed Fluorescence OLEDs by Means of Multi-(Donor/Acceptor) Emitter with Through-Space/-Bond Charge Transfer. *Advanced Science* [interactive]. 2020. Vol. **7**, no. 7, p. 1902087. [viewed on 2022-12-15]. Access via: https://onlinelibrary.wiley.com/doi/full/10.1002/advs.201902087.

121. KREIZA, Gediminas; BANEVIČIUS, Dovydas; JOVAIŠAITĖ, Justina;et al. Suppression of benzophenone-induced triplet quenching for enhanced TADF performance. *Journal of Materials Chemistry C* [interactive]. 2019. Vol. **7**, no. 37, p. 11522–11531. [viewed on 2022-12-15]. Access via: https://pubs.rsc.org/en/content/articlehtml/2019/tc/c9tc02408e.

122. SEREVIČIUS, Tomas; SKAISGIRIS, Rokas; KREIZA, Gediminas;et al. TADF parameters in the solid state: An easy way to draw wrong conclusions. *Journal of Physical Chemistry A* [interactive]. 2021. Vol. **125**, no. 7, p. 1637–1641. [viewed on 2023-07-01]. Access via: https://pubs.acs.org/doi/full/10.1021/acs.jpca.0c10391.

123. ZHANG, Dongdong; SONG, Xiaozeng; GILLETT, Alexander J.;et al. Efficient and Stable Deep-Blue Fluorescent Organic Light-Emitting Diodes

Employing a Sensitizer with Fast Triplet Upconversion. *Advanced Materials* [interactive]. 2020. Vol. **32**, no. 19, p. 1908355. [viewed on 2022-12-15]. Access via: https://onlinelibrary.wiley.com/doi/full/10.1002/adma.201908355.

124. CHEN, Xian Kai; ZHANG, Shou Feng; FAN, Jian Xun;et al. Nature of highly efficient thermally activated delayed fluorescence in organic light-emitting diode emitters: Nonadiabatic effect between excited states. *Journal of Physical Chemistry C* [interactive]. 2015. Vol. **119**, no. 18, p. 9728–9733. [viewed on 2023-07-01]. Access via: https://pubs.acs.org/doi/full/10.1021/acs.jpcc.5b00276.

125. HIRATA, Shuzo; Recent Advances in Materials with Room-Temperature Phosphorescence: Photophysics for Triplet Exciton Stabilization. *Advanced Optical Materials* [interactive]. 2017. Vol. **5**, no. 17, p. 1700116. [viewed on 2023-07-01]. Access via: https://onlinelibrary.wiley.com/doi/full/10.1002/adom.201700116.

126. SANTOS, Paloma L.; WARD, Jonathan S.; DATA, Przemyslaw;et al. Engineering the singlet–triplet energy splitting in a TADF molecule. *Journal of Materials Chemistry C* [interactive]. 2016. Vol. **4**, no. 17, p. 3815–3824. [viewed on 2022-12-15]. Access via: https://pubs.rsc.org/en/content/articlehtml/2016/tc/c5tc03849a.

127. SEREVIČIUS, Tomas; SKAISGIRIS, Rokas; DODONOVA, Jelena;et al. Temporal Dynamics of Solid-State Thermally Activated Delayed Fluorescence: Disorder or Ultraslow Solvation? *Journal of Physical Chemistry Letters* [interactive]. 2022. Vol. **13**, no. 7, p. 1839–1844. [viewed on 2022-12-15]. Access via: https://pubs.acs.org/doi/full/10.1021/acs.jpclett.1c03810.

128. SEREVIČIUS, Tomas; SKAISGIRIS, Rokas; GUDEIKA, Dalius;et al. Conformational disorder enabled emission phenomena in heavily doped TADF films. *Physical Chemistry Chemical Physics* [interactive]. 2021. Vol. **24**, no. 1, p. 313–320. [viewed on 2022-12-15]. Access via: https://pubs.rsc.org/en/content/articlehtml/2022/cp/d1cp04905d.

129. SEREVIČIUS, Tomas; SKAISGIRIS, Rokas; FIODOROVA, Irina;et al. Single-exponential solid-state delayed fluorescence decay in TADF compounds with minimized conformational disorder. *Journal of Materials Chemistry C* [interactive]. 2021. Vol. **9**, no. 3, p. 836–841. [viewed on 2022-12-15]. Access via: https://pubs.rsc.org/en/content/articlehtml/2021/tc/d0tc05503d.

130. MACIONIS, Simas; GUDEIKA, Dalius; VOLYNIUK, Dmytro;et al. Does Through-Space Charge Transfer in Bipolar Hosts Affect the Efficiency of Blue OLEDs? *Advanced Optical Materials* [interactive]. 2021. Vol. **9**, no. 7, p. 2002227. [viewed on 2024-06-27]. Access via: https://onlinelibrary.wiley.com/doi/full/10.1002/adom.202002227.

131. KUWABARA, Yoshiyuki; OGAWA, Hiromitsu; INADA, Hiroshi;et al. Thermally stable multilared organic electroluminescent devices using novel starburst molecules, 4,4′,4″-Tri(N-carbazolyl)triphenylamine (TCTA) and 4,4′,4″-Tris(3-methylphenylphenylamino)triphenylamine (m-MTDATA), as hole-transport materials. *Advanced Materials* [interactive]. 1994. Vol. **6**, no. 9, p. 677–679. [viewed on 2022-12-15]. Access via: https://onlinelibrary.wiley.com/doi/full/10.1002/adma.19940060913.

132. TAO, Youtian; YANG, Chuluo; QIN, Jingui; Organic host materials for phosphorescent organic light-emitting diodes. *Chemical Society Reviews* [interactive]. 2011. Vol. **40**, no. 5, p. 2943–2970. [viewed on 2022-12-20]. Access via: https://pubs.rsc.org/en/content/articlehtml/2011/cs/c0cs00160k.

133. TSUCHIYA, Youichi; NAKAMURA, Nozomi; KAKUMACHI, Shunta;et al. A convenient method to estimate the glass transition temperature of small organic semiconductor materials. *Chemical Communications* [interactive]. 2022. Vol. **58**, no. 80, p. 11292–11295. [viewed on 2022-12-15]. Access via: https://pubs.rsc.org/en/content/articlehtml/2022/cc/d2cc01467j.

134. KERUCKIENE, R.; GUZAUSKAS, M.; LAPIENYTE, L.;et al. An experimental and theoretical study of exciplex-forming compounds containing trifluorobiphenyl and 3,6-di-tert-butylcarbazole units and their performance in OLEDs. *Journal of Materials Chemistry C* [interactive]. 2020. Vol. **8**, no. 40, p. 14186–14195. [viewed on 2024-04-22]. Access via: https://pubs.rsc.org/en/content/articlehtml/2020/tc/d0tc02777d.

135. MCINTOSH, A.; BOUCHER, F.; JENEKHE, Samson A.;et al. Excimers and Exciplexes of Conjugated Polymers. *Science* [interactive]. 1994. Vol. **265**, no. 5173, p. 765–768. [viewed on 2024-04-22]. Access via: https://www.science.org/doi/10.1126/science.265.5173.765.

136. HUNG, Wen-Yi; FANG, Guan-Cheng; CHANG, Yuh-Chia;et al. Highly Efficient Bilayer Interface Exciplex For Yellow Organic Light-Emitting Diode. *ACS Applied Materials & Interfaces* . 2013. Vol. **5**, no. 15, p. 6826–6831. .

137. KALINOWSKI, J.; [interactive]. .2009. [viewed on 2018-09-07] Access via: http://www.materialsscience.pwr.wroc.pl/bi/vol27no3/articles/ms_15_kali.pdf.

138. CEKAVICIUTE, Monika; SIMOKAITIENE, Jurate; VOLYNIUK, Dmytro;et al. Arylfluorenyl-substituted metoxytriphenylamines as deep blue exciplex forming bipolar semiconductors for white and blue organic light emitting diodes. *Dyes and Pigments* . 2017. Vol. **140**, p. 187–202. [viewed on 2020-05-18]. .

139. COLELLA, Marco; DANOS, Andrew; MONKMAN, Andrew P.; Less is more: Dilution enhances optical and electrical performance of a TADF exciplex. *Journal of Physical Chemistry Letters* [interactive]. 2019. Vol. **10**, no. 4, p. 793–798. [viewed on 2024-04-22]. Access via: https://pubs.acs.org/doi/full/10.1021/acs.jpclett.8b03646.

140. MAMADA, Masashi; TIAN, Guojian; NAKANOTANI, Hajime;et al. The Importance of Excited-State Energy Alignment for Efficient Exciplex Systems Based on a Study of Phenylpyridinato Boron Derivatives. *Angewandte Chemie International Edition* . 2018. Vol. **57**, no. 38, p. 12380–12384. .

141. KERUCKIENE, R.; GUZAUSKAS, M.; NARBUTAITIS, E.;et al. Exciplex-forming derivatives of 2,7-di-tert-butyl-9,9-dimethylacridan and benzotrifluoride for efficient OLEDs. *Organic Electronics* . 2020. Vol. **78**, p. 105576. [viewed on 2020-05-18]. .

142. ZHAO, Juewen; ZHENG, Caijun; ZHOU, Yu;et al. Novel small-molecule electron donor for solution-processed ternary exciplex with 24% external quantum

efficiency in organic light-emitting diode. *Materials Horizons* . 2019. Vol. **6**, no. 7, p. 1425–1432. [viewed on 2020-05-18]. .

143. PU, Yong Jin; KOYAMA, Yuki; OTSUKI, Daisuke;et al. Exciplex emissions derived from exceptionally long-distance donor and acceptor molecules. *Chemical Science* . 2019. Vol. **10**, no. 40, p. 9203–9208. [viewed on 2020-05-18]. .

144. LIU, Xiao-Ke; CHEN, Zhan; ZHENG, Cai-Jun;et al. Prediction and Design of Efficient Exciplex Emitters for High-Efficiency, Thermally Activated Delayed-Fluorescence Organic Light-Emitting Diodes. *Advanced Materials* . 2015. Vol. **27**, no. 14, p. 2378–2383. .

145. LEE, Jeong-Hwan; CHENG, Shuo-Hsien; YOO, Seung-Jun;et al. *An Exciplex Forming Host for Highly Efficient Blue Organic Light Emitting Diodes with Low Driving Voltage*. . 2015. 361–366 p.

146. YUAN, Peisen; GUO, Xiaomin; QIAO, Xianfeng;et al. Improvement of the Electroluminescence Performance of Exciplex-Based OLEDs by Effective Utilization of Long-Range Coupled Electron–Hole Pairs. *Advanced Optical Materials* [interactive]. 2019. Vol. **7**, no. 9, p. 1801648. [viewed on 2024-04-22]. Access via: https://onlinelibrary.wiley.com/doi/full/10.1002/adom.201801648.

147. WEI, Xiaozhen; GAO, Long; MIAO, Yanqin;et al. A new strategy for structuring white organic light-emitting diodes by combining complementary emissions in the same interface. *Journal of Materials Chemistry C* . 2020. Vol. **8**, no. 8, p. 2772–2779. [viewed on 2020-05-18]. .

148. YANG, Shengyi; JIANG, Mingxiao; White light generation combining emissions from exciplex, excimer and electromer in TAPC-based organic light-emitting diodes. *Chemical Physics Letters* . 2009. Vol. **484**, no. 1–3, p. 54–58. [viewed on 2024-04-22]. .

7. SCIENTIFIC PAPERS

Chemical Engineering Journal 425 (2021) 131549

Contents lists available at ScienceDirect

Chemical Engineering Journal

journal homepage: www.elsevier.com/locate/cej

Polymorph acceptor-based triads with photoinduced TADF for UV sensing

Matas Gužauskas [a], Edgaras Narbutaitis [a], Dmytro Volyniuk [a,*], Glib V. Baryshnikov [b,c], Boris F. Minaev [c], Hans Ågren [d,e], Yu-Chiang Chao [f], Chia-Chih Chang [g], Martins Rutkis [h], Juozas V. Grazulevicius [a,*]

[a] Department of Polymer Chemistry and Technology, Kaunas University of Technology, Radvilenu pl. 19, LT-50254 Kaunas, Lithuania
[b] Linköping University, Department of Science and Technology, Laboratory of Organic Electronics, Norrköping, SE 60174, Sweden
[c] Department of Chemistry and Nanomaterials Science, Bohdan Khmelnytsky National University, 18031 Cherkasy, Ukraine
[d] Department of Physics and Astronomy, Uppsala University, Box 516, SE-751 20 Uppsala, Sweden
[e] College of Chemistry and Chemical Engineering, Henan University, Kaifeng, Henan 475004, PR China
[f] Department of Physics, National Taiwan Normal University, 88, Sec.4, Ting Chou Rd., Taipei 116, Taiwan
[g] Department of Applied Chemistry, National Chiao Tung University, 1001 University Road, Hsinchu 300, Taiwan
[h] Institute of Solid State Physics, University of Latvia, 8 Kengaraga St., Riga LV-1063, Latvia

ARTICLE INFO

Keywords:
Phenothiazine-5,5-dioxide
Benzophenone
Diphenylsulfone
UV sensor

ABSTRACT

In contrast to many donor–acceptor type organic luminophores exhibiting thermally activated delayed fluorescence (TADF), two deep blue TADF emitters designed in this work contain only typical electron accepting moieties with different electron accepting abilities. Derivatives of benzophenone and diphenylsulfone substituted with phenothiazine-5,5-dioxide donor moieties were synthesized and studied. In addition to the TADF, green to blue emission color switching and strong fluorescence intensity enhancement by more than 60 times was detected for THF solution of the derivative of phenothiazine-5,5-dioxide and benzophenone under increase of UV excitation dose. We proved by a variety of experimental and theoretical studies that the unusual photophysical properties of the derivative of benzophenone are mainly related to the formation of different conformers. The photostimulated intensity enhancement of the compound is due to the rise of the quantity of triplet states and their further crossing to singlet states. To our knowledge, this is the first observation of a combination of photoinduced color switching and triplet-dependent emission intensity enhancement. These properties are shown to be useful for UV sensing with very low detection limits (less than 10 $\mu W/cm^2$ for the toluene solution). Under gradual increase of UV excitation dose, the DMF solution demonstrated a green → blue color swishing from (0.34; 0.44) to (0.17; 0.18) of CIE coordinates that can be detected by naked eye.

1. Introduction

Since 2012 [1], organic donor–acceptor (D-A) type materials exhibiting thermally-activated delayed fluorescence (TADF) have attracted huge academic and commercial interest [2]. These materials have been involved in a wide verity of practical applications in optoelectronics (e.g. in OLEDs, photovoltaics, lasers, light-emitting transistors), photocatalysis, photodynamic therapy, time-resolved luminescence imaging, chemical/biochemical sensing [2–4]. In case of sensing, TADF compounds showed good efficiency for oxygen pressure, temperature and media polarity measurements [5,6]. For instance, exploiting a D-A-D-type design strategy TADF compounds with a diphenyl sulphone moiety as acceptor being substituted by two donors (5-nitroindole, 5-aminoindole or 5-acetaminoindole) have been developed as polarity sensing materials [7]. The D-A-D TADF compounds with ultra-long emission decays were recently developed and used in optical sensors of oxygen and temperature [8–10]. It is known that original molecular design of TADF compounds can provide unique properties [3,11]. We believe that further modification of TADF compounds can lead to achievement of unique properties, such as multichannel TADF from a single molecule with clear time resolution, that might be useful for sensing and bioimaging applications.

In this study, we exploit the original design strategy of TADF compounds using phenothiazine-5,5-dioxide, benzophenone and diphenylsulfone moieties with different electron accepting abilities. Phenothiazine has been extensively studied as a donor moiety in both

* Corresponding authors.
E-mail addresses: dmytro.volyniuk@ktu.lt (D. Volyniuk), juozas.grazulevicius@ktu.lt (J.V. Grazulevicius).

https://doi.org/10.1016/j.cej.2021.131549
Received 5 May 2021; Received in revised form 7 July 2021; Accepted 28 July 2021
Available online 8 August 2021

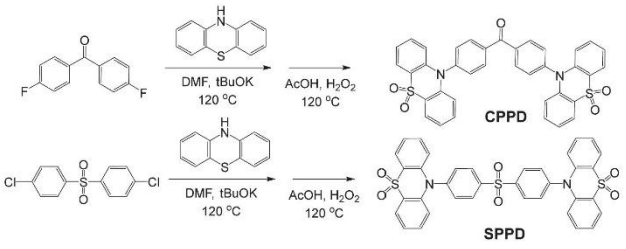

Scheme 1. Synthetic pathways leading to **CPPD** and **SPPD** compounds.

high-triplet-energy hosts and TADF compounds [12]. A more rigid oxidized analogue of this species has not yet received much scientific attention despite easily accessible synthetic routes. The only exploitation of phenothiazine-5,5-dioxide moiety reported so far was its usage as an acceptor moiety [13,14]. According to computational results of the studies in [13,14] the acceptor strength of phenothiazine-5,5-dioxide is quite low. Similarly, studies on host materials based on this fragment have indicated that it behaves as an acceptor in comparison to the carbazole moiety [15]. Following the above considerations, our design of TADF compounds is based on the popular benzophenone and diphenylsulfone acceptor frameworks utilizing phenothiazine-5,5-dioxide as the "donor" moiety aiming to achieve deep blue TADF.

In addition to the initial expectations, color switching and strong fluorescence intensity enhancement by the factor of more than 60 was observed for the solution of the derivative of bis(phenothiazine-5,5-dioxide) and benzophenone (**CPPD**) in THF under UV irradiation. Despite the similarity of the molecular structure, the derivative of bis (phenothiazine-5,5-dioxide) and diphenylsulfone (**SPPD**) did not show any enhancement of fluorescence under UV irradiation. To explore the phenomenon of fluorescence enhancement under UV irradiation, the derivative of bis(phenothiazine-5,5-dioxide) and benzophenone was exploited for UV sensing with the possibility of UV detection even by naked eye. Since human life is associated with the abundance of UV light, this compound can be of practical interest for UV sensors [16].

Using inorganic or organic semiconductors as the UV sensitive materials, many UV photodetectors and phototransistors have been proposed for UV detection [17–21]. They are based on photocurrent generation under UV excitation with relatively low detection limits of 20–200 μW/cm^2 [17–21]. Electrical-contact-free optical UV sensors have also been proposed. For example, naked-eye dosimetry of UV radiation based on a solid mixture of photoelectrochromic multi-redox polyoxometalate and electron-donating lactic acid was reported [22]. Chemical structure of many molecules, e.g. proton-responsive photochromic molecules, can be changed under UV irradiation with potential for optical UV sensing [23]. The physical structure of some the molecules in the solid state can also vary under UV irradiation. For instance, because of the aggregation induced emission effect, dicyanoacetate-containing hexaphenylbutadiene isomers demonstrate change of emission color and enhancement of emission intensity under UV irradiation due to intramolecular photocyclization reaction [16]. Using hexaphenylbutadiene derivatives, an optical UV sensor with detection limit of 8.2 μW/cm^2 was prepared [16] and allowed naked-eye UV detection. Due to crystallization, asymmetric cyano-stilbene derivatives containing trifluoromethyl substituents in a similar way demonstrated UV-induced turn-on fluorescence [24].

In contrast to the known and above-mentioned examples the conformational structure of the designed in this work derivative of bis (phenothiazine-5,5-dioxide) and benzophenone (**CPPD**) can be changed in its solutions leading to fluorescence enhancement and color switching. Combination of both conformers caused color switching and triplet caused emission intensity enhancement is for first time reported here to the best of our knowledge. The polarity of solvents has strong effect on the processes of UV-induced turn-on fluorescence of the derivative of bis(phenothiazine-5,5-dioxide) and benzophenone. The lowest UV detection limit of less than10 μW/cm^2 was achieved for the toluene solution of the compound.

2. Experimental

2.1. General information

All chemicals and starting materials were commercially available from Sigma-Aldrich and used without further purification unless otherwise stated. All reactions were carried out in open atmosphere unless otherwise indicated. NMR spectra were obtained on a Bruker Avance III spectrometer operating at 400 MHz for ^{1}H and at 100 MHz for ^{13}C analysis. Mass spectra (MS) were recorded using the Waters Acquity UPLC SQD2 mass spectrometer. Elemental analysis was performed with the Exeter Analytical CE440 Elemental Analyzer.

Photophysical properties of the studied compounds were investigated using the Edinburgh Instruments FLS980 and Avantes spectrometers. It should be noted that, under normal PL measurements, compound CPPD undergoes conformational change. Therefore, PL spectra of its solutions were recorded at such conditions at which the compound undergoes minimal conformational change. Thus, fast PL measurements of the solutions were performed due to the small dwelt time of 0.2 s and relatively big step between neighbouring wavelengths using very low intensity of excitation wavelength (λ_{ex} = 330 nm). Phosphorescence spectra were recorded at 77 K applying delay time after excitation of 50 ms. Photoluminescence (PL) decay curves were recorded using the PicoQuant LDH-D-C-375 laser (wavelength 374 nm) as the excitation source.

2.2. UV sensing

The UV sensing response of the solutions to different UV excitation intensities was evaluated recording PL intensities by the *Edinburgh Instruments FLS980* spectrometer. The samples were irradiated using different UV intensities during the same time of 10 min before recording PL spectra. A standard UV lamp was used as the irradiation source (355 nm). UV irradiation intensities [μW/cm^2] were measured by the certificated photodiode PH100-Si-HA-D0 having a sensitive area of 0.707 cm^2 together with the PC-Based Power and Energy Monitor 11S-LINK (from STANDA). The UV-treated solutions were studied and UV detection of **CPPD** was performed using constant and known intensity of UV irradiation (λ_{irr} = 355 nm) from standard UV lamp during constant/known

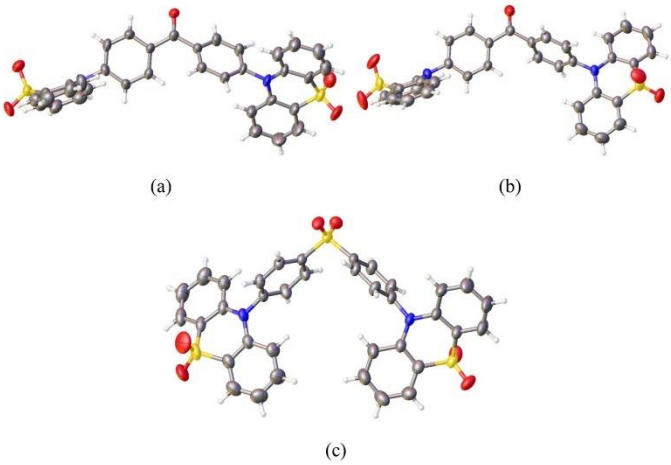

Fig. 1. ORTEP molecular structures of polymorphs of **CPPD** grown from DMF (a), acetone (b) solutions and of **SPPD** (c). Thermal ellipsoids are shown at the 50% probability level.

time.

2.3. Theoretical investigations

The structure of the molecules were initially optimized in the ground singlet electronic state (S_0) at the DFT level using the B3LYP/6-31G(d) method [25–28]. After that the first triplet excited state (T_1) structures were optimized at the same DFT level of theory using the spin unrestricted UB3LYP formalism. The first singlet excited state geometry (S_1) for the studied molecules was calculated at the time-dependent (TD) DFT [29,30] level using the same 6-31G(d) basis set. The solvent effect was accounted for through the polarizable continuum model (PCM) [31]. The calculations of relative energies and vertical spectra for the particular conformers A and B have been accomplished based on the geometries extracted from the single crystal X-ray scattering data. The control geometry optimization calculations with the frozen θ_1 and θ_2 torsion angles have also been carried out to confirm the global and local minimum positions of conformers A and B on the potential energy surface. All vibrational frequencies were found to be real for both isomers, while the relative energies of the two conformers are very closely the same as for those obtained at the X-ray extracted geometries.

3. Result and discussions.

3.1. Synthesis and structure analysis

The compounds were synthesized following a simple two-step protocol of nucleophilic substitution and oxidation with hydrogen peroxide (Scheme 1). The structures of the compounds were confirmed by ^{1}H and ^{13}C NMR, MS and single crystal X-ray diffraction analysis.

X-ray structures **CPPD** and **SPPD** showed favorable geometry for TADF with near-perpendicular torsion angle between the diphenylsulfone or benzophenone and the phenothiazine-5,5-dioxide fragments (Fig. 1). Two different polymorphs were discovered for **CPPD** showing differences in the twist angle of benzophenone phenyl rings as well as a marginally different bending of phenothiazine-5,5-dioxide fragments.

The difference between crystal state polymorphs of CPPD (Fig. 1a, b) will be discussed below in more details, in contents of difference in color and fluorescence wavelength.

3.2. Electron structure and nature of emission in different media

Similar UV absorption spectra with maxima ca. 300, 320 and 328 nm were recorded for compounds **CPPD** and **SPPD**, which can be mainly attributed to the $\pi \rightarrow \pi^*$ transitions of phenothiazine 5,5-dioxide moiety (Fig. 2a). These low-energy absorption bands of **CPPD** and **SPPD** were practically not sensitive to different polarity of the chosen solutions. The additional absorption band (tail) in the range of ca. 340–370 nm was detectable for **CPPD,** which apparently originated from intramolecular charge transfer (ICT) between the phenothiazine-5,5-dioxide and benzophenone units. This presumption is in good agreement with the results of TD DFT calculations of the S_1 state vertical excitation energy and the orbital nature (3.08 eV and 3.27 eV for **CPPD** and **SPPD**, respectively; Fig. 3). Despite that any CT absorption band is practically not seen for compound **SPPD**, emission of both the studied compounds is characterized by ICT It is evident from the bathochromic shifts of their PL spectra in highly polar solvents (Fig. 2b). Due to the different ICT abilities, different Stokes shifts ($\Delta\upsilon = \upsilon_{abs}$-$\upsilon_{em}$) were obtained for the solutions of **CPPD** and **SPPD** in various solvents. For instance, the Stokes shifts of 11,750 and 7761 cm^{-1} were obtained for acetonitrile solutions of **CPPD** and **SPPD,** respectively, which are in qualitative agreement with those obtained by TDDFT calculations (5359 and 4359 cm^{-1}, respectively). As a result, different slopes of the Lippert-Mataga plots with regression parameters of 19,859 and 8895 cm^{-1} were obtained for **CPPD** and **SPPD** respectively, reflecting the differences in the permanent dipole moments of the singlet excited states under photoexcitation (Fig. 2c). Indeed, one can see from Fig. 3 that upon excitation of the molecule of **CPPD** into the S_1 excited state a strong charge separation is induced by charge transfer from one phenothiazine 5,5-dioxide moiety

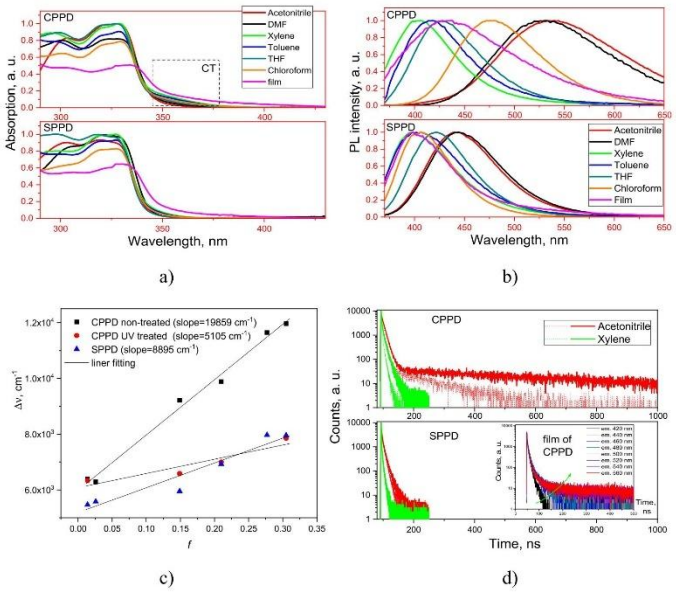

Fig. 2. Absorption (a), PL spectra (λ_{ex} – 330 nm) (b), Lippert-Mataga plots for the Stokes shifts versus solvent polarity function (*f*) dependencies (c) and PL decays (λ_{ex} = 374 nm) (d) of air-equilibrated (dotted lines) and deoxygenated (solid lines) solutions and solid films of **CPPD** and **SPPD**. Inset shows PL decays for the film of **CPPD** recorded at the different emission wavelengths.

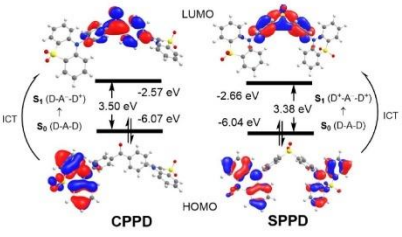

Fig. 3. Energy diagram of the frontier molecular orbitals of **CPPD** and **SPPD**. For both molecules the one-electron excitation from HOMO to LUMO corresponds to the S_1 excited state of ICT nature that is schematically presented in this figure.

to the central benzophenone fragment due to the formation of a strongly polarized bipolar D-A$^-$-D$^+$ structure (Fig. 3). As a result, the permanent dipole moment of molecule **CPPD** increases from 3.1 D in the ground state to 3.8 D in the excited S_1 state. **SPPD** demonstrates less pronounced rise of the permanent dipole moment upon photoexcitation into S_1 state (2.6 D in S_0 ground state *vs.* 3.1 D in S_1 excited state) because tripolar charge separation is induced by the HOMO-LUMO excitation (a less polarized D$^+$-A$^-$-D$^+$ structure is formed, Fig. 3). These theoretical findings are in a good quantitative agreement with the experimental observations. Particularly, the higher slope of the Lippert-Mataga plot for compound **CPPD** indeed demonstrates its stronger ICT character than compound **SPPD.** Owing the strong ICT character, the slope parameter of 19859 cm^{-1} estimated for **CPPD** is among the highest ones even comparing to that of strong donor–acceptor type TADF emitters [32,33].

As shown by the X-ray analysis, the chemical structure of compounds **CPPD** and **SPPD** is susceptible to molecular twisting which may lead to formation of hybridized local charge transfer (HLCT) states upon excitation [34,35]. However, the emission of **CPPD** and **SPPD** cannot be characterized by HLCT since the Lippert-Mataga plots are well-fitted by a single slope in contrast to the two slope fitting of the Lippert-Mataga plots typical for HLCT emitters [36,37].

One can see from Fig. 3 that the torsion angle between the phenyl ring and the phenothiazine-5,5-dioxide fragment plane strongly influences the HOMO expansion. It depends also on the C=O or SO_2 group junction but the torsion angle seems to be the main factor. It determines the spectral properties of the excited states, their charge-transfer character and transitions intensity, as it is shown below. Despite the relatively large singlet–triplet slitting of 0.49 eV observed for THF solution of **CPPD** (Fig. S1), its prompt and delayed fluorescence can be recognized by means of the time-resolved measurements of the air equilibrated and deoxygenated xylene and acetonitrile solutions (Fig. 2d). The long-lived component of fluorescence decay observed for the solution of **CPPD** in highly polar acetonitrile is apparently due to the vibronically induced TADF of **CPPD** [38,39]. This presumption is additionally

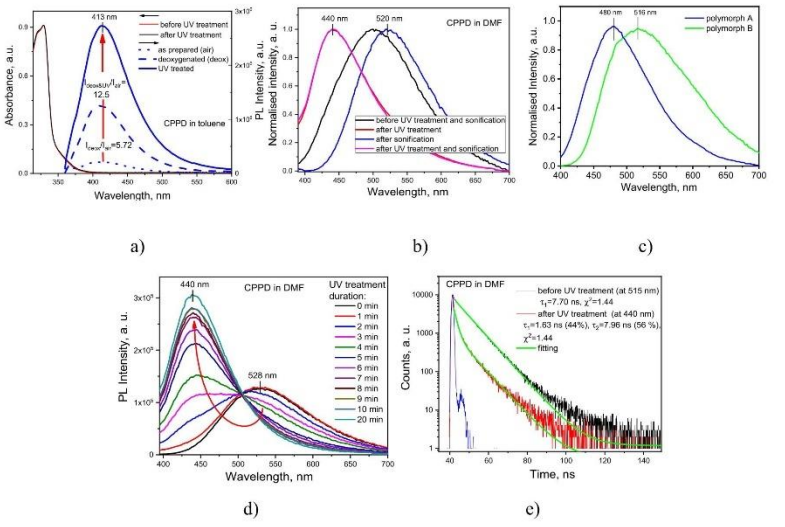

Fig. 4. PL spectra of toluene solution of **CPPD** before and after either deoxygenation or UV treatment (a); PL spectra of DMF solution of **CPPD** before and after either sonification or UV treatment (b). PL spectra of single crystals of polymorphs A and B of **CPPD.** (the single crystals were respectively grown from acetone or DMF) (c). PL spectra of DMF solution of **CPPD** after different times of UV treatment (d) and PL decays of DMF solution of **CPPD** before and after UV treatment (λ_{HT} = 355 nm, λ_{ex} = 330 or 374 nm) (e).

confirmed by the enhancement of fluorescence intensity of toluene solution of **CPPD** after deoxygenation (Fig. 4a). Interestingly, the further enhancement of blue emission intensity was observed for toluene solutions of **CPPD** under continuous UV treatment. This enhancement might be caused by the deeper UV-driven deoxygenation of the solution [40,41]. In case of solutions in more polar solvents than toluene, colour switchable emissions with intensity maxima in the range of ca. 414–440 nm were detected under UV stimulus (Fig. 4b, S2, supporting video). Different mechanisms (e.g. polymorphism, conformer formations, protonation, restriction of H-bonding) may lead to changes of both colour and intensity of emission of organic days [42–45]. To the best of our knowledge, this is the first observation for organic dye of emission phenomenon, named as photostimulated fluorescence. Supporting this statement, the origin and nature of this photostimulated fluorescence are discussed in the next section. In contrast to the PL decay of **CPPD**, the delayed fluorescence was not detected for the solutions of **SPPD** neither in low-polarity xylene nor in highly polar acetonitrile apparently due to the weak ICT transition intensity. Slightly different fluorescence lifetimes were detected for xylene and acetonitrile solutions of **CPPD** and **SPPD** due to the solvatochromic effect. Photostimulated fluorescence was not detected for compound **SPPD** which played a role for the reference compound in the investigations of photostimulated fluorescence phenomenon of **CPPD** (see next section for more details).

The absorption spectra of the films of **CPPD** and **SPPD** were only slightly red-shifted in comparison to the spectra of their solutions showing the same shapes of low-energy bands (Fig. 2a). The films emitted blue light under UV excitation in the range from 300 to 340 nm showing single-band PL spectra with maxima at 432 and 400 nm, respectively (Fig. 2b). In case of the film of **CPPD**, slight differences were detected between its PL spectra recorded under the different wavelengths of UV excitation (Fig. S3). In contrast to the same PL decays recorded at the different emission wavelengths of the **SPPD** film, a clear long-lived component of fluorescence was detected at higher emission wavelengths for the film of **CPPD** (Fig. 2d (inset), Fig. S3). Such difference in the photophysical properties of the CPPD and SPPD films is apparently related to the photostimulated fluorescence of **CPPD**.

Nevertheless, TADF nature of the emission of **CPPD** and **SPPD** is evident from the long-lived PL decays of their powders recorded at the different temperatures and from relatively small singlet–triplet splitting values (ΔE_{ST}) of 0.14 and 0.19 eV, respectively (Fig. S4). Well seen prompt and delayed components of fluorescence decay curves were observed for the powders of **CPPD** and **SPPD** at room temperature (RT) while only prompt fluorescence was detected at 77 K. This observation proves the TADF nature of **CPPD** and **SPPD emission**.

3.3. Mechanism of the photostimulated fluorescence

The photostimulated fluorescence phenomenon of **CPPD** exhibits an overlap of two rather unusual emission effects: (i) switching of emission spectra (colours) from high to low wavelengths under UV stimulus (from green to blue in case of DMF solution, as an example, see Fig. 4b, S2, supporting video); (ii) intensity enhancement of the blue emission under UV stimulus (Fig. 4 a, b, S2). Photoluminescent quantum yields of 6 and 10.5%, respectively were recorded for DMF solution of **CPPD** before (green) and after (blue) additional UV irradiation stimulus. The origin of these effects has to be carefully investigated for proper understanding of the responsible mechanisms in different media. To start with, it should be noted that changes of colour and intensity of fluorescence of **CPPD** solutions under UV treatment are not related to chemical modifications of the molecular structure of **CPPD** (degradation, protonation etc.) since no corresponding differences in ^{1}H NMR spectra of as prepared and UV-treated **CPPD** solutions were not detected (Fig. S5). Thus,

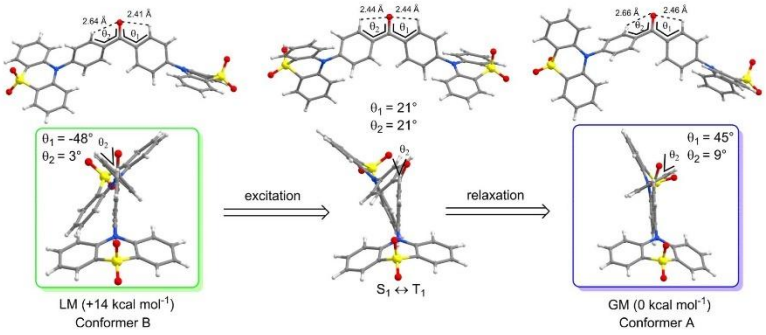

Fig. 5. The proposed mechanism of photostimulated fluorescence through conformational isomerization between local minimum green-emissive (LM) conformer B and global minimum blue-emissive conformer A through the excited S_1 or T_1 state. (For interpretation of the references to color in this figure legend, the reader is referred to the web version of this article.)

conformational differences in molecular structure of **CPPD** in the non-treated and UV-treated **CPPD** solutions most likely can be responsible for the photostimulated fluorescence phenomenon. Indeed, blue and green emission was detected for the different polymorphs, i.e., for A (crystal grown from acetone) and B (crystal grown from DMF) samples of **CPPD**, respectively, having different dihedral angels between phenothiazine 5,5-dioxide and benzophenone units as well as between phenyl rings of benzophenone moieties. Apparently, the first emission effect (switching of emission spectrum colour from the low-energy band to the high-energy band) is related to changes of the molecular conformation of the CPPD polymorphs from one stable conformer to the second stable conformer under additional UV treatment. Notably, it is not related to restriction of H-bonds since sonicated (H-bond-free and aggregation-free) DMF solutions were characterized by even red shifted PL spectrum in comparison to that of fresh (as prepared) DMF solution (Fig. 4b). In addition, switching of the emission spectrum from low- to high-energy region of **CPPD** solutions upon UV-treatment is not related to possible changes between specific quasi axial–quasi axial, quasi equatorial–quasi equatorial and quasi axial–quasi equatorial conformers of phenothiazine 5,5-dioxide moiety since such effect was not observed for the reference compound **SPPD** which contains the same number of phenothiazine 5,5-dioxide units [12]. The photostimulated fluorescence phenomenon of **CPPD** is also reproduced by our quantum-chemical calculations. The energy of the S_1 state estimated for the structure extracted from polymorph A single crystal (crystal grown from acetone) was predicted to be of 3.09 eV by TDDFT calculation, while for the structure extracted from polymorph B single crystal the S_1 state energy is considerably smaller (2.84 eV) in an excellent qualitative agreement with experimental observation (polymorphs A and B demonstrate blue and green photoluminescence, respectively (Fig. 4c)). The reason for that refers not only to the conformational differences between the polymorphs A and B, but also to the more efficient π-delocalization over the benzophenone group in polymorph B that results in a less pronounced bond-length alternation within this fragment. Consequently, the reason lies in the smaller energy of the LUMO orbital, which is highly delocalized over the benzophenone fragments (the calculated LUMO energy is of 2.69 eV for green-emissive polymorph B *vs.* 2.49 eV for blue-emissive polymorph A). At the same time, the bond length alternation is more pronounced within phenothiazine 5,5-dioxide moiety of polymorph B of **CPPD** (relative to polymorph A). Accounting for that, the HOMO orbital is localized exactly over this phenothiazine 5,5-dioxide moiety; the HOMO energy for green-emissive polymorph B (5.92 eV) is a little higher relative to that of blue-emissive polymorph A (6.02 eV). The final difference between HOMO-LUMO gaps for these polymorphs (0.3 eV) well matches with the energy difference between the S_1 states (0.25 eV) meaning that the key role of frontier MOs energy in determining the S_1 state vertical energy. One should stress here, that for both polymorphs of **CPPD** the S_1 state is represented by the HOMO → LUMO single-configuration excitation (Fig. 2).

The second effect. i.e., gradual enhancement of the blue emission band at 440 nm together with the decreasing intensity of green emission band at 528 nm upon continuous irradiation (Fig. 4c), is simply caused by the concentration redistribution between two conformers that correspond to the polymorph A and B species. Indeed, the TD DFT estimated intensity (oscillator strength *f*) of the S_0-S_1 transition for the blue-emitting conformer A is higher comparing to that estimated for the green-emissive conformer B (0.017 *vs.* 0.003, respectively) in agreement with higher intensity of the blue emission relative to the green one. This theoretical finding additionally supports the idea about conformational photo-isomerization of **CPPD** as being the origin of the photostimulated fluorescence phenomenon.

The UV-treated solutions of **CPPD** demonstrate slightly different PL spectra showing solvatochromic shifts with the increase of polarizability index of the solvents used (Fig. 4 a, b, S2). For example, UV-treated toluene solution of **CPPD** was characterized by PL spectrum with the maximum at 413 nm while the spectrum of UV-treated DMF solution of **CPPD** exhibited PL intensity maximum at 440 nm. The similar differences were also observed for PL spectra of the solutions of **CPPD** in other solvents (Fig. S2). As a result, the Lippert-Mataga plot for UV-treated **CPPD** is characterized by a relatively low slope (5105 cm^{-1}) typical for ICT states, but being very high for locally excited (LE) states (Fig. 2c). This observation means that the emission of the UV-treated solutions of **CPPD** is not related to a pure ICT or LE. Indeed, as it can be seen from the shapes of HOMO and LUMO wave functions of **CPPD**, there is a common area of non-zero contribution in the intermediate benzene ring moiety (between C = O group and the phenothiazine 5,5-dioxide moiety). Such an overlap of the HOMO and LUMO wave functions causes quite high transition dipole moment and corresponding oscillator strength of the S_0-S_1 transition, but on the other hand, the common area of HOMO and LUMO is responsible for the considerable S_1-T_1 splitting discussed above (0.49 eV). Thus, to demonstrate the TADF phenomenon discussed above, such energy-separated mixed ICT + LE S_1 and T_1 excited states should be vibronically coupled through the intermediate T_2 state of LE nature in the framework of so-called Gibson-Monkman-Penfold (GMP)

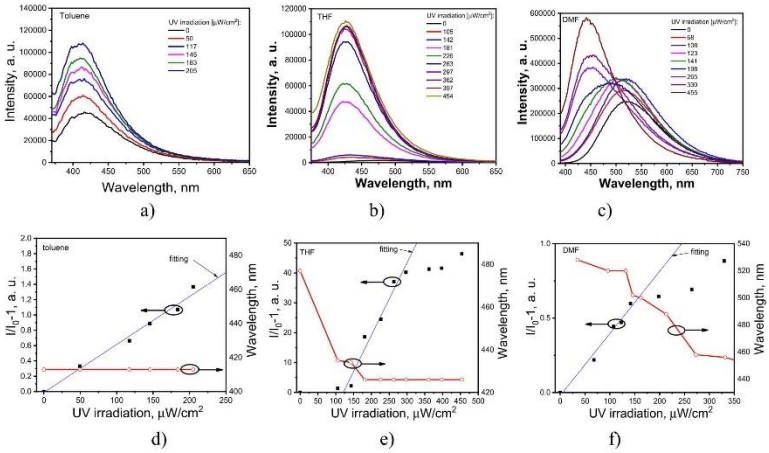

Fig. 6. a) PL spectra (a-c), Stern-Volmer plots and emission wavelength versus UV irradiation intensity plots(d-f) for the solutions of **CPPD** in different solvents (λ_{irr} = 355 nm, λ_{ex} = 330 nm).

mechanism of reverse intersystem crossing (rISC) in TADF emitters through the vibronic coupling effect [38,46].

The rise of T_1 state population and subsequent rISC-mediated delayed fluorescence are responsible for the observed intensity enhancement of the emission of toluene solution of **CPPD** upon the continuous UV stimulus. The facts that the **CPPD** emission in toluene is sensitive to the presence of oxygen (Fig. 4a) and also to the temperature (PL intensity increases with the rise of temperature, Fig. S6) confirm the idea that the photostimulated intensity enhancement is due to the rise of quantity of triplet states and their further crossing to singlets. The similar observation was previously reported for phosphorescence of the phenothiazine 5,5-dioxide derivatives and was attributed to enhanced π–π interactions [39]. It should be additionally noted that powder (which apparently contains mixtures of polymorphs A and B of compound **CPPD**) showed increase of total emission intensity (Fig. S7a) after oxygen evacuation due to the increasing of intensity of its delayed fluorescence (Fig. S7b). In solid state, compound **CPPD** demonstrated well seen delayed fluorescence even in the presence of oxygen apparently because of difficult penetration of oxygen into the crystals (Fig. S7b).

The idea about the conformational isomerization between the green- and blue-emissive forms of **CPPD** molecules as the reason of photostimulated fluorescence phenomenon is to some extent supported by the additional measurements of steady-state emission spectra of the solutions of **CPPD** containing 2,2,6,6-tetramethyl-1-piperidinyloxy free radical (TEMPO) which can inhibit transition to triplet state of **CPPD** upon UV excitation. Indeed, from below PL spectra of DMF and toluene solutions containing TEMPO additives did not show changes upon the UV radiation, which indicates that the photostimulated fluorescence mechanism may proceed via a radical intermediate (triplet state biradical in our case) (Fig. S8). On the other hand, TEMPO can lead to the restriction of the molecular twisting under UV irradiation. Indeed, if one compares the molecular structure **CPPD** extracted from single crystals of polymorphs A and B, one can see that they are different in the mutual inter-rotation of the phenothiazine 5,5-dioxide moiety and the adjacent benzene ring relative to the remaining part of the molecule (θ_2 torsion angle changes in Fig. 5). In the excited S_1/T_1 state of **CPPD** optimized by the DFT approach this rotation is less pronounced (θ_1 and θ_2 are equivalent; θ_2 in the excited S_1/T_1 state has intermediate value between the two conformers), i.e., the excitation into the S_1/T_1 states may induce the conformational isomerization of **CPPD** providing the green-to-blue emission change. Thus, approaching the TEMPO spin label to the long-living T_1 state might really restrict such a conformational isomerization in the excited state and quench the fluorescence, so we can observe only the prompt $S_1 \rightarrow S_0$ fluorescence of **CPPD** without conformational changes.

3.4. UV detection

To demonstrate the potential application of compound **CPPD** as UV sensitive material for optical sensors, the dependence of its emission on UV irradiation intensity was studied in more detail. PL spectra of **CPPD** were recorded at the different excitation power after one-by-one irradiation for 10 min (Fig. 6). PL intensity of toluene solution of **CPPD** gradually increased with increasing intensity of UV irradiation, exhibiting very low detection limit of less than 10 μW/cm^2 (Fig. 6a). Because of the low detection limit, the effect of UV sensitivity of PL of **CPPD** was initially detected under UV excitation during spectroscopic measurements. No color/wavelength changes were observed for the solution of **CPPD** in toluene as it was mentioned in the previous section. The Stern-Volmer plots $I_0/I–1$ versus UV power for fluorescence intensity enhancement of **CPPD** are plotted in Fig. 6d-f. The plot for the toluene solution of **CPPD** could be well linearly fitted (R^2 greater than 0.98) according to the Stern-Volmer relationship $I_0/I–1 = K_{SV}[UV]$ at the different UV irradiation intensities (up to 205 μW/cm^2), where I_0 is PL intensity before UV irradiation, I is PL intensity at the different UV irradiation intensities, and K_{SV} is the Stern-Volmer constant [47]. A K_{SV} value of $6.26 \cdot 10^{-3}$ [μW/cm^2]$^{-1}$ was obtained for the solution of **CPPD** in toluene.

In case of THF and DMF solutions, not only the gradual increase of PL intensity but also the blue shift of emission wavelengths were observed (Fig. 6b, c). As a result, different linear regions can be identified for the

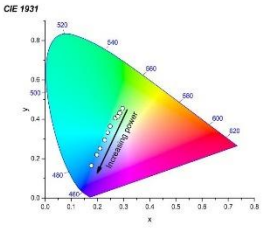

Fig. 7. Dependences of CIE 1931 coordinates of emission on UV irradiation intensities for the DMF solution of **CPPD** (supporting video).

Stern-Volmer plots of THF and DMF solutions of **CPPD**. For example, much higher K_{SV} value of 0.242 $[\mu W/cm^2]^{-1}$ was obtained for TFH solution than for toluene solution when the THF Stern-Volmer plot was fitted ($R^2 > 0.957$) in the range of 150–250 $\mu W/cm^2$ of UV irradiation energies (Fig. 6e). However, the TFH solution of **CPPD** can be used only for UV detection in the specific UV dose range. The lowest K_{SV} of $4.2 \cdot 10^{-3}$ $[\mu W/cm^2]^{-1}$ of DMF solution of **CPPD** was obtained by fitting the Stern-Volmer plot in the range up to150 $\mu W/cm^2$ of UV irradiation energy. Nevertheless, the DMF solution demonstrated the green to blue color switching with the wide range of CIE coordinates from (0.34; 0.44) to (0.17; 0.18) under the different doses of UV irradiation (Fig. 7). Such color change can be observed even by naked eye. The above results demonstrate that compound **CPPD** can be used as an active material for UV sensing. Notably, the solvent selection may provide the different UV sensitivity for specific needs.

4. Conclusions

Motivated by the search for efficient UV active materials, we synthesized two derivatives of phenothiazine-5,5-dioxide and benzophenone or diphenylsulfone following a simple two step protocol of nucleophilic substitution and oxidation with hydrogen peroxide. The solutions in low-polarity solvents and the solid films of the compounds emit deep blue light. The toluene solutions and solid layers are characterized by emission spectra peaking in the range of 400–430 nm. X-ray structures of the compounds show favorable geometry TADF characteristics with near-perpendicular torsion angle between the diphenylsulfone or benzophenone and phenothiazine-5,5-dioxide fragments. In addition to TADF, photostimulated fluorescence was detected for the solutions of the derivative of phenothiazine-5,5-dioxide and benzophenone. More than 40 times increased photoluminescence intensity was observed for THF solutions of this compound after UV irradiation at ca. 300 $\mu W/cm^2$ for 10 min. The experimental as well as the theoretical tools allowed to prove that the photostimulated fluorescence phenomenon is related to conformers with the different stabilization energy minima. The strong UV sensitivity of this compound suggests that it can be applied as UV active material of optical detectors with high Stern-Volmer constant (0.242 $[\mu W/cm^2]^{-1}$ for the THF solution) and green to blue emission color switching (between CIE color coordinates of (0.34; 0.44) and (0.17; 0.18) for the DMF solution).

Declaration of Competing Interest

The authors declare that they have no known competing financial interests or personal relationships that could have appeared to influence the work reported in this paper.

Acknowledgements

This work was supported by the project of scientific co-operation program between Latvia, Lithuania and Taiwan "Polymeric Emitters with Controllable Thermally Activated Delayed Fluorescence for Solution-processable OLEDs" (project has received funding from the Research Council of Lithuania (LMTLT), agreement No. P-LLT-19-14, No. LV-LT-TW/2018/14). G. B. thanks for support to Swedish Research Council (grant No. 2020-04600) and to the Ministry of Education and Science of Ukraine (project no. 0121U107533). The quantum-chemical computations were enabled by resources provided by the Swedish National Infrastructure for Computing (SNIC) at the High-Performance Computing Center North (HPC2N) partially funded by the Swedish Research Council through grant agreement no. 202-3-29.

Appendix A. Supplementary data

Supplementary data to this article can be found online at https://doi.org/10.1016/j.cej.2021.131549.

References

[1] J. Lee, K. Shizu, H. Tanaka, H. Nomura, T. Yasuda, C. Adachi, Oxadiazole- and triazole based highly efficient thermally activated delayed fluorescence emitters for organic light-emitting diodes, J. Mater. Chem. C 1 (30) (2013) 4599, https://doi.org/10.1039/c3tc30699b.

[2] V. N. Nguyen, A. Kumar, M.H. Lee, J. Yoon, Recent advances in biomedical applications of organic fluorescence materials with reduced singlet–triplet energy gaps, Coord. Chem. Rev. 425 (2020) 213545, https://doi.org/10.1016/j.ccr.2020.213545.

[3] M. Luo, X. Li, L. Ding, G. Baryshnikov, S. Shen, M. Zhu, L. Zhou, M. Zhang, J. Lu, H. Ågren, X.-D. Wang, L. Zhu, Integrating time-resolved imaging information by single-luminophore dual thermally activated delayed fluorescence, Angew. Chemie Int. Ed. 59 (39) (2020) 17018–17025, https://doi.org/10.1002/anie.v59.39\10.1002/anie.202009077.

[4] F. Ni, N. Li, L. Zhan, C. Yang, Organic thermally activated delayed fluorescence materials for time resolved luminescence imaging and sensing, Adv. Opt. Mater. 8 (14) (2020) 1902187, https://doi.org/10.1002/adom.v8.1410.1002/adom.201902187.

[5] V. Augusto, C. Baleizão, M.N. Berberan Santos, J.P.S. Farinha, Oxygen proof fluorescence temperature sensing with pristine C70 encapsulated in polymer nanoparticles, J. Mater. Chem. 20 (6) (2010) 1192–1197, https://doi.org/10.1039/B920673F.

[6] A. Steinegger, I. Klimant, S.M. Borisov, Purely organic dyes with thermally activated delayed fluorescence-a versatile class of indicators for optical temperature sensing, Adv. Opt. Mater. 5 (18) (2017) 1700372, https://doi.org/10.1002/adom.201700372.

[7] X. Li, G. Baryshnikov, C. Deng, X. Bao, B. Wu, Y. Zhou, H. Ågren, L. Zhu, A three-dimensional ratiometric sensing strategy on unimolecular fluorescence–thermally activated delayed fluorescence dual emission, Nat. Commun. 10 (2019) 1–9, https://doi.org/10.1038/s41467 019 08684 2.

[8] C.J. Christopherson, D.M. Mayder, J. Poisson, N.R. Paisley, C.M. Tonge, Z. M. Hudson, 1,8 Naphthalimide based polymers exhibiting deep red thermally activated delayed fluorescence and their application in ratiometric temperature sensing, ACS Appl. Mater. Interfaces 12 (17) (2020) 20000–20011, https://doi.org/10.1021/acsami.0c0525710.1021/acsami.0c05257.s001.

[9] C.M. Tonge, N.R. Paisley, A.M. Polgar, K. Lix, W.R. Algar, Z.M. Hudson, Color-tunable thermally activated delayed fluorescence in oxadiazole-based acrylic copolymers: photophysical properties and applications in ratiometric oxygen sensing, ACS Appl. Mater. Interfaces 12 (5) (2020) 6525–6535, https://doi.org/10.1021/acsami.9b2246410.1021/acsami.9b22464.s001.

[10] S.E. Zieger, A. Steinegger, I. Klimant, S.M. Borisov, TADF-emitting Zn(II)-benzoporphyrin: an indicator for simultaneous sensing of oxygen and temperature, ACS Sens. 5 (4) (2020) 1020–1027, https://doi.org/10.1021/acssensors.9b0251210.1021/acssensors.9b02512.s001.

[11] N.R. Paisley, C.M. Tonge, Z.M. Hudson, Stimuli-responsive Thermally Activated Delayed Fluorescence in Polymer Nanoparticles and Thin Films: Applications in Chemical Sensing and Imaging, Front. Chem. 8 (2020), https://doi.org/10.3389/fchem.2020.00229.

[12] M. Okazaki, Y. Takeda, P. Data, P. Pander, H. Higginbotham, A.P. Monkman, S. Minakata, Thermally activated delayed fluorescent phenothiazine–dibenzo[a, j] phenazine–phenothiazine triads exhibiting tricolor-changing mechanochromic luminescence, Chem. Sci. 8 (4) (2017) 2677–2686, https://doi.org/10.1039/C6SC04863C.

[13] Z. Lu, D. Fang, Y. Zheng, Y. Jin, B. Wang, Preparations and photophysical properties of thermally activated delayed fluorescence materials based on N-phenyl-phenothiazine-S,S dioxide, Tetrahedron 73 (1) (2017) 21–29, https://doi.org/10.1016/j.tet.2016.11.037.

[14] S. Xiang, Z. Huang, S. Sun, X. Lv, L. Fan, S. Ye, H. Chen, R. Guo, L. Wang, Highly efficient non-doped OLEDs using aggregation-induced delayed fluorescence materials based on 10-phenyl-10: H -phenothiazine 5,5-dioxide derivatives, J. Mater. Chem. C 6 (42) (2018) 11436–11443, https://doi.org/10.1039/C8TC03648A.
[15] I.H. Lee, J.Y. Lee, Phenothiazine dioxide based high triplet energy host materials for blue phosphorescent organic light-emitting diodes, RSC Adv. 5 (118) (2015) 97903–97909, https://doi.org/10.1039/C5RA19722H.
[16] H. Mao, Y. Li, Y. Zhang, L. Kong, Y. Tian, J. Shi, Z. Cai, B. Tong, Y. Dong, UV-detecting dual-responsive strips based on dicyanoacetate-containing hexaphenylbutadiene with aggregation induced emission characteristic, Dye Pigment. 175 (2020) 108169, https://doi.org/10.1016/j.dyepig.2019.108169.
[17] Z.-D. Zhang, X.u. Gao, Y.-N. Zhong, J. Liu, L.-X. Zhang, S. Wang, J.-L. Xu, S.-D. Wang, Selective solar blind UV monitoring based on organic field effect transistor nonvolatile memories, Adv. Electron. Mater. 3 (8) (2017) 1700052, https://doi.org/10.1002/aelm.201700052.
[18] Y.L. Ning, Z. Zhang, F. Teng, X. Fang, Novel transparent and self-powered UV photodetector based on crossed ZnO nanofiber array homojunction, Small 14 (13) (2018) 1703754, https://doi.org/10.1002/smll.v14.1310.1002/smll.201703754.
[19] H. Chen, P. Yu, Z. Zhang, F. Teng, L. Zheng, K. Hu, X. Fang, Ultrasensitive self-powered solar-blind deep-ultraviolet photodetector based on all-solid-state polyaniline/MgZnO bilayer, Small 12 (42) (2016) 5809–5816, https://doi.org/10.1002/smll.v12.4210.1002/smll.201601913.
[20] T. Y. Huang, C. H. Chen, C. C. Lin, Y. J. Lee, C. L. Liu, G. S. Liou, UV sensing organic phototransistor memory devices with a doped organic polymer electret composed of triphenylamine-based aggregation-induced emission luminogens, J. Mater. Chem. C 7 (35) (2019) 11014–11021, https://doi.org/10.1039/C9TC03607E.
[21] J.-L. Zhang, Y.-X. Nan, H.-G. Li, W.-M. Qiu, X.i. Yang, G. Wu, H.-Z. Chen, M. Wang, A new wide bandgap organic semiconductor and its application in organic UV sensors with tunable response wavelength, Sens. Actuat. B Chem. 162 (1) (2012) 321–326, https://doi.org/10.1016/j.snb.2011.12.088.
[22] W. Zou, A. González, D. Jampaiah, R. Ramanathan, M. Taha, S. Walia, S. Sriram, M. Bhaskaran, J.M. Dominguez-Vera, V. Bansal, Skin color-specific and spectrally-selective naked eye dosimetry of UVA, B and C radiations, Nat. Commun. 9 (2018) 1–10, https://doi.org/10.1038/s41467-018-06273-3.
[23] I.-Y. Hou, F. Berger, A. Narita, K. Müllen, S. Hecht, Proton-gated ring-closure of a negative photochromic azulene based diarylethene, Angew. Chemie Int. Ed. 59 (42) (2020) 18532–18536, https://doi.org/10.1002/anie.v59.4210.1002/anie.202007989.
[24] J.W. Chung, Y. You, H.S. Huh, B. K. An, S. J. Yoon, S.H. Kim, S.W. Lee, S.Y. Park, Shear- and UV induced fluorescence switching in stilbenic π-dimer crystals powered by reversible [2 + 2] cycloaddition, J. Am. Chem. Soc. 131 (23) (2009) 8163–8172, https://doi.org/10.1021/ja900803d.
[25] M.J. Frisch, J.A. Pople, J.S. Binkley, Self-consistent molecular orbital methods 25. Supplementary functions for Gaussian basis sets, J. Chem. Phys. 80 (7) (1984) 3265–3269, https://doi.org/10.1063/1.447079.
[26] R. Ditchfield, W.J. Hehre, J.A. Pople, Self-consistent molecular-orbital methods. IX. An extended gaussian type basis for molecular orbital studies of organic molecules, J. Chem. Phys. 54 (2) (1971) 724–728, https://doi.org/10.1063/1.1674902.
[27] A.D. Becke, Densityâ functional thermochemistry. I. The effect of the exchangeâ only gradient correction, J. Chem. Phys. 96 (1992) 2155–2160. https://doi.org/10.1063/1.462066.
[28] C. Lee, W. Yang, R.G. Parr, Development of the colle salvetti correlation energy formula into a functional of the electron density, Phys. Rev. B 37 (2) (1988) 785–789, https://doi.org/10.1103/PhysRevB.37.785.
[29] C. Adamo, D. Jacquemin, The calculations of excited-state properties with time-dependent density functional theory, Chem. Soc. Rev. 42 (3) (2013) 845–856, https://doi.org/10.1039/C2CS35394F.
[30] G. Scalmani, M.J. Frisch, B. Mennucci, J. Tomasi, R. Cammi, V. Barone, Geometries and properties of excited states in the gas phase and in solution: theory and application of a time-dependent density functional theory polarizable continuum model, J. Chem. Phys. 124 (9) (2006) 094107, https://doi.org/10.1063/1.2173258.
[31] J. Tomasi, B. Mennucci, R. Cammi, Quantum Mechanical Continuum Solvation Models, (2005). https://doi.org/10.1021/cr9904009.
[32] G. Grybauskaite Kaminskiene, D. Volyniuk, V. Mimaite, O. Bezvikonnyi, A. Bucinskas, G. Bagdziunas, J.V. Grazulevicius, Aggregation-enhanced emission and thermally activated delayed fluorescence of derivatives of 9-Phenyl-9 *H* -carbazole: effects of methoxy and *tert* -Butyl Substituents, Chem. – A Eur. J. 24 (38) (2018) 9581–9591, https://doi.org/10.1002/chem.v24.3810.1002/chem.201800822.
[33] B. Huang, Q. Qi, W. Jiang, J. Tang, Y. Liu, W. Fan, Z. Yin, F. Shi, X. Ban, H. Xu, Y. Sun, Thermally activated delayed fluorescence materials based on 3,6-di-tert-butyl-9-((phenylsulfonyl)phenyl)-9H-carbazoles, Dye Pigm. 111 (2014) 135–144, https://doi.org/10.1016/j.dyepig.2014.06.008.
[34] W. Li, Y. Pan, L. Yao, H. Liu, S. Zhang, C. Wang, F. Shen, P. Lu, B. Yang, Y. Ma, A hybridized local and charge-transfer excited state for highly efficient fluorescent OLEDs: molecular design, spectral character, and full exciton utilization, Adv. Opt. Mater. 2 (9) (2014) 892–901, https://doi.org/10.1002/adom.201400154.
[35] Z.R. Grabowski, K. Rotkiewicz, W. Rettig, Structural Changes Accompanying Intramolecular Electron Transfer: Focus on Twisted Intramolecular Charge-Transfer States and Structures, (2003). https://doi.org/10.1021/cr940745l.
[36] R. Kumar Konidena, K.R.J. Thomas, D.K. Dubey, S. Sahoo, J. H. Jou, A new molecular design based on hybridized local and charge transfer fluorescence for highly efficient (46%) deep-blue organic light emitting diodes † ChemComm, 11802 |, Chem. Commun. 53 (2017) 43, https://doi.org/10.1039/c7cc07139f.
[37] S. Zhang, L. Yao, Q. Peng, W. Li, Y. Pan, R. Xiao, Y.u. Gao, C. Gu, Z. Wang, P. Lu, F. Li, S. Su, B. Yang, Y. Ma, Achieving a significantly increased efficiency in nondoped pure blue fluorescent OLED: a quasi-equivalent hybridized excited state, Adv. Funct. Mater. 25 (11) (2015) 1755–1762, https://doi.org/10.1002/adfm.201404260.
[38] M.K. Etherington, J. Gibson, H.F. Higginbotham, T.J. Penfold, A.P. Monkman, Revealing the spin–vibronic coupling mechanism of thermally activated delayed fluorescence, Nat. Commun. 7 (2016) 13680, https://doi.org/10.1038/ncomms13680.
[39] J. Yang, X. Zhen, B. Wang, X. Gao, Z. Ren, J. Wang, Y. Xie, J. Li, Q. Peng, K. Pu, Z. Li, The influence of the molecular packing on the room temperature phosphorescence of purely organic luminogens, Nat. Commun. 9 (2018) 1–10, https://doi.org/10.1038/s41467-018-03236-6.
[40] S. Wan, W. Lu, Reversible Photoactivated phosphorescence of gold(I) arylethynyl complexes in aerated DMSO solutions and gels, Angew. Chemie Int. Ed. 56 (7) (2017) 1784–1788, https://doi.org/10.1002/anie.201610762.
[41] M. Gmelch, H. Thomas, F. Fries, S. Reincke, Programmable transparent organic luminescent tags, Sci. Adv. 5 (2) (2019) eaau7310, https://doi.org/10.1126/sciadv.aau7310.
[42] D. Liu, Z. Zhang, H. Zhang, Y. Wang, A novel approach towards white photoluminescence and electroluminescence by controlled protonation of a blue fluorophore, Chem. Commun. 49 (2013) 10001–10003, https://doi.org/10.1039/c3cc45991h.
[43] P. Data, M. Okazaki, S. Minakata, Y. Takeda, Thermally activated delayed fluorescence vs room temperature phosphorescence by conformation control of organic single molecules, J. Mater. Chem. C 7 (22) (2019) 6616–6621, https://doi.org/10.1039/C9TC00909D.
[44] I. Hladka, D. Volyniuk, O. Bezvikonnyi, V. Kinzhybalo, T.J. Bednarchuk, Y. Danyliv, R. Lytvyn, A. Lazauskas, J.V. Grazulevicius, Polymorphism of derivatives of tert -butyl substituted acridan and perfluorobiphenyl as sky blue OLED emitters exhibiting aggregation induced thermally activated delayed fluorescence, J. Mater. Chem. C 6 (48) (2018) 13179–13189, https://doi.org/10.1039/C8TC04867C.
[45] N.A. Kukhta, D.A. da Silva Filho, D. Volyniuk, J.V. Grazulevicius, G. Sini, Can fluorenone-based compounds emit in the blue region? Impact of the conjugation length and the ground-state aggregation, Chem. Mater. 29 (4) (2017) 1695–1707, https://doi.org/10.1021/acs.chemmater.6b05158.10.1021/acs.chemmater.6b05158.s001.
[46] J. Gibson, A.P. Monkman, T.J. Penfold, The importance of vibronic coupling for efficient reverse intersystem crossing in thermally activated delayed fluorescence molecules, ChemPhysChem 17 (19) (2016) 2956–2961, https://doi.org/10.1002/cphc.201600662.
[47] E.R. Carraway, J.N. Demas, B.A. DeGraff, J.R. Bacon, Photophysics and photochemistry of oxygen sensors based on luminescent transition metal complexes, Anal. Chem. 63 (4) (1991) 337–342, https://doi.org/10.1021/ac00004a007.

Journal of Materials Chemistry C

ROYAL SOCIETY OF CHEMISTRY

PAPER

View Article Online
View Journal | View Issue

Cite this: J. Mater. Chem. C, 2022, 10, 12377

Acridone and quinacridone derivatives with carbazole or phenoxazine substituents: synthesis, electrochemistry, photophysics and application as TADF electroluminophores†

Irena Kulszewicz-Bajer, *[a] Matas Guzauskas,[b] Małgorzata Makowska-Janusik,[c] Małgorzata Zagórska, [a] Malek Mahmoudi,[b] Juozas V. Grazulevicius, [b] Adam Proń *[a] and Dmytro Volyniuk *[b]

Six acridone (quinacridone) derivatives containing either carbazole or phenoxazine substituents were designed and synthesized with the aim of elucidating the effect of the donor (D) and acceptor (A) linking pattern (D–A, D–A–D or D–π–A–π–D) on their photophysical and electrochemical properties. These new electroactive compounds combine reversible electrochemical oxidation with excellent luminescent properties. Their electrochemically determined ionization potentials (IPs) are in the range from 5.09 eV to 5.45 eV, higher for derivatives with carbazole donors as compared to phenoxazine ones. The measured electron affinities (EAs) are in the range from −2.53 eV to −2.64 eV with the exception of the quinacridone derivative showing EA of −3.03 eV. Their vacuum-deposited films emit radiation in a wide spectral range from sky-blue to red. Compounds with carbazole moieties (compounds **1**, **2** and **6** in the subsequent text) showed prompt fluorescence and aggregation-caused quenching. Photoluminescent quantum yields (PLQYs) of their toluene solutions reached values up to 69%. Compounds containing phenoxazine moieties (compounds marked as **3–5**) demonstrated thermally activated delayed fluorescence (TADF) and aggregation-induced emission enhancement (AIEE). Their neat films showed PLQYs of 35%. Quinacridone disubstituted with carbazole (compound **6**) showed the highest hole mobility reaching 2.53×10^{-3} cm^2 V^{-1} s^{-1} at electric field of 3.6×10^5 V cm^{-1}. Carbazolyl disubstituted acridone (compound **2**) and phenoxazinyl monosubstituted acridone (compound **3**) turned out to be ambipolar compounds showing reasonably balanced electron and hole mobilities. The appropriate combination of redox, transport and luminescent properties makes the studied compounds suitable candidates for optoelectronic applications. Test OLEDs fabricated from **3** exhibited maximum external quantum efficiencies reaching 16.7%. Finally, an excellent agreement between the experimental results and those obtained by DFT calculations should be stressed. The basics for selection according to the user needs of either D–A, D–A–D or D–π–A–π–D types of molecular structures of TADF/AIEE luminophores are provided in this study.

Received 31st May 2022,
Accepted 5th August 2022

DOI: 10.1039/d2tc02270b

rsc.li/materials-c

1. Introduction

Acridone and quinacridone have been known and studied for decades. Acridone has been used as a building block in the synthesis of a variety of compounds known for their pharmacological activity.[1–4] Quinacridone, in turn, is an industrial pigment.[5] However, strong revival in the chemistry of these two compounds has been observed in the past decade. A plethora of low and high molecular mass compounds containing acridone or quinacridone units were synthesized, exhibiting peculiar electronic, optoelectronic or electrochromic properties, frequently unmatched by other groups of electroactive organic compounds. Acridone- or quinacridone-based donor–acceptor copolymers and terpolymers were used as components of photovoltaic cells[6–9] and photodetectors.[10,11] D–A compounds with acridone or quinacridone acceptors were examined as components of active layers in organic field effect

[a] Faculty of Chemistry, Warsaw University of Technology, Noakowskiego 3, 00-664 Warsaw, Poland. E-mail: ikulsz@ch.pw.edu.pl
[b] Department of Polymer Chemistry and Technology, Kaunas University of Technology, Barsausko 59, LT-51423, Kaunas, Lithuania. E-mail: dmytro.volyniuk@ktu.lt
[c] Faculty of Science and Technology, Jan Dlugosz University, Al. Armii Krajowej 13/15, 42-200 Częstochowa, Poland

† Electronic supplementary information (ESI) available. See DOI: https://doi.org/10.1039/d2tc02270b

transistors (OFETs) due to their excellent electrical transport properties.[12] Several acridone and quinacridone derivatives were found to exhibit interesting electrochemistry[13–15] including electrochromism.[16] Appropriately functionalized quinacridones were also tested as photocatalysts[17,18] and materials for non-linear optical applications.[19] However, the capability of generating the thermally activated delayed photoluminescence (TADF), reported for some acridone and quinacridone derivatives, seems to be the most interesting feature of these compounds,[20–22] leading to their applications as components of organic light emitting diodes (OLEDs), characterized by high external quantum efficiencies.[23,24]

Phenoxazine units are, in turn, widely used as building blocks in various organic electroactive materials such as components of dye-sensitized solar cells[25] or hole transporting materials in perovskite solar cells.[26] However, as in the case of acridone and quinacridone derivatives, their most interesting property is the TADF effect, frequently observed in molecules containing phenoxazine donors.[27–32] Similarly carbazole is a popular donor in organic molecules and macromolecules for photovoltaics[33,34] and electroluminescence.[35–37] Thus, phenoxazine or carbazole units in combination with acridone (quinacridone) seem especially interesting as building blocks of various types luminescent and electroactive molecules. For this reason, we undertook a combined theoretical and experimental study devoted to the design, synthesis and characterization of five acridone and one quinacridone donor–acceptor derivatives with two types of donors, namely phenoxazine and carbazole of possible use in optoelectronics. Quantum chemical calculations are especially important in this respect because they play a predictive role, demonstrating that appropriate combination of donors (carbazole, phenoxazine) and acceptors (acridone, quinacridone) may result in the elaboration of new electroactive and luminescent compounds of controllable redox properties, *i.e.* characterized by appropriate ionization potential (IP) and electron affinity (EA). These parameters together with electrical transport properties are of crucial importance for any electronic or optoelectronic application. Thus, experimental investigations involved detailed electrochemical characterization of the synthesized compounds with the goal to confront theoretical IP and EA values with the experimental ones as well as to elucidate their photophysical properties. The studied compounds showed good charge injecting properties with relatively low ionization potentials and high electron affinities and efficient charge transport (hole-only or bipolar). The latter unequivocally indicated that all studied luminophores exhibited either thermally activated delayed fluorescence (TADF) (so-called E-type delayed fluorescence) or aggregation-induced emission enhancement (AIEE). The emission was very sensitive to molecular structure and media. Emission colour of their vacuum-deposited films could be tuned over a wide spectral range from sky-blue to red. They have the potential for application in non-doped and doped OLEDs. 2-Phenoxazine-*N*-hexylacridone (indicated as compound **3** in the subsequent text) deserves a special emphasis since test light emitted diodes (OLEDs) with active layers consisting of **3** molecularly dispersed in 1,3-bis(*N*-carbazolyl) benzene (mCP) or 2,4,6-tris[3-(diphenylphosphinyl)phenyl]-1,3,5-triazines (PO-T2T) exhibited maximum EQEs of 13 and 16.7%, respectively. The study provides basics for the selection of either D–A, D–A–D or D–π–A–π–D types of TADF molecules according to the user needs.

2. Experimental section

Detailed description of the synthesis of new luminophores and techniques used for their characterization can be found in the ESI.† This involves:

- Description of all reagents and procedures used in the preparation of the studied compounds together with spectroscopic (NMR, IR) data of intermediate and final products as well as their elemental analyses;
- Description of cyclic voltammetry (CV) experiments;
- Optical measurements, charge carriers mobility, OLEDs fabrication and characterization.
- Methodology of quantum chemical calculations.

3. Results and discussion

3.1. Synthesis

The synthetic pathways leading to the studied compounds, namely 2-(3,6-*tert*-butylcarbazole)-*N*-hexylacridone, **1**; 2,7-bis(3,6-*tert*-butylcarbazole)-*N*-hexylacridone, **2**; 2-phenoxazine-*N*-hexylacridone, **3**; 2,7-bis-phenoxazine-*N*-hexylacridone, **4**; 2,7-bis[3-((phenoxazine)phenyl)-*N*-hexylacridone], **5**; 2,9-bis(3,6-*tert*-butylcarbazole)-*N*,*N*′-dioctylquinacridone, **6** is presented in Scheme 1.

In the applied procedures *N*-hexylacridone or *N*,*N*-dioctylquinacridone were brominated using bromine in acetic acid/sodium acetate medium as a bromination agent. The obtained bromoderivatives were then reacted with 3,6-di-*tert*-butylcarbazole in the presence of CuI/*trans*-1,2-cyclohexanediamine catalyst leading to: (i) compound **1** with (97% yield); (ii) compound **2** (64% yield) and (iii) compound **6** (61% yield). It should be noticed that the use of this catalyst results in a significant decrease of the reaction temperature with concomitant increase of the reaction yield as compared to commonly used procedures.[23,38,39] Compounds **3**, **4** were synthesized *via* Buchwald–Hartwig amination coupling of acridone bromoderivatives and phenoxazine using $Pddba_2$/*t*-Bu_3P as a catalyst. The target products were obtained in high yields: 92% in the case of **3** and 82% in the case of **4**. Compound **5** was synthesized in a three-step procedure.

In the first step **5a** was prepared from phenoxazine and 1-bromo-3-iodobenzene (95% yield), then, in the second step it was transformed into a Suzuki coupling reagent, namely 3-phenoxazine-1-phenylboronic acid pinacol ester **5b** (78% yield). The target product **5** was obtained by Suzuki coupling between **5b** and 2,7-dibromo-*N*-hexylacridone (67% yield).

3 and **4** were reported in ref. 40 whereas **1**, **2**, **5** and **6** are new. Detailed descriptions of all synthetic procedures together

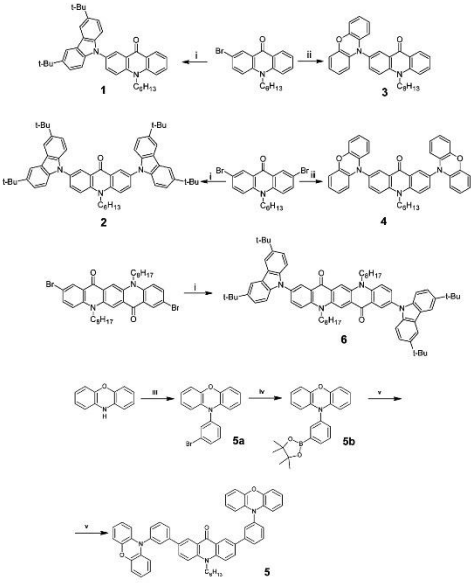

Scheme 1 Synthesis of acridone (**1–4**) and quinacridone (**6**) derivatives: (i) 3,6-di-*tert*-butylcarbazole, CuI, *trans*-1,2-cyclohexanediamine, K_3PO_4, dioxane, 110 °C; (ii) phenoxazine, $Pd(dba)_2$, *t*-Bu_3P, *t*-BuONa, toluene, 90 °C. Synthetic pathway to **5**: (iii) 1-bromo-3-iodobenzene, $Pd_2(dba)_3$, Xantphos, *t*-BuONa, toluene, 80 °C; (iv) *n*-BuLi, 2-isopropoxy-4,4,5,5-tetramethyl-1,3,2-dioxaborolane, THF, −78 °C; (v) 2,7-dibromo-*N*-hexylacridone, $Pd(PPh_3)_4$, 2 M K_2CO_3, toluene, dioxane.

with full spectroscopic characterization of the products as well as their elemental analyses can be found in ESI.†

3.2. Redox properties, ionization potentials (IP_s) and electron affinities (EA_s)

Redox properties of electroactive molecules are of crucial importance because on their basis electron affinities (EA_s) and ionization potentials (IP_s) can be determined which are predictive parameters for essentially all electronic and opto-electronic applications.

In Fig. 1a, a representative cyclic voltammogram (CV) of acridone monosubstituted with carbazole, **1**, is presented. The corresponding differential pulse voltammogram (DPV) are given in ESI† (Fig. S1). In general, carbazole moieties undergo reversible oxidation to a radical cation. This can be followed by consecutive irreversible oxidation processes possibly involving oligomerization or polymerization if appropriate coupling positions in the carbazole aromatic rings are available.[41] Cyclic voltammogram of **1** reveals however two oxidation processes of reversible and quasi-reversible nature at $E^0_{ox1} = 0.653$ V and $E^0_{ox2} = 1.132$ V, which essentially excludes dimerization or oligomerization. This is not unexpected since the most probable coupling sites in **1** are blocked by bulky *tert*-butyl groups. Thus, the first peak can be attributed to the oxidation of the carbazole substituent to a radical cation,[38] whereas the second one to the oxidation of the acridone unit. Unsubstituted acridone undergoes quasi-reversible oxidation at 1.020 V.[40] Its shift in **1** to a potential which is higher by 0.112 V is a consequence of the fact that the removal of an additional electron from **1** in its radical cation form is more difficult than the abstraction of the first electron from neutral acridone. The reduction of **1** is essentially irreversible and occurs at relatively low potentials, with a maximum of the cathodic peak at −2.399 V *vs.* Fc/Fc^+.

2 contains two carbazole substituents symmetrically connected to the acridone central unit, thus it can be considered as a D–A–D molecule. Consecutive oxidations of two carbazole groups occur at potentials $E^0_{ox1} = 0.639$ V and $E^0_{ox2} = 0.804$ V (Fig. 1b). Note that the first oxidation potential is very similar to that registered for the oxidation of **1**. An increase of the oxidation potential of the second carbazole unit may indicate some delocalization of the radical cation charge through the

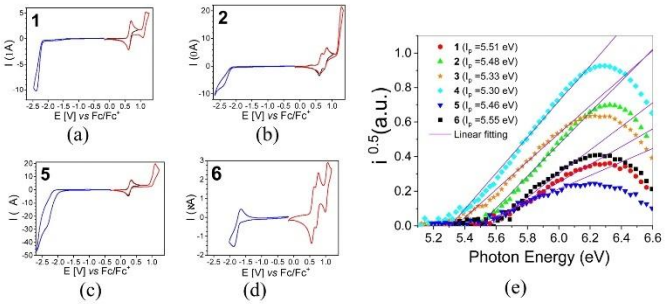

Fig. 1 Cyclic voltammograms registered for **1** (a), **2** (b), **5** (c) and **6** (d). Electrolyte: 0.1 M Bu_4NBF_4/CH_2Cl_2, scan rate: 50 mV s^{-1}. Photoelectron emission spectra of vacuum-deposited thin layers of **1–6** (e).

whole molecule making the abstraction of the second electron more difficult. Further oxidation of this dication requires polarization to relatively high potentials. As a result the central acridone unit is being irreversibly oxidized as evidenced by an anodic peak with a maximum at E = 1.297 V *i.e.* at a potential significantly higher than those of the oxidation of neutral acridone and the oxidation of the radical cation form of **1**. Irreversible reduction of **2** starts at a low potential of −2.22 V, yielding a cathodic peak without a clear maximum. **2**, *i.e.* 2,7-bis(3,6-*tert*-butylcarbazole)-*N*-hexylacridone is slightly easier to oxidize than its unsubstituted analogue (2,7-di(carbazole-9-yl)-*N*-hexylacridone), whose redox properties are reported in ref. 42. It can be rationalized by weak electrodonating properties of *tert*-butyl substituents in this compound. **2** is however more resistant to oxidation than diphenylamino- and dinaphthylamino-substituted alkylacridones, whose oxidation starts at potentials lower by 0.42 V.[42] Higher resistance against oxidation of acridones with carbazole substituents makes these compounds more suitable for applications in electronic devices operating in ambient conditions.

6 differs from **2** by its central acceptor unit (quinacridone *vs.* acridone). Following the same reasoning as in the case of **2**, we can attribute the first two reversible oxidation processes at potentials $E^0_{ox1} = 0.600$ V and $E^0_{ox2} = 0.729$ V to consecutive oxidations of carbazole substituents (see Fig. 1d). It should be noted that the oxidation of carbazole units in **6** occurs at lower potentials and in narrower potential range as compared to **2**. This reflects the effect of central acceptor unit which in the case of **6** is more extended and better delocalizes the charge of the radical cation formed in the first oxidation step. The third anodic peak in the cyclic voltammogram of **6** corresponds to reversible oxidation of the quinacridone central unit at E^0_{ox3} = 1.026 V, a value which is by *ca.* 0.4 V higher than the potential of the oxidation of neutral quinacridone.[43] Note that the reduction potential of **6** (−1.938 V) is higher than those of **1** and **2**, consistent with easier reducibility of quinacridone[43] as compared to acridone.[40]

Electrochemical data of **3** and **4** are reported in our previous paper.[40] In general, phenoxazine derivatives of acridone are easier to oxidize than the corresponding carbazole derivatives but their reduction potential is similar. Both phenoxazine substituents in **5** undergo reversible oxidation at the same potential of E^0 = 0.293 V, followed by irreversible oxidation of the acridone central unit at E = 1.097 V (Fig. 1c). Reduction of the acridone unit in **5** starts at −2.23 V, yielding a cathodic peak without a clear maximum, as in the case of **2** (compare Fig. 1b and c).

For the calculations of IP and EA of **1–6** from the electrochemical data we have taken the potentials of the onsets of the first oxidation and first reduction peaks. They are listed in Table 1. As seen from these data, **1–5** exhibit similar and low reduction potential and, by consequence, low electron affinities (EA) in the range 2.50–2.65 eV. The only exception is **6** containing significantly more extended quinacridone core. Its reduction potential is by *ca.* 400–500 mV higher as compared to **1–5** leading to |EA| exceeding 3 eV.

The studied derivatives differ, however, in the onsets of their oxidation potentials. Phenoxazine-functionalized acridones (**3–5**) exhibit $E_{ox1onset}$ values lower by 300–320 mV as compared to carbazole-substituted ones (**1**, **2** and **6**). Consequently, their IP_s are lower, only barely exceeding 5.0 eV (see Table 1).

Table 1 Redox potentials, electron affinities (EA_{el}) and ionization potentials (IP_{el}) determined electrochemically and ionization potentials (IP_{UPS}) derived from UPS

Compound	$E_{red,onset}$[a] [V]	$E_{ox,onset}$[a] [V]	EA_{el}[b] [eV]	IP_{el}[c] [eV]	IP_{UPS}[d] [eV]
1	−2.27	0.651	−2.53	5.45	5.51
2	−2.22	0.637	−2.58	5.44	5.48
3	−2.23	0.317	−2.57	5.12	5.33
4	−2.16	0.332	−2.64	5.13	5.3
5	−2.23	0.294	−2.57	5.09	5.46
6	−1.77	0.600	−3.03	5.40	5.55

[a] Potential *vs.* Fc/Fc^+. [b] Calculated according to equation: EA = $e(E_{red,onset} + 4.8)$ [eV]. [c] Calculated according to equation: IP = $-e(E_{ox,onset} + 4.8)$ [eV]. [d] Measured by photoelectron spectroscopy in air (Fig. 1e).

Finally, it is instructive to verify whether a correlation exists between IP values derived from the electrochemical data (IP_{el}) and those obtained by photoelectron spectroscopy (IP_{UPS}). The photoelectron emission spectra registered for **1–6** are shown in Fig. 1e whereas IP_{UPS} values, calculated on their basis, are collected in Table 1.

It should be stressed that in both cases different physical quantities are measured. IP_{el}, determined for compounds dissolved in an nonaqueous solvent, corresponds to the ionization energy which is modified by electrostatic interactions between the ionized molecule and its polarizable environment (P_{sol}). In the case of IP_{UPS}, the measurements are carried out for surfacial molecules in a thin solid film. In this case the ionized molecule interacts with the solid polarizable environment (P_c), and the polarization energy again modifies the ionization energy. IP_{UPS} values are higher than the IP_{el} ones but the observed values for phenoxazine derivatives are systematically lower than those measured for carbazole ones (Table 1). It should also be noted that the difference between IP_{el} and IP_{UPS} is slightly more pronounced in the case of phenoxazine derivatives. This is not unexpected since P_{sol} and P_c energies usually are not equal, which inevitably leads to differences in the IP values determined by CV and UPS. However, in a series of papers Sworakowski *et al.*[44–46] demonstrated that a clear correlation can be found between the measured redox potentials (and by consequence IP_{el}) and IP_{UPS} for a large number of organic semiconductors of low molecular and high molecular nature.

3.3. Photophysical properties

Absorption spectra of **1–6** are characterized by bands attributable to their D and A segments *i.e.* acridone (Acr) and *tert*-butylcarbazole (*t*Cz) for **1** and **2**, acridone (Acr) and phenoxazine (PhNZ) for **3–5** and quinacridone (QAcr) and *t*Cz in the case of **6**. This can be clearly deduced from Fig. 2a and b where the spectra of toluene solutions of **1–6** are presented together with those registered for Acr, QAcr, PhNZ and *t*Cz dissolved in the same solvent. Bands characteristic of the D and A moieties are marked by thin vertical lines: at 389 nm for Acr, at 290 nm ($\pi \rightarrow \pi^*$) and 307–335 nm ($n \rightarrow \pi^*$) for *t*Cz; at 313 nm for PhNZ and at 290 and 504 nm for QAcr. Slight red-shifts and broadening of these bands are observed in the spectra of all studied compounds (**1–6**), especially in the low-energy regions. This observation can apparently be explained by the formation of intramolecular charge transfer (ICT) states due to interactions

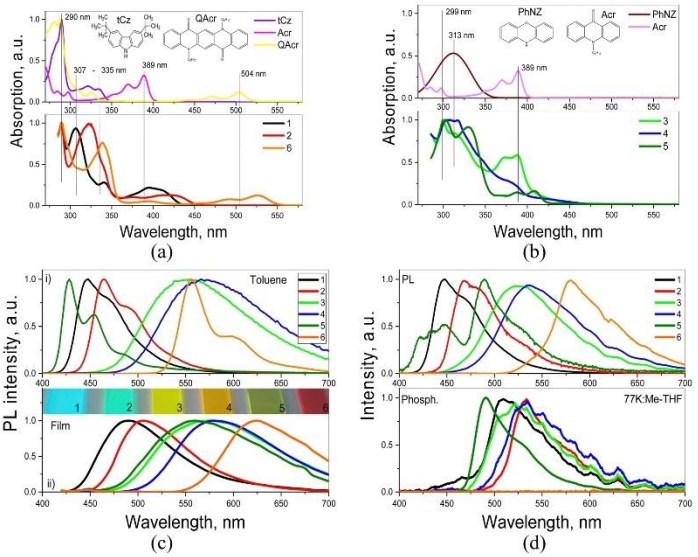

Fig. 2 Absorption spectra (a and b) of toluene solutions of **1–6**, together with the spectra of *t*Cz, QAcr, PhNZ, Acr shown for comparison; photoluminescence (PL) spectra (c) of **1–6** dissolved in toluene and their vacuum-deposited films; and PL and phosphorescence (Phosph.) spectra (d) of **1–6** dissolved in Me-THF, recorded at 77 K. The delay time of 1 ms after excitation was used recording phosphorescence spectra. The excitation wavelength of 330 nm was used. Inset of (c) shows photos of vacuum-deposited films under UV excitation.

between the electron-donating and electron-accepting moieties. These issues are discussed in greater detail in the next subsection (Quantum chemical calculations).

Absorption spectra of solid thin films of **1–6** are similar to those of the corresponding toluene solutions (Fig. S2a, ESI†). However, they are characterized by even larger broadening. Two origins of these effects can be proposed either aggregation or stronger ICT. The latter seems more plausible, taking into account the ICT-induced shapes (non-structured) of the corresponding PL spectra of all studied compounds (Fig. 2c). In contrast, specific features of PL spectra of toluene solutions of **1**, **2** and **5**, **6** originate from recombination of the locally excited (LE) states formed mainly by electron-accepting moieties (acridone or quinacridone). **3** and **4** demonstrate ICT-shaped, PL spectra both in toluene solutions and in the solid-state, which is apparently caused by strong D–A interactions. These problems are also additionally discussed in the subsection Quantum chemical calculation. PL decays (typically few nanoseconds) registered for toluene solutions of **1–6** are presented in Fig. S2b (ESI†).

In the PL spectrum of 10% molecular dispersion of **5** in 1,3-bis(*N*-carbazolyl)benzene (mCP) two bands are observed at 452 and 525 nm, resulting from recombination of LE and ICT states respectively (see Fig. 3 and Table 2). In the case of the dispersions of the remaining compounds (**1–4**, **6**) only one band can be distinguished. In all cases the PL spectra of molecular dispersions in the host of low polarity (dielectric constant of mCP = 2.84)[47] undergo a hypsochromic shift as compared to the corresponding spectra of thin films of neat compounds (compare Fig. 2c and 3a). This trend additionally proves the predominance of ICT character of the excited states in solid films of **1–6**. Time-resolved spectroscopic studies show long-lived emission of molecular dispersions of compounds **3–5** in mCP under vacuum conditions (see Fig. 3b). The attribution of this long-lived emission to fluorescence is supported by the absence of visible changes in the shape of PL spectra before and after evacuation (Fig. 3c). Evacuation-induced increase of the intensity of PL spectra of solutions and molecular dispersions of **3–5** strongly indicates the triplet origin of that delayed fluorescence (Fig. 3c and d). As previously demonstrated in ref. 48, the long-lived fluorescence of **3** and **4** is TADF in nature. This supposition is in a very good agreement with the observed small singlet–triplet splitting, in the studied compounds, as derived from the high energy onsets of their fluorescence and phosphorescence spectra (Fig. 2d and Table 2).

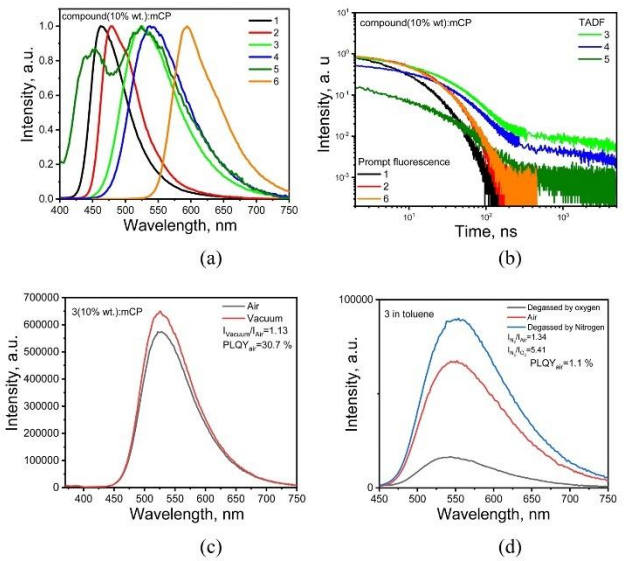

Fig. 3 Normalized PL spectra of molecular dispersions (10 wt% in mCP) of compounds **1–6** (a); PL decays of these dispersions (b); normalized PL spectra of the dispersion of compound **3** (10 wt% in mCP) in air and under vacuum (c); PL spectra of toluene solutions of compound **3**: as prepared (in air), after deoxygenation and reoxygenation (d).

Table 2 Photophysical parameters including singlet and triplet energies of compounds **1–6**

Compound	$\lambda_{MAX}^{tol.}$, nm	λ_{MAX}^{solid}, nm	λ_{MAX}^{solid}, nm	PLQY, %	E_{S_1}, eV	E_{T_1}, eV	ΔE_{ST}
Media	Tol.	Film of neat comp.	Mol. disp. in mCP	Tol./mol. disp. in mCP	Me-THF at 77 K		
1	448, 469	490	462	69/66	2.92	2.58	0.34
2	464, 490[a]	506	479	61/68	2.79	2.46	0.33
3	551	565	525	1.5/35	2.68	2.59	0.09
4	571	581	541	2/31	2.59	2.53	0.06
5	429, 454, 488[a]	558	452, 525	8.6/15.4	3.02	2.64	0.38
6	555, 600	625	594	92/35	2.31	—	—

[a] Shoulder. First singlet (E_{S_1}) and triplet (E_{T_1}) energies were taken at the onset of the high-energy edges of photoluminescence (fluorescence) and phosphorescence spectra, respectively, registered for Me-THF solutions of **1–6** at the temperature of liquid nitrogen (77 K). PLQYs of **1–6** measured in oxygen-free conditions.

In addition, to support the conclusion on TADF nature of the delayed fluorescence the PL decay measurements were performed for the films of compound **3** in air and vacuum conditions at the different temperatures (Fig. 4a–d). The PL decay curves of TADF compounds are characterized by the component prompt fluorescence in nanoseconds range and by the component microseconds range. The delayed fluorescence intensity increased with the increase of the temperature (Fig. 4d). This observation proves that thermally activated process was responsible for the delayed fluorescence. TADF properties of compound **3** are in good agreement with its small singlet-triplet splitting of 0.06 eV and with low activation energy (E_a) of 12 meV of reverse intersystem crossing (RICS) (Fig. 4e and f). E_a value was obtained by fitting the temperature dependence of RICS rates of compound **3** shown in Fig. 5f using the Arrhenius dependence $k = A \times \exp(-E_a/k_BT)$, where E_a is activation energy, k_B is Boltzmann constant and A is the frequency factor involving the spin–orbit coupling constant.[49]

PLQY values, determined for **1–6** dissolved in toluene or dispersed (10 wt%) in mCP, are collected in Table 2. Solutions of **1**, **2** and **6**, in toluene, which exhibit fluorescence generated by recombination of LE states, are characterized by relatively high PLQY values up to 92% (the PLQY values were measured using integrated sphere and recalculated using I_{N2}/I_{air} coefficients which expresses the PL intensity ratio determined for deoxygenated and air-equilibrated solutions). Compounds **3–5** are characterized by rather low PLQY values in solutions and significantly increased PLQY values of their dispersion in solid matrices. This behaviour should be attributed to AIEE.[50] More detailed information on PLQY of **1–6** is provided by theoretical calculation presented in the subsequent subsection. To study the photophysical properties of compounds **1–6** in solid-state in

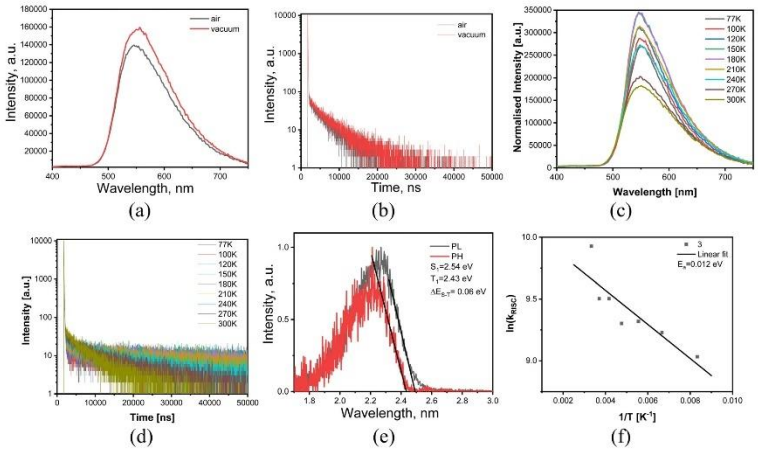

Fig. 4 PL spectra (a) and PL decay curves (b) recorded in vacuum and air at room temperature; PL and phosphorescence spectra (c) recorded at 77 K; PL spectra (d) and PL decay curves recorded at the different temperatures in an inert atmosphere; RISC rate as the function of temperature (e).

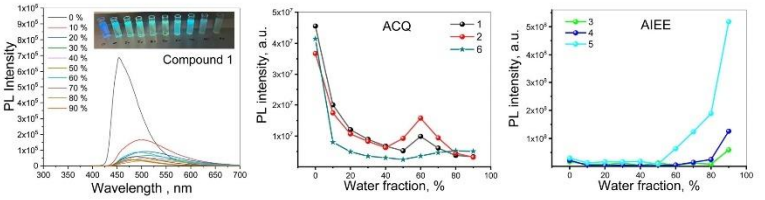

Fig. 5 PL spectra of the dispersions of compound **1** in THF/water mixtures with various water fractions (a). Inset shows photographs of the dispersions under UV excitation. Integrated areas of PL spectra *versus* water volume fractions for the dispersions of the compounds in the mixtures of THF and water (b and c).

more detail PL measurements for their dispersions in the THF and water mixtures were provided (Fig. 5 and Fig. S3, ESI†).

Emission intensities (integrated area of PL spectra) of the dispersions of **1–6** in the THF–water mixtures with water fractions from 0 to 90% are shown in Fig. 5a and Fig. S3 (ESI†). Decrease in the emission intensity of compound **1** with increasing water fractions in the solution mixture was observed (Fig. 5a and b). Such observation is typical for compounds exhibiting aggregation-caused quenching (ACQ).[51] ACQ was also detected for compounds **2** and **6** (Fig. 5b and Fig. S3, ESI†). In the case of the dispersions of compounds **3–5** in the THF–water mixtures, the emission intensity constantly increased with the increase of water fraction, due to the increasing amount of the solid aggregates (Fig. 5c and Fig. S3, ESI†). This observation indicates that compounds **3–5** exhibit AIEE.

3.4. Quantum chemical calculations

Quantum chemical calculations were carried out with the goal to support experimental results. In particular, they were aimed at the determination of the geometries of all molecules studied (**1–6**), elucidation of the frontier orbitals spatial distribution and calculation of their energies. Finally, theoretical calculations of IP_s and EA_s values were performed, considered as a theoretical support of the electrochemical and UPS data.

As already stated, each molecule consists of either one donor (carbazole or phenoxazine) and one acridone-type acceptor (molecules **1** and **3**) or two donors (carbazole or phenoxazine) and one acceptor (acridone or quinacridone, molecules **2**, **4** and **6**, respectively). Molecule **5** is different in the sense that its acceptor part (acridone) is connected to two donor parts (phenoxazine) *via* 1,3-phenylene linkers. As derived from the geometry optimization procedure, donor and acceptor parts of each molecule are flat but they are mutually twisted. Geometries of all investigated molecules relaxed in vacuum and in dichloromethane are presented in ESI† (Fig. S9). In the case of **1–4** and **6** dihedral angles between the planes of the donor and the acceptor moieties were calculated for molecules relaxed in vacuum and in dichloromethane, *i.e.* the same solvent which was used in electrochemical experiments. They are listed in Table S1 presented in ESI.† In the case of **5** (also relaxed in vacuum and in dichloromethane) the listed angles correspond to the torsion of planar acceptor and donor moieties with respect to the plane of 1,3-phenylene linker. From these data, it is clear that the twist angles in carbazole containing molecules are smaller by *ca.* 25° as compared to the corresponding angles in molecules with phenoxazine substituents (compare molecules **1**, **3** and molecules **2**, **4**). This relationship is seen for molecules relaxed in vacuum as well as in dichloromethane. Additionally, in all cases, the solvent effect enhances the twisting of the acceptor part of the molecule with respect to the donor part but, again, it is more pronounced for the molecules with carbazole donors than for those with phenoxazine ones. Atom coordinates of all investigated molecules are listed in ESI.†

Electronic parameters calculated for **1–6** are collected in Table 3. Note that HOMO levels of acridones substituted with carbazole (molecules **1**, **2**) are lower lying than the corresponding levels of acridones functionalized with phenoxazine (molecules **3**, **4**, **5**). **6**, which is the only quinacridone derivative studied, exhibits the low-lying level of HOMO, characteristic of the carbazole-substituted molecules, as well as the lowest-lying LUMO level of all examined molecules. As a result, significantly smaller band gap is observed for this compound as compared to the other carbazole derivatives (**1** and **2**), consistent with experimental electrochemical data. The solvent effect leads to an increase of the band gap for all investigated molecules, except **6**. It is due to more pronounced decrease of the HOMO level and only a slight decrease of the LUMO level. Solvent molecule interactions increase the electric dipole moment of **1–5** molecules and decrease the polarity of **6**, which is still very small as compared to the value calculated for molecules **1–5**. Carbazole derivatives (**1**, **2**) are less polar than phenoxazine ones (**3–5**) whose dipole moment is directed along the short axis of the planar acridone moiety. The dipole moment of **6** is perpendicular to the plane of the quinacridone moiety and the charges are symmetrically distributed around the quinacridone segment (see Fig. S9 in ESI† for the electron distribution density in this molecule). Additionally, the aliphatic chains

Table 3 Electron parameters calculated for **1–6** molecules in vacuum using DFT/B3LYP-GD3BJ/6-311++G(d,p) method

Molecule		HOMO [eV]	LUMO [eV]	$\Delta E_{\text{HOMO-LUMO}}$ [eV]	μ [D]	IP_{vertical} [eV]	$IP_{\text{adiabatic}}$ [eV]	EA_{vertical} [eV]	$EA_{\text{adiabatic}}$ [eV]
1	Vacuum	−5.34	−2.07	3.27	6.22	6.51	6.43	0.71	0.83
	DCM[a]	−5.49	−2.17	3.32	8.53	5.51	5.43	2.13	2.28
2	Vacuum	−5.32	−2.20	3.12	6.26	6.23	6.17	0.95	1.09
	DCM	−5.43	−2.25	3.18	8.81	5.42	5.36	2.22	2.37
3	Vacuum	−5.04	−2.16	2.88	7.41	6.49	6.65	0.78	0.54
	DCM	−5.23	−2.21	3.02	9.99	5.30	5.12	2.17	2.31
4	Vacuum	−5.12	−2.37	2.75	8.00	6.14	6.02	1.09	1.22
	DCM	−5.25	−2.33	2.92	10.97	5.27	5.13	2.29	2.44
5	Vacuum	−5.00	−2.18	2.82	7.23	5.98	6.37	0.93	0.53
	DCM	−5.19	−2.19	3.00	9.98	5.27	5.10	2.17	2.31
6	Vacuum	−5.31	−2.70	2.61	0.21	9.19	9.69	1.58	1.16
	DCM	−5.38	−2.77	2.61	0.18	5.37	5.32	2.75	2.89

[a] Dichloromethane, DCM.

are perpendicular to the quinacridone plane. As a result, the polarity of **6** is negligible.

Distributions of frontier orbitals within different parts of the studied molecule, together with their energies, determine spectroscopic and redox properties of electroactive compounds. These distributions are also strongly related to the molecular geometry. As already stated, in the case of **3** and **4** their donor and acceptor parts are almost perpendicular. The same applies to **5**, where the phenoxazine unit is almost perpendicular to the 1,3-phenylene linker. For these reasons HOMO and LUMO of **3**, **4** and **5** are located on different parts of the molecules, HOMO being essentially limited to the phenoxazine unit whereas HOMO−1, LUMO and LUMO+1 to the acridone one (see Fig. 6 for the shapes and distribution of frontier orbitals).

The spatial separation of HOMO and LUMO orbitals in **3**, **4** and **5** is manifested in the calculated transitions. It inhibits transitions of dominant HOMO → LUMO configurations *i.e.* $S_0 \rightarrow S_1$ transitions which in the case of these compounds exhibit either zero or negligible oscillator strength (see ESI,† Table S2). The lowest energy transition of non-negligible

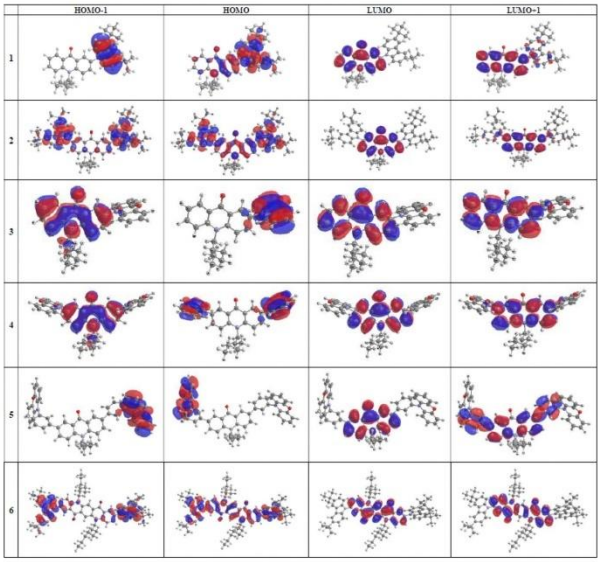

Fig. 6 Frontier orbitals of the **1–6** molecules in vacuum calculated by DFT/B3LYP-GD3BJ/6-311++G(d,p) method.

oscillator strength is HOMO−1 → LUMO in the case of **3** whereas for **4** and **5** it corresponds to the HOMO−2 → LUMO transition. Smaller dihedral angle in carbazole derivatives of acridone and quinacridone significantly changes the distribution of frontier orbitals. Although LUMO in the case of **1**, **2** and **6** is limited to the acridone (quinacridone) unit, HOMO extends from the carbazole substituent to the acridone (quinacridone) moiety. This means that no separation in space of frontier orbitals exists in these molecules and the lowest energetic transition ($S_0 \rightarrow S_1$) of a HOMO → LUMO configuration is not inhibited. As demonstrated by the calculations (see ESI,† Table S2) these transitions exhibit reasonably high oscillator strengths, although the transitions of the highest oscillator strength correspond to HOMO−2 → LUMO, HOMO → LUMO+1 and HOMO → LUMO+2 for **1**, **2** and **6**, respectively.

It is instructive to confront these calculations with experimental findings. First, it should be expected that the photoluminescence quantum yield (PLQY) of phenoxazine derivatives (compounds **3**, **4** and **5**) should be significantly smaller than that of carbazole ones (**1**, **2** and **6**) since, as evoked by the Kasha rule, small oscillator strength of the $S_0 \rightarrow S_1$ transition hinders the fluorescence. This is indeed the case, since PLQY of **1**, **2** and **6** measured for solutions in toluene is over one order of magnitude higher than that determined for **3**, **4** and **5** (see Table 2). Moreover, experimental UV-vis spectra of **3**, **4** and **5** (Fig. 2) clearly show that the absorption bands of the lowest energy significantly exceed the expected energy of the HOMO → LUMO, ($S_0 \rightarrow S_1$), indicating that they originate from $S_0 \rightarrow S_n$ transition, $n > 1$.

To the contrary, in the case of UV-vis spectra of **1**, **2** and **6** the lowest energy bands clearly correspond to the energy of the HOMO → LUMO transition. Finally, the calculations are fully consistent with the observed voltamperometric behavior of the studied compounds. Strict spatial separation of HOMO and LUMO, with HOMO being located on the phenoxazine moiety, results in one-step oxidation of both substituents in **4** and **5** which are being oxidized independently at the same potential. Extension of HOMO orbitals over the whole molecule in carbazole derivatives results, in turn, in a two-step oxidation of carbazole moieties in **2** and **6**, since the charge formed in the oxidation of one carbazole unit is then transmitted to the second substituent *via* delocalization, making its consecutive oxidation more difficult.

In Table 3 vertical and adiabatic ionization potentials (IP_s) and electron affinities (EA_s) calculated for **1–6** molecules are presented. They were evaluated from the differences of the total energies of the neutral molecules and their respective radical-ions. By comparing $IP_{vertical}$ with $IP_{adiabatic}$ it can be concluded that for all molecules relaxing in dichloromethane the values of $IP_{adiabatic}$ are lower. An excellent agreement between $IP_{adiabatic}$ and the experimental values derived from electrochemical investigations (IP_{el}) should be pointed out (compare the data collected in Tables 1 and 3). It involves not only the same trend but also close proximity of the experimentally determined and calculated values. The values of $EA_{adiabatic}$ are consistently lower than experimental EA_{el} but the trend within the series of compounds **1–6** is the same.

3.5. Charge transport properties

Electrical transport in emissive layers of OLEDs is of crucial importance for proper operation of the device. In particular, electroluminophores in one-component layers or hosts in guest/host OLEDs should exhibit ambipolar transport properties. In view of applications of **1–6** as electroluminophores in OLEDs, their charge transport properties were examined by the time of flight (TOF) technique. The experiments were carried out using diode-type indium tin oxide (ITO)/thick organic layer/Al samples. Dispersive TOF current transients but with observed transit times (t_{tr}) in log–log scales were recorded either under applied positive (for holes) or negative (for electrons) voltages to the side of optically transparent electrode (ITO) (see Fig. 7a and Fig. S4 in ESI†). In these conditions compounds **1**, **4–6** turned out unipolar exhibiting measurable mobility for holes only. **2** and **3** were bipolar exhibiting both p-type (hole) and n-type (electron) transport (Fig. 7b).

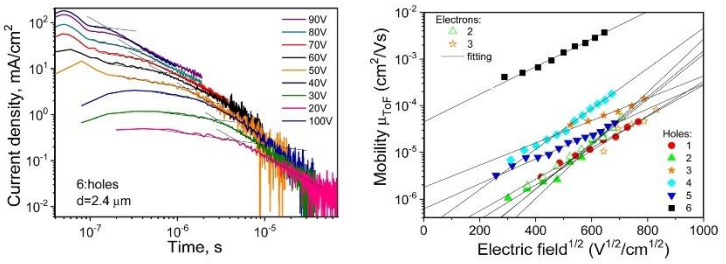

Fig. 7 TOF signals for holes (a) in the vacuum-deposited layer of compound **6** and charge mobilities as the function of electric field (b) measured for vacuum-deposited layers of **1–6**.

Table 4 Hole and electron mobility parameters at RT, obtained for vacuum-deposited layers of **1–6**

	Holes			Electrons		
Compound	μ_h[a] ($cm^2 V^{-1} s^{-1}$)	μ_0[b] ($cm^2 V^{-1} s^{-1}$)	β[c] ($cm V^{-1})^{1/2}$	μ_e ($cm^2 V^{-1} s^{-1}$)	μ_0[b] ($cm^2 V^{-1} s^{-1}$)	β[c] ($cm V^{-1})^{1/2}$
1	1.25×10^{-5}	1.89×10^{-7}	7.75×10^{-3}	—	—	—
2	1.59×10^{-5}	1.91×10^{-8}	11.1×10^{-3}	1.8×10^{-5}	1.75×10^{-8}	11.4×10^{-3}
3	4.62×10^{-5}	1.77×10^{-7}	5.49×10^{-3}	1.3×10^{-5}	6.6×10^{-8}	8.55×10^{-3}
4	8.5×10^{-5}	2.17×10^{-7}	10×10^{-3}	—	—	—
5	2.39×10^{-5}	6.8×10^{-7}	6.13×10^{-3}	—	—	—
6	2.53×10^{-3}	4.48×10^{-5}	6.8×10^{-3}	—	—	—

[a] Taken from the TOF measurements (Fig. 7), hole (μ_h) and electron (μ_e) mobilities at electric field (E) of 3.6×10^5 V cm^{-1}. [b] Mobilities at absent electric field (μ_0). [c] Field dependence parameter (β) of a Poole–Frenkel type mobility: $\mu = \mu_0 \times \exp(\beta \times E^{1/2})$.

Taking t_{tr} values from the TOF current transients, hole and electrons mobilities were estimated at the different electric fields displaying their hole-only or bipolar charge transport (see Fig. 7b). The highest value of hole mobility $\mu_h = 2.53 \times 10^{-3}$ $cm^2 V^{-1} s^{-1}$ at $E = 3.6 \times 10^5$ V cm^{-1} was found for the quinacridone derivative (compound **6**, see Table 4). This was not unexpected since high hole mobilities, measured either in the field effect transistor[52,53] or diode configurations,[54] were reported for various quinacridone core-containing compounds. Hole mobilities of the remaining compounds were from over one order (**4**) to two orders (**1**) of magnitude lower (Fig. 7b). The measured hole mobility values are typical of donor–acceptor compounds exhibiting TADF in which the molecular segments are highly twisted.[55,56] Among acridone derivatives (**1–5**), those containing phenoxazine donors (**3–5**) showed slightly higher hole mobilities than the compounds with carbazole donors (**1, 2**).

Results of fitting of the Poole–Frenkel electric field dependences of experimental charge carrier mobilities, led to relatively high field dependence parameters. β values differed within the range from 5.49×10^{-3} for **3** to 11.1×10^{-3} for **2** as determined at room temperature for all investigated compounds (**1–6**) (Table 4). They can be attributed to the relatively strongly dispersive transport. The weakest dispersity was observed for compound **3**, characterized by the lowest β value (Fig. S4, ESI†).[57] **2** and **3** turned out to be bipolar, exhibiting at the same electric field similar electron mobilities of 1.8×10^{-5} and 1.3×10^{-5} $cm^2 V^{-1} s^{-1}$, respectively. Moreover, μ_e values of **2** and **3** were comparable to their μ_h values indicating well-balanced hole and electron transport. This property is of crucial importance for the use of these compounds in electroluminescent devices such as OLEDs.

3.6. Electroluminescence

The results of spectroscopic, electrochemical and electrical transport investigations supported by quantum chemical calculations seem to indicate that the synthesized acridone and quinacridone derivatives are very well suited for a variety of applications such as electrochromic materials, components of active layers in ambipolar or p-channel field effect transistors and electroluminophores in light-emitting diodes. In the research described here we focused on this last application. Thus, **1–6** were used as emitters in test OLEDs of the following structure: ITO/MoO_3 (0.3 nm)/NPB (40 nm)/mCP (4 nm)/EML (24 nm)/TSPO1 (4 nm)/TPBi (40 nm)/LiF (0.3 nm)/Al (120 nm), where EML stands for "emissive layer". Chemical formulae of particular components of the devices are shown in Fig. 8. Two

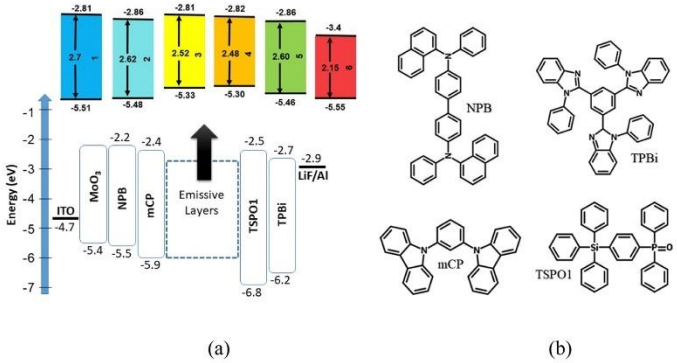

Fig. 8 Equilibrium energy diagram (a) and chemical structures of selected components of test OLEDs (b).

types of emissive layers were fabricated by vacuum deposition: (i) non-doped, *i.e.* consisting of neat compounds **1–6** and in the subsequent text termed as A1–A6 series, the number being related to the number of the synthesized compound; (ii) doped, *i.e.* 10 wt% molecular dispersions of a given compound in a mCP matrix, subsequently abbreviated as B1–B6 series, the number corresponding to the number of the synthesized compound. To assure good injection of holes from the anode (ITO) and electrons from the cathode (Al), additional layers were deposited (MoO_3/LiF) as well as hole/electron transporting layers (NPB/TPBi). They were selected on the basis of their energy levels (see Fig. 8). Hole/electron (mCP/TSPO1) blocking layers were also carefully chosen for ensuring recombination of hole–electron pairs within the EML. They additionally acted as exciton blocking layers due to their high triplet energy levels that can prevent from exciton leakages to the neighbouring layers. Therefore, it can be claimed that the observed electroluminescence is fully attributed to the emission of EMLs (Fig. 9a).

Indeed, the positions and shapes of the obtained EL spectra closely remind the corresponding PL spectra of neat (non-doped) and molecularly dispersed in mCP (doped) films of **1–6** (compare Fig. 9a and 4a). EL spectra were stable under different voltages for the majority of devices except B2, B5 and A6 (Fig. S5 in ESI†). Possible explanation of these differences has to involve several factors. Emissions from these luminophores are of LE and ICT character (see Fig. 3c and d). Thus, their LE/ICT emission ratio can differ, depending on the type of the excitation source (optical *vs.* electrical), leading to meaningful differences between the PL and EL spectra. B5 device can be considered here as an instructive example. Its EL emission is mainly of LE character (high energy spectrum with structured bands) whereas LE and ICT emissions equally contribute to the PL spectrum of **5** molecularly dispersed in mCP (Fig. 4a).

Functionalization of acridone or quinacridone with only two types of donors, namely *t*Cz and PhNZ, results in a series electroluminophores whose emission spectra cover large part of the visible spectrum from blue to orange. In particular, non-doped and doped EMLs of *t*Cz substituted acridone (compounds **1** and **2** in devices A1, A2, B1 and B2) emit blue electroluminescence of similar CIE 1931 colour coordinates (see Fig. 9b, Fig. S6 and Table 5, Table S1, ESI†). A3 and A4, *i.e.* devices with non-doped EMLs consisting of PhNZ substituted acridone emit green (CIE1931 of (0.336; 0.567)) and yellow (CIE1931 of (0.439; 0.541)) light, respectively. The observed bathochromic shift of the spectra of A3 and A4 as compared to those recorded for A1 and A2 is attributed to stronger donor–acceptor interactions in acridone-phenoxazine derivatives. However, dispersions of **3** and **4** in mCP (devices B3 and B4) yield EL spectra which are hypsochromically shifted with respect to the spectra measured for A3 and A4 devices with CIE1931 colour coordinates characteristic of blue region (see Table 5). This colour change can be attributed to the luminophore interactions with the mCP host, a phenomenon somehow similar to solvatochromism. Interestingly, yellow *versus*

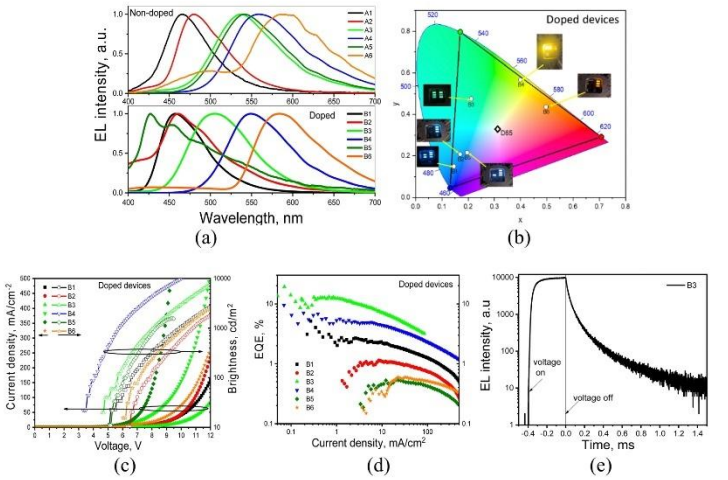

Fig. 9 EL spectra recorded at 10 V (a) and CIE colour diagram (b) with the corresponding CIE coordinates. Current density and brightness as the function of applied voltages (c), EQE *versus* current density plots (d) and TREL curves of device B3 (e).

Table 5 Output electroluminescent parameters of OLEDs with doped (B1–B6) EMLs

Device name	EML	λ_{EL},[c] nm	V_{ON},[c] V	L_{MAX},[c] cd m^{-2}	CE_{MAX},[c] cd A^{-1}	PE_{MAX},[c] lm W^{-1}	EQE_{MAX},[c] %	CIE 1931,[c] x; y
B1[a]	1(10%):mCP	458	5.0	4270	6.7	3.8	4.0	0.146; 0.149
B2[a]	2(10%):mCP	459	6.4	2150	1.7	0.7	1.2	0.170; 0.208
B3[a]	3(10%):mCP	505	4.7	7950	37.1	19.8	13.0	0.212; 0.475
B4[a]	4(10%):mCP	548	3.5	22 520	23.5	20.5	7.2	0.399; 0.567
B5[a]	5(10%):mCP	426, 455	5.4	1820	0.8	0.4	0.5	0.196; 0.216
B6[a]	6(10%):mCP	587	6.0	4010	1.4	0.5	0.6	0.497; 0.436
C3[b]	3(50%):POT2T	520	4.6	6820	52.5	28.5	16.7	0.26; 0.54

[a] Device structure is ITO/MoO_3/NPB/mCP/EML/TSPO1/TPBi/LiF/Al. [b] Device structure is ITO/MoO_3/TCTA/EML/TSPO1/TPBi/LiF/Al. [c] Collected parameters are: EL maximum (λ_{EL}); turn-on voltage (V_{ON}); maximum brightness (L_{MAX}); maximum current (CE_{MAX}); power (PE_{MAX}) and external quantum (EQE_{MAX}) efficiencies; colour coordinates (CIE 1931).

blue electroluminescence was obtained for EMLs in A5 and B5 devices, respectively, *i.e.* layers exhibiting different electroluminescence mechanisms. This difference cannot be attributed to solvatochromism but rather to a different combination of ICT and LE emissions, as previously reported for indolocarbazole-type emitters.[58,59] Thus, weakening of donor–acceptor interactions in compound **5** dispersed in mCP as compared to the film of neat luminophore (undoped EML) results in switching from ICT to LE emission, which is more intensive under electrical excitations than under optical ones.

Undoped and doped EMLs of the only quinacridone derivative studied in this research (**6**) yields orange, close to red, electroluminescence (see Fig. 9 for the spectra and Table 5 for CIE 1931 coordinates). Unexpectedly, a high energy band peaked at *ca.* 490 nm can be observed in the EL spectrum of device A6. This band was not present in the photoluminescence spectrum of the film of neat **6** and its nature was not yet clarified. Tentatively, this band could be attributed to the electroplex emission of **6**, taking into account that it appeared only under electrical excitation. Its presence could be exploited in the development of white OLEDs, as previously proposed.[58]

Concluding this part of the paper, non-doped EMLs, consisting of neat **1–6** compounds (devices A1–A6) demonstrated CIE_x values in a rather wide range from 0.15 to 0.439. Expectably, the CIE_x range of EMLs fabricated as dispersions of **1–6** in mCP (devices B1–B6) was narrower (0.17 to 0.399), which could be ascribed to lowering of their polarity in the matrix. CIE_y values varied in the ranges from 0.161 to 0.57 and from 0.149 to 0.567 for A1–A6 and B1–B6 devices, respectively. These results clearly show that using only two donor and two acceptor building blocks in the synthesis of D–A, D–A–D or D–π–A–π–D compounds, it is possible to fabricate electroluminophores covering large part of the visible spectrum.

The lowest value of the turn on voltage (3.5 V) was measured for device B4 (Fig. 9c and Table 5), consistent with the lowest ionization potential of **4** (IP = 5.3 eV) as determined by UPS and its second highest hole mobility (see Tables 1 and 4). Despite high hole mobility and relatively good charge injecting properties of **6**, devices fabricated with the use of this compound (A6 and B6) demonstrated rather high turn on voltages. This could be tentatively ascribed to electroplex formation, as judged from their EL spectra. Large differences in the maximum brightness values of the fabricated devices are related to different emitter efficiencies and to varying sensitivity of the human eye to different emission colours (Table 5).

Outstanding TADF/AIEE emissive and bipolar charge-transporting properties of compound **3** should be pointed out (see Tables 2 and 4). As a result, A3 and B3 demonstrated the highest maximum EQEs of 2.3% and 13%, respectively (Fig. 9d, Fig. S7 and Table 5, Table S1, ESI†). The transient electroluminescence (TREL) signal reaching milliseconds helps to prove the significant participation of triplet excitons in electroluminescence of the device B3 based on the TADF emitter **3** (Fig. 9e). OLEDs based on compound **3** after the additional optimization can apparently show better output parameters in comparison to those described in the present manuscript. To support this claim, we fabricated OLED using an electron-transporting host and slightly modified device structure (Table 5). Improved maximum extremal quantum efficiency of 16.7% was obtained for device C3 with the emitting layer of compound **3** dispersed in the host PO-T2T in comparison to that of device B3 (Fig. S8, ESI†). Such improvement is mainly related to electron-transporting properties of PO-T2T.[60] The lower electron mobility in comparison to hole mobility of compound **3** can be compensated by good electron-transporting properties of PO-T2T in the light-emitting layer of device C3 leading to improved hole–electron balance within light-emitting layer of device C3 (Table 5).

Emissive properties of compound **4** were comparable to those of compound **3**, however, devices A4 and B4 showed *ca.* twice lower maximum EQE efficiencies of 1.32 and 7.2%, respectively. This result could be tentatively explained by unbalanced hole–electron transport within the EML, since, in contrast to bipolar **3**, compound **4** was found to be a hole-only conductor (Fig. 7 and Table 4). Compound **1** is also an interesting case. Although it did not show TADF due to relatively high singlet-triplet splitting of 0.34 eV (Table 2), devices A1 and B1 demonstrated, high maximum EQEs of 1.6 and 4%, respectively, *i.e.* values which could be considered very promising for simple fluorescent OLEDs (Table 5). These relatively high efficiencies were mainly related to high PLQY value of **1** in the solid state (66%, Table 2). Indeed, despite high PLQY values of the films of the doped compounds **1** (66%) and **2** (68%) (Table 2), the EQEs of OLEDs based on these compounds were relatively low. This result is not surprising since the compounds were not characterized by TADF (Fig. 3b). Thus, they

do not allow harvesting of triplets in OLEDs. As a result, their maximum theoretical EQE values should not be higher than 5% according to the formula:[61]

$$\eta_{ext} = \gamma \times \Phi_{PL} \times \chi \times \eta_{out} \quad (1)$$

where γ corresponds to the charge-balance factor, Φ_{PL} is the photoluminescence quantum efficiency, χ is the efficiency of exciton production, and η_{out} corresponds to the outcoupling efficiency.

The maximum EQE of 4% of device B1 based on the compound **1** is very close to the theoretical maximum of η_{ext} = 4.65% taking γ = 1, χ = 0.25 (as for prompt fluorescence compounds) and η_{out} = 0.3 (Table 5). OLEDs based on compounds **3** and **4** exhibiting TADF showed considerably higher EQE values due to their efficiency of exciton production χ = 1. Thus, our result demonstrates the effect of the mode of linking of the donor and acceptor moieties (D–A, D–A–D or D–π–A–π–D) on the electroluminescent properties of the compounds.

4. Conclusion

To summarize, we have demonstrated that using only one acceptor (acridone) and two donors (*tert*-butyl carbazole or phenoxazine) it was possible to design and synthesize a series of D–A, D–A–D and D–π–A–π–D compounds of interesting and reversible electrochemistry and tunable emissive properties. Photoluminescence of their vacuum-deposited films covered a large part of visible spectrum from sky-blue to red. Replacement of the acridone moiety by quinacridone (compound **6**) allowed the extension of the emission spectral range to red of the vacuum-deposited film. Compounds **3** (phenoxazinyl substituted acridone), **4** (phenoxazinyl disubstituted acridone) and **5** (phenoxazinyl disubstituted acridone through the phenyl bridges) exhibited excellent emissive properties due to the AIEE and TADF effects. This property, combined with the ambipolar character of **3** which facilitated balanced electron/hole transport, made this compound an excellent candidate for its application in active layers of OLEDs as an electroluminophore. The fabricated test diode exhibited maximum external quantum efficiency of 16.7%. Finally, an excellent agreement between the experimental and theoretically predicted results was obtained pointing out the adequacy of the applied quantum chemical calculations.

Conflicts of interest

The authors declare no conflict of interest.

Acknowledgements

I. K. B., M. Z. and A. P. acknowledge financial support from National Science Centre, Poland (NCN, Grant No. 2019/33/B/ST5/00582). M. G. and D. V. acknowledge the Research Council of Lithuania (Project "ELOS" No. S-MIP-21-30). This research was carried out with the support of the Interdisciplinary Centre for Mathematical and Computational Modelling at the University of Warsaw (ICM UW) under computational allocation no G85-922.

References

1 H. T. Nguyen, M. C. Lallemand, S. Boutefnouchet, S. Michel and F. Tillequin, *J. Nat. Prod.*, 2009, **72**, 527–539.
2 P. Singh, J. Kaur, P. Kaur and S. Kaur, *Bioorg. Med. Chem.*, 2009, **17**, 2423–2427.
3 V. Nadaraj, S. Thamarai Selvi and S. Mohan, *Eur. J. Med. Chem.*, 2009, **44**, 976–980.
4 R. Hegde, P. Thimmaiah, M. C. Yerigeri, G. Krishnegowda, K. N. Thimmaiah and P. J. Houghton, *Eur. J. Med. Chem.*, 2004, **39**, 161–177.
5 A. Shakhnovich and J. Belmont, *Chem. Inkjet Inks*, 2009, pp. 101–122.
6 J. Su, X. Wen, W. Chen, Y. Miao, F. Li and Y. Wang, *New J. Chem.*, 2018, **42**, 5005.
7 C. Li, N. Zheng, H. Chen, J. Huang, Z. Mao, L. Zheng, C. Weng, S. Tan and G. Yu, *Polym. Chem.*, 2015, **6**, 5393.
8 C. Wang, W. Chen, S. Chen, S. Zhao, J. Zhang, D. Qiu and Y. Wang, *New J. Chem.*, 2012, **36**, 1788–1797.
9 I. Javed, Z. Zhang, T. Peng, T. Zhou, H. Zhang, M. Issa Khan, Y. Liu and Y. Wang, *Sol. Energy Mater. Sol. Cells*, 2011, **95**, 2670–2676.
10 K. H. Lee, D. S. Leem, J. S. Castrucci, K. B. Park, X. Bulliard, K. S. Kim, Y. W. Jin, S. Lee, T. P. Bender and S. Y. Park, *ACS Appl. Mater. Interfaces*, 2013, **5**, 13089–13095.
11 K. H. Lee, G. H. Lee, D. S. Leem, J. Lee, J. W. Chung, X. Bulliard, H. Choi, K. B. Park, K. S. Kim, Y. W. Jin, S. Lee and S. Y. Park, *J. Phys. Chem. C*, 2014, **118**, 13424–13431.
12 H. Li, C. Gu, L. Jiang, L. Wei, W. Hu and H. Fu, *J. Mater. Chem. C*, 2013, **1**, 2021–2027.
13 K. D. Thé, C. Radford, M. Parvez and T. C. Sutherland, *Phys. Chem. Chem. Phys.*, 2015, **17**, 20903.
14 B. K. Sharma, A. M. Shaikh, N. Agarwal and R. M. Kamble, *RSC Adv.*, 2016, **6**, 17129–17137.
15 H. T. Le, R. Saleah, N. Kungwan, M. P. Nghiem, F. Goubard and T. T. Bui, *ChemistrySelect*, 2020, **5**, 15180–15189.
16 T. Takeda, H. Sugihara, Y. Suzuki, J. Kawamata and T. Akutagawa, *J. Org. Chem.*, 2014, **79**, 9669–9677.
17 M. Xu, K. Kong, H. Ding, Y. Chu, S. Zhang, F. Yu, H. Ye, Y. Hu and J. Hua, *J. Mater. Chem. C*, 2020, **8**, 930.
18 P. Yang, S. Guo, X. Yu, F. Zhang, B. Yu, H. Zhang, Y. Zhao and Z. Liu, *Ind. Eng. Chem. Res.*, 2019, **58**, 9636–9643.
19 J. Jia, Y. Li, W. Wang, C. Luo, L. Han, Y. Li and J. Gao, *Dyes Pigm.*, 2017, **146**, 251–262.
20 Y. Mei, D. Liu, J. Li, H. Li and W. Wei, *J. Mater. Chem. C*, 2021, **9**, 5885–5892.
21 A. A. Awasthi, N. Gupta, T. Siddiqui, P. Parab, D. K. Palit, S. Bose and N. Agarwal, *J. Chem. Sci.*, 2019, **131**, 94.
22 M. Mamada, K. Inada, T. Komino, W. J. Potscavage, H. Nakanotani and C. Adachi, *ACS Cent. Sci.*, 2017, **3**, 769–777.

23 Q. T. Siddiqui, A. A. Awasthi, P. Bhui, P. Parab, M. Muneer, S. Bose and N. Agarwal, *RSC Adv.*, 2019, **9**, 40248–40254.
24 J. Xu, X. Wu, J. Guo, Z. Zhao and B. Z. Tang, *J. Mater. Chem. C*, 2021, **9**, 15505–15510.
25 L. Li, X. Dai, X. Liao, X. Zang, J. Huang, H. Zhang, X. Yin and Y. Hong, *Sol. Energy*, 2021, **225**, 173–183.
26 N. Cai, F. Li, Y. Atong Chen, R. Luo, T. Onghui Hu, F. Lin, S.-M. Yiu, D. Liu, D. Lei, Z. Zhu and A. K.-Y. Jen, *Angew. Chem., Int. Ed.*, 2021, **60**, 20437–20442.
27 A. Kumar Gupta, Z. Zhang, E. Spuling, M. Kaczmarek, Y. Wang, Z. Hassan, I. D. W. Samuel, S. Bräse and E. Zysman-Colman, *Mater. Adv.*, 2021, **2**, 6684.
28 Y. P. Zhang, X. Liang, X. F. Luo, S. Q. Song, S. Li, Y. Wang, Z. P. Mao, W. Y. Xu, Y. X. Zheng, J. L. Zuo and Y. Pan, *Angew. Chem., Int. Ed.*, 2021, **60**, 8435–8440.
29 J.-X. Chen, Y.-F. Xiao, K. Wang, D. Sun, X.-C. Fan, X. Zhang, M. Zhang, Y. i-Zhong Shi, J. Yu, F. eng-Xia Geng, C.-S. Lee and X.-H. Zhang, *Angew. Chem., Int. Ed.*, 2021, **60**, 2478–2484.
30 W. Yang, Y. Yang, X. Cao, Y. Liu, Z. Chen, Z. Huang, S. Gong and C. Yang, *Chem. Eng. J.*, 2021, **415**, 128909.
31 Y. Y. Jing, X. D. Tao, M. X. Yang, X. L. Chen and C. Z. Lu, *Chem. Eng. J.*, 2021, **413**, 127418.
32 G. Li, A. Klimash, E. Zysman-Colman, I. D. W. Samuel idws, P. Address, G. Copley, S. Krotkus, T. Matulaitis, S. Diesing, E. Archer, C. Keum, D. B. Cordes, A. M. Z. Slawin, M. C. Gather and I. D. W. Samuel, *Front. Chem.*, 2021, **1**, 572862.
33 S. Do Sung, M. Soo Kang, I. Taek Choi, H. Mo Kim, H. Kim, M. Hong, H. Kyu Kim and W. In Lee, *Chem. Commun.*, 2014, **50**, 14161–14163.
34 Y. Zhao, X. Wang, T. Yu, Z. C. Wei, X. Liu and J. Chem, *New J. Chem.*, 2017, **41**, 4702.
35 X. Yang, X. Xu and G. Zhou, *J. Mater. Chem. C*, 2015, **3**, 913–944.
36 P. Heimel, A. Mondal, F. May, W. Kowalsky, C. Lennartz, D. Andrienko and R. Lovrincic, *Nat. Commun.*, 2018, **9**, 4990.
37 A. Zampetti, A. Minotto and F. Cacialli, *Adv. Funct. Mater.*, 2019, **29**, 1807623.
38 P. Pander, R. Motyka, P. Zassowski, M. Lapkowski, A. Swist and P. Data, *J. Phys. Chem. C*, 2017, **121**, 11027–11036.
39 C. Wang, S. Chen, K. Wang, S. Zhao, J. Zhang and Y. Wang, *J. Phys. Chem. C*, 2012, **116**, 17796–17806.
40 I. Kulszewicz-Bajer, M. Zagorska, M. Banasiewicz, P. A. Gunka, G. Gunka, P. Toman, B. Kozankiewicz, G. Wiosna-Salyga and A. Pron, *Phys. Chem. Chem. Phys.*, 2020, **22**, 8522.
41 K. Karon and M. Lapkowski, *J. Solid State Electrochem.*, 2015, **19**, 2601–2610.
42 M. Vasylieva, P. Pander, B. K. Sharma, A. M. Shaikh, R. M. Kamble, F. B. Dias, M. Czichy and P. Data, *Electrochim. Acta*, 2021, **384**, 138347.
43 P. Kurzep, Ł. Skórka, S. Skórka, M. Zagorska, P. A. GúNka, M. Banasiewicz, B. Kozankiewicz and I. Kulszewicz-Bajer, *RSC Adv.*, 2017, **7**, 8627–8632.
44 J. Sworakowski, J. Lipiński and K. Janus, *Org. Electron.*, 2016, **33**, 300–310.
45 J. Sworakowski and K. Janus, *Org. Electron.*, 2017, **48**, 46–52.
46 J. Sworakowski, *Synth. Met.*, 2018, **235**, 125–130.
47 E. Skuodis, O. Bezvikonnyi, A. Tomkeviciene, D. Volyniuk, V. Mimaite, A. Lazauskas, A. Bucinskas, R. Keruckiene, G. Sini and J. V. Grazulevicius, *Org. Electron.*, 2018, **63**, 29–40.
48 I. Kulszewicz-Bajer, M. Zagorska, M. Banasiewicz, P. A. Guńka, P. Toman, B. Kozankiewicz, G. Wiosna-Salyga and A. Pron, *Phys. Chem. Chem. Phys.*, 2020, **22**, 8522–8534.
49 A. E. Nikolaenko, M. Cass, F. Bourcet, D. Mohamad and M. Roberts, *Adv. Mater.*, 2015, **27**, 7236–7240.
50 Z. Zhao, H. Aoke Zhang, W. Y. Lam and B. Z. Tang, *Angew. Chem., Int. Ed.*, 2020, **59**, 9888–9907.
51 Y. Zuo, X. Wang and D. Wu, *J. Mater. Chem. C*, 2019, **7**, 14555.
52 T. Marszalek, I. Krygier, A. Pron, Z. Wrobel, P. M. W. Blom, I. Kulszewicz-Bajer and W. Pisula, *Org. Electron.*, 2019, **65**, 127–134.
53 C. Wang, D. Chen, W. Chen, S. Chen, K. Ye, H. Zhang, J. Zhang and Y. Wang, *J. Mater. Chem. C*, 2013, **1**, 5548–5556.
54 H. D. Pham, S. M. Jain, M. Li, S. Manzhos, K. Feron, S. Pitchaimuthu, Z. Liu, N. Motta, H. Wang, J. R. Durrant Bd and P. Sonar, *J. Mater. Chem. A*, 2019, **7**, 5315–5323.
55 H. Lee, K. J. Kim, Y. J. Moon, Y. K. Kim and T. Kim, *Org. Electron.*, 2020, **84**, 105816.
56 D. Gudeika, J. H. Lee, P. H. Lee, C. H. Chen, T. L. Chiu, G. V. Baryshnikov, B. F. Minaev, H. Ågren, D. Volyniuk, O. Bezvikonnyi and J. V. Grazulevicius, *Org. Electron.*, 2020, **83**, 105733.
57 S. Heun and P. M. Borsenberger, *Chem. Phys.*, 1995, **200**, 245–255.
58 D. Luo, X. L. Li, Y. Zhao, Y. Gao and B. Liu, *ACS Photonics*, 2017, **4**, 1566–1575.
59 E. Jatautiene, J. Simokaitiene, G. Sych, D. Volyniuk, K. Ivaniuk, P. Stakhira, V. Fitio, H. Petrovska, V. Savaryn, Y. Nastishin and J. V. Grazulevicius, *Appl. Mater. Today*, 2021, **24**, 101121.
60 Y. Zuo, X. Wang and D. Wu, *J. Mater. Chem. C*, 2019, **7**, 14555.
61 T. Tsutsui, *MRS Bull.*, 1997, **22**(6), 39–45.

RESEARCH ARTICLE

ADVANCED OPTICAL MATERIALS
www.advopticalmat.de

Thermally Controllable Tuning of Emission Properties of Phenoxazine-Substituted Acridones as One Step Forward to Efficient Organic Light-Emitting Diodes Based on Crystalline Emitters

Matas Guzauskas, Dmytro Volyniuk, Irena Kulszewicz-Bajer,* Malek Mahmoudi, Algirdas Lazauskas, Vidmantas Jasinskas, Vidmantas Gulbinas, Adam Pron,* and Juozas V. Grazulevicius**

The overwhelming majority of efficient organic light-emitting diodes (OLEDs) are based on amorphous emitting layers. The devices with crystalline emitters usually show significantly worse performance. It is demonstrated that controlled thermal treatments of phenoxazine-substituted acridones may lead to a spectacular improvement of photo- and electroluminescence of these luminophores. The three acridone derivatives studied, namely 2-phenoxazine-*N*-hexylacridone (PHhA), 2,7-bis-(phenoxazine)-*N*-hexylacridone (bPHhA), and 2,7-bis[3-(phenoxazine)phenyl]-*N*-hexylacridone (PHPhhA), are characterized by relatively narrow photoluminescence spectra and photoluminescence quantum yields approaching 100%. These spectra can be reversibly tuned through appropriate thermal treatment of the deposited layers, undergoing shifts up to 92 nm upon transformation from amorphous to crystalline states. Strong thermally activated delayed fluorescence (TADF) observed for these compounds is manifested by a significantly higher reverse intersystem crossing rate of 1.92×10^6 s^{-1} as compared to the intersystem crossing rate of 5.68×10^5 s^{-1}. These improvements are attributed to the annealing-induced conformational equilibration due to crystallisation in combination with hosting. Adequacy of the proposed concept is demonstrated by the fabrication of devices exhibiting external quantum efficiencies reaching 20.7% – a record value for OLEDs with crystalline emitting layers. The presented approach of annealing-induced conformational equilibration can lead to improved TADF properties for other fluorescent organic emitters presently considered inefficient.

1. Introduction

Crystallinity is an essential feature of the overwhelming majority of semiconductors used in inorganic, hybrid, and organic electronic devices since it usually assures superior charge-transporting properties of the active layers.[1–3] In this respect, organic light-emitting diodes (OLEDs) should be considered as somehow atypical since amorphous emissive layers in these devices show, so far, their superiority as compared to the crystalline ones.[4–6] It seems, however, that the effect of the electroluminophores crystallinity in OLEDs has not yet been sufficiently explored. In addition to superior charge-transporting properties, crystalline molecular materials may offer other advantages such as improved emission color purity.[7,8] Some more or less successful attempts of the use of crystalline light emitting semiconductors were reported in the past decade. In 2018, D. Yan et al.[9] described "crystalline" OLEDs that showed a maximum external quantum efficiency (EQE) of 1.44% at the brightness of 5000 cd m^{-2}. In these devices the emissive layer of parasexiphenyl (p-6P)/tris(8-hydroxyquinoline) aluminium (Alq_3) was fabricated by the weak epitaxy growth method. A year later,

M. Guzauskas, D. Volyniuk, M. Mahmoudi, J. V. Grazulevicius
Department of Polymer Chemistry and Technology
Kaunas University of Technology
Barsausko 59, Kaunas LT-51423, Lithuania
E-mail: dmytro.volyniuk@ktu.lt; juozas.grazulevicius@ktu.lt

I. Kulszewicz-Bajer, A. Pron
Faculty of Chemistry
Warsaw University of Technology
Noakowskiego 3, Warsaw 00–664, Poland
E-mail: irena.bajer@pw.edu.pl; adam.pron@pw.edu.pl

A. Lazauskas
Institute of Materials Science
Kaunas University of Technology
K. Baršausko St. 59, Kaunas LT51423, Lithuania

V. Jasinskas, V. Gulbinas
Centre for Physical Sciences and Technology
Vilnius LT-10257, Lithuania

The ORCID identification number(s) for the author(s) of this article can be found under https://doi.org/10.1002/adom.202301059

DOI: 10.1002/adom.202301059

the same authors fabricated "crystalline" Alq_3-based OLEDs with a maximum EQE value of 2.44%.[10] Organic semiconductors exhibiting liquid crystallinity (LC) were also used in the fabrication of OLEDs. Photopolymerizable organic semiconductors exhibiting LC were also used in the fabrication of OLEDs.[11] For example, OLEDs in which LC perylene-3,4,9,10-tetracarboxylic tetraethyl ester served as an emitter showed a maximum EQE of 0.8%.[12] Tetraphenylethylene LC emitter, exhibiting aggregation-induced emission enhancement (AIEE), was also used in OLEDs yielding a maximum EQE value of 4.4%.[13] These rather low EQE values reported for the above described OLEDs are related to the origin of the emitters used. The emitters of this type are not able to harvest triplet excitons under electrical excitation that limits the theoretical EQE of the fluorescent OLEDs to ≈5% by the spin statistics.[14] Significantly more efficient are fluorescent emitters exhibiting the thermally activated delayed fluorescence (TADF) effect. For OLEDs based on TADF emitters the theoretical EQE limit of 25% is predicted.[15] To the best of our knowledge, the first example of OLEDs with LC TADF emitters was only recently reported by Y. Wang et al. [16] who improved the EQE of the devices from 6.52% to 14.9% by inducing molecular ordering in the emissive layer through the formation of a smectic phase.

On the other hand, glass-forming TADF emitters have been widely used in multi-color OLEDs exhibiting EQE values exceeding 30%.[17,18] The TADF effect originates from the relaxation of singlet charge transfer (^{1}CT) states present in donor–acceptor (D–A) compounds characterized by a high value of the dihedral angle between the donor and the acceptor segments of the electroluminophore molecule. This type of geometry results in a small value of the singlet-triplet splitting (ΔE_{ST}), favoring the reverse intersystem crossing (RISC) of triplet excitons from non-emissive ^{3}CT states to emissive ^{1}CT states.[19] Photoluminescence (PL) and electroluminescent (EL) spectra of TADF compounds are very sensitive to their conformation and static dielectric disorders in the solid-state.[20,21] This sensitivity of conventional TADF emitters, involving the efficiency and emission color purity changes, severely limits their application in displays.[22]

Several synthetic approaches were proposed to minimize the solid-state solvation and conformation disorder. These include the design of more sterically confined molecules, introduction of bulky substituents or hydrogen bond-forming moieties as well as attachment of specific anchoring groups to molecules exhibiting the TADF effect.[23–25] The synthesis of fused borane/amine type nanographenes such as 5,9-diphenyl-5,9-diaza-13b-boranaphtho[3,2,1-de]anthracene deserves a special interest in this respect. This compound exhibits multiresonant thermally activated delayed fluorescent (MR-TADF) resulting from the relaxation of local singlet exciton (^{1}LE) states.[26–29] However, complicated synthesis of nanographene-type of compounds may limit wide applications of these superior MR-TADF emitters. Optoelectronic properties of TADF emitters can be further improved by using hosts differing in their dielectric constants and rigidity or by depositing TADF emitters from specially selected solvents that assure a significant reduction of the conformational disorder in the emitting layer.[30] In the best case, when single crystalline form is used, it is possible to generate TADF from one conformer only of an emitter of polymorphic nature.[31,32] However, TADF OLEDs with crystalline emitting layers are not yet known. These instructive examples clearly demonstrate a crucial role of the conformer disorder restriction in the improvement of the electroluminescent properties of TADF emitters.

Aiming at developing OLEDs with the crystalline emitting layers and improved properties, we have selected three recently synthesized, relatively simple compounds, namely 2-phenoxazine-*N*-hexylacridone (**PHhA**), 2,7-bis-(phenoxazine)-*N*-hexylacridone (**bPHhA**), and 2,7-bis[3-(phenoxazine)phenyl]-*N*-hexylacridone (**PHPhhA**) as TADF emitters (**Figure 1**a). These compounds combine bipolar charge transport properties with AIEE resulting in high photoluminescent quantum yields (PLQYs) in the solid-state and good electroluminescence performances (yellow TADF OLEDs fabricated using luminophore **PHhA** exhibit maximum EQEs of 16.7%).[33,34]

In this article, we report on thermally controllable tuning of emission properties of **PHhA**, **bPHhA** and **PHPhhA** as well as on their mechanochromic luminescent properties. The emission spectrum of amorphous **PHhA** films (peaked at 557 nm) is hypsochromically shifted by 92 nm (from yellowish orange to blue) upon its crystallization. In contrast to many other mechanochromic luminophores,[35–37] phenoxazine-substituted acridones demonstrate thermally controllable self-assembly effects. Reversible switching of the emission color is observed for **PHhA** without application of largely "uncontrollable" stimuli such as mechanical forces or solvent vapors. Amorphous vacuum-deposited films of **PHhA**, **bPHhA** and **PHPhhA** exhibit TADF properties that are lost upon crystallization. However, in the presence of hosts turn on of TADF is observed. This TADF effect results from equalization of the fixed LE state and CT state moveable by the solid-state solvation effect.[20] Host-based films are characterized by relatively inefficient TADF due to the "dark" states of molecules exhibiting large dihedral angles between the donor and the acceptor moieties approaching 90°. This structural arrangement efficiently breaks the overlap of π orbitals. When the dihedral angle is decreased due to annealing-induced conformational equilibration, the TADF efficiency is significantly improved. In particular, TADF with PLQY of 100% and reverse intersystem crossing rates (k_{RISC}) of 1.92×10^6 s^{-1} are achieved in the case of **PHhA**. A very similar behavior is observed for **bPHhA**. However, equalization of LE and CT states is not observed for the crystalline form of **PHPhhA** because of a rather wide energy gap between these states. Notably, by exploiting the concept of annealing-induced conformational equilibration we were able to fabricate devices exhibiting a record value of EQE (up to 20.7%), ever reported for OLEDs with the crystalline emitter.

2. Results and Discussion

2.1. Thermal Analysis

In view of the application of **PHhA**, **bPHhA** and **PHPhhA** as thermally tuneable crystalline electroluminophores in OLEDs, their thermal properties were investigated by thermogravimetry (TG) and differential scanning calorimetry (DSC). The results of these analyses allow us to precisely determine the optimal annealing temperature of the deposited films. Representative DSC and TG scans are presented in Figure 1b and Figure S1 (Supporting Information) whereas the complete set of the obtained data can be found in **Table 1**. **PHhA** is thermally stable to temperatures exceeding 300 °C. Its 5% mass loss temperature

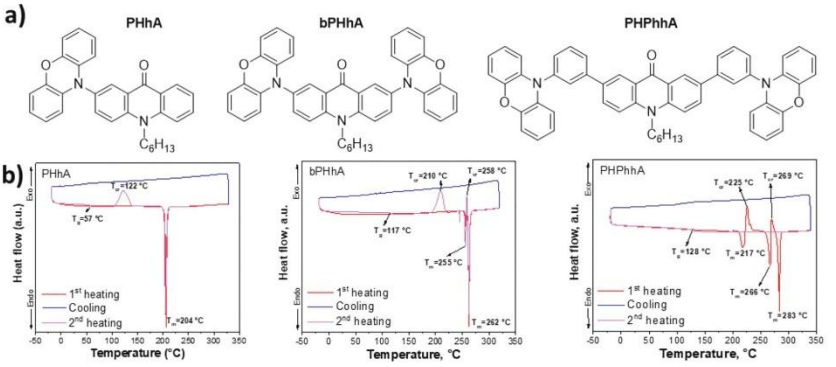

Figure 1. Molecular structures a) and TGA curves b) of PHhA, bPHhA and PHPhhA.

Table 1. Thermal characteristics of **PHhA**, **bPHhA** and **PHPhhA**.

Compound	$T_{d\text{-}5\%}$, °C	T_g, °C	T_{cr}, °C	T_m, °C
PHhA	343	57	122	204
bPHhA	408	117	210, 258	255, 262
PHPhhA	441	128	225, 269	217, 266, 283

5% mass loss temperature ($T_{d\text{-}5\%}$); glass-transition temperature (T_g); crystallization temperature (T_{cr}); melting temperature (T_m).

($T_{d\text{-}5\%}$, °C) is of 343 °C (Figure S1, Supporting Information). As prepared **PHhA** is crystalline. This is evidenced by a distinct endothermic melting peak appearing at 204 °C in the first DSC scan. Upon cooling, **PHhA** forms a molecular glass with no crystallization peak detectable. Its glass-transition temperature (T_g) of 57 °C can be determined from the second heating scan. In this scan the glass transition is followed by crystallization at 122 °C, manifested by the appearance of a clear exothermic peak (Figure 1b). Thermal behaviours of **bPHhA** and **PHPhhA** are similar, however their T_m, T_g and T_{cr} are, significantly higher (Table 1).

2.2. Photophysical Properties of Solutions

To reveal possible solvatochromic properties of **PHhA**, **bPHhA** and **PHPhhA**, two solvents differing in their dielectric constants were selected, namely hexane (ϵ = 1.88)) and tetrahydrofuran (THF, ϵ = 7.58). Absorption spectra of the studied compounds dissolved in hexane and THF were essentially identical (**Figure 2**a–c), closely resembling those previously reported for toluene solutions.[33] In addition to the spectral features of acridone and phenoxazine, a weak absorption band at the wavelengths exceeding 400 nm is observed, which should be attributed to the CT electronic transition. Because of higher solvent polarity, PL spectra of THF solutions of **PHhA** and **bPHhA** were red-shifted and characterized by the increased full width at half maximum (FWHM) as compared to the corresponding spectra of the hexane solutions (Figure 2a–c). This observation together with the presence of the CT absorption band confirms the CT luminescence.[20] In particular, the first singlet excited state (^{1}CT) of **PHhA**, determined from the onsets of the corresponding PL spectra, was found solvent dependent, i.e., lower for the solution in more polar THF ($^1CT_{THF}$ = 2.58 eV) as compared to the solution in less polar hexane ($^1CT_{Hex}$ = 2.8 eV). The determined ^{1}CT state of **PHhA** was energetically inferior to the ^{1}LE states of phenoxazine (^1LE_D = 3.51 eV) and N-hexylacridone (^1LE_A = 3.16 eV), i.e., molecules mimicking the electron donating and electron accepting parts of **PHhA** (Figure 2d,e). Very similar regularity was observed in the case of **bPHhA**.

In contrast, PL spectrum of **PHPhhA** dissolved in THF revealed the presence of two distinct bands, whereas the spectrum of its solution in hexane nearly coincided with the corresponding spectrum of N-hexylacridone. The observed two fluorescence bands can be treated as a typical feature of twisted internal charge transfer (TICT) states attributed to different molecular conformations with a barrier between them.[38]

2.3. Tuning of Emission Properties of Powders

As prepared crystalline powders of **PHhA**, **bPHhA** and **PHPhhA** emit blue, yellow and green light, respectively, yielding PL spectra peaked at 486, 571, and 558 nm (**Figure 3**a). These spectra are shifted with respect to the corresponding spectra of their vacuum-deposited films that show maxima at 565, 581, and 549 nm (Figure S2a–c, Supporting Information), indicating mechanochromic-type (MC) luminescence of the studied derivatives. Indeed, their emissions properties can be widely tuned by different external stimuli such as grinding, fuming in solvent vapours, heating up to the melting temperature, heating (thermal annealing) up to their crystallization temperature (see Table 1).

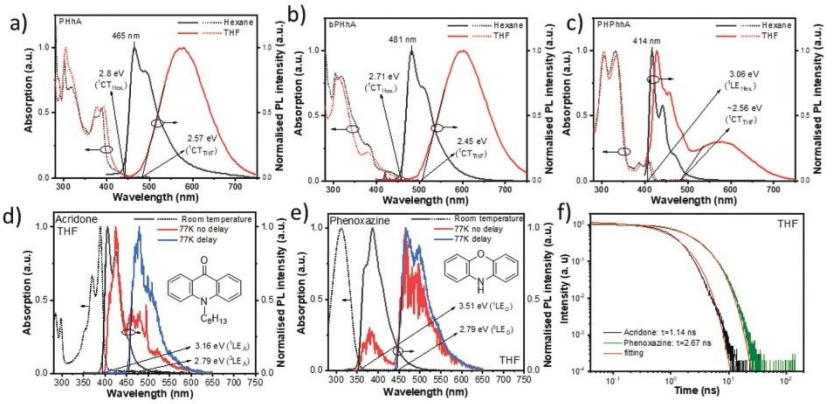

Figure 2. Absorption and PL spectra a–e) of the solutions of **PHhA**, **bPHhA** and **PHPhhA** together with the corresponding spectra of the solutions of electron accepting N-hexyl acridone and electron donating phenoxazine. PL decay curves f) of THF solutions of N-hexylacridone and phenoxazine. The spectra recorded with delay of 1 ms after excitation are considered as the spectra of phosphorescence of acridone or phenoxazine.

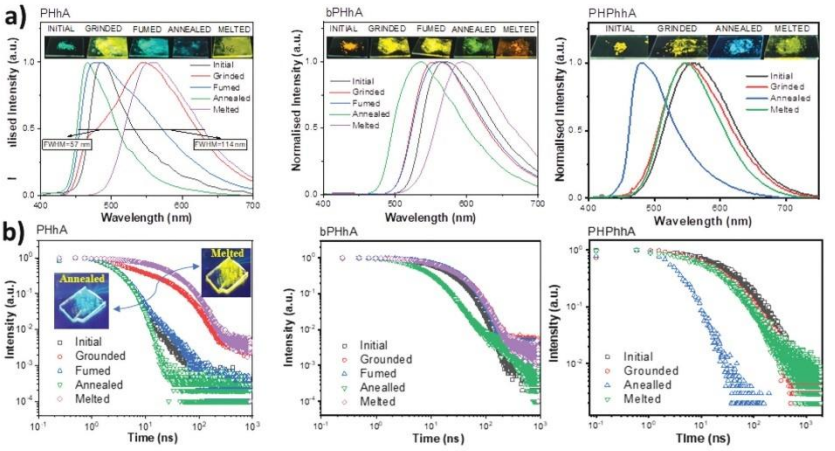

Figure 3. Mechanoluminescent properties of **PHhA**, **bPHhA** and **PHPhhA**. PL spectra a) and PL decay curves b) of their pristine samples and after the action of external stimuli (grinded, fumed, annealed, melted). Insets (a) show photos of the samples under UV excitation. Insets (b) show photos of reversible switchable PL colours of PHhA observed in air (Video S1, Supporting Information).

The PL spectrum of melted **PHhA** shows a clear maximum at 557 nm, i.e., in the yellow spectral range, thus it is bathochromically shifted with respect to that registered for the pristine crystalline sample. Its PL decay curve exhibits a short-lived component with the lifetime (τ_1) of 42.3 ns typical of prompt fluorescence (PF) and a long-lived component with the lifetime (τ_2) of 3108 ns characteristic of delayed fluorescence (DF) (Figure 3b; Figure S2d, Supporting Information).

The annealed sample of **PHhA** shows strikingly different luminescent properties. Its emission spectrum peaked at 465 nm is hypsochromically shifted with respect to that of the pristine sample. Moreover, it closely resembles the PL spectrum of **PHhA** dissolved in hexane. It is also bathochromically shifted with respect to the LE emission bands of the solutions of N-hexylacridone and phenoxazine (Figure 2d,e). The discussed hypsochromic shift of the ^{1}CT emission of annealed crystalline sample has its origin in the conformation restrictions and solvation disorders characteristic of the solid state. These phenomena will be discussed below. The blue shifted ^{1}CT emission of the annealed **PHhA** is characterized by a short lifetime (τ_1) of 2.8 ns typical of prompt fluorescence. The long-lived fluorescence is not detectable. This lifetime is slightly longer than those estimated for ^{1}LE emissions of the solutions of N-hexylacridone (1.14 ns) and phenoxazine (2.67 ns) (Figure 2f). PL spectra and PL decay curves of the annealed **PHhA** are practically insensitive to the presence of oxygen in contrast to those recorded for melted **PHhA** (Figure S3a,b, Supporting Information). It can therefore be concluded that the yellow emission of melted **PHhA** is TADF in nature, whereas the blue emission of annealed **PHhA** is not TADF. Similar observations were previously reported for different MC compounds that demonstrated the turn-on/turn-off TADF properties under external stimuli.

Variation of emission colors of the studied compounds in their powder form upon application of the external stimuli can be attributed to their different crystallinity (Figure S4, Supporting Information). This attribution is confirmed by X-ray diffractograms for the pristine sample of **PHhA** and powders subjected to grinding, then annealing, then melting, then annealing which show the crystallinity indices of 46.3, 88.6, 86.2, 49.8, 61.1%, respectively (see Supporting Information for the crystallinity estimation). Combining the results of X-ray diffraction and photophysical studies, it can be concluded that the thermal annealing at T_{cr} leads to an increase of the powders crystallinity which, in turn, results in hypsochromic shifts of their emission spectra. It should be noted that such emission alterations are reversible. For example, the yellow emission of melted **PHhA** can be tuned to blue by heating and thus converting melted **PHhA** into more crystalline annealed **PHhA**. Blue emission of the latter can be tuned back to yellow by melting (Video S1, Supporting Information).

The molecular arrangement of **PHhA** in the solid state is tuneable upon crystallization. As a result, PL spectra of different shapes are observed for various forms of **PHhA**. The yellow emission of melted **PHhA** is characterized by a structureless PF spectrum with FWHM of 114 nm and a lifetime τ_1 of 42.3 ns. Distinctly different spectral characteristics are observed for blue emission of annealed **PHhA**. Its PF spectrum exhibits a resolved vibronic structure with FWHM of 57 nm and a short lifetime of 2.8 ns (cf. Figure 3a,b). As already stated, the emission spectrum of annealed **PHhA** is very similar to the PL spectrum of this compound dissolved in hexane (Figure 2a). It can therefore be postulated that the crystallization makes the ^{1}CT emission of annealed **PHhA** insensitive to polarity of the environment.

The spectral features of **bPHhA** and **PHPhhA** can be also interpreted as originating from ^{1}CT emissions (Figure 3a). PL spectra characterized by FWHM of ca. 103 nm are obtained for the pristine powder of **bPHhA** and powders subject to external stimuli (grinding, fuming, annealing or melting). MC properties of **bPHhA** and **PHPhhA** are most plausibly caused by different changes of dihedral angles between the phenoxazine and acridone moieties. Apart from hexane solution (Figure 2c), no manifestation of ^{1}LE emission is detected for other forms of **PHPhhA** (Figure 3a). PL spectra of the powders reveal the following lowest FWHMs: 57 nm for **PHhA**, 103 nm for **bPHhA** and 73 nm for **PHPhhA**. Thus, **PHhA** is the most promising emitter for OLED applications as far as the device color purity is considered. Similar FWHM values are found for PL spectra of **PHhA** and **bPHhA** dispersed in ZEONEX matrices (73 nm and 87 nm, respectively) (**Table 2**). **PHPhhA** dispersed in ZEONEX is characterized by the widest PL spectrum with FWHM of 156 nm, due to overlapping of ^{1}LE and ^{1}CT emissions. Such overlapping is also observed for THF solutions of this compound (Figure 2a; Figure S5, Supporting Information).

2.4. Tuning Emission Properties of Vacuum Deposited Films

Emission properties of vacuum-deposited films of phenoxazine-substituted acridones **PHhA**, **bPHhA** and **PHPhhA** can also be tuned by thermally controllable crystallization (**Figure 4**; Figure S6, Supporting Information). Vacuum-deposited **PHhA** films are fully amorphous as it is evidenced by their XRDGI diffractograms (Figure 4c). Their PL spectra are very similar to that registered for **PHhA** in its melted powder form (Figure S2, Supporting Information). The thermal annealing of this amorphous film at T_{cr} of 122 °C results in a hypsochromic shift of its spectrum from 565 to 467 nm (Figure 4a). Similarly, as in the case of powders, this shift is induced by crystallization. The crystallinity index determined from the diffractograms reaches 68%. The turn-on/turn-off TADF properties for the amorphous and crystalline films of **PHhA** are demonstrated by their distinctly different PL decay curves (Figure 4b). The crystalline films of **PHhA** show no TADF due to large ΔE_{ST} of 0.28 eV (Figure S3c, Supporting Information). It should be noted that by changing the degree of crystallinity through the variation of the annealing time, it is possible to tune the emission color of the vacuum deposited films (Figure 4e). As in the case of powders (Video S1, Supporting Information), these color changes are reversible. Thus, yellow emission of **PHhA** can be tuned to green or blue by thermal annealing at T_{cr} and then returned back to yellow by heating up to T_m followed by cooling (Figure 4e).

It should be noted that TADF properties of as-prepared films of **PHhA** are very similar to those of 9,9-dimethyl-9,10-dihydroacridin4,6-triphenyl-1,3,5-triazine (DMAC-TRZ).[120] The steady–state and time-resolved PL spectra of the dispersions of DMAC-TRZ in matrices of low and high polarity vary as a consequence of different conformational and static dielectric disorders. These data are in a very good agreement with the results of the theoretical calculations, which additionally predict a blue-shifted spectrum at the relaxation time of zero that is not

Table 2. Photophysical parameters of the annealed films of the molecular dispersions of **PHhA**, **bPHhA** and **PHPhhA** in ZEONEX obtained under inert atmosphere.

Sample	FWHM, nm	PLQY, %	τ_{PF}, ns	τ_{DF}, ns	A1, %	A2, %	Φ_{PF}, %	Φ_{DF}, %	k_{PF}, s^{-1}	k_{DF}, s^{-1}	k_{ISC}, s^{-1}	k_{RISC}, s^{-1}
PHhA :ZEONEX	73	99.45	16.6	53 776	0.96	99.04	0.95	98.50	5.7×10^5	1.83×10^4	5.68×10^5	1.92×10^6
bPHhA :ZEONEX	87	99.82	22.8	44 157	1.5	98.5	1.52	98.3	6.7×10^5	2.234×10^4	6.58×10^5	1.46×10^6
PHPhhA :ZEONEX	156	36.5	26.6	44 908	2.4	97.60	0.88	35.63	3.3×10^5	7.93×10^3	3.2×10^5	3.3×10^5

FWHM, PLQY, prompt fluorescence lifetime (τ_{PF}), delayed fluorescence lifetime (τ_{DF}), fractional intensities of prompt (A1) and delayed (A2) fluorescence obtained through fitting of photoluminescence decay curve using the formula $I_{PL} = A1^{*}\exp(-t/\tau_{PF}) + A2^{*}\exp(-t/\tau_{DF})$,[40] quantum yields of prompt (Φ_{PF}) and delayed fluorescence (Φ_{DF}), prompt (k_{PF}) and delayed (k_{DF}) fluorescence rate constant, intersystem crossing rate constant (k_{ISC}), reverse intersystem crossing rate constant (k_{RISC}).

experimentally reachable for DMAC-TRZ. In line with the theoretical predictions,[20] the annealed films of **PHhA** show blue-shifted emission spectra. The shift can apparently be attributed to the crystallization-driven restrictions of conformational and static dielectric disorders. The theoretical predictions suggest for DMAC-TRZ different TADF efficiencies depending on the dihedral angles between the donor and acceptor parts of the molecule. X-ray analyses of of **PHhA** in its single crystal form (Figure 4d), reveal the dihedral angle between the phenoxazine and N-hexylacridone moieties of 81.83°. It seems that large majority of **PHhA** molecules in annealed films should also be characterized by the same dihedral angle. This observation supports the postulate of a drastic decrease of the conformational and static dielectric disorders due to crystallization in the annealed films of **PHhA**. The observed annealing induced blue-shift of the PL spectrum can be considered as a spectroscopic manifestation of these phenomena. In contrast, considerable conformational and static dielectric disorders can be predicted for pristine amorphous films of **PHhA**. Such disorders lead to the bathochromically shifted PL spectrum. It is expected that molecules in these films are more twisted and the dihedral angle between their donor and acceptor parts significantly exceeds 81.83° and approaches 90°. This, in turn, leads to the redshifted emission. This expectation is clearly confirmed by the results of theoretical investigations presented in our previous study.[33] The bathochromic shift of the emission observed for amorphous films of **PHhA** could be also caused by molecular freedom (vibration) leading to conditions in which the dihedral angles are not constant. Spectroscopic investigation of vacuum-deposited films of **bPHhA** and **PHPhhA** yield very similar results (Figure S5, Supporting Information).

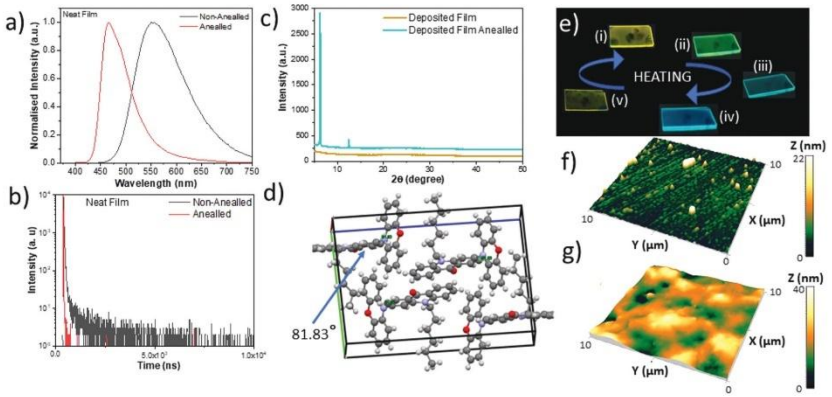

Figure 4. PL spectra a) and PL decay curves b) of vacuum deposited film of PHhA recorded before and after annealing. XRDGI diffractograms c) of vacuum deposited film of PHhA recorded before and after thermal annealing. Molecular packing and the estimated dihedral angle of 81.83° between phenoxazine and acridone moieties of PHhA d). The Figure was prepared using the data published in ref.[33] Images e) of the vacuum deposited film of PHhA after different annealing conditions (initial film (i) (before annealing), annealed films at ≈T_{cr} during ca. 5 (ii), 10 (iii), 15 (iv) min, and film obtained after reaching T_m and rapidly cooled down (v) under UV excitation. AFM topographical images with normalized Z axis in nanometres of as prepared f) and annealed g) vacuum deposited films of PHhA. The images were acquired in air using contact mode.

Table 3. Electroluminescent parameters of devices based on non-annealed and annealed light-emitting layers containing **PHhA** as the emitter and one of the following hosts: NPB, mCBP, SM-66, TCTA.

Device	Light-emitting layer	λ_{max}, nm	V_{on}, V	L_{MAX}, cd/m^2	Max. CE, cd/A	Max. PE, lm/W	Max. EQE, %
MoO_3(0.35 nm)/ NPB(44 nm)/ Light-emitting layer (24 nm)/ TSPO1(4 nm)/ TPBi(40 nm)/LiF(0.35 nm)/Al							
1	NPB:PHhA	523	5.9	5710	3.6	1.5	1.1
1A	Annealed NPB:PHhA	524	6.1	10 210	3.4	1.3	1.0
2	mCBP:PHhA	527	4.7	21 080	15.3	8.1	4.2
2A	Annealed mCBP:PHhA	527	5.3	16 910	21.9	9.5	5.9
3	SM-66:PHhA	500	5.7	4410	15.1	6.9	5.8
3A	Annealed SM-66:PHhA	495	5.2	3280	21.3	12.2	10.11
4	TCTA:PHhA	526	4.3	15 990	30.1	17.5	8.6
4A	Annealed TCTA:PHhA	526	3.8	14 800	62.4	49.1	20.7
5	PHhA	545	5.6	17 250	6.2	2.4	1.9
5A	Annealed PHhA	520	5.7	9700	3.5	1.6	1.1

EL maximum (λ_{max}); turn-on voltage (V_{on}); maximum brightness (L_{MAX}); maximum current (CE); power (PE) and EQE efficiencies.

To check whether the surface morphology of thermally annealed films is appropriate for the fabrication of "crystalline" OLEDs, atomic force microscopy (AFM) measurements were performed for as prepared and annealed films of PHhA vacuum-deposited on a glass substrate (Figure 4f,g). The AFM image of the nonannealed film shows relatively homogeneous surface with some morphological features having a mean height of 4.44 nm and the root mean square roughness (R_q) of 2.50 nm. The surface is dominated by peaks with skewness (R_{sk}) value of 4.26 and has a leptokurtoic distribution of the morphological features with kurtosis (R_{ku}) value of 27.3, indicating relatively many high peaks and low valleys. In contrast, the annealed film surface is slightly rougher with randomly oriented surface mounds having a mean height of 18.83 nm and R_q value of 6.35 nm. It exhibits different symmetry and platykurtoic distribution of the morphological features with R_{sk} and R_{ku} values of 0.15 and 2.89, respectively. Both non-annealed and annealed films exhibit relatively low roughness values which are acceptable for OLEDs.

2.5. Tuning Emission Properties of the Films of Guest-Host Molecular Mixtures

As it is stated above, vacuum-deposited annealed films of PHhA showed no TADF effect. Thus, their use as emissive layers did not yield OLEDs with high EQE (**Table 3**: Device 5 and Device 5A). To achieve triplet harvesting, hosting effects were additionally investigated for PHhA. PL spectrum of a molecular dispersion of PHhA (1 wt.%) in an inert polymer matrix (ZEONEX) is shown in **Figure 5**a. Its emission band peaking at 513 nm hypsochromically shifts to 476 nm upon thermal annealing at T_{cr}.

The different shapes of the PL spectra of the non-annealed and annealed samples suggest that annealing reduces the conformational and/or solvation disorder. Conformationally equilibrated molecules exhibit better TADF properties.[20] It should be noted that such differences of emission may also be caused by the crystallization of PHhA in the annealed film. The crystallinity indices, determined from the XRDGI diffractograms, are of 37.5% and 78.6% for the annealed samples of 10% and 20% molecular dispersions of PHhA in ZEONEX, respectively (Figure 5b; Figure S6, Supporting Information). Thus, annealing-induced crystallization plays a significant role in the improvement of luminescent properties of the studied PHhA /ZEONEX films.

The PL decay curves of the non-annealed and annealed samples of PHhA dispersed in ZEONEX exhibit shapes characteristic of TADF emitters (Figure 5d).[15] Annealing significantly increases the TADF efficiency. In the case of pristine dispersions of PHhA, emission intensities measured in vacuum (I_{vac}) were higher than those recorded in air (I_{air}) by a factor of 2.3 (Figure S8, Supporting Information). In the case of annealed dispersions, the recorded value of I_{vac} was 6 times higher than that of I_{air} (Figure 5c). This observation can be rationalized by the sensitivity of triplet states to oxygen. In vacuum, i.e., in the absence of oxygen, the non-emissive relaxation of triplet states essentially does not exist. The triplet harvesting ability is improved via reverse intersystem crossing. This improvement is manifested in the PL decay curves as an enhancement of the component of the long-lived emission (Figure 5d). The following PLQY values were measured in air with an integrated sphere for the molecular mixtures of the studied compounds with ZEONEX: 14.6% PHhA 15.4% for bPHhA and 6.7% for PHPhhA. The following ratios of the emission intensities determined in vacuum and in air (I_{vac}/ I_{air}) were found: 6.8, 6.5, and 5.44, respectively for PHhA, bPHhA and PHPhh molecular mixtures in ZEONEX. Thus, it can be concluded that the annealed dispersions of compounds PHhA and bPHhA in ZEONEX reach the total PLQY values close to 100% (Table 2). These high PLQY values originate from the combination of AIEE and TADF. The lifetimes of prompt fluorescence (PF) and delay fluorescence (DF), obtained from the biexponential fitting of the PL decay curves are collected in Table 2, Tables S1 and S2 (Supporting Information). By integrating the areas under the PL decay curves recorded in vacuum for the dispersions of PHhA and bPHhA in ZEONEX, percentages of PF and DF contributions as well as the quantum yields of PF (Φ_{PF}) and DF (Φ_{PF}) were obtained. These data were used for the calculation of the rate constants of decays of prompt fluorescence (k_{PF}) and

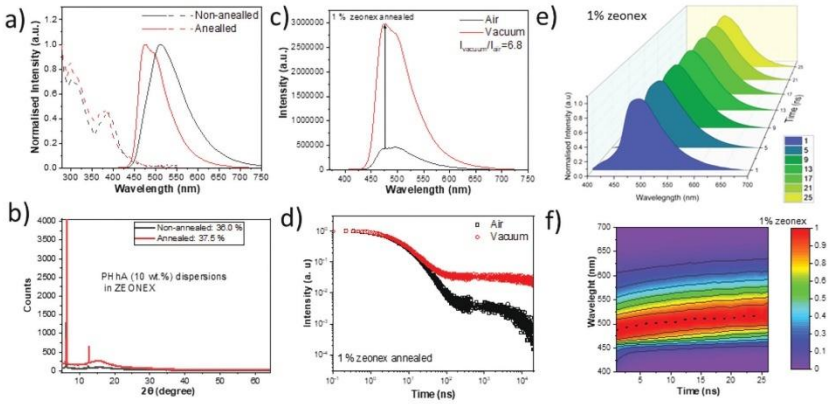

Figure 5. Absorption and PL spectra of molecular dispersions of PHhA (1 wt.%) in ZEONEX a), XRDGI diffractograms of molecular dispersion of PHhA (10 wt.%) in ZEONEX before and after annealing b). PL spectra c), PL decay curves d) and time-resolved PL spectra e,f) of the annealed films of molecular dispersion of PHhA (1 wt.%) in ZEONEX recorded in air and in vacuum.

delayed fluorescence (k_{DF}) as well as rate constants of intersystem crossing (k_{ISC}) and reverse intersystem crossing (k_{RISC}). Details of these calculations can be found in Supporting Information. Those calculations were provided according to the previously reported procedure.[39,40] Using that calculation procedure, the proportion of delayed fluorescence of PHhA molecularly dispersed in ZEONEX reached 99%. The authors of the referenced papers [39,40] also observed much lower efficiency of prompt fluorescence in comparison to the efficiency of delayed fluorescence of the studied TADF emitters. Thus, our result is in good agreement with the corresponding proportions of the previously studied TADF emitters.[39,40] The obtained k_{RISC} values (1.92×10^6 s^{-1} for PHhA, 1.46×10^6 s^{-1} for bPHhA and 3.3×10^5 s^{-1} for PHPhhA) are among the highest ever reported for TADF emitters.[39–42] In addition, the k_{RISC} values are higher than the corresponding k_{ISC} values (5.68×10^5 s^{-1} for PHhA, and 6.58×10^5 s^{-1} for bPHhA and 3.2×10^5 s^{-1} for PHPhhA). The ratios k_{RISC}/k_{ISC} exceeding 1 indicate faster RISC than ISC which efficiently prevents from the non-emissive energy losses via triplet states. In order to better understand why the process of RISC with the energy barrier is faster than the process of ISC without the energy barrier, we consider El Sayed's rule which suggests that RISC between electronic states of a similar nature such as π-π^* CT states is forbidden.[43] Thus, RISC in TADF compounds occurs via the intermediate ^{3}LE excited state but not via the direct interconversion between pure triplet ^{3}CT and singlet ^{1}CT excited states. Similarly, the efficient ISC process in donor–acceptor compounds can be expected when there is an intermediate 3LE excited state between singlet ^{1}CT and triplet ^{3}CT excited states.[44] In the case of compounds PHhA, bPHhA and PHPhhA, the energies of ^{1}LE states of phenoxazine ($^1LE_D = 3.51$ eV) and N-hexylacridone ($^1LE_A = 3.16$ eV) are higher than those of the corresponding ^{1}CT and 3CT states (Figure 2). Thus, both ISC and RISC processes might not be as efficient as could be expected at the first glance. In that case, the other parameters, e.g., different relaxation rates of singlets and triplets should be considered. In addition, the mixing of the energy levels should be considered.[45] Since the emissive relaxation rates of singlets are much higher than the non-emissive relaxation rates of triplets, RISC processes can be more efficient than the ISC processes for the annealed dispersions of PHhA, bPHhA and PHPhhA in ZEONEX according to the data collected in Table 2.

2.6. Ultrafast Time-Resolved Spectroscopy

Ultrafast time-resolved photoluminescence and transient absorption (TA) studies were performed with the goal to elucidate the mechanism of the strong TADF enhancement measured for annealed samples of PHhA dispersed in ZEONEX. Pristine and annealed samples of two different molecular dispersions of PHhA in ZEONEX (1 wt.% and 10 wt.%) were investigated. **Figure 6**a,e show time-resolved PL spectra for pristine and annealed samples recorded at the different delay time after excitation. PL spectra of the pristine samples are broader. However, the PL spectra of both pristine and annealed samples show no significant changes in their shape with time. In the case of annealed sample of 1 wt.% dispersion of PHhA in ZEONEX continuous shift of the PL spectrum in broader timescale (Figure 5e,f). In general, time-resolved shifts of the solid state PL spectra of compounds exhibiting the TADF are attributed to the conformation disorder.[46,47] They are common for practically all conventional TADF compounds since it is very difficult to elaborate the conformation disorder-free TADF systems.[24,48] The important difference between pristine and annealed samples appears in their

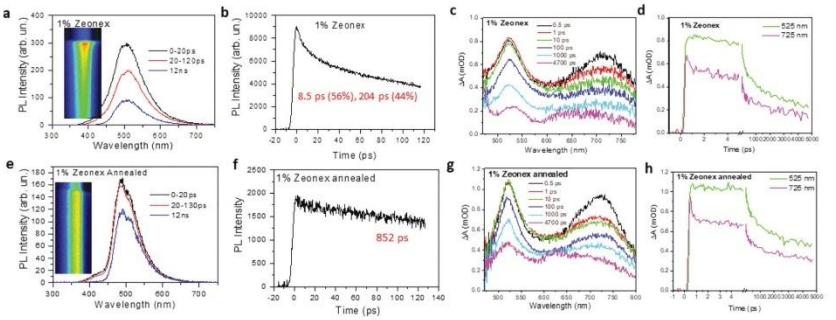

Figure 6. PL spectra a,e) and PLdynamics b,f), as well as TA spectra c,g) and dynamics d,h) of pristine (top plots) and annealed (bottom plots) films of 1% dispersion of PHhA in Zeonex.

PL decay dynamics (Figure 6b,f). The PL of the pristine sample shows a ps decay component which is absent in the PL decay curve of the annealed sample.

Figure 6c,g and Figure 6d,h show the TA spectra recorded at different delay times after excitation and the TA decay dynamics determined for the pristine and the annealed samples. The spectra are dominated by two induced absorption bands. No negative band due to the stimulated emission is observed in the fluorescence band region. This can be considered as an additional indication of the CT origin of the PL bands. CT transitions are characterized by the low dipole moment, apparently much lower than that typical of the transitions to higher excited states. Therefore, the latter dominate in TA spectra.

In contrast to the PL decay, the TA dynamics show no significant differences between the pristine and the annealed samples. Different PL and TA behaviors indicate that the fast PL decay observed for the pristine samples may hardly be caused by the relaxation of excited molecules to the ground state. Such decay would also result in significant differences in the TA decays determined for the pristine and the annealed samples, which is not observed. More likely, a fraction of excited molecules in the pristine sample experience fast relaxation to a nonradiative excited state. Such "dark" state can be formed if the N-hexylacridone and phenoxazine moieties twist perfectly perpendicularly to each other, efficiently breaking the overlap of π orbitals. It can therefore be postulated, that a fraction of conformationally disordered PHhA molecules in ZEONEX have sufficient freedom to twist to the perpendicular conformation in the excited state, causing fast PL decay.

Better time resolution of TA measurements reveals additional processes which are not observed in the PL decay curves. The long wavelength induced absorption band experiences ultrafast partial decay during less than 1 ps. Although it is difficult to unambiguously attribute these spectral dynamics to some electronic or conformational process, we tentatively attribute it to the expected process of relaxation of the local excited state (initially created by the 400 nm excitation light) to the CT state. It should also be noted that ultrafast PL and TA dynamics are quantitatively very similar for the film containing 10 wt.% of PHhA in ZEONEX (Figure S9, Supporting Information).

In contrast to the case of pristine samples, no PL and TA spectral changes within the studied timescale are observed for the annealed samples of 1 and 10 wt.% dispersion in ZEONEX (Figure 6; Figure S9, Supporting Information). In addition, PL decays of these samples are characterized by one component in the picosecond range (Figure 6f; Figure S9f, Supporting Information). Considering these spectral features, it can be postulated that essentially all PHhA molecules in the film adopt the most favorable conformations upon annealing. This has to be at least partly caused by the annealing-induced crystallization. This postulate is in a good agreement with the above-described thermally controlled self-assembly/crystallization of neat PHhA and PHhA dispersed in ZEONEX (see diffractograms in Figures 4 and 5).

2.7. Electroluminescence

The effect of the annealing-induced alignment of singlet and triplet excited states of **PHhA** is of crucial importance in view of the application of this compound as a component of OLEDs. For this reason, the detailed studies of its electroluminescent properties were undertaken. OLEDs of the following structure were fabricated and tested: MoO_3(0.35 nm)/ NPB(44 nm)/ light-emitting layer (24 nm)/ TSPO1(4 nm)/ TPBi(40 nm)/LiF(0.35 nm)/Al. The emission layers consisted of 10 wt.% dispersion of **PHhA** in different hosts, namely *N*,*N*′-di(1-naphthyl)-*N*,*N*′-diphenyl-(1,1′-biphenyl)−4,4′-diamine (NPB), 3,3′-di(9*H*-carbazol-9-yl)−1,1′-biphenyl (mCBP), 3,6-di-tert-butyl-9-(2-(1-phenyl-1*H*-benzo[d]imidazol-2-yl)phenyl)−9*H*-carbazole (SM-66), tris(4-carbazoyl-9-ylphenyl)amine (TCTA). Non-annealed and annealed light-emitting layers were investigated in parallel. In the subsequent text the series 1–4 and 1A-4A denote diodes with non-annealed or annealed emissive layers,

respectively. In devices 5 and 5A, fabricated for comparative reasons, the non-annealed and annealed emission layers of neat **PHhA**, respectively were used. The main output parameters of the fabricated devices are listed in Table 3 whereas their photo- and electroluminescent characteristics are collected in Figures S10–S19 (Supporting Information).

The maximum EQE of 1.9% determined for device 5 was slightly lower than the maximum EQE of 2.3% previously reported for the similar devices.[34] Thermal annealing of the emitting layer of neat PHhA resulted in deterioration rather than improvement of the electroluminescent properties. The EQE values estimated for OLED 5A only slightly exceeded 1% (Table 3). This was not unexpected since the annealed layers of neat PHhA did not show any TADF (Figure 3a,b). OLEDs based on non-annealed layer of PHhA(10%) dispersed in mCP, reported in our previous paper also showed higher EQE (13%) than devices (1-4) investigated in this research (Table 3).[34] These differences could be tentatively attributed either to the different hosting properties or to the absence of the exciton blocking mCP layer, or to the unoptimized concentration of the emitter. The non-annealed devices 1–4 demonstrated EQE up to 8.6% when TCTA was used as a host (Table 3). However, a very strong improvement of the maximum EQE values, up to 20.7%, was reached for device 4A containing the annealed emission layer of PHhA dispersed in TCTA. This result is mainly related to the very strong improvement in the TADF properties of the annealed layer of PHhA dispersed in the matrix of an appropriately selected host. The improvement should, at least partly, be attributed to the emitter crystallization. This crystallization is clearly demonstrated by the presence of crystalline phases in the diffractogram of the guest-host emissive layer (see Figure 5b and Table 1). For the same reason, devices 2A and 3A also showed an impressive improvement in their maximum EQE upon annealing of the emissive layer. It should be noted that the studied devices exhibit a large efficiency roll-off. The emitter PHhA was characterized by the bipolar charge-transporting properties, exhibiting higher hole mobility of 1.77×10^{-7} $cm^2 V^{-1} s^{-1}$ than electron mobility of 6.6×10^{-8} $cm^2 V^{-1} s^{-1}$ at the zero electric fields.[34] Moreover, the host TCTA is characterized by hole-transporting properties with hole mobility of 1.77×10^{-7} at the zero electric fields.[49] Because of the hole-electron mobility disbalance in the light-emitting layer, the devices demonstrated large efficiency roll-offs. These explanations well correlate with previously reported discussions on the effects of charge balance and trap state on their output parameters of TCTA-based devices.[50]

Nevertheless, these results unequivocally show that thermal annealing of emissive layers of guest-host nature, containing PHhA as a luminophore, is a key factor in the improvement of the device performance. Most probably, the thermal treatment induces conformational equilibration of singlet and triplet excited states in PHhA favoring, in this manner the efficient TADF. The highest EQE values of device 4A of 20.7% should be attributed to the high rigidity of the of the host. TCTA possess the highest T_g of 151 °C [51] as compared to T_g of other hosts used (95 °C of NPB,[52] 90 °C or mCBP[53] and 100 °C of SM66). It can therefore be expected with high probability that the annealing-induced conformational equilibration, partly caused by crystallization, might lead to large improvement of electroluminescent properties of many organic luminophores, presently considered as inefficient.

3. Conclusions

We have demonstrated that the efficiency and color purity of thermally activated delayed fluorescence of donor–acceptor and donor–acceptor-donor type organic dyes, namely phenoxazine-substituted acridones, can be largely improved by strict control of their conformation and static dielectric disorder in the condensed state. This effect can be relatively easily achieved through appropriate thermal treatment of the emissive layer. Thermally-induced conformational equilibration of the emitter within the host matrix results in: i) strongly improved TADF, characterized by PLQY approaching 100 %; ii) emission spectra with full width at half maxima of 56 nm; iii) high reverse intersystem crossing rate of 1.92×10^6 s^{-1}, and iv) reversible hypsochromic and bathochromic shifts of emission spectra within a broad spectral range (up to 92 nm).

The most promising luminophore, namely 2-phenoxazine-N-hexylacridone (PHhA), was used as an emitter in organic light-emitting diodes in combination with various hosts. The device maximum external quantum efficiency of 8.6% was obtained for diodes with tris(4-carbazoyl-9-ylphenyl)amine host. This value was almost three times improved to 20.7% by thermal annealing of the guest-host emissive layer at the temperature of crystallization of the emitter. The increment of the efficiency of organic light-emitting diodes is attributed to the modification of their light-emitting layers exhibiting thermally activated delayed fluorescence by thermally-induced crystallisation in combination with hosting. Generalization of this approach may result in the development of new efficient TADF luminophores, presently considered inefficient.

Supporting Information

Supporting Information is available from the Wiley Online Library or from the author.

Acknowledgements

This research was supported by the Research Council of Lithuania (Project "ELOS" No S-MIP-21-7). I.K.B. and A.P. acknowledge financial support from the National Science Centre, Poland (NCN, Grant No. 2022/45/B/ST5/02120).

Conflict of Interest

The authors declare no conflict of interest.

Data Availability Statement

The data that support the findings of this study are available on request from the corresponding author. The data are not publicly available due to privacy or ethical restrictions.

Keywords

mechanochromic luminescence, organic light-emitting diodes, thermally activated delayed fluorescence, transient absorption spectroscopy, ultrafast time-resolved spectroscopy

Received: May 8, 2023
Revised: August 4, 2023
Published online: September 8, 2023

[1] Y. Shirota, H. Kageyama, *Chem. Rev.* **2006**, *107*, 953.
[2] Y. Ding, B. Ding, H. Kanda, O. J. Usiobo, T. Gallet, Z. Yang, Y. Liu, H. Huang, J. Sheng, C. Liu, Y. Yang, V. I. E. Queloz, X. Zhang, J. N. Audinot, A. Redinger, W. Dang, E. Mosconic, W. Luo, F. De Angelis, M. Wang, P. Dörflinger, M. Armer, V. Schmid, R. Wang, K. G. Brooks, J. Wu, V. Dyakonov, G. Yang, S. Dai, P. J. Dyson, et al., *Nat. Nanotechnol.* **2022**, *17*, 598.
[3] S.-J. Wang, S. Meister, M. Sawatzki, H. Kleemann, K. Leo, **2020**, *11473*, 114730Q.
[4] C. Wang, X. Zhang, H. Dong, X. Chen, W. Hu, *Adv. Energy Mater.* **2020**, *10*, 2000955.
[5] C. Murawski, K. Leo, M. C. Gather, C. Murawski, K. Leo, M. C. Gather, *Adv. Mater.* **2013**, *25*, 6801.
[6] N. B. Kotadiya, P. W. M. Blom, G. J. A. H. Wetzelaer, *Nat. Photonics* **2019**, *13*, 765.
[7] H. Zhang, D. Q. Lin, W. Liu, Y. C. Wang, Z. X. Li, D. Jin, J. Wang, X. W. Zhang, L. Huang, S. S. Wang, C. X. Xu, Y. H. Kan, L. H. Xie, *Adv. Mater. Interfaces* **2022**, *9*, 2200194.
[8] A. F. Paterson, R. Li, A. Markina, L. Tsetseris, S. Macphee, H. Faber, A. H. Emwas, J. Panidi, H. Bristow, A. Wadsworth, D. Baran, D. Andrienko, M. Heeney, I. McCulloch, T. D. Anthopoulos, *J. Mater. Chem. C* **2021**, *9*, 4486.
[9] X. Yang, X. Feng, J. Xin, P. Zhang, H. Wang, D. Yan, *J. Mater. Chem. C* **2018**, *6*, 8879.
[10] X. Yang, X. Feng, J. Xin, H. Wang, D. Yan, *Org. Electron.* **2019**, *64*, 236.
[11] G. Hu, B. Zhang, S. M. Kelly, J. Cui, K. Zhang, W. Hu, D. Min, S. Ding, W. Huang, *Addit. Manuf.* **2022**, *55*, 102861.
[12] C. Keum, D. Becker, E. Archer, H. Bock, H. Kitzerow, M. C. Gather, C. Murawski, *Adv. Opt. Mater.* **2020**, *8*, 2000414.
[13] J. De, A. H. Abdul, R. A. K. Yadav, S. P. Gupta, I. Bala, P. Chawla, K. K. Kesavan, J. H. Jou, S. K. Pal, *Chem. Commun.* **2020**, *56*, 14279.
[14] Y. Tao, K. Yuan, T. Chen, P. Xu, H. Li, R. Chen, C. Zheng, L. Zhang, W. Huang, *Adv. Mater.* **2014**, *26*, 7931.
[15] H. Uoyama, K. Goushi, K. Shizu, H. Nomura, C. Adachi, *Nature* **2012**, *492*, 234.
[16] Y. Zhu, S. Zeng, B. Li, A. J. McEllin, J. Liao, Z. Fang, C. Xiao, D. W. Bruce, W. Zhu, Y. Wang, *ACS Appl. Mater. Interfaces* **2022**, *14*, 15437.
[17] F. Tenopala-Carmona, O. S. Lee, E. Crovini, A. M. Neferu, C. Murawski, Y. Olivier, E. Zysman-Colman, M. C. Gather, *Adv. Mater.* **2021**, *33*, 2100677.
[18] F. Fang, L. Zhu, M. Li, Y. Song, M. Sun, D. Zhao, J. Zhang, *Adv. Sci.* **2021**, *8*, 2102970.
[19] S. Ullbrich, J. Benduhn, X. Jia, V. C. Nikolis, K. Tvingstedt, F. Piersimoni, S. Roland, Y. Liu, J. Wu, A. Fischer, D. Neher, S. Reineke, D. Spoltore, K. Vandewal, *Nat. Mater.* **2019**, *18*, 459.
[20] D. K. A. Phan Huu, S. Saseendran, R. Dhali, L. G. Franca, K. Stavrou, A. Monkman, A. Painelli, *J. Am. Chem. Soc.* **2022**, *144*, 15211.
[21] T. Serevičius, R. Skaisgiris, J. Dodonova, K. Kazlauskas, S. Juršėnas, S. Tumkevičius, *Phys. Chem. Chem. Phys.* **2019**, *22*, 265.
[22] S. Reineke, *Nat. Mater.* **2015**, *14*, 459.
[23] W. Yuan, H. Yang, C. Duan, X. Cao, J. Zhang, H. Xu, N. Sun, Y. Tao, W. Huang, *Chem* **2020**, *6*, 1998.
[24] T. Serevičius, R. Skaisgiris, I. Fiodorova, G. Kreiza, D. Banevičius, K. Kazlauskas, S. Tumkevičius, S. Juršėnas, *J. Mater. Chem. C* **2021**, *9*, 836.
[25] R. S. Nobuyasu, J. S. Ward, J. Gibson, B. A. Laidlaw, Z. Ren, P. Data, A. S. Batsanov, T. J. Penfold, M. R. Bryce, F. B. Dias, *J. Mater. Chem. C* **2019**, *7*, 6672.
[26] T. Hatakeyama, K. Shiren, K. Nakajima, S. Nomura, S. Nakatsuka, K. Kinoshita, J. Ni, Y. Ono, T. Ikuta, *Adv. Mater.* **2016**, *28*, 2777.
[27] X. Wu, J.-W. Huang, B.-K. Su, S. Wang, L. Yuan, W.-Q. Zheng, H. Zhang, Y.-X. Zheng, W. Zhu, P.-T. Chou, X. Wu, J.-W. Huang, S. Wang, W.-Q. Zheng, H. Zhang, W. Zhu, B.-K. Su, P.-T. Chou, L. Yuan, Y.-X. Zheng, *Adv. Mater.* **2022**, *34*, 2105080.
[28] D. Hall, K. Stavrou, E. Duda, A. Danos, S. Bagnich, S. Warriner, A. M. Z. Slawin, D. Beljonne, A. Köhler, A. Monkman, Y. Olivier, E. Zysman-Colman, *Mater. Horiz.* **2022**, *9*, 1068.
[29] S. Oda, B. Kawakami, Y. Yamasaki, R. Matsumoto, M. Yoshioka, D. Fukushima, S. Nakatsuka, T. Hatakeyama, *J. Am. Chem. Soc.* **2022**, *144*, 106.
[30] P. Data, M. Okazaki, S. Minakata, Y. Takeda, *J. Mater. Chem. C* **2019**, *7*, 6616.
[31] M. Okazaki, Y. Takeda, P. Data, P. Pander, H. Higginbotham, A. P. Monkman, S. Minakata, *Chem. Sci.* **2017**, *8*, 2677.
[32] K. Zheng, F. Ni, Z. Chen, C. Zhong, C. Yang, K. Zheng, Z. Chen, C. Zhong, C. Yang, F. Ni, *Angew. Chem., Int. Ed.* **2020**, *59*, 9972.
[33] I. Kulszewicz-Bajer, M. Zagorska, M. Banasiewicz, P. A. Guńka, P. Toman, B. Kozankiewicz, G. Wiosna-Salyga, A. Pron, *Phys. Chem. Chem. Phys.* **2020**, *22*, 8522.
[34] I. Kulszewicz-Bajer, M. Guzauskas, M. Makowska-Janusik, M. Zagórska, M. Mahmoudi, J. V. Grazulevicius, A. Proń, D. Volyniuk, *J. Mater. Chem. C* **2022**, *10*, 12377.
[35] S. Ito, *J. Photochem. Photobiol. C Photochem. Rev.* **2022**, *51*, 100481.
[36] Z. Chen, D. dian Deng, S. Pu, *Tetrahedron Lett.* **2022**, *107*, 154096.
[37] Y. J. Yu, F. M. Liu, X. Y. Meng, L. Y. Ding, L. S. Liao, Z. Q. Jiang, *Chem. – A Eur. J.* **2023**, *29*, e202202628.
[38] S. Sasaki, G. P. C. Drummen, G. I. Konishi, *J. Mater. Chem. C* **2016**, *4*, 2731.
[39] G. Kreiza, D. Banevičius, J. Jovaišaitė, K. Maleckaitė, D. Gudeika, D. Volyniuk, J. V. Gražulevičius, S. Juršėnas, K. Kazlauskas, *J. Mater. Chem. C* **2019**, *7*, 11522.
[40] T. Serevič, R. Skaisgiris, G. Kreiza, J. Dodonova, K. Kazlauskas, E. Orentas, S. Juršėnas, E. Nas, *J. Phys. Chem. A* **2021**, *125*, 1637.
[41] D. Zhang, X. Song, A. J. Gillett, B. H. Drummond, S. T. E. Jones, G. Li, H. He, M. Cai, D. Credgington, L. Duan, D. D. Zhang, X. Z. Song, G. M. Li, H. Q. He, M. H. Cai, L. Duan, A. J. Gillett, B. H. Drummond, S. T. E. Jones, D. Credgington, *Adv. Mater.* **2020**, *32*, 1908355.
[42] X. Zheng, R. Huang, C. Zhong, G. Xie, W. Ning, M. Huang, F. Ni, F. B. Dias, C. Yang, X. Zheng, C. Zhong, G. Xie, W. Ning, M. Huang, C. Yang, F. Ni, R. Huang, F. B. Dias, *Adv. Sci.* **2020**, *7*, 1902087.
[43] X. K. Chen, S. F. Zhang, J. X. Fan, A. M. Ren, *J. Phys. Chem. C* **2015**, *119*, 9728.
[44] S. Hirata, *Adv. Opt. Mater.* **2017**, *5*, 1700116.
[45] V. Andruleviciene, K. Leitonas, D. Volyniuk, G. Sini, J. V. Grazulevicius, V. Getautis, *Chem. Eng. J.* **2021**, *417*, 127902.
[46] T. Serevičius, R. Skaisgiris, J. Dodonova, I. Fiodorova, K. Genevičius, S. Tumkevičius, K. Kazlauskas, S. Juršėnas, *J. Phys. Chem. Lett.* **2022**, *13*, 1839.
[47] P. L. Santos, J. S. Ward, P. Data, A. S. Batsanov, M. R. Bryce, F. B. Dias, A. P. Monkman, *J. Mater. Chem. C* **2016**, *4*, 3815.
[48] T. Serevičius, R. Skaisgiris, D. Gudeika, K. Kazlauskas, S. Juršėnas, *Phys. Chem. Chem. Phys.* **2021**, *24*, 313.
[49] C. Y. H. Chan, K. K. Tsung, W. H. Choi, S. K. So, *Org. Electron.* **2013**, *14*, 1351.
[50] J. H. Lee, J. Lee, Y. H. Kim, C. Yun, B. Lüssem, K. Leo, *Org. Electron.* **2014**, *15*, 16.
[51] Y. Kuwabara, H. Ogawa, H. Inada, N. Noma, Y. Shirota, *Adv. Mater.* **1994**, *6*, 677.
[52] Y. Tao, C. Yang, J. Qin, *Chem. Soc. Rev.* **2011**, *40*, 2943.
[53] Y. Tsuchiya, N. Nakamura, S. Kakumachi, K. Kusuhara, C. Y. Chan, C. Adachi, *Chem. Commun.* **2022**, *58*, 11292.

Journal of Materials Chemistry C

ROYAL SOCIETY OF CHEMISTRY

PAPER

View Article Online
View Journal | View Issue

Cite this: J. Mater. Chem. C, 2020, 8, 14186

An experimental and theoretical study of exciplex-forming compounds containing trifluorobiphenyl and 3,6-di-*tert*-butylcarbazole units and their performance in OLEDs†

R. Keruckiene, [a] M. Guzauskas,[a] L. Lapienyte,[a] J. Simokaitiene,[a] D. Volyniuk, [a] J. Cameron, [b] P. J. Skabara, *[b] G. Sini *[c] and J. V. Grazulevicius *[a]

Received 11th June 2020,
Accepted 8th September 2020

DOI: 10.1039/d0tc02777d

rsc.li/materials-c

Derivatives of trifluorobiphenyl and 3,6-di-*tert*-butylcarbazole were synthesised as potential components of emitting layers of OLEDs. Molecular design of the compounds was performed taking into consideration the hydrogen bonding ability of the fluorine atom and electron-donating ability of the carbazole moiety. Their toluene solutions exhibited very high triplet-energy values of 3.03 eV and 3.06 eV. Ionisation energies of the compounds in the solid-state were found to be in the range from 5.98 to 6.17 eV. Density functional theory (DFT) calculations using the ωB97XD functional, with the ω parameter tuned in the presence of the solvent, uncovered singlet–triplet energy splitting in good agreement with the experimental results. The materials were tested in the emissive layers of OLEDs, showing the ability to form exciplexes with complementary electron-accepting 2,4,6-tris[3-(diphenylphosphinyl)phenyl]-1,3,5-triazine. Using the synthesised compounds as exciplex-forming materials, highly efficient exciplex emission-based OLEDs were developed. In the best case, a high maximum current efficiency of 24.8 cd A^{-1}, and power and external quantum efficiencies of 12.2 lm W^{-1} and 7.8%, respectively, were achieved.

Introduction

Metal-free organic compounds are widely used in the active layers of organic light emitting diodes (OLEDs).[1–3] Optimization of the properties of emitting layers in OLEDs remains a key research goal in this field. Recently, delayed emission has been extensively adopted for efficient OLEDs, but not all challenges have been solved yet.[4–7] One of the promising ways to obtain cost-effective OLEDs is to employ exciplex-forming systems.[8] An exciplex is defined as an excited-state complex obtained under photo- and electrical excitation between two molecules, one being electron-donating and the other electron-accepting.[9] Exciplex formation plays a role in the conversion from the triplet excited state to the singlet state and hence provides a strategy to improve the performance of OLEDs.[10,11] Due to their dominant CT character, exciplexes are not very effective in light emission. Nevertheless, as these systems possess a small ΔE_{ST}, they have the potential to effectively convert triplet excited states to singlets.[9,12] Furthermore, the intermolecular interactions of the exciplex, involving non-covalent interactions such as hydrogen bonding or van der Waals interactions, between π-conjugated molecular units impact the morphology of the active layers, which also has a close link to the device performance.[13,14] Consequently, the potential to establish such intermolecular interactions is an important criterion in the design of molecular structures, which is manifested through the functionalisation of organic molecules. In addition to making an impact on the stability, oxidation potential, and electrical and optical properties of materials,[15] the number and position of substituents can provide molecules with the potential to establish intermolecular hydrogen and halogen bonds. Intermolecular hydrogen bonding can drive the formation of molecular assemblies with charge-transfer character and dipolar interactions.[16,17] Halogen bonding offers versatility in interaction directions and structurally tuned packing fragments,[18] which was proven to be useful in altering molecular packing for efficient charge transport.[19] Fluorine can be regarded as a useful component of organic electroactive compounds. Recent studies have revealed that fluorine-induced intramolecular interactions including S···F and H···F interactions can promote backbone planarity,[20] enhance the frontier orbital overlaps, tune the solubility, and change the packing motif

[a] Department of Polymer Chemistry and Technology, Kaunas University of Technology, K. Barsausko St. 59, Kaunas, LT-50254, Lithuania. E-mail: juozas.grazulevicius@ktu.lt
[b] WestCHEM, School of Chemistry, University of Glasgow, Joseph Black Building, University Place, Glasgow, G12 8QQ, UK. E-mail: Peter.Skabara@glasgow.ac.uk
[c] Laboratoire de Physicochimie des Polymères et des Interfaces, CY Paris Cergy Université, EA 2528, 5 mail Gay-Lussac, Cergy-Pontoise Cedex 95031, France. E-mail: gjergji.sini@u-cergy.fr

† Electronic supplementary information (ESI) available. See DOI: 10.1039/d0tc02777d

of molecules.[21–23] The extreme electronegativity of the fluorine atom pulls electrons from the backbone to stabilise frontier molecular orbitals, impacting electron transporting characteristics and resulting in a change in intermolecular interactions.[24–26] The hydrophobic nature of fluorinated compounds can also induce air stability of devices by providing resistance to oxygen or water.[27] The particular properties of fluorinated compounds, especially in establishing relatively strong intermolecular interactions, make them interesting candidates for use in exciplex-based OLED devices. To the best of our knowledge, only one fluorinated compound has been used in exciplex-forming systems so far.[28]

In this work, two new compounds bearing trifluorophenyl and carbazole fragments are introduced. Molecular design of the compounds was performed taking into consideration the hydrogen bonding abilities of the fluorine atom and efficient electron-donating abilities of the carbazole moiety.[21]

The impact of the number of donor groups on the properties of the materials is discussed on the bases of results obtained by means of theoretical and experimental approaches. The compounds were shown to be capable of forming exciplexes with appropriate electron-accepting molecules. The exciplex forming molecular mixtures were tested as the emissive materials in OLEDs.

Results and discussion

Synthesis and thermal properties

Compounds **1** and **2** were obtained by a three-step synthesis as illustrated in Scheme 1. Pd-Catalysed Suzuki–Miyaura[29] cross-coupling of 2,4,6-trifluorophenylboronic acid with electron-donating 9-(3-bromophenyl)-3,6-di-*tert*-butylcarbazole or 9,9′-(5-bromo-1,3-phenylene)bis(3,6-di-*tert*-butylcarbazole) was utilised. The yields of products **1** and **2** were 37% and 39%, respectively. They were found to be soluble in common organic solvents.

Table 1 Thermal characteristics of **1** and **2**

Compound	**1**	**2**
T_M,[a] °C	134	292
T_{Cr},[b] °C	—	134
T_{1D},[c] °C	277	369

[a] Melting point observed during the first heating scan of DSC measurement. [b] Crystallisation temperature recorded during the cooling scan of DSC measurement. [c] Initial weight loss temperature obtained from TG curves.

Their structures were confirmed by ^{1}H NMR and ATR-IR spectroscopies and mass spectrometry. Descriptions of the synthesis and characterization of the compounds are given in the ESI.†

Morphological transitions and thermal stabilities of derivatives **1** and **2** were investigated by using DSC and TGA (Fig. S1, ESI†). Their thermal characteristics are shown in Table 1.

As both compounds were isolated after the synthesis and purification as crystalline materials, endothermic melting signals were observed in the 1st heating scans of DSC measurements. Crystallisation and subsequent melting signals were observed during the cooling and 2nd heating scans for compound **2**. The higher melting and crystallisation temperatures of **2** could be attributed to its more symmetrical crystalline structure and overall higher molar mass. No further morphological transitions of sample **1** were detected during cooling and heating scans of DSC measurements, indicating its tendency to be transformed to a solid amorphous state. TGA experiments revealed the complete weight loss of compound **1**, indicating its sublimation, and the impossibility to determine the temperature of onset of thermal degradation.

Geometry and frontier orbitals

The geometries of the target molecules were analysed using DFT calculations at the ωB97XD/6-31++G(d,p) level of theory.

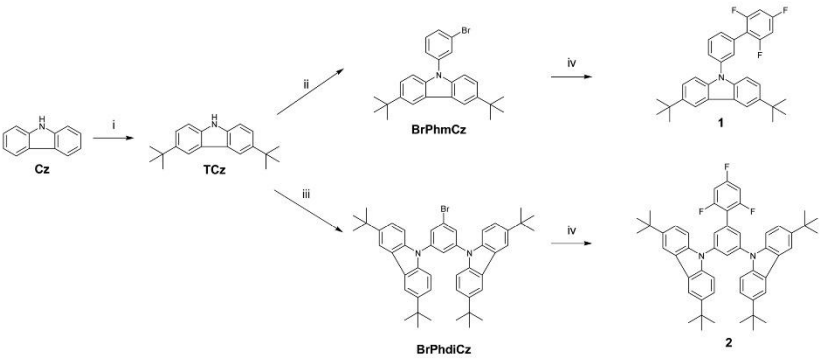

Scheme 1 Synthesis of 2- and 4-trifluoromethylphenyl-substituted di-*tert*-butylcarbazole derivatives: (i) *tert*-butylchloride, $ZnCl_2$, nitromethane, RT, and 24 h; (ii) 1-bromo-3-iodobenzene, Cu, 18-crown-6, KOH, *o*-dichlorobenzene, 180 °C, and 24 h; (iii) 1-bromo-3,5-difluorobenzene, Cs_2CO_3, DMF, 60 °C, and 24 h; (iv) 2,4,6-trifluorophenylboronic acid, Cs_2CO_3, $Pd(PPh_3)_4$, DMF, reflux, and 24 h.

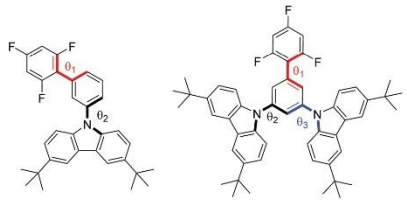

Fig. 1 Structures of **1** (left) and **2** (right) with dihedral angles 1, 2 and 3 denoted in red, black and blue, respectively.

Table 2 Dihedral angles of compounds **1** and **2**. The notation ω-default/diethyl ether means that the CPCM method was used in conjunction with the default value for the ω parameter; ω-CPCM means that the impact of diethyl ether has been included in the ω value, but the corresponding results in the table were obtained with gas phase calculations in conjunction with the tuned ω value

		Dihedral 1 (°)	Dihedral 2 (°)	Dihedral 3 (°)
1	ω-default/diethyl ether	55.7	53.9	—
	ω-CPCM	89.5	81.5	—
2	ω-default/diethyl ether	59.5	53.9	52.8
	ω-CPCM	90.4	80.4	81.5

The dihedral angles are defined in Fig. 1 and summarised in Table 2, whilst the optimised structure and the HOMO and LUMO plots are presented in Fig. 2. The geometry of both compounds was sensitive to the ω-value. It is worth briefly noting

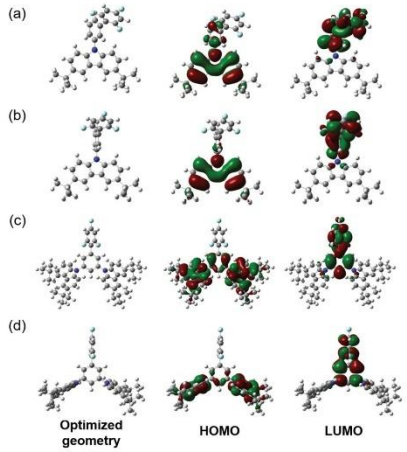

Fig. 2 Optimised geometries (left), the HOMO (centre) and the LUMO (right) for (a) **1** optimised with the default ω; (b) **1** optimised with ω-CPCM; (c) **2** optimised with the default ω and (d) **2** optimised with ω-CPCM.

at this point that the role of the ω-parameter is to split the space of electron–electron interactions into long- and short ranges, the short range being treated at the DFT level, as opposed to the Hartree–Fock level for the long range interactions. By tuning the value of ω in the presence of a solvent, a good part of the medium polarization effect can be included in the geometry and electronic structure of the molecules, resulting in a better description of molecular properties in the bulk. Indeed, the optimisation of **1** carried out by using the default ω-value showed each of the dihedral angles to be in the range of 50–60°, showing significant twisting whilst being far from orthogonal. However, when this geometry was optimised using ω-CPCM instead of the default value, an increase in the dihedral angle was observed, with the trifluorobenzene-phenyl twist essentially orthogonal and the phenyl-carbazole dihedral angle ~80°. An increase in the dihedral angle of ~20–30° when using a tuned ω-value compared to the default (0.2 $Bohr^{-1}$) is consistent with observations reported by Sallenave and co-workers studying carbazole-based materials.[30]

Electrochemical and photoelectrical properties

Cyclic voltammetry was applied to study the electrochemical properties of derivatives **1** and **2** (Fig. S2, ESI†). Both compounds showed reversible oxidation waves. Ionisation energy (IE_{CV}, Table 3) values were estimated from the oxidation onset potentials against ferrocene (E_{ox} onset *vs.* Fc). These values were found to be comparable and correlate well with the energy gap values estimated from the edges of the UV-Vis spectra, indicating similar π-electron conjugated systems in molecules **1** and **2**.

Ionisation energy values (Table 3 and Fig. 3) of the solid samples of compounds **1** and **2** were estimated by photoelectron emission spectrometry. The values of ionisation energies were found to be comparable for both the compounds and were a little higher than those estimated by cyclic voltammetry. Small differences in the values of ionisation energy obtained by employing different methods can be explained by the different environments in the solution and the solid-state.

Optical absorption properties

UV-Vis absorption spectra of the solutions and films of compounds **1** and **2** are shown in Fig. 4. Photophysical characteristics of the compounds are collected in Table 3. Energy gap values determined from the edges of the UV spectra of solutions of derivatives **1** and **2** in toluene were found to be close due to the presence of the same electron-donating moiety in both compounds. The spectra were similar to the absorption spectrum of a toluene solution of carbazole (Fig. S3, ESI†). This observation shows that in solutions and solid films of **1** and **2**, mainly donor local excited states contribute to the absorption properties. Indeed, the oscillator strength corresponding to S_1, which is a CT donor → acceptor transition, exhibits a negligible value, in turn stemming from the nearly orthogonal donor/acceptor dihedral angle. In this situation, the CT $S_0 \rightarrow S_1$ transition becomes invisible or hidden by the more intense local-carbazole low energy band corresponding to the transition $S_0 \rightarrow S_n$ (Table 3). This is consistent with observations from the theoretical calculations. Similarly, structured vibronic absorption bands were observed for the layers of **1** and **2**.

Table 3 Photophysical, electrochemical and photoelectrical characteristics of **1** and **2**

	Toluene solution/thin film								
Compound	λ_{Abs} (nm)	λ_{FL} (nm)	E_g^{opt} (eV)	Stokes shift (cm^{-1})	S1 : T1 (eV)	ΔE_{ST} (eV)	PLQY (%)	IE_{CV} (eV)	IE_{PE} (eV)
1	297, 346/298, 347	354, 370/355, 366, 460	3.49	653/649	3.67 : 3.03/—	0.64	13/1	5.15	5.98
2	297, 346/230, 345	352, 367/352, 374, 439	3.41	493/577	3.63 : 3.05/—	0.58	28/1	5.28	6.17

λ_{Abs} are wavelengths of absorption maxima; λ_{FL} are wavelengths of emission maxima; Stokes shift = $\lambda_{Fl} - \lambda_{Abs}$; S_1 is the singlet energy estimated as $1240/\lambda_{Flu\ onset}$; T_1 is the triplet energy estimated as $1240/\lambda_{PH\ onset}$; $\Delta E_{ST} = T_1 - S_1$; E_g^{opt} is optical gap estimated as $1240/\lambda_{Abs\ onset}$ where $\lambda_{Abs\ onset}$ is the wavelength of the onset of absorption; IE_{PE} is the ionisation potential estimated by photoelectron emission spectrometry in air; IE_{CV} is the ionisation potential estimated by CV as $IE_{CV} = E_{onset\ ox\ vs.\ Fc} + 5.1$ eV.[31,32]

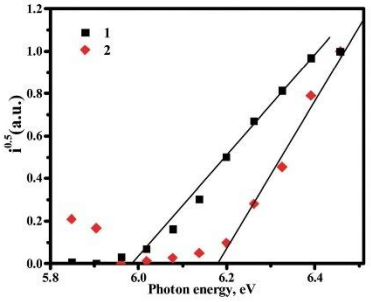

Fig. 3 Photoelectron emission spectra of solid samples of compounds **1** and **2** recorded in air.

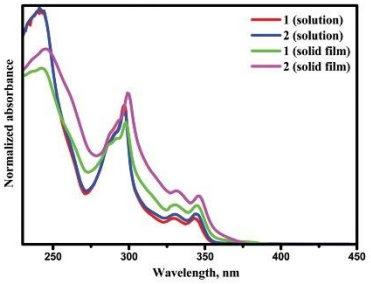

Fig. 4 UV spectra of dilute solutions and thin films of compounds **1** and **2**.

In order to obtain insights into the optical properties of compounds **1** and **2**, TDDFT calculations were carried out on each of the optimised structures using geometries obtained with both default- and tuned ω-values. The results of these calculations are summarised in Table 4. When calculating S_1 and T_1 transitions, it is important that the nature of the excitation is described appropriately. In order to maximise the reverse intersystem crossing, there should be a change in the symmetry of the excited state, so typically in donor–acceptor compounds, the T_1 excitation is a local excitation (LE) and S_1 excitation is a charge transfer (CT) state.[33] Natural transition orbitals (NTOs)[34] for holes and electrons corresponding to the S_1 and T_1 states of compounds **1** and **2** are shown in Fig. 5 and 6, respectively, whilst the full list of TDDFT transitions for both compounds is presented in Fig. S4–S11 (ESI†). In order to further characterise these transitions, the spatial overlap (Λ) for all excitations has been reported.

The NTOs corresponding to the T_1 states of compounds **1** and **2** (Fig. 5 and 6) indicate that both holes and electrons are globally localised on the electron-donating carbazole units, irrespective of the geometry used, highlighting the ^{3}LE nature of these transitions. The calculated T_1 energies using both default ω and ω-CPCM methods show good agreement with one another for both compounds and show generally similar spatial overlap for the transitions.

However, the calculated S_1 energies are significantly different when using the separate methods. Calculations with the default ω show an increased S_1 energy in both compounds, resulting in a large calculated ΔE_{ST}. The NTOs with the default ω have a generally large spatial overlap with occupied and unoccupied orbitals involved in the dominant transitions localised on the carbazole units. Therefore, the S_1 state does not show the CT character that would be expected for a donor–acceptor compound.

When the ω-CPCM value is used for the TDDFT calculations, the S_1 energy is significantly reduced and this can be explained by the increased CT nature of the transitions. The spatial overlap, Λ, is significantly reduced with the electron-NTOs of **1** and **2** (Fig. 5 and 6) localised on the electron-deficient 1,3,5-trifluorobenzene groups. The predicted ΔE_{ST} energy is significantly reduced and in good agreement with experimental values (see optical emission properties section), although it is too high for the material to be used alone as a thermally activated delayed fluorescence (TADF) candidate. Furthermore, the individual T_1 and S_1 energies show relatively good agreement compared to experimentally determined values, which is useful in the design of exciplex emissive layers.

The singlet excitations from the TDDFT calculations are listed in Table S1 (ESI†). As previously mentioned, the S_1 transitions show local excitations when default ω is used but CT states are observed in both compounds when ω-CPCM is used. The nature of the excitation is important when comparing with the experimental absorption spectrum. Compound **1** shows the S_1 excitation to have a small oscillator strength ($f = 0.01$), whilst that of the first local excitation, S_3, is higher ($f = 0.04$). In compound **2**, there is a similar

Table 4 Summary of TDDFT calculations for **1** and **2** carried out using default ω or ω-CPCM

		T_1 (eV)	T_1 (nm)	f T_1	S_1 (eV)	S_1 (nm)	f S_1	ΔE_{ST}
1	Default ω	3.21 (H−1 → L+1)[a]	385.7	0.68	4.21 (H → L+1)[a]	294.7	0.67	1.00
	ω-CPCM	3.17 (H−1 → L+2)[a]	390.6	0.72	3.81 (H → L)[a]	325.1	0.16	0.64
2	Default ω	3.21 (H−2 → L+1)[a]	386.2	0.72	4.24 (H → L+1)[a]	292.6	0.67	1.03
	ω-CPCM	3.17 (H−3 → L+3)[a]	390.8	0.61	3.66 (H → L)[a]	338.7	0.20	0.49

[a] The most dominant individual transitions from TDDFT calculations are shown in parentheses. Full lists of these transitions, with molecular orbital diagrams, are presented in Fig. S4–S11 (ESI).

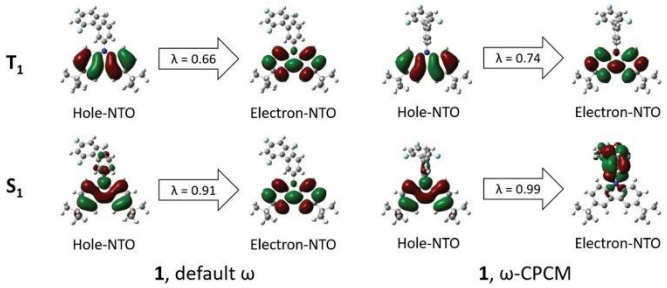

Fig. 5 NTOs corresponding to S_1 and T_1 states for compound **1** obtained by means of the TDDFT method at the ωB97XD/6-31++G(d,p) level by using default ω (left) and ω-CPCM (right). λ = NTO eigenvalue.

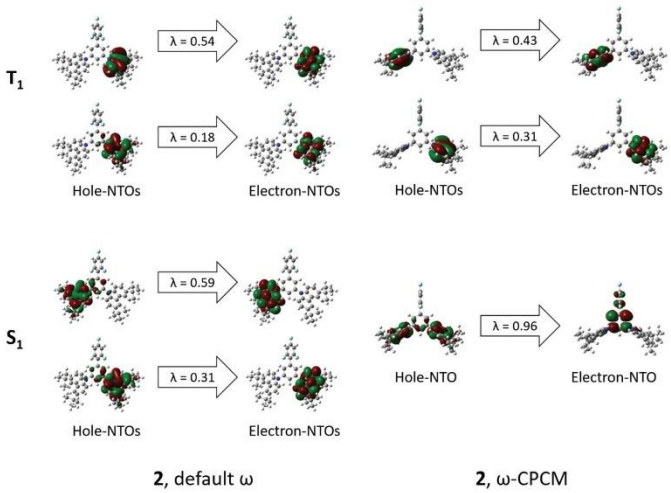

Fig. 6 NTOs corresponding to S1 and T1 states of **2** obtained by means of the TDDFT method at the ωB97XD/6-31++G(d,p) level by using default ω (left) and ω-CPCM (right). λ = NTO eigenvalue.

trend where the S_1 excitation ($f = 0.02$) also has a lower oscillator strength than the lowest energy local excitation S_5 ($f = 0.07$). This suggests that the UV/Vis absorption spectrum will be dominated by the absorption of the carbazole unit. The lowest energy local excitations for compounds **1** and **2** occur at 313 and 312 nm, respectively, which is in good agreement with the experimental peaks at 297 nm for both compounds (Table 3).

The sensitivity of the S_1 excitation to the environment in TDDFT calculations has been shown and therefore it is important that this is taken into consideration when estimating ΔE_{ST}, using the ω-tuned functional as an effective means of improving the accuracy of the estimation.

Optical emission properties

The photophysical properties of compounds **1** and **2** are determined by their geometrical structures and the changes after excitation. The vibronically structured emission bands of the solutions of **1** and **2** in toluene at room temperature were observed in the deep blue region (Fig. 7), with PLQY values of 13% and 28%. This is supplemented by small Stokes shift values, which can be explained by minimal changes in geometry and solvent reorganisation upon excitation in the dilute toluene solutions of both the compounds. The triplet energy values determined from the onsets of the phosphorescence (PH) spectra of compounds **1** and **2** were found in the blue region. The experimental ΔE_{ST} values were found to be relatively high (Table 3). This observation is in good agreement with the results of theoretical calculations. Due to the potential application of **1** and **2** in the emissive layers of OLEDs, we further focused on the investigation of the solid-state photophysical properties of the compounds.

The PL spectra of thin films of compounds **1** and **2** were also vibronically structured in the same range of *ca.* 350–400 nm as those of their toluene solutions (Fig. 7). The PLQY values of the solid samples were found to be low ($\sim$1%) due to aggregation-induced quenching.[35] The origin of the low-energy band was studied more extensively. PL spectra of the non-evacuated and evacuated neat thin films were recorded at room temperature (Fig. S12a and c, ESI†). The PL spectrum of compound **1** was found to be sensitive to oxygen. The ratio of PL intensities ($I_{evac}/I_{pre\text{-}evac}$) was 1.9. The PL intensity change in the low-energy band of compound **1** confirms the impact of triplet states possibly through reverse intersystem crossing (RISC). PL decay curves of the solid sample of **1** were recorded (Fig. S12b, ESI†). They contained two components, *i.e.* a short-lived component in the ns range corresponding to a local excited (^{1}LE) state at higher energies and a CT component at lower energies.

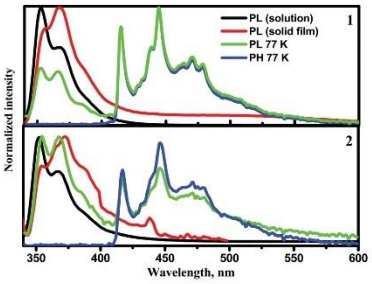

Fig. 7 PL spectra of toluene solutions and of solid films of compounds **1** and **2** recorded at room temperature (λ_{exc} = 330 nm) and PL and PH spectra recorded at 77 K.

The PL spectrum of the solid sample of compound **2** was not significantly sensitive to oxygen. A slight increase of PL intensity was observed after evacuation (Fig. S12c, ESI†). PL decay curves of the solid sample of compound **2** (Fig. S12d, ESI†) contained two short-lived components in the ns range corresponding to ^{1}LE emission. Slight differences in emission spectra and their sensitivity to oxygen in the solid samples of compounds **1** and **2**, and in sensitivity of the PL spectra to oxygen, are apparently related to the different substitution patterns of the trifluorobiphenyl moiety. Taking into account the aggregation-induced quenching of emission of **1** and **2**, it was decided to test the photophysical properties of these compounds in doped systems.

Compounds **1** and **2** formed sky-blue exciplexes with the electron acceptor 2,4,6-tris[3-(diphenylphosphinyl)phenyl]-1,3,5-triazine (PO-T2T), which is one of the most widely studied exciplex-forming acceptors (Fig. 8).[36,37] The spectra of solid films of molecular mixtures of **1** and **2** with PO-T2T showed significant red shifts in comparison to the PL spectra of non-doped films of the compounds. PL spectra of both exciplex-forming systems were found to be broad and typical of CT. The exciplex-forming mixtures **1**: PO-T2T and **2**: PO-T2T exhibited rather low PLQY values of 4% and 2% in air, respectively. The PL spectra of exciplexes **1**: PO-T2T and **2**: PO-T2T peaked at the wavelengths of 489 and 470 nm (2.48 and 2.67 eV), respectively (Fig. 8a). This observation can be explained by the relatively high I_P^D values of compounds **1** and **2** 5.98 eV for compound **1** and 6.17 eV for compound **2** (Fig. 3 and Table 3) taking into account the equation[38] $h\nu_{ex}^{max} \simeq I_P^D - E_A^A - E_C$ (2.54 eV for **1**: PO-T2T and 2.67 eV for **2**: PO-T2T), where I_P^D is the ionization potential of the donor (compound **1** or **2**), E_A^A is the electron affinity of the acceptor (3.5 eV for PO-T2T), and E_C is the electron–hole Coulombic attraction energy. It should be noted that the trifluorobiphenyl moiety was mainly used to increase the ionization potential of compounds **1** and **2**, resulting in blue-shifted emission of exciplexes formed between compound **1** (or **2**) and PO-T2T.

The molecular mixtures **1**: PO-T2T and **2**: PO-T2T were characterised by PL decays in the μs region with shapes attributed to exciplex emission but not to monomer emission (Fig. 8b). The nanosecond-lived components of the decay curves represent prompt fluorescence, whilst the longer-lived components can be attributed to thermally activated delayed fluorescence. This assumption is in agreement with the PL decays of exciplexes **1**: PO-T2T and **2**: PO-T2T recorded at room temperature (295 K) and at the temperature of liquid nitrogen (77 K) (Fig. S13, ESI†). The intensity of the long-lived component is higher at 295 K than at 77 K, proving the TADF nature of the exciplex emissions.

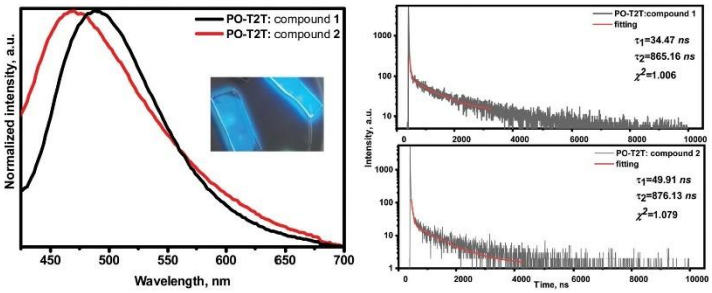

a) b)

Fig. 8 Normalised PL spectra with photo of emissive layers inset (a) and PL decay curves (b) of solid molecular mixtures of **1** or **2** with PO-T2T (λ_{exc} = 330 nm).

PL decay curves for the films of the mixtures of **1** with PO-T2T and of **2** with PO-T2T in air and under vacuum were recorded. The increasing intensity (shown by the arrows) of the delayed component of their emission under an inert atmosphere indicates a triplet contribution to the whole emission intensity (Fig. S14, ESI†). The TADF origin of the delayed fluorescence of the exciplex-forming systems **1**: PO-T2T and **2**: PO-T2T was additionally confirmed by recording the dependence of PL intensity on laser pump pulse. The slope values of the straight lines were found to be *ca.* 1 (Fig. S15, ESI†).[39]

Devices

Fig. 9 shows the simplified structure and the equilibrium energy diagram of OLEDs with emitting layers (EMLs) of exciplex-forming mixtures of acceptor PO-T2T and donors **1** and **2**. Components of the EML were deposited in a molar ratio of 1 : 1. For better device performance, additional layers were used. A layer of 1,4,5,8,9,11-hexaazatriphenylenehexacarbonitrile (HAT-CN) was used as a hole injection layer (HIL), a layer of 4,4′-cyclohexylidenebis[*N*,*N*-bis(4-methylphenyl)benzenamine] (TAPC) was used as the hole transporting layer (HTL), a layer of 1,3-bis(*N*-carbazolyl)benzene (mCP) was used as the electron blocking layer (EBL), a layer of diphenyl[4-(triphenylsilyl)phenyl]phosphine oxide (TSPO1) was used as a hole blocking layer (HBL) and a layer of 1,3,5-tris(1-phenyl-1*H*-benzimidazol-2-yl)benzene (TPBi) was employed as an electron transporting layer (ETL). Thus, exploiting the device structure HAT-CN (10 nm)/TAPC (40 nm)/mCP (4 nm)/compound **1** or **2**: PO-T2T (1 : 1) (24 nm)/PO-T2T (4 nm)/TPBi (36 nm)/LiF (0.5 nm)/Al, OLEDs **D1** and **D2** containing compounds **1** or **2**, respectively, were fabricated.

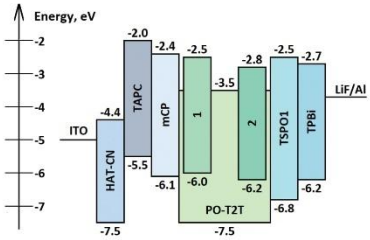

Fig. 9 Equilibrium energy diagram and structures of OLEDs.

Fig. 10 and Table 5 show the EL characteristics of the exciplex-based OLEDs with derivatives **1** and **2**. The overall OLED characteristics were better with **D2**, which was based on the emissive layer of the exciplex system **2**: PO-T2T. OLED **D2** showed a higher brightness of 4100 cd m^{-2}, while that of **D1** reached 1250 cd m^{-2}. Also, **D2** showed higher maximum current (CE), power (PE) and external quantum (EQE) efficiencies of 24.8 cd A^{-1}, 12.2 lm W^{-1} and 7.8%, respectively. The corresponding characteristics of **D1** were found to be 19.7 cd A^{-1}, 12.2 lm W^{-1} and 6.5% (Table 5). The efficiency roll-off of **D2** was better than that of **D1** possibly because of the higher thermal stability of compound **2** relative to that of compound **1** (Table 1). When brightness was increased from 100 cd m^{-2} to 1000 cd m^{-2}, the current, power and external quantum efficiencies also increased apparently due to the better charge carrier balance within the light-emitting layer at higher applied voltages. It should be noted that EQE values of both devices did not correlate with the PLQY values of solid films of **1** and **2**. A similar observation was reported by Monkman *et al.*,[38] who also used exciplex-forming mixtures with low PLQYs of films to obtain OLEDs with a high EQE. To the best of our knowledge, these are the best characteristics so far obtained from exciplex systems containing a fluorinated acceptor.[28]

Fig. 10c shows the electroluminescence (EL) spectra of **D1** and **D2**. The EL spectra of the devices did not correlate with the PL spectra of **1**: PO-T2T and **2**: PO-T2T (Fig. 7). PL spectra were observed in the blue region (Fig. 7), while the EL spectra were in

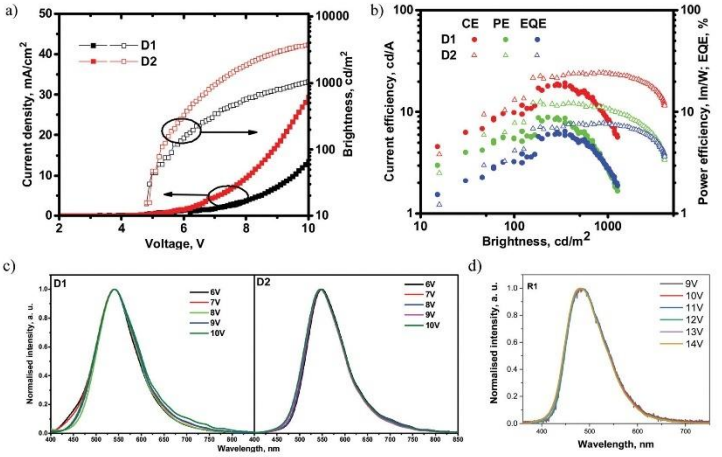

Fig. 10 (a) Current density and brightness *versus* voltage plots, (b) EQEs, and current and power efficiencies *versus* brightness plots, and (c) EL spectra recorded at different driving voltages of devices **D1**, **D2** and (d) device R1.

Table 5 EL characteristics of exciplex-based OLEDs with compounds **1** and **2**

Device	λ_{max} (nm)	V_{on} (V)	Brightness$_{max}$ (cd m^{-2})	CE/PE/EQE (cd A^{-1}/lm W^{-1}/%) Max	CE/PE/EQE (cd A^{-1}/lm W^{-1}/%) @100 cd m^{-2}	CE/PE/EQE (cd A^{-1}/lm W^{-1}/%) @1000 cd m^{-2}
D1	541	4.8	1250	19.7/8.4/6.5	9.9/5.5/3.3	8.5/2.7/2.8
D2	546	4.8	4100	24.8/12.2/7.8	13.2/7.8/4.2	24.3/10.7/7.7

the green region (Fig. 10c). This result is quite intriguing since there is no such functional material in the device structure that could be characterized by a similar green emission. This observation may be explained by the formation of lower energy exciplexes, which were detected for other exciplex-forming mixtures such as mCP:PO-T2T.[37] To prove this presumption, PL spectra of the films of the mixtures **1**: PO-T2T and **2**: PO-T2T were recorded before and after thermal annealing at *ca.* 120 °C trying to separate the lower energy exciplexes (Fig. S16, ESI†). Indeed, the annealed film of **1**: PO-T2T showed a red-shifted PL spectrum peaking at 505 nm in comparison to the PL spectrum of the non-annealed film (489 nm). Meanwhile, the PL spectra of the non-annealed and annealed films of **2**: PO-T2T were practically identical. This experimental result does not fully explain the differences between the PL and EL spectra of **1**: PO-T2T and **2**: PO-T2T (Fig. 8a, 10c and Table 5).

On the another hand, the EL spectra of devices **D1** and **D2** can be affected by exciplex emission of other exciplex-forming systems, especially knowing that exciplexes can be formed at the interfaces or even through spacers.[39,40] In principle, at least several exciplex-forming systems, such as: mCP:PO-T2T (472 nm),[41–43] TAPC:PO-T2T (550 nm),[44] and TAPC:TPBi (442 nm),[44] could be formed in the devices. In addition, TAPC is characterized by excimer (450 nm) and electromer (580 nm) emission,[45] although none of these species emit in the green region. To determine the origin of EL emission, the device structure was simplified to the following one: ITO/HAT-CN (10 nm)/TCTA (40 nm)/compound **1** (4 nm)/compound **1**: PO-T2T (24 nm)/PO-T2T (40 nm)/LiF/Al (device R1). This device R1 was used as the reference, and the layers of TAPC, mCP and TPBi were replaced by those of tris(4-carbazoyl-9-ylphenyl)amine (TCTA), compound **1**, and PO-T2T, respectively. As a result, the EL spectrum of device R1 peaking at 480 nm was very similar to the PL spectrum of **1**: PO-T2T (Fig. 7 and 10d). The simplified device R1 showed a relatively high turn-on voltage of 9.8 V and maximum EQE of 3.4% (Fig. S17, ESI†). Having the EL spectra of the device R1, it can be concluded that the EL spectra of devices **D1** and **D2** most probably resulted from overlapping of emissions of exciplexes of **1**: PO-T2T (**2**: PO-T2T) and the TAPC-based exciplex TAPC: PO-T2T (or electromer of TAPC). As a result of such overlapping, green electroluminescence was obtained for devices **D1** and **D2**. Similar EL behaviour was previously discussed elsewhere.[46] Blue- and red-shifted EL spectra were well reproduced for other configurations of TAPC-free and TAPC-containing devices, respectively

(Fig. S18, ESI†). These observations prove the presumption of overlapping of two or more EL species.

Conclusions

Two derivatives of trifluorobiphenyl and 3,6-di-*tert*-butylcarbazole were synthesised as potential components for emitting layers in OLEDs. Different experimental characterization methods and different DFT methods using the default- and tuned ω parameter were used to explore the structural, redox, and optoelectronic properties of the two compounds. The results indicate that the additional carbazole on compound **2** adds an additional electron rich unit for the formation of the donor–acceptor exciplex, but it has a minimal effect on the energy levels of compound **2** relative to compound **1**. The synthesised compounds exhibited very high triplet-energy values of 3.03 eV and 3.06 eV in solutions, respectively. However, the singlet–triplet energy splitting, reaching 0.64 eV, was too high for the materials to be used alone as TADF emitters, but the compounds showed good exciplex-forming abilities in combination with the electron acceptor 2,4,6-tris[3-(diphenylphosphinyl)phenyl]-1,3,5-triazine. Using the synthesized compounds, highly efficient exciplex-based OLEDs were developed. In the best case, high maximum current, power and external quantum efficiencies of 24.8 cd A^{-1}, 12.2 lm W^{-1} and 7.8%, respectively, were achieved for the devices based on exciplex electroluminescence.

Conflicts of interest

There are no conflicts to declare.

Acknowledgements

R. K. and L. L. acknowledge the Research, Development and Innovation Fund of Kaunas University of Technology (project grant no. PP-91C/19) for the financial support. The authors acknowledge the European Union's Horizon 2020 Research and Innovation Programme under the Marie Skłodowska-Curie grant agreement no. 823720. J. C. and P. J. S. also thank the EPSRC for funding (EP/N035496/2). Data associated with theoretical calculations is available at http://dx.doi.org/10.5525/gla.researchdata.1061.

References

1 T.-A. Lin, T. Chatterjee, W.-L. Tsai, W.-K. Lee, M.-J. Wu, M. Jiao, K.-C. Pan, C.-L. Yi, C.-L. Chung, K.-T. Wong and C.-C. Wu, *Adv. Mater.*, 2016, **28**, 6976–6983.
2 X. Liang, H. B. Han, Z. P. Yan, L. Liu, Y. X. Zheng, H. Meng and W. Huang, *New J. Chem.*, 2018, **42**, 4317–4323.
3 K. Shizu, H. Noda, H. Tanaka, M. Taneda, M. Uejima, T. Sato, K. Tanaka, H. Kaji and C. Adachi, *J. Phys. Chem. C*, 2015, **119**, 26283–26289.
4 P. Data, M. Okazaki, S. Minakata and Y. Takeda, *J. Mater. Chem. C*, 2019, **7**, 6616–6621, DOI: 10.1039/C9TC00909D.
5 D. Wei, F. Ni, Z. Wu, Z. Zhu, Y. Zou, K. Zheng, Z. Chen, D. Ma and C. Yang, *J. Mater. Chem. C*, 2018, **6**, 11615–11621.
6 R. Komatsu, H. Sasabe, Y. Seino, K. Nakao and J. Kido, *J. Mater. Chem. C*, 2016, **4**, 2274–2278.
7 T. Komino, H. Nomura, T. Koyanagi and C. Adachi, *Chem. Mater.*, 2013, **25**, 3038–3047.
8 J. W. Sun, J.-H. Lee, C.-K. Moon, K.-H. Kim, H. Shin and J.-J. Kim, *Adv. Mater.*, 2014, **26**, 5684–5688.
9 H.-B. Kim, D. Kim and J.-J. Kim, *Highly Efficient OLEDs*, Wiley-VCH Verlag GmbH & Co. KGaA, Weinheim, Germany, 2018, pp. 331–376.
10 M. Chapran, E. Angioni, N. J. Findlay, B. Breig, V. Cherpak, P. Stakhira, T. Tuttle, D. Volyniuk, J. V. Grazulevicius, Y. A. Nastishin, O. D. Lavrentovich and P. J. Skabara, *ACS Appl. Mater. Interfaces*, 2017, **9**, 4750–4757.
11 T.-C. Lin, M. Sarma, Y.-T. Chen, S.-H. Liu, K.-T. Lin, P.-Y. Chiang, W.-T. Chuang, Y.-C. Liu, H.-F. Hsu, W.-Y. Hung, W.-C. Tang, K.-T. Wong and P.-T. Chou, *Nat. Commun.*, 2018, **9**, 3111.
12 B. Zhang and Z. Xie, *Front. Chem.*, 2019, **7**, 306.
13 D. D. Gebler, Y. Z. Wang, J. W. Blatchford, S. W. Jessen, D.-K. Fu, T. M. Swager, A. G. Macdiarmid and A. J. Epstein, Exciplex emission in bilayer polymer light-emitting devices, *Appl. Phys. Lett.*, 1997, **70**, 1644–1646.
14 K. Goushi, K. Yoshida, K. Sato and C. Adachi, *Nat. Photonics*, 2012, **6**, 253–258.
15 V. Lukeš, D. Cagardová, M. Michalík and P. Poliak, *Synth. Met.*, 2018, **240**, 67–76.
16 M. D. Curtis, J. Cao and J. W. Kampf, *J. Am. Chem. Soc.*, 2004, **126**, 4318–4328.
17 S. A. Sharber, R. N. Baral, F. Frausto, T. E. Haas, P. Müller and S. W. Thomas III, *J. Am. Chem. Soc.*, 2017, **139**, 5164–5174.
18 A. Mukherjee and G. R. Desiraju, *Cryst. Growth Des.*, 2011, **11**, 3735–3739.
19 Y. Kumar, S. Kumar, S. Kumar Keshri, J. Shukla, S. S. Singh, T. S. Thakur, M. Denti, A. Facchetti and P. Mukhopadhyay, *Org. Lett.*, 2016, **18**, 472–475.
20 G. Conboy, H. J. Spencer, E. Angioni, A. L. Kanibolotsky, N. J. Findlay, S. J. Coles, C. Wilson, M. B. Pitak, C. Risko, V. Coropceanu, J.-L. Brédas and P. J. Skabara, *Mater. Horiz.*, 2016, **3**, 333–339.
21 P. Boufflet, Y. Han, Z. Fei, N. D. Treat, R. Li, D.-M. Smilgies, N. Stingelin, T. D. Anthopoulos and M. Heeney, *Adv. Funct. Mater.*, 2015, **25**, 7038–7048.
22 J. R. Loader, S. Libri, A. J. H. M. Meijer, R. N. Perutz and L. Brammer, *CrystEngComm*, 2014, **16**, 9711–9720.
23 H. Luo, X. Dong, Z. Cai, L. Wang and Z. Liu, *Asian J. Org. Chem.*, 2018, **7**, 592–597.
24 Y. Sakamoto, T. Suzuki, M. Kobayashi, Y. Gao, Y. Fukai, Y. Inoue, F. Sato and S. Tokito, *J. Am. Chem. Soc.*, 2004, **126**, 8138–8140.
25 Z. Chen, W. Zhang, J. Huang, D. Gao, C. Wei, Z. Lin, L. Wang and G. Yu, *Macromolecules*, 2017, **50**, 6098–6107.
26 T. X. Carroll, T. D. Thomas, H. Bergersen, K. J. Børve and L. J. Sæthre, *J. Org. Chem.*, 2006, **71**(5), 1961–1968.
27 M. Gsänger, D. Bialas, L. Huang, M. Stolte and F. Würthner, *Adv. Mater.*, 2016, **28**, 3615–3645.

28 M. Mamada, G. Tian, H. Nakanotani, J. Su and C. Adachi, *Angew. Chem., Int. Ed.*, 2018, **57**, 12380–12384.
29 L. Liu, B. Yang, H. Zhang, S. Tang, Z. Xie, H. Wang, Z. Wang, P. Lu and Y. Ma, *J. Phys. Chem. C*, 2008, **112**, 10273–10278.
30 X. Sallenave, A. Bucinskas, S. Salman, D. Volyniuk, O. Bezvikonnyi, V. Mimaite, J. V. Grazulevicius and G. Sini, *J. Phys. Chem. C*, 2018, **122**, 10138–10152.
31 C. M. Cardona, W. Li, A. E. Kaifer, D. Stockdale and G. C. Bazan, *Adv. Mater.*, 2011, **23**, 2367–2371.
32 R. Rybakiewicz, P. Gawrys, D. Tsikritzis, K. Emmanouil, S. Kennou, M. Zagorska and A. Pron, *Electrochim. Acta*, 2013, **96**, 13–17.
33 M. Y. Wong and E. Zysman-Colman, *Adv. Mater.*, 2017, **29**(22), 1605444, DOI: 10.1002/adma.201605444.
34 R. L. Martin, *J. Chem. Phys.*, 2003, **118**, 4775–4777.
35 S. A. Jenekhe and J. A. Osaheni, *Science*, 1994, **265**, 765–768.
36 W.-Y. Hung, G.-C. Fang, Y.-C. Chang, T.-Y. Kuo, P.-T. Chou, S.-W. Lin and K.-T. Wong, *ACS Appl. Mater. Interfaces*, 2013, **5**, 6826–6831.
37 M. Guzauskas, D. Volyniuk, A. Tomkeviciene, A. Pidluzhna, A. Lazauskas and J. V. Grazulevicius, *J. Mater. Chem. C*, 2019, **7**, 25–32.
38 M. Colella, A. Danos and A. P. Monkman, *J. Phys. Chem. Lett.*, 2019, **10**, 793–798.
39 M. Cekaviciute, J. Simokaitiene, D. Volyniuk, G. Sini and J. V. Grazulevicius, *Dyes Pigm.*, 2017, **140**, 187–202.
40 Y. J. Pu, Y. Koyama, D. Otsuki, M. Kim, H. Chubachi, Y. Seino, K. Enomoto and N. Aizawa, *Chem. Sci.*, 2019, **10**, 9203–9208.
41 J. H. Lee, S. H. Cheng, S. J. Yoo, H. Shin, J. H. Chang, C. I. Wu, K. T. Wong and J. J. Kim, *Adv. Funct. Mater.*, 2015, **25**, 361–366.
42 P. Yuan, X. Guo, X. Qiao, D. Yan and D. Ma, *Adv. Opt. Mater.*, 2019, **7**, 1801648.
43 X.-K. Liu, Z. Chen, C.-J. Zheng, C.-L. Liu, C.-S. Lee, F. Li, X.-M. Ou and X.-H. Zhang, *Adv. Mater.*, 2015, **27**, 2378–2383.
44 X. Wei, L. Gao, Y. Miao, Y. Zhao, M. Yin, H. Wang and B. Xu, *J. Mater. Chem. C*, 2020, **8**, 2772–2779.
45 S. Yang and M. Jiang, *Chem. Phys. Lett.*, 2009, **484**, 54–58.
46 E. Skuodis, A. Tomkeviciene, R. Reghu, L. Peciulyte, K. Ivaniuk, D. Volyniuk, O. Bezvikonnyi, G. Bagdziunas, D. Gudeika and J. V. Grazulevicius, *Dyes Pigm.*, 2017, **139**, 795–807.

8. CURRICULUM VITAE

Matas Gužauskas
Matas.guzauskas@ktu.lt

Education:

2014 – 2018 Bachelor's degree "Material Science and Nanotechnology", Kaunas University of Technology

2018 – 2020 Master's degree "Material Science", Kaunas University of Technology

2020 – 2024 PhD studies "Material Engineering", Kaunas University of Technology

Professional experience:

2018 – 2020 Project Engineer

2020 – now Junior researcher

Secondments:

2020 – 2021 Guest researcher at TU Dresden, Dresden Germany (6 months)

2021 Guest researcher at Lviv Polytechnic National University, Lviv, Ukraine (1 month)

2022 Guest researcher at National Taiwan University, Taipei, Taiwan (3 months)

2020 Guest researcher at TU Dresden, Dresden Germany (3 months)

9. LIST OF SCIENTIFIC PAPERS AND CONFERENCES

List of scientific publications on the topic of dissertation

1. **Gužauskas, M**.; Narbutaitis, E.; Volyniuk, D.; Baryshnikov, G. V.; Minaev, B. F.; Ågren, H.; Chao, Y.; Chang, C.; Rutkis, M.; Grazulevicius, J. V. Polymorph acceptor-based triads with photoinduced TADF for UV sensing // Chemical engineering journal. Lausanne: Elsevier. ISSN 1385-8947. eISSN 1873-3212. 2021, vol. 425, art. no. 131549, p. 1-9. DOI: 10.1016/j.cej.2021.131549. [IF: 16,744; AIF: 8,626; IF/AIF: 1,941; Q1(Web of Science)]

2. Kulszewicz-Bajer, I.; **Guzauskas, M**.; Makowska-Janusik, M.; Zagórska, M.; Mahmoudi, M.; Grazulevicius, J. V.; Proń, A.; Volyniuk, D. Acridone and quinacridone derivatives with carbazole or phenoxazine substituents: synthesis, electrochemistry, photophysics and application as TADF electroluminophores // Journal of materials chemistry C. Cambridge: Royal society of chemistry. ISSN 2050-7526. eISSN 2050-7534. 2022, vol. 10, iss. 34, p. 12377-12391. DOI: 10.1039/d2tc02270b. [IF: 6,400; AIF: 5,750; IF/AIF: 1,113; Q1 (Web of Science)]

3. **Guzauskas, M**.; Volyniuk, D.; Kulszewicz-Bajer, I.; Mahmoudi, M.; Lazauskas, A.; Jasinskas, V.; Gulbinas, V.; Pron, A.; Grazulevicius, J. V. Thermally controllable tuning of emission properties of phenoxazine-substituted acridones as one step forward to efficient organic light-emitting diodes based on crystalline emitters // Advanced optical materials. Weinheim: Wiley- VCH. ISSN 2195-1071. 2023, vol. 11, iss. 24, art. no. 2301059, p. 1-11. DOI: 10.1002/adom.202301059. [IF: 9,000; AIF: 4,900; IF/AIF: 1,836; Q1(Web of Science)]

4. Keruckiene, R.; **Guzauskas, M**.; Lapienyte, L.; Simokaitiene, J.; Volyniuk, D.; Cameron, J.; Skabara, P.J.; Sini, G.; Grazulevicius, J.V. An experimental and theoretical study of exciplex-forming compounds containing trifluorobiphenyl and 3,6-di-tert-butylcarbazole units and their performance in OLEDs // Journal of materials chemistry C. Cambridge: Royal society of chemistry. ISSN 2050-7526. eISSN 2050-7534. 2020, vol. 8, iss. 40, p. 14186-14195. DOI: 10.1039/d0tc02777d. [IF: 7,393; AIF: 5,532; IF/AIF: 1,336; Q1 (Web of Science)]

Scientific conferences:

1 **GUŽAUSKAS, Matas**; KULSZEWICZ-BAJER, Irena; MAKOWSKA-JANUSIK, Małgorzata; VOLYNIUK, Dmytro; GRAŽULEVIČIUS, Juozas Vidas. Investigation of the annealing effect on the photophysical and elevtro-optical properties of acridone derivatives with phenoxazine substitutes. In: Chemistry and Chemical Technology: proceedings of international scientific conference, Kaunas, 2022. Kaunas: Kaunas University of technology, 2022, pp. 149-150. ISSN 2538-7359.

2 **GUŽAUSKAS, Matas**; KULSZEWICZ-BAJER, Irena; MAKOWSKA-JANUSIK, Małgorzata; VOLYNIUK, Dmytro; GRAŽULEVIČIUS, Juozas Vidas. From green to blue: how annealing affects emission properties acridone derivatives with phenoxazine substitutes. In: Advanced materials and technologies: book of abstracts of 24th international conference-school, 22-26 August 2022, Palanga, Lithuania. Kaunas: Kaunas University of Technology, 2022, B-P57, pp. 94-94 [žiūrėta 2022-09-29]. ISSN 2669-1930.

3 **GUZAUSKAS, Matas**; NARBUTAITIS, Edgaras; VOLYNIUK, Dmytro; GRAZULEVICIUS, Juozas Vidas. Investigation of photo induced conformational changes in organic fluorescence emitters. In: Open readings 2020: 63rd international conference for students of physics and natural sciences, March 17-20, Vilnius, Lithuania: abstract book. Vilnius: Vilnius University, 2020, P3-21, pp. 349-349 [žiūrėta 2020-05-12]. ISBN 9786090703779.

4 **GUZAUSKAS, Matas**; VOLYNIUK, Dmytro; KULSZEWICZ-BAJER, Irena; LAZAUSKAS, Algirdas; PRON, Adam; GRAZULEVICIUS, Juozas V. Controllable crystallisation of emissive layers in OLEDs: investigating the role of conformational stabilization and properties enhancement for higher efficiencies and colour tuning. In: ICOE2023: 16th international conference on organic electronic, Madrid, 2023, July 3-7: book of abstracts. [S.l.]: [s.n.], 2023, pp. 157-157.

5 **GUŽAUSKAS, Matas**; KULSZEWICZ-BAJER, Irena; MAKOWSKA-JANUSIK, Małgorzata; VOLYNIUK, Dmytro; GRAŽULEVIČIUS, Juozas Vidas. Thermally-induced conformational equilibration for enhanced efficiency and colour purity in organic light-emitting diodes. In: Multidisciplinary international school of nanobiomaterials engineering: workshop on bionanomaterial and nanomaterial engineering, 18-23 June 2023: poster session abstract book. [Lodz]: [Lodz university of technology], 2023, pp. 21-21.

6 **GUŽAUSKAS, M**.; KULSZEWICZ-BAJER, I.; MAKOWSKA-JANUSIK, M.; VOLYNIUK, D.; GRAŽULEVIČIUS, J.v. Acridone derivatives with phenoxazine subtitutes: investigation of annealing effect on photophysical and electrooptical properties. In: Baltic polymer symposium 2022, Tallinn, Estonia, September 21–23, 2022: programme and abstracts. Tallinn: Tallinn University of technology, 2022, pp. 50-50.

7 **GUZAUSKAS, Matas**; NARBUTAITIS, Edgaras; VOLYNIUK, Dmytro; CHAO, Yu-Chiang; RUTKIS, Martins; GRAZULEVICIUS, Juozas. Organic emitters with photo induced conformational changes for ratiometric and colourimetric UV sensing. In: 63rd electronic materials conference (EMC 2021), June 23-25, 2021, Columbus, USA. Columbus: Ohio State University, 2021, PS2.27, pp. 77-77.

10. ACKNOWLEDGEMENTS

I would like to express my gratitude to my supervisor Dr. Hab. Dmytro Volyniuk for mentoring me throughout these years, for all the discussions, insights, and for allowing me to delve deeper into the world of organic semiconductors.

My thanks to Prof. Dr. Hab. Juozas Vidas Gražulevičius, who kindly invited me to his group and provided opportunities for me to pursue my goals in the scientific world.

I am very grateful to Dr. Jūratė Simokaitienė, Dr. Rasa Keruckienė, Dr. Asta Dabulienė, and Dr. Viktorija Andrulevičienė for the countless times they helped me solve both scientific and personal matters.

I would also like to thank my advisor, Dr. Rita Butkutė, for her constructive comments on my dissertation, which led to significant improvements.

I acknowledge my partners from Poland and Edgaras Narbutaitis for their synthesis of the materials that provided unique properties for me to investigate.

Thanks to the reviewers, Prof. Dr. Jolita Ostrauskaitė, Dr. Šarūnas Meškinis, and Assoc. Prof. Audrius Bučinskas, for their numerous comments and insights, which helped refine my dissertation.

Enormous thanks to all the colleagues I befriended along the way at Kaunas University of Technology, Technical University of Dresden, National Taiwan University, who helped me grow as a scientist.

I am especially grateful to Karolis Leitonas, with whom I began this scientific journey, for all the adventures we shared, and to my parents, Aušra and Arvydas, who, to this day, do not fully understand what I do but still show love and support.

Special thanks to my lovely wife, Justina, who picked me up when I was down, pushed me forward when I got stuck, and patiently waited each time I was away.

Finally, I want to dedicate this work to my grandmother, Aldona, to whom I am eternally thankful for her love, support, and encouragement.

UDK 547-3+621.383.52+621.315.59](474.5)(043.3)

SL344. 20xx-xx-xx, xx leidyb. apsk. l. Tiražas 14 egz. Užsakymas xxx.
Išleido Kauno technologijos universitetas, K. Donelaičio g. 73, 44249 Kaunas
Spausdino leidyklos „Technologija“ spaustuvė, Studentų g. 54, 51424 Kaunas